KU LEUVEN

DOCTORAL SCHOOL of
BIOMEDICAL SCIENCES

Biomedical Sciences Group
Faculty of Medicine
Department of Imaging and Pathology
Division of Nuclear Medicine & Molecular Imaging

Rigid Motion Correction for Positron Emission Tomography Brain Imaging

Matthew Gilbert BICKELL

Promoter:
Professor Johan Nuyts

Jury Members:
Professor Steve Meikle
Professor Jörg van den Hoff
Professor Karolien Goffin
Professor Jan D'hooge

Session Chair:
Professor Michel Koole

Dissertation presented in partial fulfilment of the requirements for the degree of Doctor in Biomedical Sciences

January 2017

Acknowledgements

It did not take long for me to realise how fortunate I was to have a supervisor like Johan. He has supervised between six and eight students and researchers at any one time over the past 4 years, and yet his ability to stay completely engaged in every project is unfailing. Any of us could walk into his office at any time, and he would give us his full attention. The benefit this provides to our research is immense, and I know that very few students have this privilege. His input into my research has been invaluable; he has offered me so much of his knowledge and experience while still allowing me to follow my own line of research when I wanted to. So thank you, Johan, I could not have done this without you.

Many thanks to my jury members, Prof. Steve Meikle, Prof. Jörg van den Hoff, Prof. Karolien Goffin, and Prof. Jan D'hooge. Your input into my thesis was very much appreciated, and I enjoyed receiving your comments, implementing them, and knowing that the thesis had improved as a result.

A special thanks to Prof. Roger Fulton who has been like a co-supervisor to me. I was fortunate enough to be able to collaborate with him on various aspects of the motion correction project, and it has been a great honour to work with such a giant in the field. I am very grateful to him for giving me the opportunity to visit his group in Sydney, Australia, which was such a special time for me. I thoroughly enjoyed the experience and being able to become close friends with the other researchers in his group.

I would like to thank our collaborators at New York University, Prof. Fernando Boada and Dr. Thomas Kösters, for providing me with data from the mMR scanner, together with our collaborators at Siemens Healthcare, especially Dr. Mike Casey, for details regarding their scanners. Thanks also to our collaborators at GE Healthcare and GE Global Research, Dr. Floris Jansen, Dr. Michel Tohme, and their team, for the data from and details of their Signa scanner, and Dr. Roland Bammer from HobbitView Inc. for the motion data. I look forward to continuing our collaborations in the future.

I am very grateful to my supervisor for my master's degree, Prof. Andy Buffler from the University of Cape Town, who got me involved and interested in medical imaging technology. He put me in touch with Prof. James Warwick from Tygerberg Hospital near Cape Town, who in turn introduced me to

Prof. Patrick Dupont from KU Leuven. Prof. Dupont saw that I was interested in image reconstruction and then introduced me to my current supervisor. Johan happened to have a project and a position available which suited my background very nicely. There were thus many people involved in my ending up in Leuven, and I am very grateful to you all for the part you played.

When I started my PhD I was still quite new to the field of medical imaging, and I knew that I had a lot to learn. The first year I was very fortunate to be able to work very closely with Dr. Lin Zhou, a post-doctoral researcher who had been supervised by Johan for her PhD and had continued working in his group. Lin had done a lot of the hard work in setting up the motion correction project, and I was able to join her in developing it further. In that first year she taught me so much about the medical imaging field. Lin, we spent so many hours together during experiments or at each other's desks, and I will always appreciate the help you gave me. The fact that you still appeared as a co-author on the papers I published two years after you left the group gives an indication of your impact on my PhD.

I conducted a great many experiments during the course of my PhD, and one person in particular helped me extensively in so many of those experiments: Julie Cornelis. Thank you Julie, for all your help! I know that the experiments were often tedious and involved many hours of preparation, but I could not have done them without you. I so enjoyed our many conversations during the experiments and I'm glad I had the opportunity to get to know you better.

A fellow colleague, Bart de Laat, also had an integral role to play in the development of my experimental protocol. I always knew that when I had a practical problem, or one with a more biological nature, I could go and have a chat to Bart and come away with a solution. We had so many interesting conversations because we shared similar interests but with different knowledge bases, and so we were able to learn much from each other. We also got on very well and I am very glad to have been able to get to know him better in the three years that our PhDs have overlapped. He is one of the few people who recognised my South African accent when we met, which I took as an auspicious start.

Throughout my PhD there have been many people who have had various levels of input, all of which are necessary for a successful PhD. Whether that input was technical, administrative, academic, or social, all were very much appreciated. A big thank you to Prof. Koen Van Laere, the head of the Department of Nuclear Medicine, for the support he has shown to my project over the years, and for always giving me access to the scanners for my experiments. He was also kind enough to provide funding for the tracking equipment used in the clinical studies. I owe a great thanks to my funding sources, namely the IMIR and MIRIAD projects, which, of course, made this PhD possible. Many thanks also to the head of those projects Prof. Guy Bormans for his input into my research and his support of the motion correction

project. Thanks also to the small animal imaging centre, the MoSAIC, for providing the opportunity to use the microPET scanner, on which so many of my experiments were conducted. Thank you to Dr. Peter Vermaelen, Dr. Ann Van Santvoort, and Dr. Cindy Casteels for all your help on the academic, administrative, and practical aspects. I am very appreciative of all the help that our departmental secretary, Francine Reniers, has given me over the years. I think I bothered her more than my fair share, but regardless she was always eager to help. Thanks to Dr. Willy Gsell for all the interesting conversations we had in the MoSAIC, and the advice he gave on various aspects of the data analysis. I really appreciated all the help I received from Prof. Michel Koole. As the kinetic modelling expert in our department, he is a great asset and he was always willing to give advice whenever I knocked on his door. I am also honoured to be the first person on whom he conferred a PhD degree, being the chairman at my doctoral defence. Many thanks for Marc Verbeeck and Joris De Ruyter from the technical services department for always being willing to lend their time, knowledge, experience, and tools whenever I needed to have something made for my experiments. Thanks to Kwinten Porters and Jef Van Loock for their technical help in all the clinical scans I conducted. Thanks to Dr. Tjibbe De Groot for producing the PE2i tracer for my later experiments, which I know was a very difficult task. And, of course, many thanks to the whole radiopharmaceutical team who produced FDG for me throughout the years. Our encounters seldom went further than a brief phone call, but I know that there was hard work being done on the other side of the transport tube. Many thanks to Dr. Kristof Baete, our resident medical physicist, for his support in many technical and practical aspects.

I had the opportunity to enjoy a great collaboration with some really amazing people in Sydney. I met Dr. Georgios Angelis first when he spent some time in Leuven, and we very quickly became good friends. I also worked closely with Dr. Andre Kyme, which has been a great pleasure. I have learnt so much while collaborating with Andre and Georgios, and I am so thankful to have had the opportunity to do so. I also thoroughly enjoyed my many conversations with Dr. John Gillam, who always had a very novel and interesting way of tackling and solving problems. Thanks also to Dr. Jung-Ha Kim for the collaboration we shared; the experiments were always more fun when we did them together.

Where would I be without my colleagues? There is a special bond formed between people going through a similar challenging experience, and I feel fortunate to share such a bond with the colleagues that I have had throughout these four years. The first time that I met Johan, he introduced me to the rest of the group knowing that I would need to get on with them if I was to be successful. From that first meeting I could tell that that would not be a problem. Thank you Lin, Katrien, Kathleen, Koen and Ahmad for so quickly helping me to feel welcome in Leuven. A short month after I arrived Anna started her PhD with the group and so we formed a close friendship since we

have gone through our PhDs in parallel, with all their ups and downs. Thank you Anna for always being willing to share in the joys and commiserations of this rollercoaster. Thanks especially to Ahmad, and the newest member of our group, Georg, for always being there when I got stuck on some problem. Thanks also to Esmaeel, and especially Tao for helping me out with so many of my experiments.

Thank you to all the other people in the MIRC with whom I have worked, conversed, laughed, complained, and shared a cup of tea. It was always a pleasure to go make a cup of tea and find a friend there to have a break with. Thank you all for your support over these four years.

A very big thank you to all my friends in Leuven. Whether it was over dinner, a beer, on a squash court, or on a rock, you have all supported and helped me in a multitude of ways. Thank you especially to Elien Lemmens for her help in translating the summary of my thesis into Dutch. A special thanks to the Catholic communities of Leuven of which I have been a part: St Pieter, St Geertrui, and St Kwinten. I have always appreciated your support and prayers.

Even though my family has not been close by during this PhD, their support from South Africa and California has helped me so much. I would not have been able to get to where I am today if it wasn't for the upbringing and education that my parents have given me. Thank you so much Mom, Dad, Kat and Adri for always supporting me and giving me whatever I needed to succeed.

Lastly, and most importantly, I want to thank my amazing wife, Caitlin. None of this would have been possible without you by my side, your love and support has kept me going, and every hard day was made easier knowing that I would be coming home to you at the end of it. Wherever I find myself in the world, my home will always be wherever you are. Chez moi, c'est toi.

Matthew

Abstract

During a PET scan the subject is required to be completely stationary for the duration of the scan. Any motion of the subject will translate into motion blur in the final reconstructed image and may reduce the diagnostic value of the image. Motion during a PET scan can be classified into two main categories: non-rigid and rigid motion. Non-rigid motion deforms the subject and is primarily caused by motion in the abdomen and thorax due to the cardiac and respiration cycles. Rigid motion is where the subject moves without any deformation, and occurs primarily during brain imaging when there is motion of the head. Non-rigid motion is largely periodic and there exist a number of techniques which attempt to handle it. Rigid motion of the head, however, is not periodic and thus one cannot use the same techniques. It is usually mitigated by using a head restraint - although with the high resolution of modern scanners this sometimes proves insufficient - or a sedative or anaesthesia, but these may carry significant risks to the patient.

In preclinical PET studies, an anaesthetic is usually used to ensure that the animal remains motionless for the duration of the scan (this of course does not solve the problem of motion due to the respiratory and cardiac cycles). The anaesthetic used may have a confounding effect on the drug under study, and these effects are usually not well understood. This is especially problematic for translational studies since anaesthetics are usually avoided in the clinic and thus the findings of the preclinical studies may not be directly applicable.

The problem of head motion in the clinical and preclinical settings can be solved by tracking the motion of the head during the scan and correcting the PET data for the recorded motion after the acquisition. The work presented in this thesis focusses entirely on developing and implementing such a rigid motion correction technique for brain imaging.

For preclinical studies, a motion correction technique was implemented which utilises a stereo-optical system to track a marker attached to the head of a rat. The experimental protocol and parameters, as well as the data processing, were optimised. The technique was applied in a proof-of-principal investigation into the effect of the anaesthetic isoflurane on the uptake of ^{18}F-FDG (a very common drug used for PET imaging) in the rat brain. Scanning of fully conscious and unrestrained rats was performed for more than an hour from the

moment of injection, which had not been reported on before. A significant effect of the isoflurane was observed, which confirmed other studies investigating isoflurane using different approaches.

A motion correction protocol was also implemented in the clinical setting for four different PET scanners. In addition to proof-of-principal studies, the technique was also used in a clinical study involving long brain scans of dementia patients, who were prone to moving.

In addition, an algorithmic technique of the form known as spatially variant resolution modelling was developed to improve the reconstruction, which could be used in conjunction with motion correction. Resolution modelling aims to improve the reconstruction by incorporating a model of the scanner uncertainties. To be accurate the model must account for variation in the uncertainties within the scanner field-of-view. Common techniques apply the model in image- or sinogram-space, and thus do not allow for the use of motion correction. The technique developed applies the model to the list-mode data directly, before motion correction, thereby correctly handling the spatial variance.

Contents

List of Abbreviations

2D	Two dimensional
3D	Three dimensional
ACF	Attenuation correction factor
APD	Avalanche photodiode
CT	Computed tomography
DOF	Degrees of freedom
DOI	Depth of interaction
FDG	2-fluoro-2-deoxy-D-glucose
FOV	Field of view
FWHM	Full width at half maximum
ISRA	Image space reconstruction algorithm
LM	List-mode
LOR	Line of response
MAF	Multiple acquisition frame
MC	Motion correction
MLAA	Maximum likelihood activity and attenuation
MLACF	Maximum likelihood attenuation correction factors
MLEM	Maximum-likelihood expectation-maximisation
MLTR	Maximum-likelihood transmission reconstruction
MR	Magnetic resonance
MT	MicronTracker
OS-ISRA	Ordered subsets image space reconstruction algorithm
OSEM	Ordered subsets expectation-maximisation
OT	OptiTrack
PCA	Principal component analysis
PET	Positron emission tomography
PMT	Photomultiplier tube
ROI	Region of interest
SDK	Software development kit

SiPM	Silicon photomultiplier
SPECT	Single photon emission computed tomography
SUV	Standard uptake value
TAC	Time activity curve
TOF	Time of flight
TOR	Tube of response
USB	Universial serial bus

Chapter 1

Introduction

Molecular imaging is the process of observing the metabolic processes in living organisms using an imaging device. Two imaging modalities which exist within the field of nuclear medicine are single photon emission computed tomography (SPECT) and positron emission tomography (PET). These modalities detect radioactive molecules introduced into the body. This thesis focusses entirely on PET, which will be introduced in the next section, followed by two sections on background related to the topic of this thesis. Thereafter the research objectives will be clarified. The main body of this thesis is made up of a collection of publications, as they appeared in print.

1.1 Positron Emission Tomography

Positron Emission

At a fundamental level, PET relies on the decay of a radioactive isotope where a positron (the anti-particle of an electron) is emitted, and the annihilation of that positron with an electron in the surrounding matter. This decay process is referred to as β^+ decay, with β^+ referring to the emitted positron. An example of β^+ decay is the decay of ^{18}F:

$$^{18}_{9}\mathrm{F} \rightarrow {}^{18}_{8}\mathrm{O} + e^+ + \nu_e, \tag{1.1}$$

where the products of the decay are ^{18}O, a positron, and an electron-type neutrino. A wide variety of isotopes decay via positron emission, such as ^{11}C, ^{13}N, ^{15}O, ^{22}Na, ^{26}Al, ^{40}K, ^{68}Ga, and ^{124}I. These isotopes undergo β^+ decay at varying rates, and with varying branching ratios (i.e. the probability of the isotope decaying via β^+ decay rather than another decay channel). A suitable isotope for PET studies is one with a high β^+ decay branching ratio and a half-life (i.e. the time taken for half the number of particles to decay) on the order of a few minutes to one or two hours. Isotopes which satisfy these criteria are ^{11}C, ^{13}N, ^{15}O, ^{18}F, ^{68}Ga, and ^{124}I, amongst others.

Once the positron is emitted from the decayed isotope it travels some distance, known as the "positron range", which depends on the kinetic energy of the positron and ranges from less than 1 to several millimetres. After losing most of its kinetic energy the positron will annihilate with an electron in the surrounding material or form a short-lived electron-positron system (called "positronium") which also quickly collapses and annihilates. The annihilation results in the emission of 2 or more γ (gamma) photons, with 2 photons accounting for almost all cases, and the number of 3 or more photons being almost negligible. Due to the conservation of energy, the sum of the photon energies must be equal to that of the sum of the electron and positron masses, i.e. 1022 keV. In the case where 2 photons are emitted each will have an energy of 511 keV. In the centre-of-mass reference frame of the electron-positron system, where the linear momentum of the system is zero, the 2 emitted photons will have equal but opposite momenta and thus travel in exactly opposite directions. However, in an external reference frame (also known as the laboratory frame), the electron-positron system will usually have a non-zero linear momentum, thus the sum of the 2 photons' momenta must also be non-zero and hence they would not travel in exactly opposite directions. This effect is called the "acollinearity" of the photon pair. The magnitude of this acollinearity is small, with the photons deviating from travelling 180° apart by $\pm 0.29°$ (standard deviation) (Levin et al. 1999).

Each emitted photon will traverse the surrounding material and may interact with it. γ photons with an energy of 511 keV can interact with matter via the photoelectric effect, Compton scattering, or Rayleigh scattering. During a photoelectric effect interaction the photon is absorbed by an electron in an atom, which is then ejected from the atom. After such an interaction the photon can no longer be detected. Compton scattering occurs when a photon interacts with a valence electron, causing the photon to lose some of its energy and be deflected from its flight path. Rayleigh scattering is similar except that the photon interacts with the entire atom and loses almost no energy; this interaction is extremely rare for 511 keV photons and mentioned only for completeness. Scattered photons can still be detected but, since they have deviated from their original flight path, they are no longer collinear with their paired photon. Any of these three interactions may cause one or both annihilation photons to not be detected; the consequent decrease in the total number of detected photons is referred to as "attenuation". Attenuation is dependent on the extent and density of material the photons travel through.

If the two photons are detected by some array of surrounding detector material within a short timing window (usually on the order of nanoseconds) of each other, then they constitute what is called a "coincidence event". There are three types of coincidence events: true, scattered, or random. A true event is one where both photons of an electron-positron annihilation do not interact with the surrounding material before both being detected, and therefore the

point of decay of the isotope must lie along or near to the line joining the detected photons. This line is called a "line-of-response" (LOR) and constitutes the desired raw PET data. A scattered event occurs when one or both photons undergo Compton scattering before being detected, and therefore the resulting LOR does not necessarily pass near to the point of isotope decay. If the photon energy can be measured then it is possible to identify these events since during the Compton scattering interaction the photon loses some of its energy. However, detectors have a finite energy resolution and thus can only discern some scattered events. Lastly, a random event is where two photons are detected in a timing window which do not originate from the same decay and are therefore not a valid photon pair.

Since all photons travel at the speed of light, using the difference in detection times of the 2 photons it is possible to narrow the range along the LOR that the annihilation (and hence the decay) could have occurred. This timing information is referred to as "time-of-flight" (TOF). Without TOF information it is assumed that the decay event could have occurred anywhere along the LOR with uniform probability.

For PET we are interested in knowing where the isotope decay occurred. The factors which contribute to the uncertainty in that location are the positron range, the acollinearity of the photon pair, the spatial resolution of the photon detectors, and, if available, the resolution of the TOF information. Further confounding factors which need to be taken into account are attenuation, scatter, and randoms.

Tomography

Tomography is the process of accumulating a set of line integrals through an object. A set of parallel line integrals are usually referred to as a single projection. In one such projection all depth information is lost (unless TOF is available, which provides some depth information). However, if sufficient projections are acquired from different perspectives, then it becomes possible to reconstruct the full 3 dimensional object. A PET scanner acquires such a set of projections of the distribution of the radioactive isotope within the scanner.

The computed tomography (CT) scanner is another tomographic system which acquires a set of projections through an object. An X-ray emitter and detector rotate around the object, sequentially acquiring X-ray images through the object. The major difference between PET and CT is that in the former photons are emitted from within the object, while in the latter photons are transmitted through the object from an external source. PET predominantly measures metabolic, or functional, processes in the body, while CT measures anatomical, or structural, features.

1.1.1 PET Scanners

Since its discovery at the end of the 19th century, ionising radiation has been investigated as a tool for medical diagnostics. While the use of X-rays was quickly adopted for transmission medical imaging (used, for example, by Marie Skłodowska Curie in military clinics during World War I), it was not until the 1950s that the first emission scanner was developed by Hal Anger. Anger developed a gamma camera, also commonly referred to as an Anger camera, which used a large monolithic scintillator crystal (i.e. a crystal which absorbs ionising radiation and emits optical light photons) to acquire an image of the distribution of a radioactive isotope within a body. This gamma camera still forms the basis of almost all SPECT systems today, which are usually made up of one or more gamma cameras rotating around a body to acquire a set of projections. Modern PET scanners are based on a similar technology, but use instead a pixelated array of scintillator crystals to be able to detect both photons emitted during positron decay. PET systems are particularly well-suited to clinical use since they have a very high sensitivity, meaning that they can detect even a very small amount of radioactivity present in the body. This allows for the use of very small quantities of molecules labelled with a radioactive isotope such that, while they are processed by the body and therefore trace these processes, they have no noticeable effect on the systems processing them. Such molecules are referred to as *tracers*. The first human PET scans were conducted by Ter-Pogossian, Hoffman, Phelps, and others in the 1970s. PET scanners were mostly used for research until the mid-1990s when it was realised that the compound 2-fluoro-2-deoxy-D-glucose (FDG) could be very useful in oncology studies (i.e. cancer detection and treatment follow-up), together with the development of smaller and more affordable cyclotrons which could be installed close to clinical sites. FDG can easily be labelled with the positron emitting isotope ^{18}F, and is phosphorylated within the cells in the same manner as glucose and at a rate proportional to that of glucose, thus providing a tracer for glucose metabolism (it had already been used for glucose metabolism studies for some time). Glucose metabolism plays an important role throughout the body, and is of particular interest in oncology (since tumours usually metabolise glucose at a higher rate than organs), cardiology, and neurology. In many PET centres today, FDG studies account for more than 90% of the scans.

Modern PET scanners have a very similar design to the early PET scanners. Scintillation crystals are still used to detect the γ photons, although new crystals have been developed. A summary of scintillation crystals is shown in table 1.1. An ideal crystal would have a high density to ensure the absorption of as many incident photons as possible, a fast decay time to handle a large rate of arrival of photons and allow for high resolution timing information, and a high luminosity (i.e. number of output photons at a given energy of the incident photon) for more reliable detection and energy discrimination (since

the energy of the incident photon can be deduced from the number of photons emitted by the crystal). Currently the most commonly used crystal is LSO (or LYSO) since it has a high luminosity and a fast decay time, which makes it suitable for TOF measurements. The previous generation of PET scanners used predominantly BGO crystals. Due to cost and a complicated manufacturing process $LaBr_3$ is not yet being used for PET systems although it has promising characteristics.

Table 1.1: Scintillation crystals used in PET scanners

	NaI	BaF_2	GSO	BGO	LSO	$LaBr_3$
Density (g/cm^3)	3.67	4.88	6.71	7.13	7.40	5.1
Decay time (ns)	230	0.8	60	300	40	30
Luminosity (photon/keV)	45	10	12	8	29	61

The crystals are attached to a device which converts the scintillation photons into an electrical signal. Currently photo-multiplier tubes (PMTs) are the most commonly used device. When a scintillation photon is incident on the PMT an electron may be expelled due to the photoelectric effect, which occurs with a less than perfect efficiency. A potential difference is applied across the PMT to accelerate the electron towards a series of plates, at each of which more electrons are ejected in an avalanche effect, resulting in a detectable electric signal at the back of the PMT. A higher energy γ photon incident on the scintillator crystal results in more scintillation photons, which result in more electrons passing through the PMT, and a larger electronic signal at the back of the PMT. Hence the energy of the incident photon can be estimated. An energy discriminator then determines whether the incident photon had an energy of 511 keV, implying that it most likely did not undergo scattering before being detected. With advancements in electronics, many scanners are now being constructed with avalanche photodiodes (APDs) or silicon photo-multipliers (SiPMs) instead of PMTs. These two alternatives are much more compact than PMTs and, in contrast to PMTs, can operate inside a magnetic field which is becoming increasingly important with the advent of combined PET and magnetic resonance (MR) scanners.

Most modern PET scanners are made up of an array of BGO, LSO or LYSO scintillation crystals and PMTs arranged in a cylinder, with some axial extent. A typical PET scanner can be seen in figure 1.1. For higher resolution it is desirable to have the crystals as small as possible (current crystals are a few millimetres across), most PMTs, however, are quite large (around 25 mm across). Therefore a common arrangement is the so-called "block detector" which has a square array of many crystals (usually around 12×12) connected to a square array of (usually) 2×2 PMTs (Casey et al. 1986). The scintillation light from a crystal is propagated through a light guide which intentionally

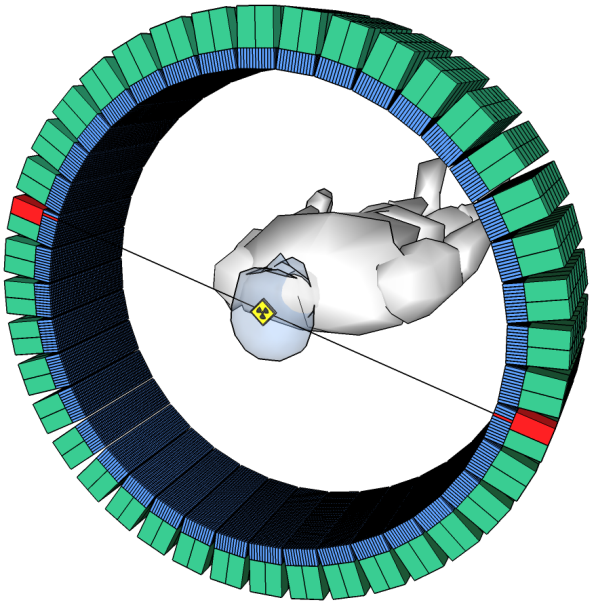

Figure 1.1: Most modern PET scanners have detectors arranged in a cylindrical array. The individual crystals here are blue, and the PMTs are green. The patient enters along the axial direction of the scanner. A radioactive decay within the patient causes a photon pair to be emitted which, when detected by the scanner (indicated by the red elements), causes an LOR to be recorded (black line).

diffuses the light so that it is spread over the PMTs. Then, by measuring and comparing the intensity of light measured in each of the PMTs it is possible to calculate in which crystal the scintillation occurred, as well as estimate the energy of the incident photon be summing the outputs of the PMTs.

Some modern scanners are being built with block detectors which can report the depth-of-interaction (DOI) information, i.e. information about the depth at which the photon was absorbed in the crystal. This allows for more accurate positioning of the LOR endpoints and can improve the spatial resolution of the scanner.

There are three main manufacturers of PET systems, namely Siemens Healthineers, General Electric Healthcare, and Philips Healthcare. All vendors produce PET, SPECT, CT and MR systems, as well as dual modality systems such as PET/CT, SPECT/CT, and, more recently, PET/MR. While the vendors focus on clinical scanners, Siemens has in the past also produced a preclinical system dedicated to imaging small animals such as mice, rats, rabbits, and some primates. These systems are now predominantly manufactured by smaller companies. Throughout the duration of my studies I worked primarily

Table 1.2: Specifications of a selection of scanners.

	Focus 220	Hirez	Signa
Ring diameter (mm)	258	830	620
Transaxial FOV (mm)	220	700	600
Axial length (mm)	76	162	250
Crystal	LSO	LSO	LYSO
Scintillation converter	PMT	PMT	SiPM
Coincidence window (ns)	6	4.5	4.6
TOF resolution (ps)	n/a	n/a	< 400
Detector size (mm)	1.51×1.51×10	4.0×4.0×20	4.0×5.3×25
No. rings	48	39	45
No. detectors per ring	168	624	448
Tangential resolution (mm) *	1.30	4.61	4.1
Radial resolution (mm) *	1.30	4.61	4.4
Axial resolution (mm) *	1.46	5.10	5.3

* At a radial distance of 1 cm from the FOV centre.

with a Siemens preclinical system, namely the microPET Focus 220, but I also worked with the Siemens Hirez PET/CT, the Siemens mCT PET/CT, the Siemens mMR PET/MR, and the General Electric Signa PET/MR scanners. Table 1.2 shows the specifications of the Siemens microPET Focus 220 (Tai et al. 2005), the Siemens Hirez PET/CT (Brambilla et al. 2005), and the GE Signa PET/MR (Grant et al. 2016) scanners, and further scanner specifications are given in table 4.1 in chapter 4.

1.1.2 PET Data Acquisition

When two photons are detected within a specified timing window (usually on the order of several nanoseconds), the photons are recorded as a photon pair in a "list-mode" format data file, so called since it stores a list of all the events in chronological order. Each photon pair event in this list corresponds to a particular LOR connecting two detectors. The data are often histogrammed by counting the number of events which occurred along each LOR. If the total number of possible LORs is less than the number of events in a scan, this histogrammed data will be more memory efficient than the list-mode data. However, a disadvantage of this histogrammed format is that the time stamps of the events are lost.

Any set of parallel, histogrammed LORs arranged in a 2 dimensional array which corresponds to their location in space can be considered as a projection through the object within the scanner. A set of such projections can thus be created which covers a full rotation of the object. This form of the data, referred

to as a "sinogram" and which is simply a rearrangement of the histogrammed LORs, is very common in current scanners.

1.1.3 PET Reconstruction

Reconstructing an image from PET data falls within the mathematical category of inverse problem solving. The process of measuring an object and acquiring data is referred to as the "forward process", and during reconstruction we attempt to somehow invert that process and determine a voxelised representation of the object that was scanned. The mathematical description of solving for a two dimensional object from a series of one dimensional projections through the object was formulated by Johann Radon in 1917; such a projection is known as a Radon transform. The three dimensional extension of this formulation (known as the X-ray transform) describes data (in the form of a sinogram) from a tomograph.

Analytical Reconstruction

The most elementary reconstruction can be performed by creating a voxelised image space within the scanner field-of-view (FOV), tracing each LOR corresponding to a list-mode event through that image and incrementing each voxel through which it passes. This is referred to as a "backprojection". Such a reconstruction suffers from severe blurring which can be corrected for, in Fourier space, by using an appropriate filter, such as the "ramp" filter: a linear filter designed to remove the inverse frequency dependent blurring introduced by the backprojection. A reconstruction of this form is called filtered backprojection (FBP). FBP is an analytical reconstruction, meaning that it solves the inverse problem directly, in a single step. FBP is a very quick reconstruction, but it assumes certain ideal characteristics of the data acquisition and can suffer from artefacts in some cases.

Iterative Reconstruction

An alternative approach is iterative reconstruction where, instead of directly solving the inverse problem, an approximation of the measurement process is modelled and utilised to iteratively check and update a reconstruction until convergence. The most used algorithm is the maximum-likelihood expectation-maximisation (MLEM) algorithm (Shepp et al. 1982), which is derived from a Poisson model of the emission data. Starting from an initial estimate of the reconstruction, a simulation of the measurement process is performed, referred to as a "forward projection", and the resulting projections are compared to the measured data. From this comparison an update of the reconstruction estimate can be determined, after which the process is repeated until the reconstruction

converges. A forward projection, p, of an image ξ, is formulated as,

$$p_i = \sum_j c_{ij}\xi_j, \tag{1.2}$$

where i is the detector index, or LOR, j is the image voxel index, and c_{ij} an element of the so-called system matrix which represents the probability of activity in pixel j contributing photon pairs to LOR i. In practice c_{ij} is computed as (an approximation of) the overlap between the LOR i and the voxel j. The transpose of this operation, referred to as a "backprojection", will distribute a projection value for an LOR in an image, χ, along the LOR, i.e.

$$\chi_j = \sum_i c_{ij}p_i. \tag{1.3}$$

Note that ξ and χ are not equal to each other since the backprojection is the transpose of the forward projection, not its inverse.

Using these two operations, the sinogram-based implementation of MLEM is formulated as

$$\lambda_j^{n+1} = \frac{\lambda_j^n}{\sum_i c_{ij}s_i a_i} \sum_i c_{ij}s_i a_i \frac{y_i}{\sum_k c_{ik}s_i a_i \lambda_k^n + S_i + R_i}, \tag{1.4}$$

where λ_j^n is the intensity of the reconstruction in voxel j at iteration n, c_{ij} is the system matrix, s_i is the sensitivity factor for LOR i accounting for crystal efficiencies and geometric effects, a_i is the attenuation correction factor for LOR i, y_i is the measured number of counts in LOR i, and S_i and R_i are the scatter and randoms contribution for LOR i, respectively. As an alternative, MLEM can be implemented in a list-mode-based framework, using the recorded events directly without first histogrammming them into a sinogram (Parra et al. 1998; Reader et al. 1998). Such an implementation can be formulated as

$$\lambda_j^{n+1} = \frac{\lambda_j^n}{\sum_i c_{ij}s_i a_i} \sum_m c_{i_m j}s_{i_m} a_{i_m} \frac{1}{\sum_k c_{i_m k}s_{i_m} a_{i_m} \lambda_k^n + S_{i_m} + R_{i_m}}, \tag{1.5}$$

where i_m is the LOR i corresponding to the m^{th} element in the list of recorded events. The primary difference in this formulation is that the forward projection along i_m is compared to 1 since it represents a single recorded event, rather than y_i which is the number of histogrammed events corresponding to LOR i. It should be noted however that equations (1.4) and (1.5) are equivalent: we observe that

- $y_i = \sum_m \delta(i_m - i)$ where $\delta(x) = 1$ when $x = 0$ and $\delta(x) = 0$ otherwise; and,

- the set of measured events, M, (which may have repeated elements) is a subset of possible LORs, I, and if $i \in I$ but $i \notin M$ then $\delta(i_m - i) = 0$,

therefore equation (1.5) can be rewritten as,

$$\lambda_j^{n+1} = \frac{\lambda_j^n}{\sum_i c_{ij} s_i a_i} \sum_i \sum_m c_{ij} s_i a_i \frac{\delta(i_m - i)}{\sum_k c_{ik} s_i a_i \lambda_k^n + S_i + R_i}, \tag{1.6}$$

$$= \frac{\lambda_j^n}{\sum_i c_{ij} s_i a_i} \sum_i c_{ij} s_i a_i \frac{\sum_m \delta(i_m - i)}{\sum_k c_{ik} s_i a_i \lambda_k^n + S_i + R_i}, \tag{1.7}$$

$$= \frac{\lambda_j^n}{\sum_i c_{ij} s_i a_i} \sum_i c_{ij} s_i a_i \frac{y_i}{\sum_k c_{ik} s_i a_i \lambda_k^n + S_i + R_i}, \tag{1.8}$$

which is equivalent to (1.4).

The image space reconstruction algorithm (ISRA) (Daube-Witherspoon et al. 1986) is an alternative iterative algorithm which performs the comparison between the reconstruction estimate and the measured data in image space (rather than projection space). It can be formulated as

$$\lambda_j^{n+1} = \lambda_j^n \frac{\sum_i c_{ij} y_i}{\sum_i c_{ij} \left(\sum_k c_{ik} s_i a_i \lambda_k^n + S_i + R_i \right)}, \tag{1.9}$$

using the same definitions as in (1.4). ISRA is derived from a least squares estimate, and therefore does not model the noise properties of the data as accurately as MLEM. For this reason MLEM is usually the preferred iterative algorithm.

Corrections with Iterative Reconstruction

Iterative algorithms have the advantage of being able to more accurately account for factors influencing the measured data such as attenuation, scatter, randoms, and spatial resolution.

Attenuation The correction factors that need to be applied to account for photon attenuation are calculated from a measured map (a "μ-map") of linear attenuation coefficients for the subject being scanned. This μ-map can be measured by acquiring a PET scan of a source external to the subject such that the emitted photons pass through the subject; by comparing this "transmission" scan to a similar scan without the subject present, the photon attenuation of the subject can be estimated and a μ-map constructed. Alternatively, and more commonly these days, a CT scan of the subject can be acquired, which directly gives an image of the μ-map, albeit at a different photon energy, but this difference can be corrected for. It is also possible to derive a μ-map from a measured MR scan (although this is more difficult and currently a popular

topic of research). This is an important reason why any current commercially available PET scanner always comes as a dual modality with either a CT or an MR. A forward projection of the μ-map yields the necessary attenuation correction factors a_i.

Scatter The scatter contribution, S_i, is estimated from the μ-map and the emission image using a simplified simulation of the scattering during the measurement process; a common technique is single scatter simulation (SSS) by Watson et al. (1996).

Randoms The randoms contribution, R_i, can be estimated in one of two ways (Hoffman et al. 1981): noting that photon pairs are identified when two photons are detected within a specified timing window, then by inserting a delay into that timing window any photon pairs which are recorded could not have originated from the same annihilation event and can therefore be counted as a random event, thus enabling an estimation of the randoms; or the rate of single photons which are detected can also be used to estimate the randoms rate.

Resolution Modelling Spatial resolution modelling, which will discussed in more detail in section 1.3, can be incorporated into the forward model by adjusting the system matrix, c_{ij}, in (1.4) and (1.9).

Image Noise & Bias Iterative algorithms slowly converge on a reconstruction, with each iteration consisting of a forward and a backprojection, and they are thus much slower than FBP. Knowing when an iterative reconstruction has converged to a final solution is a difficult problem, especially since different regions of the reconstruction may converge at different rates. As the iterations proceed, initially the lower and then the higher frequencies converge, and thus at later iterations the noise (which is high frequency) in the image becomes dominant. A common practice to balance the image bias (which approaches zero with increasing iterations) and noise is to iterate for a long time and then apply a post-smoothing to the image. Another technique is "early-stopping", i.e. stopping the iterations before the noise becomes too dominant. Yet another approach is to use prior information during the reconstruction to force the algorithm to, for example, favour having smooth regions, or sharp edges, or to incorporate known anatomical information. These approaches are, however, beyond the scope of this thesis.

1.2 Motion Correction

During a PET scan the data are accumulated over some time, depending on the study. A single brain scan can last between 15 and 40 minutes, depending on the tracer used. Dynamic scans, which acquire data over an hour or longer, allow for the kinetics of the tracer to be observed by reconstructing short subsequent frames. Any substantial motion of the subject during the scan will result in motion blur in the final reconstructed image. When performing a whole-body or thorax scan, the motion of the organs due to respiration and the beating heart can substantially affect the reconstruction. Such motion is non-rigid since the organs will usually deform. A common strategy to handle such motion is to separate the acquired data into frames within each of which the motion of the organs is negligible, and then, since the motion is periodic, the frames corresponding to the same respiratory or cardiac phase can be summed. In the case of brain scans any motion of the head will of course not be periodic and thus cannot be handled in the same way. It is common practice to physically restrain the head to minimise the possible motion of the patient. Nonetheless, even with a head restraint, some patients struggle to remain motionless throughout the scan, especially paediatric, psychiatric and elderly patients. In addition, patients who suffer from claustrophobia may have their phobia exacerbated by a head restraint. Investigations into intrascan head motion have found that translations between 1 and 20 mm are common (Green et al. 1994; Dinelle et al. 2006), even with head restraints. In some cases an anaesthetic or sedative is used to ensure that the patient remains motionless, but these approaches carry significant risks of hypoxaemia, respiratory depression, and oxygen desaturation (Malviya et al. 2000).

CT scans, even though they are much faster than PET, taking between a few seconds and a few minutes to acquire, are nonetheless also susceptible to motion (Yazdi et al. 2007). Indeed, the high resolution of CT makes it more sensitive to smaller motions. The expected motion due to respiration or the cardiac cycle is often handled by either acquiring very quick scans, or acquiring sequential framed scans as in PET. When unexpected motion occurs, however, during such a CT scan (such as head or bulk body motion), an additional scan is often performed, increasing the patient dose and scan time per patient. Paediatric patients, who are more likely to move during a scan than adult patients, are more vulnerable to the long-term effects of a high radiation dose (Brenner et al. 2001). Modern PET scanners are attached to a CT scanner which is used (in part) to supply the attenuation correction map for the PET reconstruction. Any motion between the CT and the PET scans, be it due to respiration, the cardiac cycle, head motion, etc., will likely cause artefacts in the PET reconstruction.

In preclinical PET studies, an anaesthetic, such as isoflurane, ketamine, or chloral hydrate, etc., is usually used to ensure that the animal remains

motionless for the duration of the scan (this of course does not solve the problem of motion due to the respiratory and cardiac cycles). The anaesthetic used may have a confounding effect on the drug or radioactive tracer under study, and these effects are usually not well understood (Alstrup et al. 2013). This is especially problematic for translational studies since anaesthetics are usually avoided in the clinic and thus the findings of the preclinical studies may not be directly applicable. Some groups have attempted to avoid using anaesthetics by physically fixating the animal's head during the scan to avoid motion (Hosoi et al. 2005). However, stress induced by such a fixation may have confounding effects on the tracer or drug kinetics under study (McLaughlin et al. 2007; Patel et al. 2008). A novel approach to avoid relative motion between a rat's brain and the PET scanner is the RatCAP (Vaska et al. 2004; Schulz et al. 2011), a miniaturised PET scanner which is surgically attached to the rat's head and which moves rigidly with the brain. While this system is promising it has a lower sensitivity than commercial scanners and may inhibit the natural movement of the rat, possibly inducing stress in the animal.

The field of PET motion correction aims to correct motion of the subject such that no motion blur is observed in the final reconstruction regardless of how the subject moved, and it can be divided into the rigid (generally brain imaging) and non-rigid (generally abdomen and thorax imaging) cases, each of which require very different strategies. This thesis focuses entirely on the rigid motion correction case for brain imaging.

Rigid motion correction techniques applied to brain imaging derive the position and orientation of patient's head (referred to as the pose) throughout the scan (either by tracking the head position during the scan, or extracting it from the data after the acquisition), since it can be assumed that the brain moves rigidly with the skull and the outside of the head. This assumption is invalid when there is motion of the skin relative to the brain due to changing facial expression. The acquired data are then corrected for motion during (or after) the reconstruction such that an image free of motion blur is produced in some chosen reference frame.

1.2.1 Motion Tracking

Different approaches to track head motion using some external device have been investigated by various groups, starting in the 1990s. Of the earliest investigations, Daube-Witherspoon et al. (1990) and Green et al. (1994) made use of a transducer attached to a patient's head which was tracked by an external radio device to measure the head motion during the scan. Goldstein et al. (1997) made use of three miniature lamps attached by a wire frame to the head, and which could be tracked by optical cameras. Fulton et al. (1999) used a mechanical arm directly attached to a band on the patient's head which tracked the motion by registering the motion of the end effector of the arm.

Lopresti et al. (1999) utilised the Polaris (Northern Digital, Inc., Waterloo, Canada), a stereo-optical system operating in the near infrared spectrum which tracked small reflective markers on a plate attached to the patient's head. Due to its high accuracy, the Polaris proved very successful and was widely implemented in several institutions (Bloomfield et al. 2003; Fulton et al. 2003; Carson et al. 2003). More recently, the OptiTrack system (NaturalPoint Inc. Corvallis, OR, USA), consisting of several individual infrared cameras, has been investigated at the University of Sydney, Australia, (Kim et al. 2015) with whom I have collaborated while I implemented the same system at KU Leuven (Bickell et al. 2015a). The OptiTrack system tracks reflective markers arbitrarily arranged on a subject, and offers more flexibility and robustness than the Polaris system. This system is described in more detail later in this section, and my research with this system is reported on in chapter 4.

For preclinical studies Weisenberger et al. (2005) developed a system for SPECT imaging whereby an unrestrained mouse can be tracked over a long period of time by tracking reflective markers attached to its body using infrared cameras.

For PET studies, the MicronTracker (ClaroNav Inc., Toronto, Canada), a stereo-optical system operating in the visible spectrum, proved very successful at accurately resolving sufficiently small markers to be attached to a rat's head (Kyme et al. 2008); this system was implemented at KU Leuven and used for much of the research presented in this thesis (see chapters 2 and 3), and is described in more detail later in this section.

All of these tracking systems made use of some kind of marker attached to the subject's head, assuming that the motion of the marker accurately represented the motion of the brain. In general this assumption is justified, but motion of the marker relative to the brain is possible due to slippage or changing facial expression, etc. Such relative motion will result in residual motion blur in the reconstructed images. Different approaches to attach the marker to the patient's head have been investigated, including: using a wire frame attached to the forehead and in the ear canal (Goldstein et al. 1997); attaching the marker via a bite plate to the upper jaw of the patient (Menke et al. 1996); using a plate holding the markers attached to a dense, high-friction foam following the contours of the head (Lopresti et al. 1999); using customised goggles with protruding markers (Bühler et al. 2004; Langner 2009); using a cap with a marker plate attached to it (Bloomfield et al. 2003); and using a cap with markers attached directly on to the cap (Kim et al. 2015; Bickell et al. 2015a). For preclinical studies, as already mentioned, Kyme et al. (2008) used a small planar, printed marker attached directly onto the forehead on a rat using an adhesive. Miranda et al. (2015) attached radioactive point sources to a rat's head which could then be localised in the reconstructed images and used to determine the motion parameters. While this approach avoids certain complications, such as the temporal and spatial calibration, the resolution of

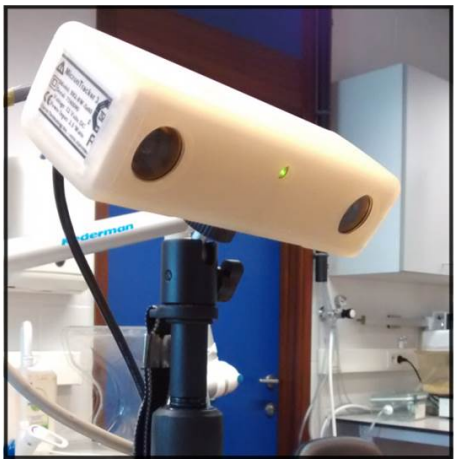

Figure 1.2: The MicronTracker, a marker-based stereo-optical system.

the motion tracking is limited to that of the scanner.

External tracking systems which do not make use of a marker attached to the subject but rather identify and track features of the subject itself are a novel and very promising approach. By avoiding the use of markers the impact of the system on the clinical protocol is negligible, and thus such a system is more likely to be accepted by the medical community and adopted by the scanner manufacturers. Noonan et al. (2015) adapted the commercially available Kinect v2 (Microsoft, Redmond, WA, USA) system, which uses a time-of-flight system to measure depth information, to detect and track facial features. Olesen et al. (2013) performed a similar tracking using a customised set up of individual cameras. Their setup was operable in high magnetic fields and is therefore compatible with the newly introduced PET/MR scanners. For preclinical studies, Kyme et al. (2014) also investigated using a series of individual optical cameras to identify and track features on a rat's head. As in the marker-based case, markerless techniques also assume that the features on the head move rigidly with the brain. In addition, any markerless approach has the potential to suffer from non-rigid changes to the features on the face being tracked, such as changes in facial expression, movement of the lower jaw, and, in the case of rats, movement of the whiskers.

MicronTracker

The MicronTracker (MT, shown in figure 1.2) was used for all preclinical studies conducted during my research. The MT consists of two optical cameras operating in the visible spectrum. These two cameras are housed within a single casing and so the distance between them is fixed. Two spatially offset and simultaneous images are acquired by the cameras, providing stereoscopic vision and hence enabling the system to determine depth information.

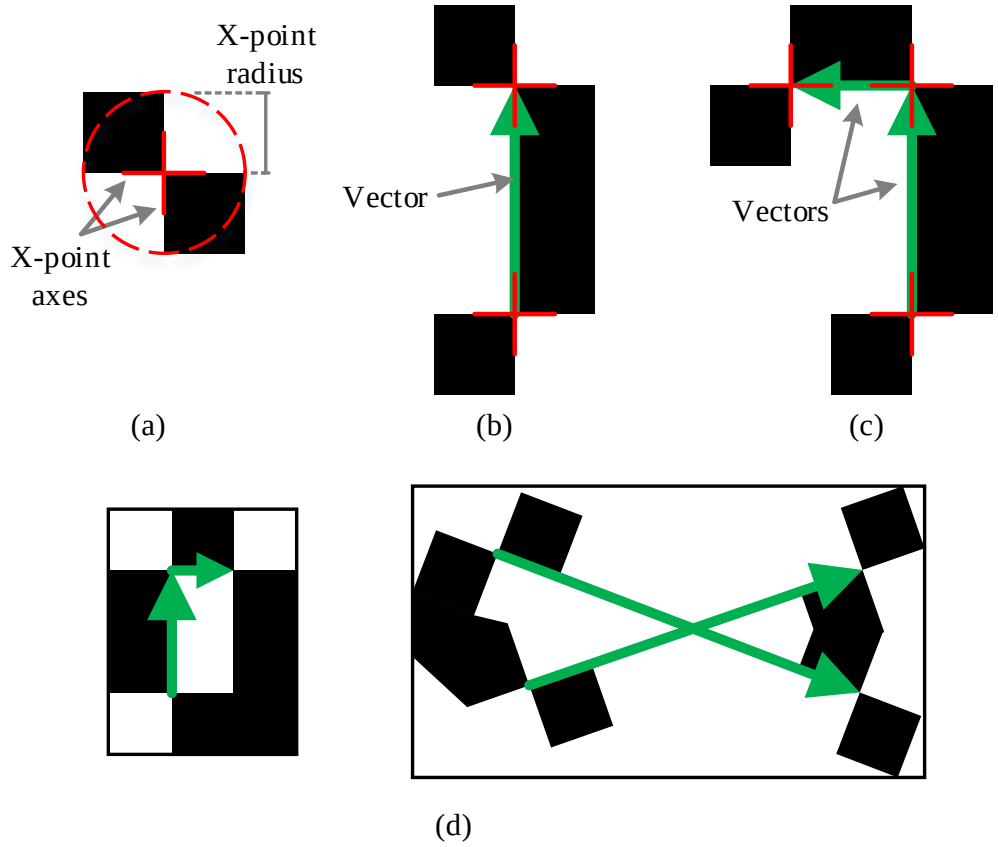

Figure 1.3: (a) The most basic element of a marker, a single X-point, made up of touching black and white regions. The red cross indicates the X-point location, and the arms of the cross indicate the X-point axes. (b) Two X-points with their axes aligned form a vector (green arrow). (c) Two vectors together form a marker. (d) Two examples of possible markers, with their vectors indicated by the green arrows. Note that the red crosses and green arrows are shown only for demonstrating purposes.

The MT tracks planar markers, designed according to certain rules and which typically have a checkerboard nature. The elements of a marker are shown in figure 1.3. The most basic element of a marker is the so-called X-point, which is the point of contact between black and white regions, as indicated by the red crosses in the figure. The black and white regions need not be perpendicular to each other but the lines along their edges through the point of intersection (the X-point) need to be straight. The size of the X-point is determined by the radius from the X-point to the nearest point where the black or white regions change or are interrupted. According to the manufacturer the size of the X-point does not influence the accuracy with which it can be located, however it should be at least around 4 mm to be detectable. Two

X-points with their black and white edges aligned form a vector (e.g. each of the green arrows in figure 1.3). Two vectors which differ in length by around 2 mm and which have at least an angle of 8 degrees between them can form a marker (e.g. pairs of green arrows in figures 1.3(c) and 1.3(d)). A marker can have more than two vectors. The accuracy with which a marker can be tracked generally increases with the number of X-points, and also with the length of the vectors.

Markers were designed in Microsoft Visio 2013. Visio allows for a high resolution and a large magnification, and has the capability to simply and accurately create and align shapes and edges. The designs can be printed exactly to scale, which is not always true in other applications. Markers were printed on paper with adhesive on one side, and then attached to a perspex plate usually 2 mm thick. The perspex plates were flat, rigid, light, and had very low photon attenuation.

A new marker must be registered in the MT software (referred to as "Template registration"). This is a simple process of holding the marker in front of the cameras for a number of seconds while running the "Template registration" tool. After this the marker will be recognised by the MT whenever it is in the field-of-view (FOV).

The accuracy with which the MT locates a marker is dependent on many factors and is a complex quantity to determine. The manufacturer of the MT quotes the root-mean-square error of a stationary X-point measured 10000 times at varying locations, to arrive at a value of 0.25 mm. This is pessimistic since in general a marker, which consists of several X-points, will have better accuracy.

The MT can track markers at a maximum frequency of 48 Hz. In practice however the software was found to struggle at frequencies much above 30 Hz, due to the significant processing requirements. The recorded images are processed in real-time, and the processed images are discarded. Data sets usually occupy on the order of 50 MB per hour of tracking at around 30 Hz. If a new set of recorded images arrives before the previous set have been processed, then the new set will be discarded and no pose will be recorded. At higher frequencies the chance of this occurring increases. Such dropped poses can cause problems during the temporal synchronisation of the MT and the list-mode data. The optimal frequency at which to run the MT depends on the power of the controlling computer, the number of markers being tracked, the settings of the tracking software, etc. We found that operating at 30 Hz produced reliable results, although a thorough optimisation of this was not performed.

The MT has a focal length of 700 mm. The maximum range at which it can detect an X-point with a radius of 12 mm is 1600 mm, since the CCD cameras each have a pixel resolution of 640×480 and there is a minimum number of pixels an X-point must span in order to be detected.

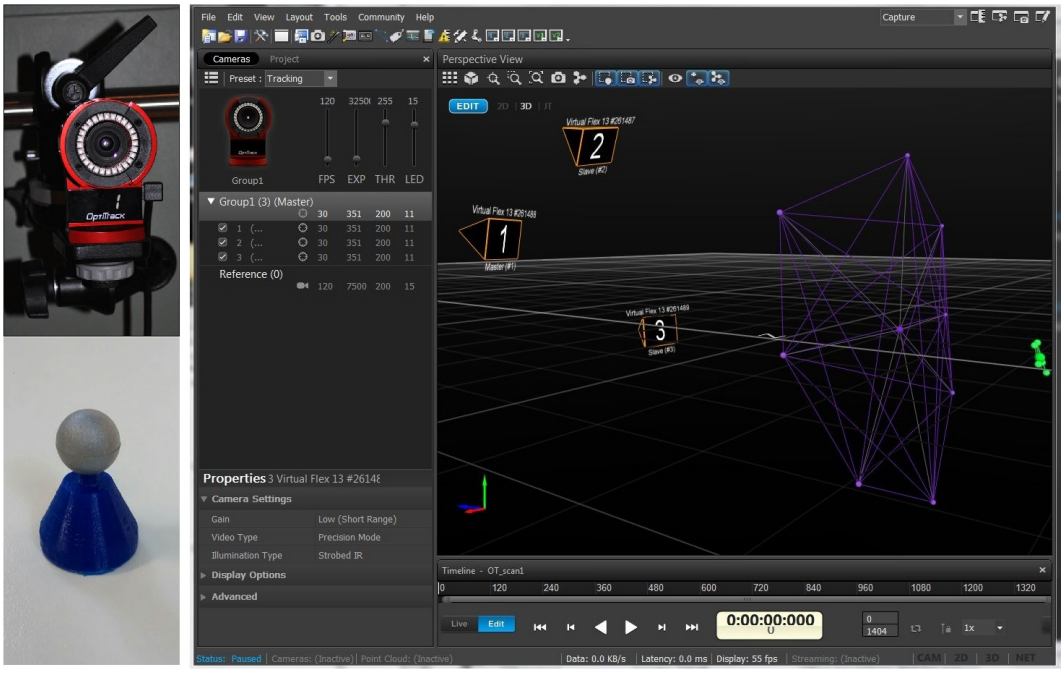

Figure 1.4: On the top left a single Flex 13 camera from the OptiTrack system is shown, and on the bottom left is a single OT retro-reflective marker. On the right is a screen shot of the Motive software used to operate the OT system.

OptiTrack

The OptiTrack (OT, shown in figure 1.4) was used for much of the clinical studies conducted during my research. The OT system consists of an array of individual cameras which are separate and can be arranged arbitrarily around the FOV. For this research three to six Flex 13 cameras were used. The OT cameras emit infrared light from LEDs on the camera itself, which then reflects off retro-reflective, passive markers (figure 1.4). The markers are then detected and their locations determined.

Since the OT cameras can be positioned arbitrarily, an internal calibration needs to be conducted so that the relative positions of the cameras will be known to the system. This is performed by moving a pre-registered array of three markers throughout the FOV; by comparing what each camera records of this array the relative positions of the cameras can be determined.

The OT system comes with a powerful and user-friendly graphical user interface called “Motive” (figure 1.4), which controls all aspects of the system including the camera specifications (e.g. shutter time, frequency, emitted LED strength, etc.), the internal calibration, the tracking of markers, and the editing of the recorded data. By selecting at least three markers attached to a single

object, a "rigid body" can be created and tracked.

The OT system can operate reliably at a frequency of up to 120 Hz. While the recorded images can be processed in real-time, they are highly compressed and stored. Data sets are therefore larger than for the MicronTracker, usually on the order of 1 GB per hour of tracking at a frequency of 30 Hz. Each Flex 13 camera has a CCD pixel resolution of 1280×1024, and an adjustable focal length.

1.2.2 Spatial Calibration

Since the PET and the motion tracker have different coordinate systems whose axes are not necessarily aligned, it is necessary to find the transformation from the tracker coordinates to the PET coordinates such that the recorded motion data can be applied to the PET data. Two methods were employed during the course of this research, referred to as the absolute and relative positions calibration. Both methods rely on measuring an object which both the PET and the tracker can detect simultaneously so that the two measurements can be compared and a transformation between them derived. The transformation is a 4×4 matrix derived from six DOF, and there are, therefore, six parameters to determine from the calibration. Thus, at least six measurements are needed to solve for the transformation parameters.

Absolute Position Calibration

This method was used initially for the MT system. When the position of a marker is recorded by the MT, that position corresponds to the midpoint along the longest vector connecting two X-points, referred to as the centre of the marker. We designed a marker with a known centre and placed an active point source at that centre. The point source and the marker could then be measured within the PET FOV at various static positions (usually around 10 positions scattered throughout the FOV). The PET data was then reconstructed (using the standard software from the manufacturer) and the centroid of the point source in each reconstruction was determined. By comparing the MT translations to the corresponding point source centroids using the algorithm suggested by Horn (1987), a transformation matrix can be determined. This can be formulated as,

$$X_n^{\mathrm{PET}} = T_c X_n^{\mathrm{MT}}, \tag{1.10}$$

where X_n^{MT} is the recorded motion in MT coordinates at index n, and T_c is the transformation (or calibration) matrix.

A disadvantage of this method is that if the point source is not accurately placed at the marker centre, this will lead to an inaccurate transformation matrix.

Relative Position Calibration

For an arrangement of markers registered by the OT system, referred to as a "rigid body", the reported position of that rigid body is the centre-of-mass of the markers. This is not always easy to determine in real space, thus, to avoid the complication of having to accurately place a point source at the centre of a marker, the relative position calibration method was suggested by Prof. Roger Fulton at the University of Sydney. Instead of comparing absolute positions of the object in PET and tracker coordinates, the relative motion between two static positions is rather compared. A relative motion in the two systems is independent of any offset between the object's position in the PET and tracker coordinates. Given two positions, X_m and X_n, as 4×4 transformation matrices, the relative motion between them is,

$$\Delta X_{mn} = X_n X_m^{-1}. \tag{1.11}$$

Then the relation between the PET and tracker coordinates, via a calibration matrix T_c, is,

$$\Delta X_{mn}^{\mathrm{PET}} = T_c \Delta X_{mn}^{\mathrm{OT}} T_c^{-1}. \tag{1.12}$$

Several static positions of an active phantom with markers attached were recorded in the PET and with the OT. The reconstructions of the phantom can be registered to each other to determine $\Delta X_{mn}^{\mathrm{PET}}$, and these can be compared to the corresponding $\Delta X_{mn}^{\mathrm{OT}}$ for the OT measurements using a least squares optimisation algorithm to determine a suitable T_c matrix.

The advantage of this method is that it requires no careful measurement of the recorded centre of the object in PET or tracker space, and, since a complex phantom can be measured, the relative position matrices for the PET data can be determined to a greater precision than the absolute position of the point source in the former method.

1.2.3 Temporal calibration

Synchronising the PET and tracker data streams is necessary to determine which pose measurements should be applied to which list-mode events. This is usually achieved by inserting a "gate" tag (tags which are usually used to trigger physiological events such as a heart beat or a respiratory phase) into the list-mode stream for each pose that is recorded, allowing the recorded poses to be aligned with the inserted gate tags. Alternatively, the clocks of the PET and the tracker can be synchronised so that the time stamps of both data streams can be used directly. The details of how the synchronisation was achieved during this research are given in section 2.2.5 of chapter 2.

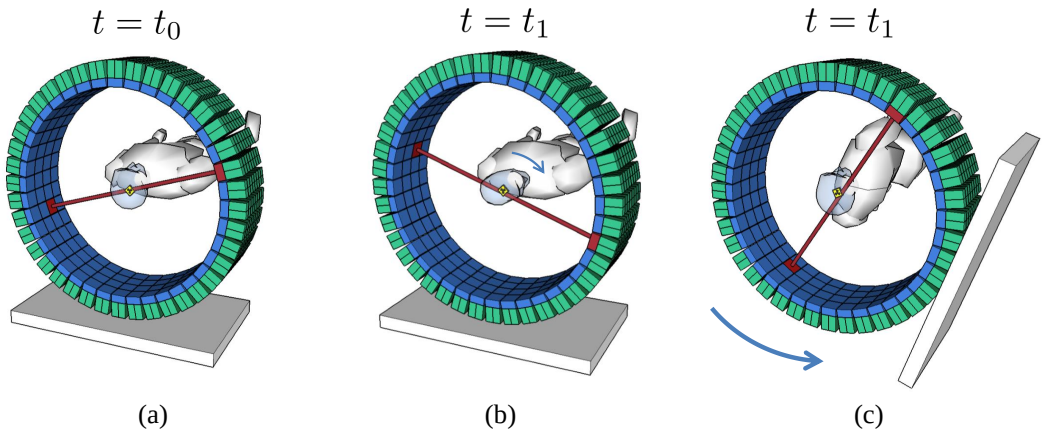

Figure 1.5: (a) At the time of the reference pose ($t = t_0$) an event is recorded. The LOR for this event is used as it is during the reconstruction. (b) At a later time point ($t = t_1$) the patient moves her or his head and the motion and another emission event are recorded. (c) For the event-based motion correction technique, it is assumed that the patient's head remained stationary (in the reference position) while the scanner (and everything else) moved opposite to the recorded motion, thus moving the LOR to where it would have been recorded if the patient's head had not moved.

1.2.4 Correcting for Motion

Daube-Witherspoon et al. (1990) were the first to propose a so-called "event-based" motion correction procedure whereby the endpoints of each recorded list-mode event are corrected according to the corresponding subject position at the time of that event, thereby determining where the event would have been recorded had the subject not moved. This process is illustrated in figure 1.5. In SPECT studies, Fulton et al. (1994) implemented a technique whereby the head motion is tracked and, if motion is detected, the recorded events are binned to a separate sinogram (in real time) representing where the data would have been measured had the patient not moved. Seperate sinograms are built up for each motion, and are then used together in an iterative reconstruction. Menke et al. (1996) assigned each event to a corrected sinogram bin (using look-up tables based on typical head positions) in real-time, however this is not a common implementation and most approaches perform the motion correction after the acquisition. Therefore, the data is usually recorded in list-mode format so that the time-stamp of each event is recorded, allowing the corresponding motion to be identified.

In (Bloomfield et al. 2003; Fulton et al. 2003) the recorded list-mode events were motion corrected and rebinned into a sinogram. A standard reconstruction could then be performed on this sinogram. List-mode events may, after motion

correction, end up at a location with no sinogram bin, such as outside of the scanner or in a gap between detecting elements. Such events are usually excluded from the motion corrected sinogram, thereby losing counts and information, which needs to be accounted for during the reconstruction. Additionally, since corrected events are rebinned into the nearest sinogram bin, a rounding error may be introduced.

In the event-based implementation (illustrated in figure 1.5), the endpoints of each measured event can be transformed according to the measured poses using,

$$\vec{l}'_t = T_c X_0^{\mathrm{MT}} \left(T_c X_t^{\mathrm{MT}}\right)^{-1} \vec{l}_t, \tag{1.13}$$

where $\vec{l}_t$ is the 4-vector in homogeneous coordinates (with the 4^{th} element being 1) of an endpoint of the LOR at time t, with $\vec{l}'_t$ being its motion corrected counterpart, T_c is the calibration transformation matrix, and X_t^{MT} is the measured pose at time t. The reference pose here is the first pose, X_0^{MT}, but it could be any other pose; it is usually chosen to match that of the attenuation map.

By using a list-mode formulation of the MLEM algorithm, as shown in (1.5), a more accurate reconstruction can be performed which avoids the problems of LORs moving out of the field-of-view and the additional rounding errors due to the rebinning, since the exact endpoints of the motion corrected events can be used directly in the reconstruction (Carson et al. 2003; Rahmim et al. 2004b). This approach was used throughout this research. For such a formulation though there are a number of complications that need to be addressed, due to the normalisation, attenuation, scatter, and randoms corrections.

Normalisation & Attenuation Each LOR in the scanner has a unique normalisation factor (the inverse of the sensitivity factor related to crystal efficiencies, etc.). When list-mode events are reoriented during motion correction, their corresponding normalisation factors should move with them, which affects the calculation of the sensitivity image (the term $\sum_i c_{ij} s_i a_i$ in equation (1.5)). For each possible LOR i, the average of the sensitivity factors for all measured LORs k which align with i after motion correction must be calculated, and then backprojected. This can be formulated as,

$$\bar{s}_j = \frac{1}{T} \sum_i c_{ij} a_i \int_0^T s_{i'(t)} dt, \tag{1.14}$$

where T is the scan duration, and $i'(t)$ is the result of motion correcting LOR i at time t. This is a very computationally expensive procedure since every possible LOR must be reoriented according to each measured pose.

A solution to this problem was proposed by Rahmim et al. (2004b), whereby the sensitivity factors are averaged in image space rather than in LOR space.

This involves backprojecting the sensitivity factors for all possible LORs, and then, for each voxel in this image, averaging over all voxels through which it passes as it moves according to the measured poses. A disadvantage of this approach however is that the attenuation correction factors, a_i, cannot be included in the calculation of $\bar{s}_j$. This is due to the fact that the attenuation correction factors are calculated for the subject at some static position (usually the reference position to which all events are motion corrected), therefore the factors corresponding to the motion corrected events should be used, in contrast to the sensitivity factors which use the factors of the uncorrected events. For this reason it is necessary to pre-correct the data for attenuation before reconstruction, meaning that the number of counts per data point (i.e. 1 in the case of list-mode reconstruction) are scaled by the attenuation correction factor along that event, thereby removing the attenuation factor from the sensitivity image calculation. While this approach is not ideal and may cause an increase in the noise of the reconstruction, the computational advantages gained during the calculation of the sensitivity image provide adequate justification. For scans with a high count rate this pre-correction becomes less significant, and for small animal imaging the attenuation correction factors are usually close to unity and so have a small impact on the reconstruction.

Rahmim's proposal begins by rewriting equation (1.14),

$$\bar{s}_j = \frac{1}{T}\sum_i c_{ij}\int_0^T s_{i'}dt = \frac{1}{T}\int_0^T \sum_i c_{ij}s_{i'}dt. \tag{1.15}$$

The observation is then made that if an LOR i becomes i' after motion, and a voxel j becomes j' due to the same motion, then,

$$c_{ij} = c_{i'j'}. \tag{1.16}$$

Observing that the sum over i for all LORs coincides with the sum over all LORs i' after motion, we can replace i with i' in (1.15), and incorporate (1.16):

$$\begin{aligned}\bar{s}_j &= \frac{1}{T}\int_0^T \sum_{i'} c_{i'j'}s_{i'}dt \\ &= \frac{1}{T}\int_0^T \tilde{s}_{j'}dt,\end{aligned} \tag{1.17}$$

where,

$$\tilde{s}_j = \sum_{i'} c_{i'j}s_{i'} = \sum_i c_{ij}s_i. \tag{1.18}$$

This solution thus requires the transformation of each voxel in the sensitivity image $\tilde{s}_j$ according to each measured pose, but since there are usually far fewer

voxels than possible LORs, this is an easier computational task than (1.14). Incorporating this into the list-mode MLEM equation (1.5), together with the pre-correction of the data for attenuation, we have,

$$\lambda_j^{n+1} = \frac{\lambda_j^n}{\bar{s}_j} \sum_{i_m} c_{i'_m j} s_{i_m} \frac{1/a_{i'_m}}{\sum_k c_{i'_m k} s_{i_m} \lambda_k^n + \frac{S_{i'_m}}{a_{i'_m}} + \frac{R_{i'_m}}{a_{i'_m}}}, \tag{1.19}$$

where i'_m is the result of motion correcting the measured event i_m, with m being the data point index. It should be noted that if there is any hardware within the FOV which does not move with the patient's head (e.g. the bed, MR coils, etc.), the attenuation correction factors for these elements would not be affected by the motion and should be multiplied by the sensitivity factors s_i when calculating the sensitivity image $\bar{s}_j$.

Scatter & Randoms For scatter and randoms correction, as for the attenuation correction, the motion corrected events should be used to determine their contribution. However, for most patient scans the motion is very limited, and since both the scatter and randoms are very smooth they will not be affected very much by the motion. Additionally, any hardware in the scanner (e.g. the bed, MR coils, etc.) will not move with the patient and should therefore not be affected by the motion. Therefore, as a simplifying approximation in my implementation, the uncorrected scatter and randoms correction factors were used during the reconstruction. The scatter and randoms contributions are then also pre-corrected for the sensitivity factors, which allows for a simplification of the forward and backprojections during the reconstruction. The final formulation of the algorithm, which was used predominantly throughout this research, is thus,

$$\lambda_j^{n+1} = \frac{\lambda_j^n}{\bar{s}_j} \sum_{i_m} c_{i'_m j} \frac{1/a_{i'_m}}{\sum_k c_{i'_m k} \lambda_k^n + \frac{S_{i_m}}{a_{i'_m} s_{i_m}} + \frac{R_{i_m}}{a_{i'_m} s_{i_m}}}. \tag{1.20}$$

As discussed above, the incorporation of the attenuation and sensitivity correction factors complicate the motion corrected reconstruction. With the advent of TOF-PET systems it appears that the additional information provided by the TOF allows for a data-driven estimation of both the attenuation and sensitivity factors during the reconstruction directly from the emission data, with no additional scans needed, and which can be used in conjunction with motion correction (although some additional method of tracking the motion is still required, such as an external tracker). I contributed to a conference proceeding presenting this approach, which is included as chapter 6.

1.2.5 Image-Based & Data-Driven Approaches

An alternative to the event-based approach discussed above is to separate the acquired data into short frames, perform a reconstruction on each frame, and, if motion has occurred between the frames, they can all be registered (i.e. aligned) to a reference frame, and then summed. An external motion tracking device can be used to detect when a significant motion occurred to define more effective framing of the data and reduce the number of frames needed (Picard et al. 1997; Fulton et al. 2002). However, this approach can only correct for motion between frames, and not intraframe motion, and it does not allow for a reconstruction of the complete data set at once. In general, if a patient moves during a scan, it is either very slow or only intermittently, and therefore the intraframe motion may be small enough to allow for a reasonable motion correction. This approach is not appropriate for animal studies since an animal will usually exhibit a wide range of motion with varying speeds.

A data-driven version of this method was presented by Thielemans et al. (2013) whereby the raw data is framed into many, short, low resolution sinograms, a principal component analysis (PCA) is performed on these sinograms to determine when significant motion occurred, and the raw data is then framed again according to when motion occurred. While this approach allows for a more optimal framing of the data without the use of external tracking devices, it can still only handle slow or intermittent motion.

Some researchers have attempted to estimate and correct the motion directly from the data, without framing as discussed above. An example is the approach presented by Hutton et al. (2002) and Kyme et al. (2003) and applied to SPECT data where two dimensional projections are acquired sequentially, and any motion between projections is estimated and corrected for. A similar approach has recently been demonstrated for CT by Sun et al. (2016) whereby the motion is iteratively estimated projection-by-projection. Unfortunately such approaches are unlikely to be successful in PET since the signal-to-noise ratio for each two dimensional projection is much lower than in the latter two modalities.

1.3 Resolution Modelling

PET scanners have a finite spatial resolution since the location of the isotope decay is inferred from the measurement of a photon pair, which is affected by a number of sources of uncertainty during the measurement process. Uncertainties during the measurement process arise from the positron range, the photon acollinearity, the response of the detector crystals to the incoming photons, photon scattering within the crystal, and imperfect transmission of the scintillation light in the crystals to the PMTs. These effects are illustrated

Table 1.3: Emitted positron energies and the width of their point spread function (PSF)

	Maximum β^+ energy (keV)	PSF FWHM in water (mm) *	PSF FWTM in water (mm) *
^{18}F	635	0.102	1.03
^{11}C	970	0.188	1.86
^{13}N	1190	0.282	2.53
^{15}O	1720	0.501	4.14

* Levin et al. 1999. Note that the positron range distribution is very sharp and has longer tails than a Gaussian distribution with the same FWHM.
FWTM: Full width at tenth maximum.

in figure 1.6. In this section an overview of these sources of uncertainty is presented before techniques for handling them are discussed.

For scanners with a transaxial diameter of between 60 and 100 cm, the spatial resolution at the centre of the FOV is usually between 4 and 6 mm (Brambilla et al. 2005; Jakoby et al. 2011). Dedicated brain scanners with a smaller diameter of around 30 cm have a resolution of around 2.5 mm (Jong et al. 2007), and preclinical scanners for small animals with a diameter of between 15 and 25 cm have a resolution of around 1.3 mm (Balcerzyk et al. 2009; Tai et al. 2005).

1.3.1 Sources of Uncertainty

Positron Range

The positron emitted during the isotope decay has a non-zero kinetic energy, which it loses through scattering interactions with the surrounding material as it travels. Thus the higher the positron energy the further it travels before annihilating with an electron in the surrounding material. The energy and positron range of a selection of common PET radioisotopes is shown in table 1.3. These positron ranges contribute directly to the uncertainty in the location of the isotope decay.

Photon Acollinearity

It is likely that the electron-positron system has a non-zero linear momentum. Therefore, when it annihilates and emits two photons, the sum of these photons' momenta must be non-zero, and therefore have acollinear trajectories. During a PET reconstruction it is assumed that the photons were indeed collinear, and so, while the magnitude of the acollinearity is small, it contributes some uncertainty in the location of the decay event. The offset between the midpoint

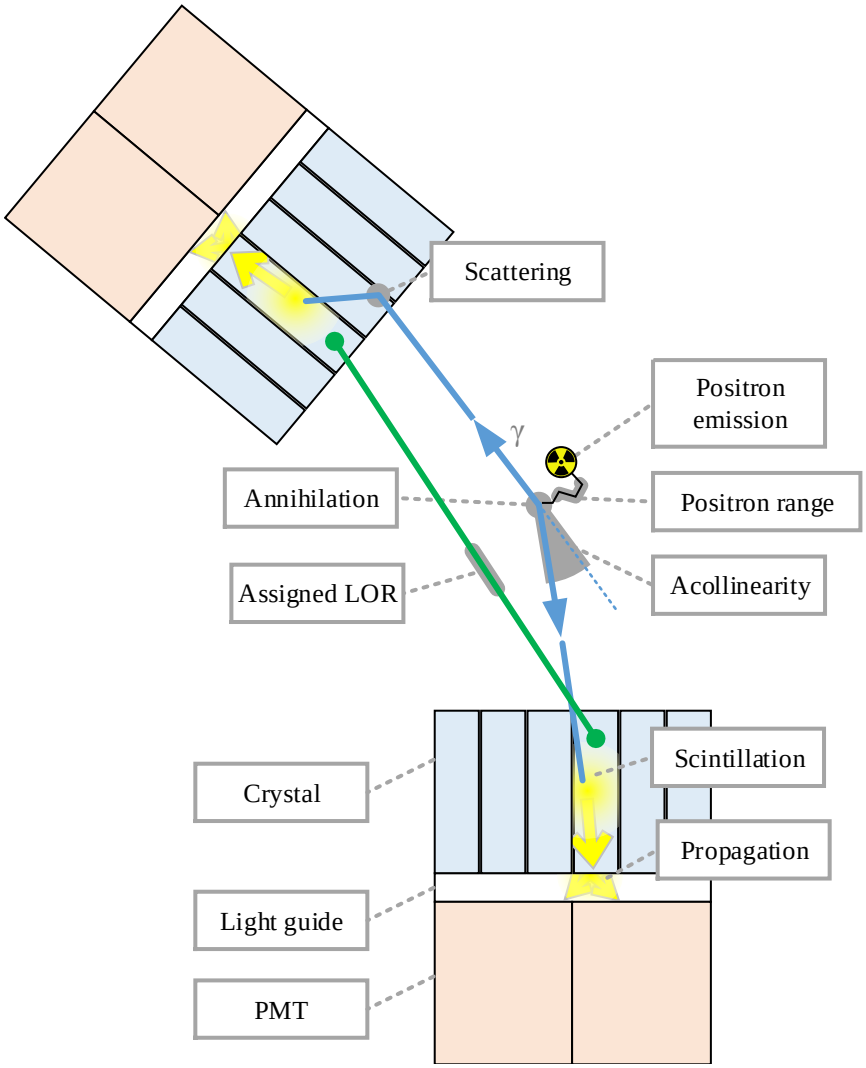

Figure 1.6: Illustrating the factors contributing to the uncertainties during a PET measurement, namely the positron range, photon acollinearity, inter-crystal scattering, imperfect assignment of the LOR endpoints to the scintillation location, and imperfect light propagation through the light guide.

of the measured LOR and the decay location due to photon acollinearity is dependent on the scanner radius, R, by,

$$a = \frac{R}{2} \sin\theta, \tag{1.21}$$

where θ is the angle of acollinearity as indicated in figure 1.6, and is generally accepted as having a FWHM value of 0.50° (Levin et al. 1999); this is discussed in more detail in chapter 5. The value of a can be considered to be the FWHM of the blur due to the photon acollinearity effect. For larger scanners the effect is more pronounced, from about 1.7 mm for clinical scanners with a radius of around 40 cm, to about 0.5 mm for preclinical scanners with a radius of around 12 cm.

Detector Response Function

Each detecting crystal has some spatial extent, as can be seen in table 1.2. This extent thus defines the resolution with which the LOR endpoints are spread over the scanner's detecting surface, and has a substantial impact on the spatial resolution within the FOV of the scanner. At the centre of the FOV this effect contributes a FWHM of half the crystal width to the decay location uncertainty, and therefore approximately 2 mm for clinical scanners, and approximately 0.75 mm for preclinical scanners.

Photons will traverse some distance within a scintillation crystal before being absorbed and causing a scintillation. This distance is largely dependent on the crystal density and is referred to as the "depth-of-interaction" (DOI). A photon which is obliquely incident on a crystal surface may traverse through that crystal and be absorbed in a neighbouring crystal. Since the recorded LOR will be between the detecting crystals, there may be a discrepancy between that LOR and the true photon flight paths, as can be seen in figure 1.6. This effect becomes more pronounced for locations away from the centre of the FOV, for photons which strike the detecting surface obliquely, and thus is the main contributor to the variation in the spatial resolution within the scanner FOV. Near the centre of the FOV this effect is negligible, but, for a clinical scanner, at a distance of 20 cm away from the centre the resolution drops to 6 - 8 mm, largely due to this effect. Scanners which can record and report DOI information for a detected photon can improve the uniformity of the spatial resolution across the scanner FOV.

Crystal Scattering

A photon traversing through a crystal may undergo scattering before being completely absorbed. If the scattering causes it to be absorbed in a crystal other than the one it entered originally, then the resulting LOR may not pass

through the annihilation location. As with scattering events occurring within the FOV, such photons can be identified since they have a lower energy than an unscattered photon, but since the system has only a finite energy resolution not all such events can be discerned.

Scintillation Transmission

An absorbed photon causes a scintillation within the crystal. This scintillation propagates to the back of the crystal, through a light guide which diffuses the light onto the array of PMTs. This propagation may be imperfect with possible cross-talk with the neighbouring crystals, or imperfect diffusion through the light guide, and may vary for crystals near the edge of the block detector. This contributes to the uncertainty in the estimation of where the scintillation occurred, usually assumed to be approximately $\frac{d}{3}$ where d is the crystal width (Moses 2011).

Total Uncertainty

Although several of these sources of uncertainty do not have a Gaussian shape, it is nonetheless generally assumed that they can be combined together in quadrature (Moses 2011) to estimate the total uncertainty. Moses (2011) has proposed the following formulation for the expected spatial resolution Γ at a radial position r in the scanner FOV,

$$\Gamma(r) = 1.25\sqrt{\left(\frac{d}{2}\right)^2 + \frac{(12.5r)^2}{r^2+R^2} + s^2 + \left(\frac{R}{2}\sin 0.50^\circ\right)^2 + \left(\frac{d}{3}\right)^2}, \qquad (1.22)$$

where d is the crystal width, s is the positron range, and R is the detector ring radius. The factors added in quadrature are, respectively, the detector size, detector response function, positron range, acollinearity, and imperfect scintillation transmission. The factor of 1.25 is an empirically determined factor introduced by the reconstruction algorithm.

1.3.2 Modelling the Resolution

Iterative reconstruction algorithms model the forward process of the measurement, and update the reconstruction based on some comparison with the measured data. The final resolution of the reconstruction is affected by how accurately the forward model corresponds to the actual measurement process. By including a model for the sources of uncertainty discussed above, known as "modelling the resolution", the final resolution of the reconstruction can be improved. There are several methods for modelling the resolution, and most approaches can be classed as either a projection-based or an image-based approach. Both classes effectively adjust the system matrix (c_{ij} in equation

(1.2)) to allow overlap between each LOR and voxels which do not lie exactly along that LOR, in a manner which models the uncertainty associated with that LOR. A common implementation assumes that the resolution is uniform across the FOV (i.e. spatially invariant), and applies a smoothing to the image which matches the resolution of the scanner (Reader et al. 2003). A Gaussian kernel is usually used for the smoothing. At each iteration of the reconstruction the smoothing is applied to the image before forward projection and after backprojection. In a projection-based approach a smoothing kernel can be applied to the sinogram, after forward projection and before backprojection. The resolution of the scanner throughout the FOV can be measured using point sources and a more accurate smoothing kernel, which varies in the FOV, can be constructed (Panin et al. 2006). The kernel can also be estimated using Monte Carlo techniques (i.e. an accurate and comprehensive, but time-consuming, simulation of the physical processes involved during the measurement) (Mumcuoglu et al. 1996; Qi et al. 1998), or by using analytical techniques (Lecomte et al. 1984; Huesman et al. 2000). In chapters 2 to 4 the image-based, spatially invariant convolution approach was used to model the resolution.

Instead of using a simple line to represent the LOR during the forward and backprojection, it is possible to instead use a "tube-of-response" (TOR) which connects the entire surfaces of the detecting crystals. Similarly to the convolution techniques, this is also effectively adjusting the system matrix. Again, the more accurately this TOR represents the true distribution of possible decay locations for the recorded LOR, the higher the resolution of the final reconstruction. An alternative approach is to replicate an LOR multiple times, each time adjusting the endpoints of the line slightly to cover the surface of the detecting crystals. In this way the TOR is approximated. This approach is referred to as a "multi-ray" approach, a version of which I developed during this research and present in chapter 5.

1.3.3 Disadvantages of resolution modelling

Resolution modelling attempts to deconvolve the imperfect acquired data to remove the blurring due to the uncertainties in the measurement process. This is an ill-posed mathematical problem and therefore has its limitations. Near sharp edges in the image, the reconstruction with resolution modelling will tend to overshoot and undershoot at the high and low regions of the edge, respectively, with these artefacts oscillating away from the edge. These are known as Gibbs or ringing artefacts. For small regions which are comparable in size to the period of the Gibbs artefacts the overshoot from either edge of the region can combine to form a significant increase in the region's mean value. This can affect the quantification of these regions. Two review articles of the advantages and disadvantages of resolution modelling were presented by Alessio et al. (2013) and Rahmim et al. (2013).

1.3.4 Resolution modelling with motion correction

As already mentioned, a resolution model can be spatially variant or invariant. For most brain scans where the subject is motionless at the centre of the FOV, using a spatially invariant resolution model is sufficiently accurate. However, for motion correction studies where the subject may move significantly throughout the scanner and thus move through different resolution regimes, modelling the resolution in a spatially variant manner may be necessary. Additionally, when the subject extends over a significant portion of the FOV, such as in abdomen or thorax imaging, a spatially variant model is preferred. In chapter 5 I present a spatially variant resolution model developed with the aim of being used in conjunction with motion correction.

1.4 Research Objectives

The research conducted during this PhD sought to further develop and improve rigid motion correction techniques for PET brain scanning, especially for small animal studies but also extending them to clinical studies. This was achieved by optimising the experimental setup, data analysis and reconstruction. Using the improvements in the technique, specific studies were conducted to evaluate the effect of anaesthetics on common radioactive tracers used in PET imaging. Such studies would not be possible without motion correction, and the knowledge they provided filled a significant gap in the literature. The motion correction technique was applied to many different PET scanners to broaden the impact of the work and investigate how well the techniques could be adapted to these various scanners.

A spatially variant resolution model was developed with the aim of incorporating it into a motion correction reconstruction algorithm in a manner which accurately preserved the variation of the resolution while applying motion correction.

Specific research question which were addressed during this PhD were:

- How can the experimental setup for rigid motion correction studies be optimised, for preclinical and clinical studies?
- What techniques can be utilised during data analysis and reconstruction to improve the final motion corrected image?
- Can a protocol be developed to apply motion correction to studies involving fully conscious animals?
- Is it possible to develop a spatially variant resolution modelling technique which would be applicable to motion correction studies?

Investigating these questions involved developing software for data analysis, reconstruction, simulation, etc., primarily using the Interactive Data Language (IDL) and C languages, developing experimental procedures and performed experiments for phantom, rat, and human studies, constructing and programming a robotic arm to conduct phantom studies, developing 3 dimensional models for 3D printing, and constructing various pieces of hardware for experiments.

1.5 Overview

This thesis is composed primarily of articles which have been published or submitted for publication. Chapter 2 concerns various developments and optimisations in motion correction and has been published in Physics in Medicine and Biology. My co-author, Dr. Zhou, contributed significantly to this work since we worked together in implementing the motion correction technique at our institution. After she left our group I continued with the experiments and data analysis, and composed the paper. In chapter 3 results are presented on the study into the effect of isoflurane on FDG uptake in the rat brain, using motion correction, and has been resubmitted for publication in the European Journal of Nuclear Medicine and Molecular Imaging - Research after being revised as requested by the reviewers. Chapter 4 discusses the application of the developed motion correction techniques in the clinical setting, and shows results from various scanners. This chapter has not been submitted for publication, but the work therein has appeared in two conference proceedings for the IEEE Medical Imaging Conference (2015) and the Conference on PET/MR and SPECT/MR (2014). In chapter 5 the spatially variant resolution modelling technique which was developed during this research is presented, and has been published in IEEE Transactions on Medical Imaging. Chapter 6 is a proceeding from the IEEE Medical Imaging Conference (2015) on a list-mode implementation of a joint estimation algorithm for emission and attenuation. I am the second author on this work where I contributed an implementation of the list-mode ISRA algorithm (which is used during the joint estimation), expertise on handling list-mode data, and helped in extending the work to incorporate motion correction (which was not reported on in this proceeding). In chapter 7 the findings of the thesis are discussed and future prospects are presented. Finally, at the end of this thesis, a number of appendices are given on more technical aspects of the work, such as a description of a simulator which was developed to aid in the research, the work-flow of a typical motion corrected reconstruction, the experiment hardware developed and utilised, and of how the rat training was performed.

Chapter 2

Optimising Rigid Motion Compensation for Small Animal Brain PET Imaging

Published as[1]:

M. G. Spangler-Bickell, L. Zhou, A. Z. Kyme, B. de Laat, R. R. Fulton, and J. Nuyts (2016a). "Optimising rigid motion compensation for small animal brain PET imaging". In: *Physics in Medicine and Biology* 61.19, pp. 7074–7091

Abstract

Motion compensation (MC) in PET brain imaging of awake small animals is attracting increased attention in preclinical studies since it avoids the confounding effects of anaesthesia and enables behavioural tests during the scan. A popular MC technique is to use multiple external cameras to track the motion of the animal's head, which is assumed to be represented by the motion of a marker attached to its forehead. In this study we have explored several methods to improve the experimental setup and the reconstruction procedures of this method: optimising the camera-marker separation; improving the temporal synchronisation between the motion tracker measurements and the list-mode stream; post-acquisition smoothing and interpolation of the motion data; and list-mode reconstruction with appropriately selected subsets. These techniques have been tested and verified on measurements of a moving resolution phantom and brain scans of an awake rat. The proposed techniques improved the reconstructed spatial resolution of the phantom by 27% and of the rat brain

[1]Note that for publications after March 2016 I use my married name "Spangler-Bickell". Although at the time of publication of this thesis I was still registered with the university under my bachelor name "Bickell".

by 14%. We suggest a set of optimal parameter values to use for awake animal PET studies and discuss the relative significance of each parameter choice.

2.1 Introduction

Small animal positron emission tomography (PET) systems have become increasingly important in preclinical imaging since they enable *in vivo* and longitudinal investigations of animal models. Usually anaesthesia or sedatives are used to eliminate animal movement and stress during the scan. Many reports, however, suggest that anaesthesia can have confounding effects on the kinetics of the tracer or drug under study (Alstrup et al. 2013). To avoid this, researchers have tried to either physically restrain the animal during the scan (e.g. (Hosoi et al. 2005)) or, more commonly, to perform a static scan of an anaesthetised animal after allowing tracer uptake while it was awake (e.g. (Toyama et al. 2004)). However, stress induced by restraint can affect the kinetics of the drug or tracer under study, diminishing the advantage gained by avoiding anaesthesia. Moreover, performing static scans does not allow for the kinetics of the uptake to be estimated and is only possible in a few tracers.

Techniques to allow the animal to be awake and unrestrained during the scan have been investigated by various groups. A novel approach to avoid relative motion between a rat's brain and the PET scanner is the RatCAP (Vaska et al. 2004; Schulz et al. 2011), a miniaturised PET scanner which is surgically attached to the rat's head and which moves rigidly with the brain. While this system is promising it has a lower sensitivity than commercial scanners and may inhibit the natural movement of the rat, possibly inducing stress in the animal.

Motion tracking can be used in conjunction with conventional PET scanners to record the three dimensional motion of the awake animal during the scan, and correct for it offline. This motion compensation (MC) approach avoids the need for anaesthesia and minimises stress since the animal is unrestrained (although the animal is often confined to a small space during the scan). Motion tracking approaches can be either marker-based (Weisenberger et al. 2005; Kyme et al. 2011b), where a small marker is attached to the head of the animal and tracked by external cameras, or markerless, where the facial features of the animal are identified and tracked by external cameras (Kyme et al. 2014). Various marker-based (e.g. (Bloomfield et al. 2003; Fulton et al. 2003; Bühler et al. 2004; Kim et al. 2015)) and markerless (e.g. (Olesen et al. 2013; Noonan et al. 2012)) approaches have been investigated for human studies where MC is also desirable.

Kyme et al. (2011b) successfully applied a marker-based technique to rats using the MicronTracker (ClaroNav Inc., Toronto, Canada), a motion tracking system which is well suited to the application (Kyme et al. 2008). In a MC

framework there are several potential sources of error - related to both optical motion tracking and how the tracking data are applied for motion correction of the PET data, neither of which are encountered in conventional imaging. This paper builds on previous work by analysing these sources of error and investigating methods to minimise them. The key scientific questions we are trying to answer with respect to MC accuracy are: (i) What is the optimal operating distance for motion tracking? (ii) How important is smoothing and interpolation of the pose data? (iii) What is the best way to relate the discretely sampled pose measurements to what is essentially a continuously sampled PET list-mode data stream? And (iv) when using subsets in the reconstruction, how should these be selected from the motion corrected list-mode data? The paper is structured as follows: section 2.2 outlines the rationale and principles of the improvements; sections 2.3 and 2.4 detail the validation experiments and results, respectively; and sections 2.5 and 2.6 contain our discussion and conclusions.

2.2 Methods & Materials

2.2.1 Data Acquisition and Reconstruction

All scans were performed using the microPET Focus 220 small animal scanner (Preclinical Solutions, Siemens Healthcare Molecular Imaging, Knoxville, TN, USA). The microPET has an isotropic spatial resolution at the centre of the field-of-view (FOV) of 1.3 mm full-width at half-maximum (FWHM) (Tai et al. 2005). All data were acquired in 48-bit list-mode format.

Motion tracking was performed using the MicronTracker Sx60 (MT), a stereo-optical system which tracks a pre-registered planar marker, an example of which is shown in figure 2.1(b). The MT uses two simultaneously acquired, but spatially offset, images to estimate the 6 degree-of-freedom (DOF) rigid-body pose (3 components of position and 3 components of orientation) of the marker. The pose measurement rate of the MT is dependent on the processing power of the system used to process the data; for this research a rate of between 20 and 40 Hz was used.

The PET data were reconstructed using the ordered subsets expectation-maximisation (OSEM) iterative algorithm (Shepp et al. 1982; Hudson et al. 1994). A list-mode based implementation of this algorithm was used (Parra et al. 1998; Reader et al. 1998):

$$\lambda_j^{n+1} = \frac{\lambda_j^n}{\sum_i^I s_i a_{ij}} \sum_m^M a_{i_m j} \frac{1}{\sum_k^J a_{i_m k} \lambda_k^n} \tag{2.1}$$

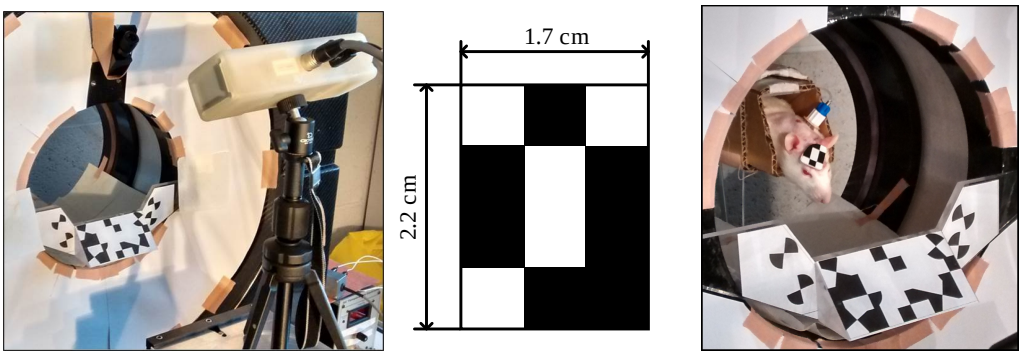

(a) (b) (c)

Figure 2.1: (a) The MicronTracker in front of the microPET scanner. The large marker attached to the front of the scanner is the reference marker used to aid in transforming from the MT coordinates to the microPET coordinates. (b) The head marker used in rat studies. (c) An unrestrained rat with an attached head marker inside a tube within the microPET. The catheter port can be seen between its shoulders.

where λ_j^n is the value of voxel j of the current reconstruction at iteration n, J is the number of voxels in the image, M is the number of measured list-mode events, i_m denotes the detector pair i associated with event m, I is the total number of possible detector pairs, s_i is the sensitivity factor for detector pair i, and a_{ij} is the system matrix element specifying the contribution of the activity in voxel j to the detection of events in detector pair i. This formulation enables event-by-event motion correction of each detected photon pair. The resolution was modelled using the image-based convolution technique with a Gaussian kernel (FWHM = 1.3 mm) (Reader et al. 2003). The sensitivity image was calculated as described in Rahmim et al. (2004b) by transforming it according to each detected pose, and summing these together as a weighted average. Calculation of this time-averaged sensitivity image accounts for most of the computational burden of the reconstruction. To accelerate this calculation we used only every fifth pose measurement; we have not observed this approach degrading reconstruction quality or introducing artefacts. Since we were only interested in relative changes due to MC, absolute quantification was not necessary and so the effects of attenuation, scatter, and randoms were ignored.

2.2.2 Spatial calibration

Pose measurements from motion tracking are reported in the coordinate system of the MT, making it necessary to determine a transformation to convert these data to the microPET coordinate system. For this, a similar procedure to that described by Kyme et al. (2008) and Fulton et al. (2002) was followed.

Briefly, a small radioactive microsieve bead was placed at the origin of an MT marker and imaged in the microPET at several discrete locations throughout the FOV. The bead locations in the PET frame were estimated as the centroids of the reconstructed point source images, and the corresponding locations in the tracker frame were measured directly using the MT. A rigid-body transformation matrix relating the two frames was then computed from these paired measurements using the method in (Horn 1987).

To apply the calibration in subsequent experiments in which the relative position of the MT and scanner has changed, we use a reference marker rigidly affixed to the gantry (figure 2.1(a)). This reference marker can be attached to the scanner highly reproducibly. Measurement of the reference marker pose enables updating of the coordinate calibration according to:

$$T_c' = T_c T_R T_R'^{-1}, \tag{2.2}$$

where T_R and T_R' are 4×4 transformation matrices of the reference marker pose at the time of original calibration and the time of experiment, respectively, using homogeneous coordinates, and T_c and T_c' are the calibration transformation matrices to convert from MT to PET coordinates at the time of original calibration and the time of experiment, respectively. The pose, ΔT^{PET}, relative to a reference pose in microPET space is given by:

$$\Delta T^{\mathrm{PET}} = T^{\mathrm{PET}} \left[T_0^{\mathrm{PET}}\right]^{-1} = T_c' T^{\mathrm{MT}} \left[T_c' T_0^{\mathrm{MT}}\right]^{-1}, \tag{2.3}$$

where the superscript denotes the coordinate space, and T and T_0 are the transformation matrices of the recorded pose and a chosen reference pose, respectively.

2.2.3 MT distance optimisation

To minimise the stress and discomfort of the rat, the head marker (figure 2.1(b)) needs to be as small as possible. However, the larger the solid angle subtended by the marker at the MT, the more accurately it can be tracked and the greater the range of motion that can be detected. The MT has a fixed focal length of 700 mm, at which the marker subtends only a small solid angle. To increase the solid angle the MT can be brought closer to the marker, however this will cause out-of-focus blurring. We conducted tests to characterise this trade-off and optimise the MT-marker separation.

An industrial robotic arm (Epson C3-A601S 6-axis, SEIKO Corp., Japan) with repeatability of ±10 μm was used to move the marker through several controlled motion sequences and to provide the ground truth of the marker motion. The robotic arm and the MT system were cross-calibrated as described by Kyme et al. (2011b). By repeating the motion sequences, the motion of the marker was measured by the MT at different MT-marker separations,

and compared to the applied (robot) motion as a function of the MT-marker separation.

We use $T^{\mathrm{MT}}_{M_n}$ and $T^{\mathrm{MT}}_{R_n}$ to denote the transformation matrices corresponding to the n-th marker pose and the n-th robot pose, respectively, in the MT coordinate system (denoted by the superscript). The corresponding incremental motions are denoted by $\Delta T^{\mathrm{MT}}_{M_n}$ and $\Delta T^{\mathrm{MT}}_{R_n}$, calculated as

$$\Delta T^{\mathrm{MT}}_{M_n} = T^{\mathrm{MT}}_{M_n} \left[T^{\mathrm{MT}}_{M_{n-1}}\right]^{-1} \tag{2.4}$$

$$\Delta T^{\mathrm{MT}}_{R_n} = T^{\mathrm{MT}}_{R_n} \left[T^{\mathrm{MT}}_{R_{n-1}}\right]^{-1}. \tag{2.5}$$

Since all calculations occur in the MT coordinate system, below we omit the superscript MT for clarity. To evaluate the discrepancy between measured and applied motion according to (2.4) and (2.5), we simulated a uniform spherical grid of points centred on a virtual microPET FOV. We set the radius of the sphere to 10 mm to approximate the size of the rat brain. Using X_p to represent the coordinates of the p-th point on the grid, applying the incremental motions to this point results in the transformed points $X_{M_{np}}$ and $X_{R_{np}}$:

$$X_{M_{np}} = \Delta T_{M_n} X_p \tag{2.6}$$

$$X_{R_{np}} = \Delta T_{R_n} X_p. \tag{2.7}$$

To quantify the similarity of marker and robot poses, we used the offset between these transformed points, calculated by

$$E_{np} = \|X_{M_{np}} - X_{R_{np}}\|. \tag{2.8}$$

Since we consider the robot pose to be the gold standard, a smaller E_{np} indicates improved accuracy of the marker detection. We used the following quantitative measures to assess the performance of the marker detection at each MT-marker separation,

$$\bar{E} = \frac{1}{N} \sum_{n}^{N} \bar{E}_n \tag{2.9}$$

$$\bar{\sigma} = \frac{1}{N} \sum_{n}^{N} \sigma_n \tag{2.10}$$

where N is the total number of incremental poses acquired at that separation, and $\bar{E}_n$ and σ_n are the mean and the standard deviation of E_{np} over all the points on the grid, respectively.

2.2.4 Pose smoothing and interpolation

To reduce the impact of pose measurement jitter and noise, the measured poses were smoothed in the temporal domain using a finite impulse response pose

filter with a Gaussian kernel (Kyme et al. 2011b; Kyme et al. 2011a) (with a FWHM of 100 ms; this kernel is discussed in section 2.4.4). The smoothing of the rotation matrices is based on the rigid-body pose interpolation approach described Stavdahl et al. (2005) using the "cosine average", but where each rotation matrix is the average of its neighbours, weighted by the kernel.

Poses are typically recorded at a rate of 30 Hz, corresponding to a 33 ms interval between successive measurements. At this rate it is possible for the subject to move up to 5 mm between poses (maximum speeds of around 150 $mm.s^{-1}$ are observed in awake rat studies). In (Kyme et al. 2011b), each pose measurement was applied in the motion compensation to all list-mode events recorded during the pose interval. However, we hypothesised that interpolating between poses may reduce blur introduced by inter-pose motion. Cubic splines were used for the interpolation and each DOF was handled independently. While this is not strictly accurate for the rotations (Stavdahl et al. 2005), the angular change from one pose to the next was sufficiently small[2] to justify this approximation. In our implementation pose smoothing was always applied before interpolation.

2.2.5 Temporal synchronisation

The poses are recorded by a system which is separate from the microPET controller. Therefore it is necessary to temporally correlate list-mode events and measured poses. This is referred to as the temporal synchronisation between the motion and PET data. As implemented in (Kyme et al. 2011b), to achieve temporal synchronisation a strobe signal was sent from the MT to the gate input of the microPET whenever a pose was recorded; triggering the gate input caused the microPET system to insert a gate tag into the list-mode data stream, which can be used for the data alignment. In practice, this can be done by aligning the first (or last) pose with the first (or last) gate. However, the reliability of this alignment is difficult to determine since poses or gates may have been missed (typically on the order of 10 gates or poses are missed during scans around an hour long), and only the quality of the reconstruction can suggest that the synchronisation may have been suboptimal.

In order to improve upon this, we developed a signal generator to trigger the MT. The generator produces a block wave pattern in which each block has a probability of $\frac{1}{32}$ of having its length increased by a predetermined factor (20%). This is achieved with a 16-bit pseudo-random generator, introducing an irregular and unique interval pattern in the MT poses and, hence, microPET gates, which enables robust alignment (figure 2.2). The pattern has a period of $2^{16} - 1$ triggers, or approximately 35 minutes at a mean triggering frequency

[2]The rat motion data from section 2.3.4 had a maximum angular change of 0.26 radians (mean 0.012 radians, with 75% of the data below 0.013 radians). This maximum can cause an error of up to 0.024 radians (Stavdahl et al. 2005) in the interpolated angles.

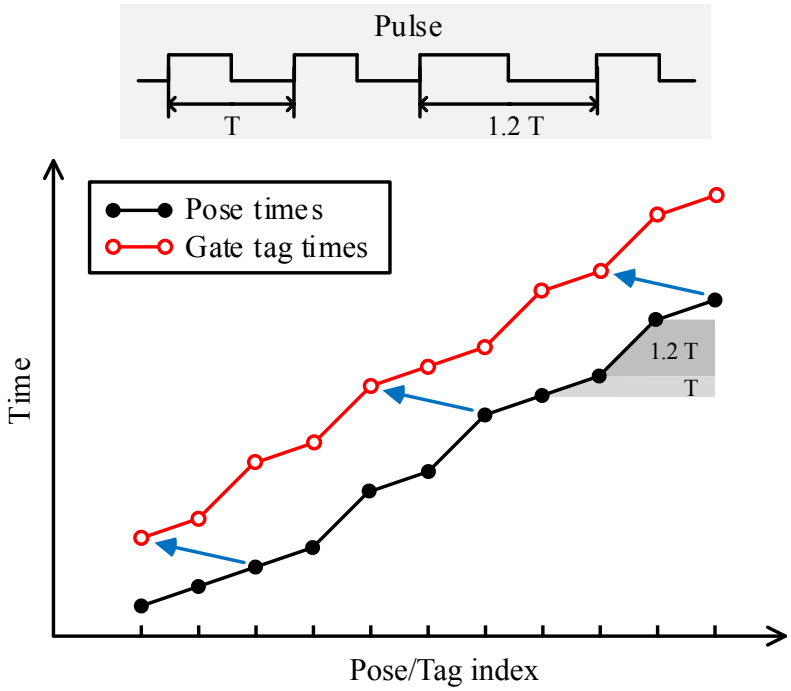

Figure 2.2: The signal generator produces pulses of a set period (T), but every pulse has a $\frac{1}{32}$ chance of being extended by 20% (top figure). The extent of the extended intervals has been exaggerated for clarity. Synchronisation between the time stamps of the poses and the gate tags is achieved by aligning the unique pattern of extended pulse lengths present in both streams. In this example there is an offset of two tag indices between the two streams. Such an offset arises if the tracking system starts before the PET acquisition, drops frames, and/or the scanner fails to insert gating tags.

of 30 Hz. If a pose or gate was missed, alignment can be maintained based on the trigger pattern before and after the missed element. Since the number of elements in each stream is relatively low (typically on the order of 10^4), an exhaustive search can be conducted to find the optimal synchronisation of the two streams, while simultaneously filling in any missing gate tags or poses. The root mean square difference between the absolute times of the gate tags and poses was used to determine the optimal alignment.

2.2.6 Optimised delay time

Synchronisation latency

When triggered by a low-high transition of the signal generator pulses, the MT begins sensor exposure for a duration equal to the specified shutter time (e in figure 2.3, typically 4 - 12 ms). After exposure, the recorded image data

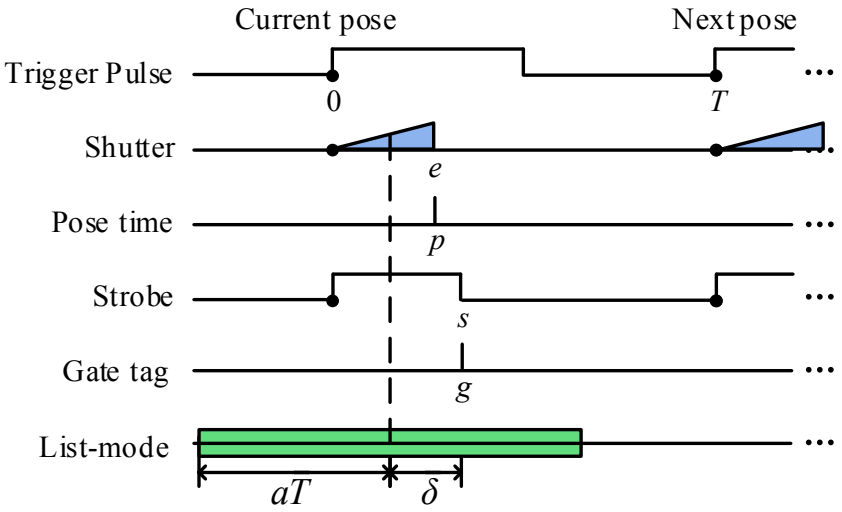

Figure 2.3: Time sequence of the pose measurement and synchronisation process. Time intervals are shown to scale with the following parameters: $T = 30$ ms, $e = 8$ ms, and $s = 10$ ms. The last row shows which events should be corrected by the current pose, and the necessary delay ($aT + \delta$) between the first event and the gate tag. In practice, however, the exact timing of these processes might differ due to unaccounted latencies.

are time stamped (p) according to the on-board Firewire clock before being transferred to the processing computer for pose computation. At the start of an exposure cycle, the MT also emits a fixed duration strobe pulse (s, typically 10 - 15 ms) to trigger the PET system (high-low transition) via the gating input. Ideally, the insertion of the gate tag (g) in response to this trigger is instantaneous. This idealised time sequence of events is illustrated in figure 2.3. In practice, there may be timing fluctuations from intermediate processes which result in deviations from the ideal scenario. We model the real delay between the inserted gate tags and the pose time stamps as a constant latency δ (as shown in figure 2.3), and fit it empirically.

Synchronisation implementation

A measured or interpolated pose is applied to the list-mode events spanning the interval associated with that pose. With no interpolation this interval is around 30 ms, with interpolation it is usually 1 ms. Therefore a particular pose can be regarded as the average of the motion over the pose interval, starting half an interval before the pose time stamp and ending half an interval after. The first list-mode event to which the pose should be applied is then at half an interval before the pose time stamp. We consider this to be an interval-dependent

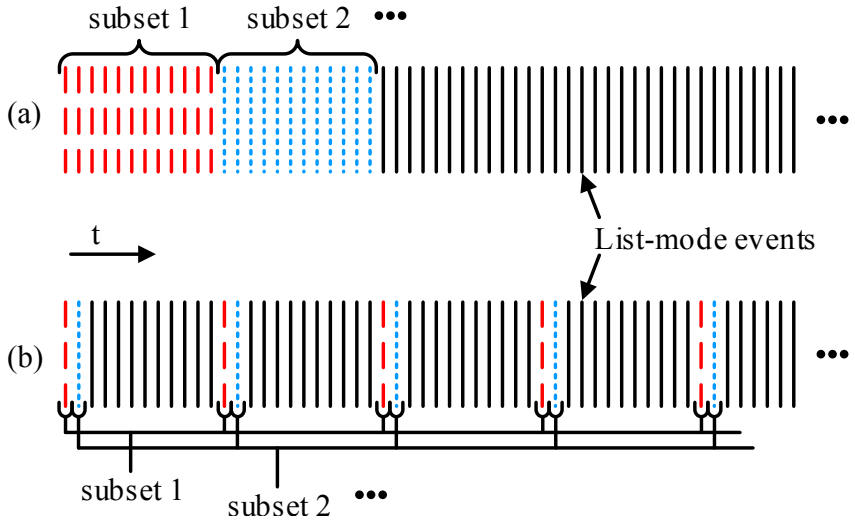

Figure 2.4: Subset selection. Subsets can be selected as chronological segments (a) or by selecting events spread evenly throughout the list-mode stream (b). The second method ensures that all subsets are subject to a similar range of motion.

contribution to the constant latency described above, viz.:

$$\Delta = -\frac{1}{2}T + \delta, \tag{2.11}$$

where T is the interval between subsequent poses.

2.2.7 Subset selection

The convergence of the reconstruction can be accelerated by using subsets of the list-mode data in each iteration (Reader et al. 1998). One possible option is to choose subsets as chronological segments of the list-mode data (figure 2.4(a)). However, since the average sensitivity image is calculated as the time-weighted average of the sensitivity image transformed by each pose throughout the scan, it is possible to introduce an error if the motion in a given subset differs significantly from the motion present in the average sensitivity image. Therefore, we propose to select each subset from the entire list-mode data set such that it incorporates the motion throughout the scan, as illustrated in figure 2.4(b). This approach was used in all reconstructions.

2.3 Experiments

2.3.1 MT distance optimisation

To optimise the MT-marker separation we used the Epson robot to manipulate a rat head marker according to known motion while it was synchronously tracked by the MT. Three motion sequences were executed by the robot: (i) arbitrary continuous motion, (ii) measured rat motion, and (iii) step-wise motion in which each pose was held for 5.5 s. All sequences were 2 minutes and involved 6 DOF changes in marker pose. Each motion sequence was repeated multiple times at a different MT-marker separation ranging from 285 mm to 575 mm. In all cases tracking was performed at 30 Hz. The MT and robot data were post-processed and compared as described in section 2.2.3.

2.3.2 Optimised delay time

The optimal delay time was determined based on motion compensated reconstructions of a moving point source. A 2 mm diameter porous bead containing 0.74 MBq ^{18}F-FDG was placed at the centre of a large MT marker (diameter 57 mm) and scanned within the microPET FOV for 2 minutes while undergoing a robot-controlled arbitrary motion in conjunction with motion tracking (strobe duration 15 ms, shutter 8 ms). The scan was repeated thirty times with the pose measurement rate varying between 18 - 39 Hz. Images were reconstructed using the method described in section 2.2.1 (using 2 subsets and 7 iterations). Reconstructions of each data set were performed using a range of delays between the measured poses and the gate tags. The optimal delay for each data set was determined by finding the reconstruction with the highest maximum value. This is based on the assumption that any motion blur due to suboptimal delays will lower the maximum value of the point source reconstruction.

2.3.3 Phantom studies

In order to quantify the impact of our optimisation strategies on spatial resolution, we performed motion compensated imaging for a hot rod phantom (radius 40 mm, rod diameter ranging from 1.5 - 3.0 mm) moved by a robotic arm in the microPET. The phantom was filled with 48 MBq of ^{18}F-FDG and several 2-minute scans were performed using the same robot-controlled arbitrary motion sequence (maximum offset 40 mm radially and 14 mm axially of the phantom marker from the FOV centre) executed at increasing speed. The speed of the phantom was determined post-acquisition and we show results from a slow (mean speed 45.0 mm.s^{-1}, maximum speed 195.3 mm.s^{-1}) and a fast (mean speed 80.1 mm.s^{-1}, maximum speed 379.3 mm.s^{-1}) case. For each speed, motion tracking was performed at 28.5 Hz for three different MT-marker

separations: 400 mm, 500 mm, and 600 mm. Reconstructions were performed as described in section 2.2.1 (using 10 subsets and 10 iterations) with a pixel size of [0.4745, 0.4745, 0.796] mm.

2.3.4 Rat studies

All animal experiments were approved by the ethical committee of KU Leuven and performed in accordance with the European Communities Council Directive (86/609/EEC).

A female Wistar rat (weight 275 g) was trained over three 30-minute sessions to remain unrestrained in a tube with its head extending into the microPET FOV (Bickell et al. 2015b). Since the body temperature of a rat can be used as an indicator of its stress level, Fulton et al. (2009) used peritoneally implanted temperature sensors in rats to show that their body temperature was not elevated to levels indicative of stress while they remained in the tube for awake scanning procedures lasting up to 60 min. The marker shown in figure 2.1(b) was attached to the rat's shaved forehead using "superglue", which bonds and dries rapidly and usually remains attached for 2 - 3 days. Firm marker attachment is crucial since rats do sometimes try to remove it during the scan. For imaging, the rat was injected with 30 MBq ^{18}F-FDG via a surgically implanted jugular catheter, with an access port protruding dorsally from between the scapulae, and scanned for 10 minutes, 65 minutes post injection. During the scan, the marker on the head was tracked using the MT (figure 2.1(c)). The MT-marker separation was 400 mm and the pose measurement rate was 30 Hz. After scanning the awake animal, the rat was anaesthetised (2.5% isoflurane in O_2 at 2 L/min) and imaged asleep for 10 minutes (starting 89 minutes post injection). Reconstructions were performed as described in section 2.2.1 (using 10 subsets and 10 iterations) with a pixel size of [0.4745, 0.4745, 0.796] mm.

2.3.5 Pose smoothing and interpolation

Data from the moving phantom experiments were used to determine the optimal FWHM of the smoothing kernel to be used on the pose data, and to quantify the effect of pose interpolation on the reconstructed spatial resolution. Both the slow and the fast motion cases were investigated. The MT-marker separation used was 400 mm. The motion data were smoothed using a Gaussian kernel with a temporal FWHM varying from 0 - 120 ms.

With interpolation the measured frequency of 28.5 Hz was interpolated to 1000 Hz, which ensures that the inter-pose motion never exceeds 0.4 mm for our phantom scans and 0.15 mm for a typical rat scan, which is sufficiently small for our purposes.

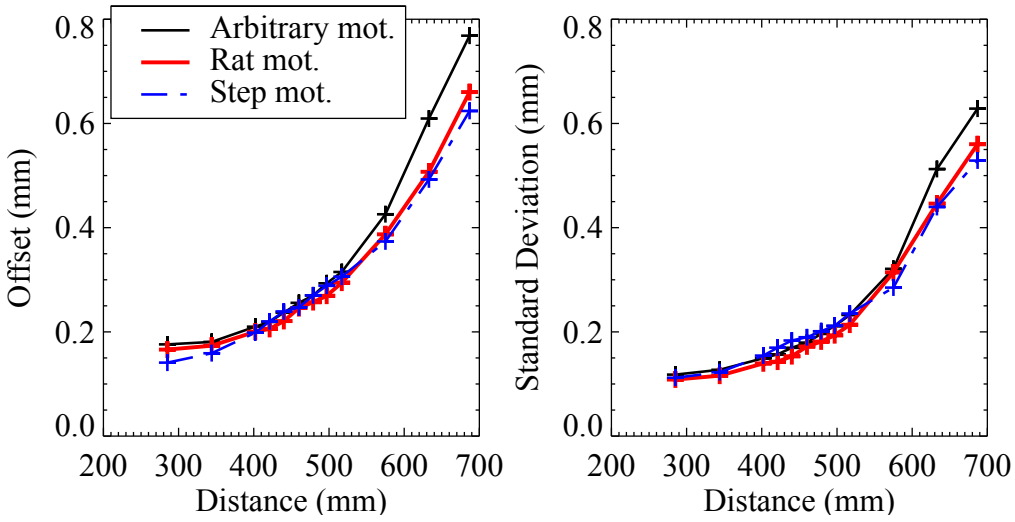

Figure 2.5: The averaged offsets ($\bar{E}$, left) and the averaged standard deviations of the offsets ($\bar{\sigma}$, right) for points in the test grid.

2.4 Results

2.4.1 MT distance optimisation

For the three motion sequences studied, the pose error ($\bar{E}$) and standard deviation ($\bar{\sigma}$) both reduced as the MT-marker separation reduced despite an increase in out-of-focus blurring (figure 2.5). Although accuracy improved down to 300 mm separation, in order to retain the gantry reference marker in the MT FOV the smallest practical MT-marker separation was 400 mm.

2.4.2 Temporal synchronisation

Based on several long scans we determined that the clocks governing the microPET and MT timestamps differed by a constant scale factor of 1.000181191, with the microPET clock running slightly slower than the MT clock. While this scale may seem small, over 10 minutes it introduces a temporal shift of several pose intervals between the poses and gate tags. We corrected for the clock scale difference before synchronising the data streams. Figure 2.6 shows an example data stream of gate tags and poses before and after synchronisation. Before synchronisation, both the pose and gate tag data streams contained a gap corresponding to missing poses or gate tags, respectively. By comparing the randomised interval pattern (section 2.2.5) before and after the gap, the two streams could be synchronised. Any data corresponding to initial gaps were ignored during MC.

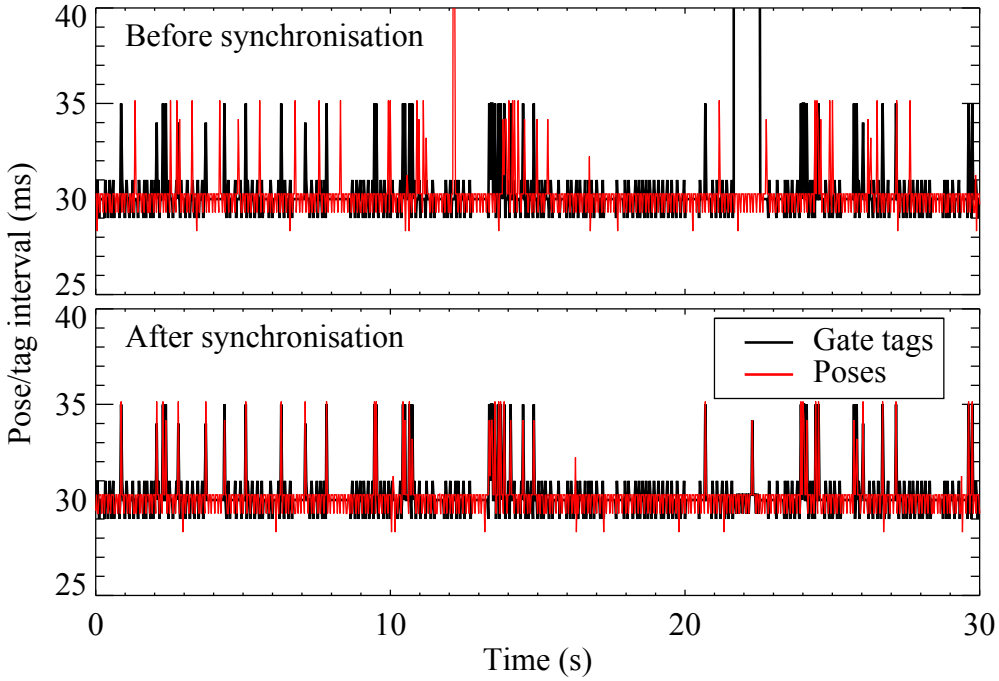

Figure 2.6: Time intervals between the gate tags and the pose measurements, before (top) and after (bottom) synchronisation. The intermittent increases from 29 ms to 35 ms are due to the randomisations in the signal generator. Before synchronisation there was one gap in both the pose stream and the gate tag stream, manifest by the large times at around 12 sec and 22 sec, respectively. This was corrected for with synchronisation (bottom).

Table 2.1: Linear fit parameters for the optimal delay time.

	a	δ (ms)	r^2
Without interp.	-0.952	21.525	0.948
With interp.	-0.429	23.741	0.652

2.4.3 Optimised delay time

Figure 2.7 shows the results of the optimal delay investigation with and without pose interpolation. A linear fit was performed using $\Delta = aT_0 + \delta$ for each case, where T_0 is the measured pose interval. The results are shown in table 2.1. Clearly the model described by (2.11) does not describe the data well, and the linear fit in table 2.1 has a poor correlation with the data in the interpolation case. Further investigation is needed to determine an accurate model for this data. For this work, the mean optimal delay values determined for the point source scans at each pose measurement rate were used in phantom and rat studies, i.e. -9 ms with no pose interpolation, and 14 ms with interpolation.

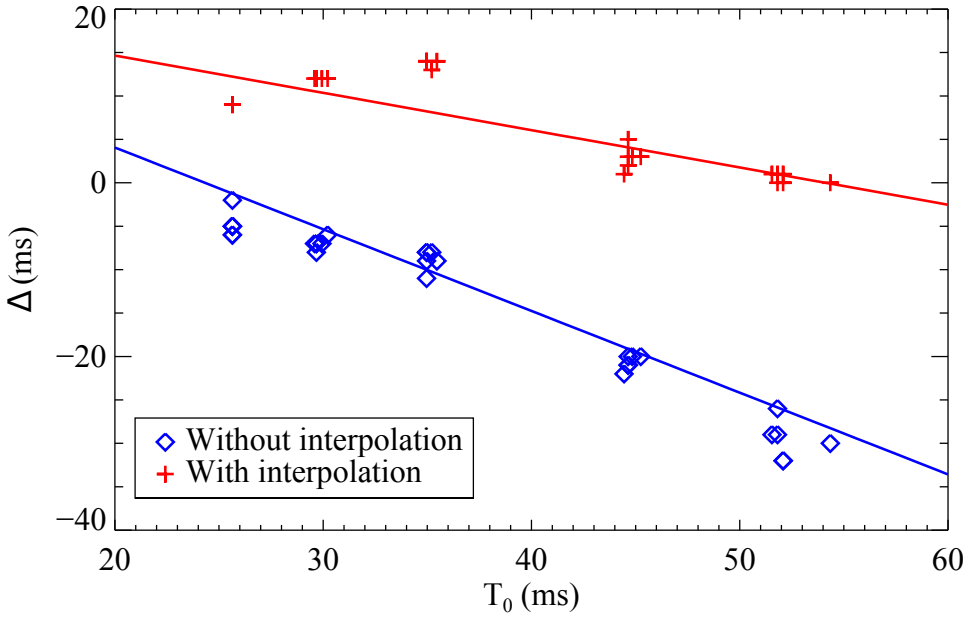

Figure 2.7: The optimal delay time for thirty point source scans at different measured pose intervals, T_0, with (red) and without (blue) pose interpolation. The solid lines show the results of the linear fit.

2.4.4 Phantom studies

Figures 2.8 to 2.11 show reconstructed images and profiles of the phantom for a slow and fast motion, respectively, and in each case using various combinations of the optimised parameters: the MT-marker separation, pose smoothing, pose interpolation, and the delay applied to the pose time stamps. The images represent a sum of 26 slices (20.7 mm) along the rods to reduce the impact of noise. By analysing the reconstructions with various pose smoothing kernels and comparing their resolution recovery, a kernel with FWHM of 100 ms was determined to be optimal for both the slow and the fast motion cases. We also verified that the optimal delay predicted from (2.11) produced the highest resolution recovery by performing reconstructions with various delays.

Pose smoothing (figures 2.8/2.10, row 1) resulted in the most dramatic improvement in image quality out of all the optimisation techniques. There was moderate improvement by reducing the MT-marker separation (figures 2.8/2.10, row 2) and using pose interpolation and an optimised synchronisation delay (figures 2.8/2.10, row 3). The reconstructed images obtained using full optimisation most closely resembled those of the static phantom.

To quantify the residual motion blur present in the MC reconstructions, and thus the resolution improvement gained when using the various optimisation techniques, pairs of images were compared by determining the FWHM of the 3D Gaussian kernel needed to smooth one image (the reference) to achieve the

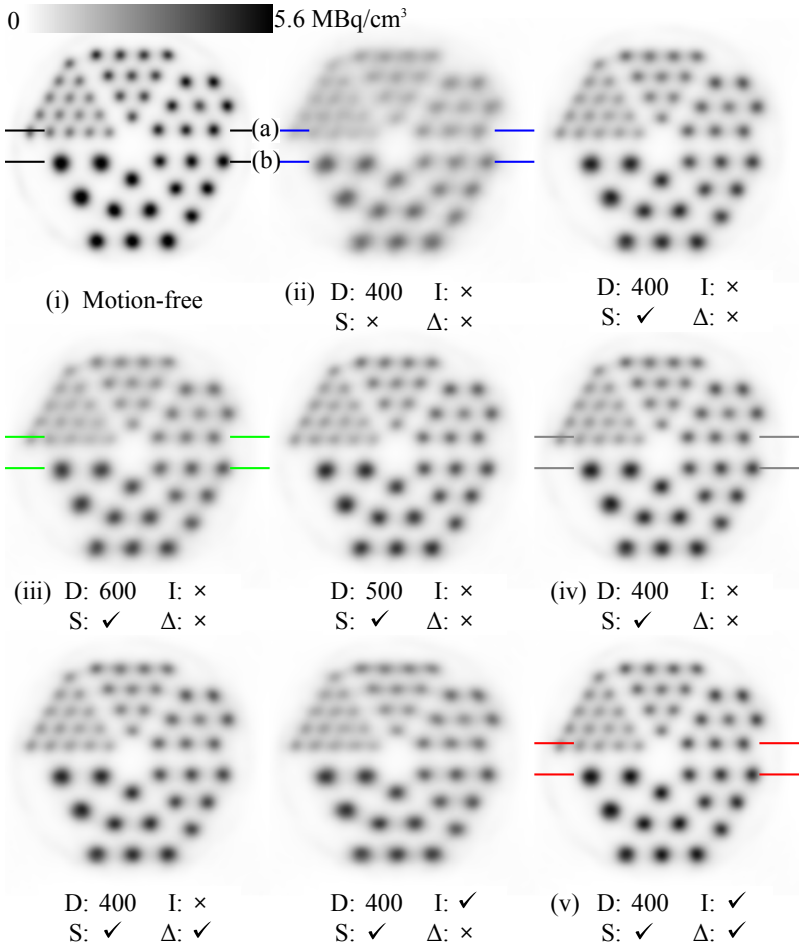

Figure 2.8: Reconstructed images of the phantom undergoing slow motion, after summing in the slice direction. The images are shown to the same scale and have been corrected for decay. The applied parameters are shown below each image: D is the MT-marker separation in mm; I refers to pose interpolation; S refers to pose smoothing; and Δ refers to the optimal delay time. A check indicates that the factor was applied. The coloured lines indicate the location of the profiles through the small and big rods, shown in figures 2.9(a) and (b), respectively, and the Roman numerals indicate the corresponding profiles in figures 2.9(a) and (b).

lowest pixel-by-pixel root mean square difference with the other image (the test image). We use a uniform Gaussian kernel since much of the residual blur is due to noise in the pose measurements, and therefore should introduce approximately uniform blurring. A digitised 3D version of the hot rod phantom was used as the reference image and compared to the motion-free, optimal MC (i.e. obtained using all optimisations), and suboptimal MC (i.e. obtained using

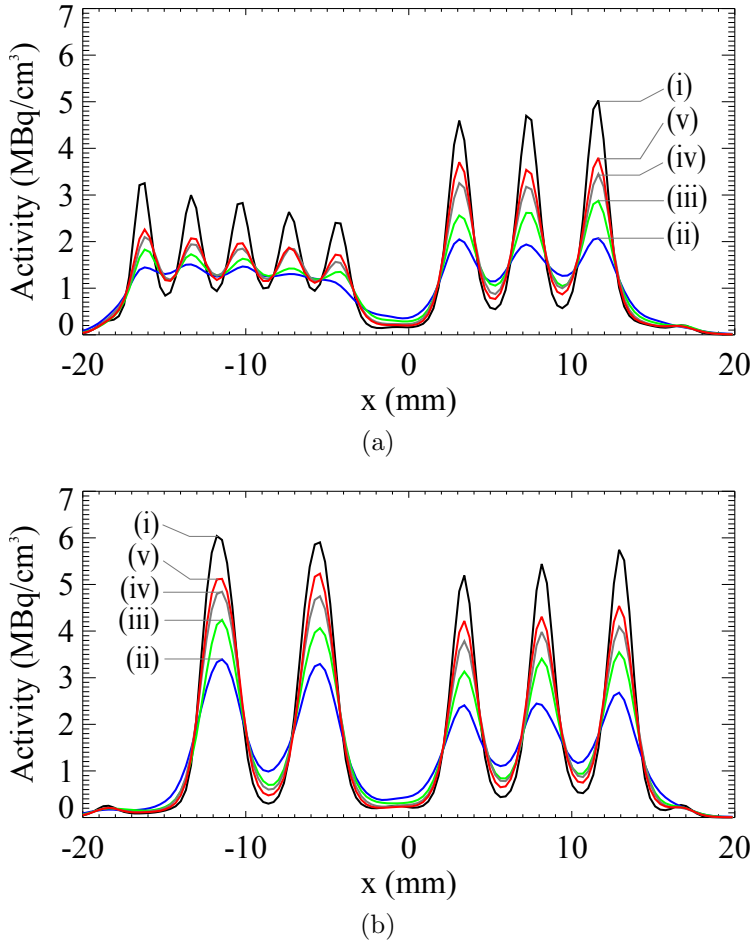

Figure 2.9: Profiles through the (a) small and (b) big rods shown in figure 2.8.

Table 2.2: Comparison of resolution recoveries.

			FWHM (mm)	
	Reference	Test image	Slow	Fast
(i)	Digitised	Motion-free	1.5	
(ii)	Digitised	Opt. MC	1.9	2.3
(iii)	Digitised	Subopt. MC	2.6	3.2
(iv)	Opt. MC	Subopt. MC	1.5	1.8

no optimisations and an MT-marker separation of 400 mm) reconstructions. Additionally, the optimal MC reconstructions were used as the reference and compared to the suboptimal MC reconstructions. The results of this analysis are shown in table 2.2. Comparing (ii) and (iii) in table 2.2, the spatial resolution improved by approximately 27%, and the magnitude of the improvement was

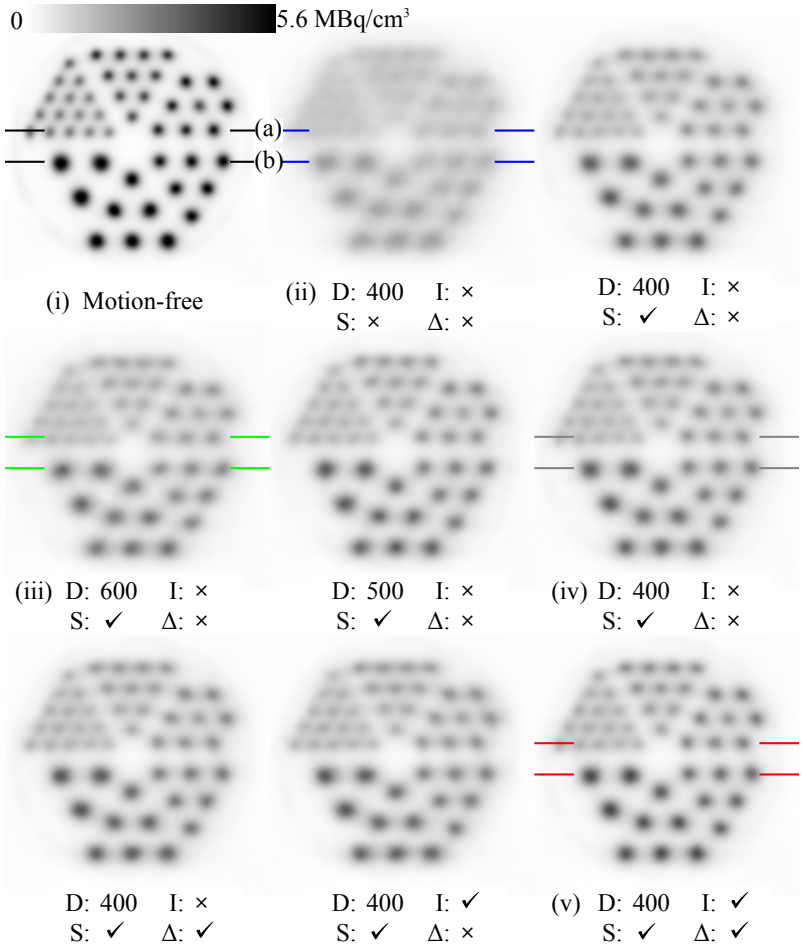

Figure 2.10: Reconstructed images of the phantom undergoing fast motion, after summing in the slice direction. The images are shown to the same scale and have been corrected for decay. The applied parameters are shown below each image: D is the MT-marker separation in mm; I refers to pose interpolation; S refers to pose smoothing; and Δ refers to the optimal delay time. A check indicates that the factor was applied. The coloured lines indicate the location of the profiles through the small and big rods, shown in figures 2.11(a) and (b), respectively, and the Roman numerals indicate the corresponding profiles in figures 2.11(a) and (b).

almost identical in the slow and fast motion cases.

2.4.5 Rat studies

Figures 2.12 to 2.14 show the reconstructed rat images, together with the recorded head motion and two profiles through the reconstructions. The mean speed of the rat's head during the "awake" scan was 6.79 mm.s^{-1} (maximum

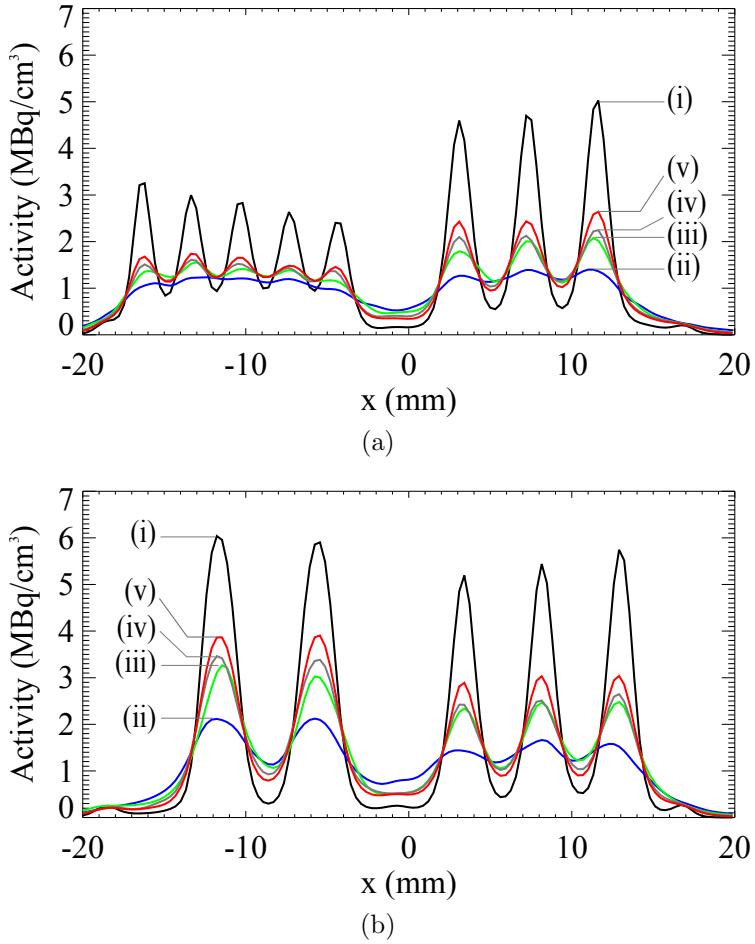

Figure 2.11: Profiles through the (a) small and (b) big rods shown in figure 2.10.

136.7 mm.s^{-1}), with a maximum offset of 37 mm radially and 40 mm axially of the marker from the FOV centre. The motion-free reconstruction is shown together with the MC reconstruction using no optimisations and all optimisations. While the motion-free and MC reconstructions correlate closely to each other, some small differences are observed. These are largely due to residual errors in the MC, but, since the scans were separated by 14 minutes, slight changes in the FDG distribution may have also contributed to these differences. Using the same quantification approach described in section 2.4.4, with the motion-free reconstruction as the reference image, the improvement in spatial resolution using MC with optimisation, compared to no optimisation, was 14% (from a kernel with FWHM of 1.08 mm to 0.93 mm).

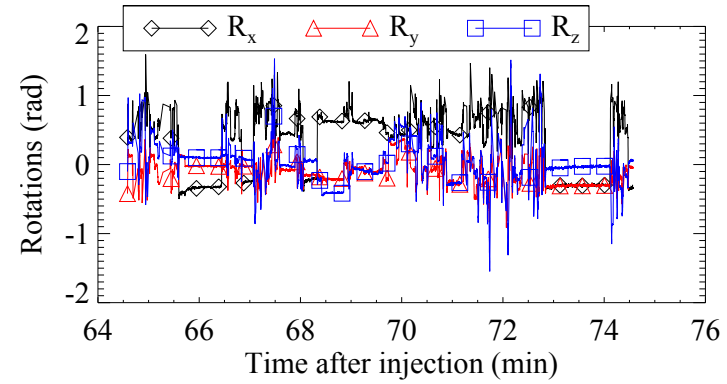

(a)

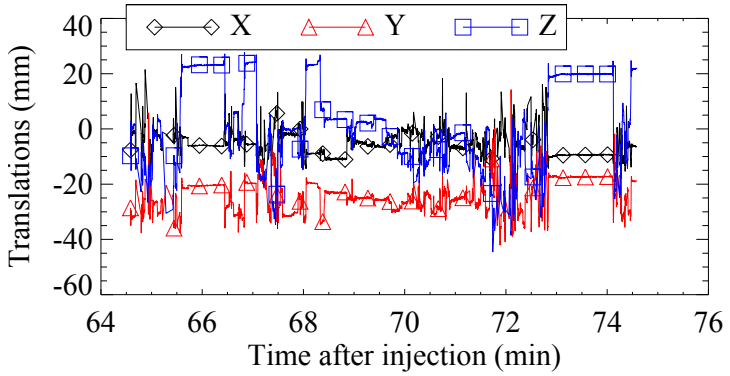

(b)

Figure 2.12: (a) and (b) The 6 DOF of the recorded motion in PET coordinates.

2.5 Discussion

In this study we have presented various optimisation techniques to improve MC reconstructions for PET imaging. Hardware (MT-marker separation and temporal synchronisation) and software (latency estimation between the poses and gate tags, pose smoothing and interpolation, and subset selection during reconstruction) optimisations have been considered. The most important optimisation parameter is the pose smoothing, which, when applied alone, produces a large improvement in reconstructed image quality. Another important factor is the separation between the MT and the marker. We have shown that bringing the MT closer than the focal distance of 700 mm to the microPET (to between 300 mm and 400 mm) the motion of the marker can be more accurately measured. Although the marker becomes increasingly out of focus away from the focal distance, evidently this blurring has less of an impact than the resultant magnification of the marker on accurately determining the marker pose. Our other optimisation factors - optimal delay time and pose

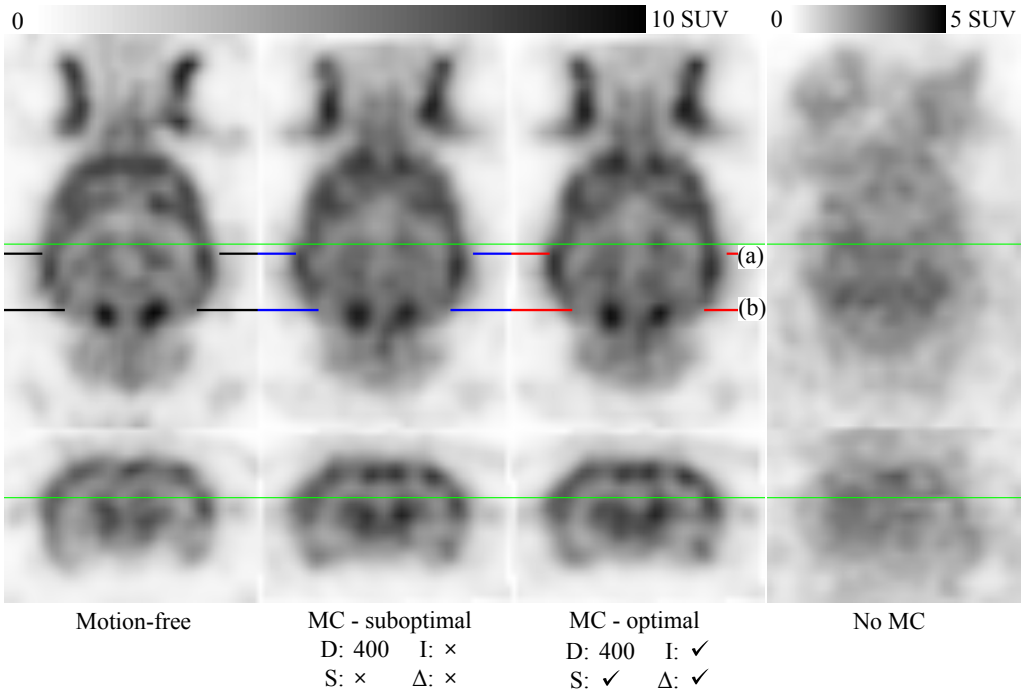

Figure 2.13: Reconstructed rat brain images showing a coronal (top) and transverse (bottom) slice. Results are shown for the motion-free case (first column), MC without optimisation (second column), with all optimisations (third column), and without MC (fourth column). The green lines indicate where the transverse and coronal slices are located, and the black, blue and red lines indicate where the profiles in figures 2.14(a) and (b) are taken.

interpolation - further improve the reconstruction, but to a lesser degree than the former two.

The synchronisation technique we describe has consistently allowed for a robust synchronisation between the MT and microPET over many experiments. When poses or gate tags are missing (due to the MT being unable to see the marker, or the microPET failing to insert a gate tag, respectively), our technique can detect and correct these gaps, in either stream, by aligning the tag and pose interval pattern throughout the scan.

The optimal delay time between the MT and the microPET was found to be on the order of a few milliseconds. While the hypothesised model did not fit the data well, the point source measurements allowed us to determine an optimal delay for the pose measurement rate we used in our studies. For a measurement rate of 30 Hz, the optimal delay time was -9 ms when no pose interpolation was used, and 14 ms with pose interpolation. Phantom data reconstructions were performed with various delays (not shown here) to verify, using the resolution recovery, that the determined delay was indeed the optimal.

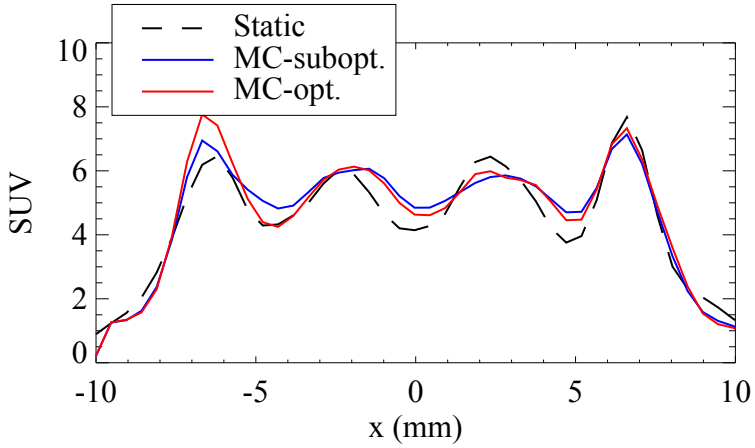

(a)

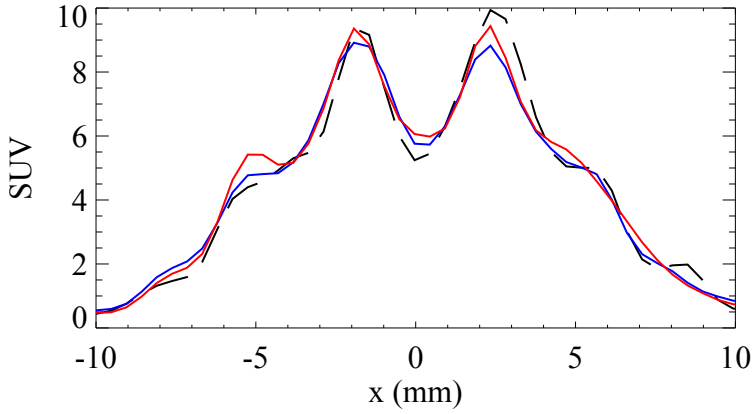

(b)

Figure 2.14: Profiles through the reconstructions shown in figure 2.13.

While the electronic elements involved should be similar for all microPET and MT systems, other groups should perform a similar delay optimisation experiment locally.

Using a motion-free reconstruction as the ground truth, the optimised parameters improved the resolution recovery in the MC reconstruction by approximately 27% in the phantom studies, and 14% in the rat study. During the rat experiment the rat was observed to occasionally touch the marker with its paws, which might have caused relative motion between the marker and the brain. This would in turn degrade the quality of the MC and cause blurring of both the suboptimal and the optimal reconstructions, thereby reducing the impact of the optimisations. This likely explains the discrepancy of the resolution gains between the rat and phantom experiments.

The total activity in the phantom reconstructions shown in figure 2.8 agree to within 1%, and those in figure 2.10 to within 3%, indicating that the MC

recovers the total activity well. However, careful attention must be given to factors like synchronisation and noise to be able to resolve small structures and enable accurate quantification in such regions.

To achieve accurate quantification we will implement an attenuation correction technique where the support of the object is found from an initial MC reconstruction, and used to create an attenuation map (Angelis et al. 2013).

While this paper has focussed on hardware and software optimisations, possible marker movement relative to the brain is a potential limiting factor in awake animal studies and care should be taken to rigidly attach the marker. Currently however, marker-based motion tracking is the state-of-the-art for this application. A more invasive form of attaching the marker (for instance, directly to the skull) would avoid this problem, but this could have significant drawbacks (stress, complicating the procedure, etc.). Ideally, one would track the features of the head directly and avoid using an attached marker; progress towards such a technique can be found in Kyme et al. (2014), but even with such methods there is still the possibility of errors introduced by non-rigid motion of the face.

In our experience, the proposed animal training and scanning protocol has allowed us to scan many rats reliably for up to 75 minutes. In (Fulton et al. 2009) it was reported that rats in a similar set up did not have elevated stress levels. Thus we are now able to study tracer kinetics in rats without the confounding effects of anaesthesia or stress.

While this work has focused on the MicronTracker and microPET systems, many of the considered optimisations are easily translatable to other motion tracking systems and scanners used for MC. In the future we plan to investigate alternative techniques to spatially calibrate the tracker and PET systems, and to adapt and apply the presented optimisations to a clinical PET scanner.

2.6 Conclusion

Various factors have been investigated to optimise MC PET imaging of awake rats: temporal synchronisation and latency estimation between the tracker and scanner, the physical separation of the tracker and scanner, pose smoothing and interpolation, and subset selection. By optimising these factors, we have demonstrated improved quantification in MC imaging studies involving phantoms and live animals using the microPET small animal scanner and MicronTracker optical tracking system. The improvements we describe are easily translatable to other MC setups involving different scanners and motion tracking systems, both for animal and human PET imaging.

Acknowledgements

This work is supported by the IMIR project of KU Leuven and the MIRIAD Strategic Basic Research (SBO) project of the Innovatie door Wetenschap en Technologie (IWT).

Chapter 3

The Effect of Isoflurane on ^{18}F-FDG Uptake in the Rat Brain: A Fully Conscious Dynamic PET Study using Motion Compensation

Published as:

M. G. Spangler-Bickell, B. de Laat, R. Fulton, G. Bormans, and J. Nuyts (2016b). "The effect of isoflurane on 18F-FDG uptake in the rat brain: a fully conscious dynamic PET study using motion compensation". In: *EJNMMI Research* 6, p. 86

Abstract

In preclinical positron emission tomography (PET) studies an anaesthetic is used to ensure that the animal does not move during the scan. However, anaesthesia may have confounding effects on the drug or tracer kinetics under study, and the nature of these effects is usually not known. We have implemented a protocol for tracking the rigid motion of the head of a fully conscious rat during a PET scan and performing a motion compensated list-mode reconstruction of the data. Using this technique we have conducted eight rat studies to investigate the effect of isoflurane on the uptake of ^{18}F-FDG in the brain, by comparing conscious and unconscious scans. Our results indicate that isoflurane significantly decreases the whole brain uptake, as well as decreasing the relative regional FDG uptake in the cortex, diencephalon, and inferior colliculi, while increasing it in the vestibular nuclei. No statistically significant changes in FDG uptake were observed in the cerebellum and striata.

3.1 Introduction

In preclinical positron emission tomography (PET) studies an anaesthetic, such as isoflurane, ketamine, or chloral hydrate, etc., is usually used to ensure that the animal remains motionless for the duration of the scan. The effect of the anaesthetic on the kinetics of the drug or radioactive tracer under study is not always known, and may confound the results of the investigation. This is especially problematic for translational studies since anaesthesia is usually avoided in the clinic. A summary of reports on the effect of anaesthetics in preclinical studies is given in (Hildebrandt et al. 2008) and (Alstrup et al. 2013). In general three methods are used preclinically to establish the effect of an anaesthetic. The first is to compare the findings of similar investigations using different anaesthetics (Alstrup et al. 2011), however inferring the individual effects of the anaesthetics separately is complex and difficult to verify. The second method is to infuse the animals with the tracer or drug while conscious and then, after some time, anaesthetise and scan them, thus acquiring a static scan where the tracer or drug metabolism is not affected by the anaesthetic (Matsumura et al. 2003); this assumes that the tracer washout is negligible. However to fully quantify the effect of anaesthesia on the tracer kinetics a dynamic scan starting from the time of injection is necessary. The third method, which does allow for dynamic scanning, is to physically restrain the animals (particularly the head for brain imaging) such that motion is impossible (Hosoi et al. 2005). In this case though the effect of stress on the kinetics is another confounding factor which is difficult to quantify, and is known to affect brain function in many cases (McLaughlin et al. 2007; Patel et al. 2008). A novel method for conducting brain scanning of conscious animals is the so-called RatCAP (Vaska et al. 2004; Schulz et al. 2011), where a miniaturised PET scanner is surgically mounted directly onto the head of a rat and thus moves rigidly with the brain, avoiding motion between the brain and the scanner. While this system is promising it has a lower sensitivity than commercial scanners and may inhibit the natural movement of the rat, possibly inducing stress in the animal.

As stated in (Alstrup et al. 2013), a study involving fully awake, unrestrained animals would be ideal for quantifying the effect of an anaesthetic. Several groups, including our own, have been conducting research into tracking the head motion of an awake animal (usually a rat) during a scan and correcting the PET data post-acquisition according the measured motion, such that a reconstruction can be made free of motion artefacts (Weisenberger et al. 2005; Kyme et al. 2011b). Such motion compensation (MC) approaches avoid the need for anaesthesia and minimise the stress of the animal since it is unrestrained (although the animal is often confined to a small space during the scan). Motion tracking can either be marker-based (Weisenberger et al. 2005; Kyme et al. 2011b), where a small marker is attached to the head of the animal and tracked

by external cameras, or markerless, where the facial features of the animal are identified and tracked (Kyme et al. 2014). These approaches have been shown to produce reconstructions of comparable quality to those of standard (anaesthetised) scans, and thus show the greatest promise for investigating the effect of anaesthetics. In (Angelis et al. 2015) a preliminary study was presented on tracer kinetics in a conscious and unrestrained rat, but otherwise, to the best of our knowledge, no other studies have been reported using this approach.

In this work we report on a study of fully conscious, tube-bound, but unrestrained, rats undergoing dynamic scans to evaluate the effect of the anaesthesia induced by isoflurane on ^{18}F-FDG uptake in the brain. An external stereo-optical system is used to track a marker attached to the rat's head (Kyme et al. 2011b; Spangler-Bickell et al. 2016a), and a list-mode based motion compensation reconstruction is then performed to achieve a reconstruction free of motion artefacts (Rahmim et al. 2004b).

This investigation was chiefly conducted as a proof-of-principle study, and therefore we made use of ^{18}F-FDG since the effect of isoflurane on this tracer is largely understood (Alstrup et al. 2013; Matsumura et al. 2003). We aim to confirm the results found by these previous studies, contribute to the understanding of the effect of isoflurane by scanning dynamically from the time of tracer infusion, and to demonstrate the efficacy of motion compensation in such studies. In the future we will conduct similar studies on tracers where the effect of the anaesthetic is not as well understood, and where a reference tissue model exists such that kinetic modelling can be performed without requiring arterial blood sampling.

3.2 Method

3.2.1 Hardware

PET measurements were performed using the microPET Focus 220 small animal PET scanner (Preclinical Solutions, Siemens Healthineers, Knoxville, TN, USA). To track the motion the MicronTracker Sx60 (ClaroNav Inc., Toronto, Canada) was used, as in (Kyme et al. 2011b). The MicronTracker (MT) is a stereo-optical system which tracks preregistered planar markers, deriving the 6 degrees-of-freedom (i.e. the marker pose) from two simultaneously acquired but spatially offset images. It was used to track a small marker (2.2×1.7 cm) attached to the rat's head, at a frequency of 25 - 30 Hz. The experimental setup is shown in Fig. 3.1.

Spatial calibration Since the PET and MT coordinate systems are not necessarily aligned to each other, the transformation matrix to convert the recorded

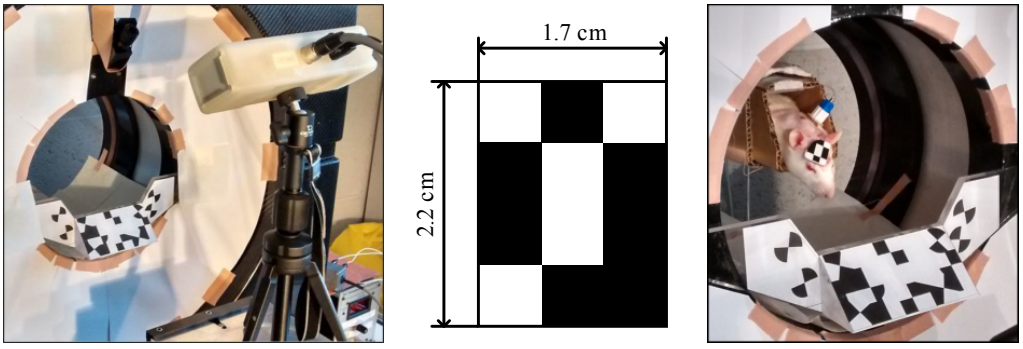

Figure 3.1: (a) The MicronTracker in front of the microPET scanner. The large marker attached to the front of the scanner is the reference marker used to aid in transforming from the MT coordinates to the microPET coordinates. (b) The head marker used in rat studies. (c) An unrestrained rat with an attached head marker inside a tube within the microPET. The catheter port can be seen between its shoulders. Figure reproduced with permission of IOP Publishing from (Spangler-Bickell et al. 2016a).

motion data into PET coordinates must be determined. A similar procedure to that described in (Kyme et al. 2008) and (Fulton et al. 2002) was used: a radioactive point source is placed on the origin of an MT marker, and scanned and tracked at various positions within the PET. The PET data were reconstructed using the commercial software of the scanner. By comparing the MT data with the PET reconstructions, it is possible to determine a suitable transformation between the coordinate systems (Horn 1987). A reference marker attached to the PET gantry (see Fig. 3.1) allows us to use the same calibration on different scan days even if the MT has been moved.

Temporal calibration As each motion data point is measured a pulse is sent to the PET gate input to cause a tag to be inserted into the list-mode stream. Aligning the recorded motion data with the gate tags allows for the temporal calibration of the two data sets.

In previous work we have optimised the experimental setup parameters for the MT and microPET (Spangler-Bickell et al. 2016a), and the same parameters were utilised for this study. Our hardware and software for MC have been quantitatively validated using phantom measurements.

3.2.2 Experiment Protocol

All animal experiments were approved by the bioethical committee of the KU Leuven and performed in accordance with the European Communities Council Directive (86/609/EEC).

Five female Wistar rats were used (200 - 281 g), designated as "A - E", three of which had repeat studies (indicated by subscripts in their designations), yielding eight data sets in total. Seven to ten days before the start of the study a surgery was performed on each rat to insert a catheter into the femoral vein, with an access port protruding dorsally between the scapulae[1]. Before the surgery medetomidine (0.3 mg/kg) and ketamine (60 mg/kg) were administered to the rats via an intraperitoneal injection. Following this the rats were put on a 3 day course of antibiotics and analgesics. After recovery, each rat was then acclimatised to having the marker attached to its head, as well as being unrestrained inside a tube in the scanner, over a period of 3 days leading up to the scan for 30 minutes initially and increasing to 60 minutes. Since the rat was not restrained it was possible for it to exit the tube onto the scanner gantry since the tube is approximately 10 cm above the scanner bore. If this occurred the rat was then manually placed back in the tube, and made fewer attempts to exit the tube as the days progressed. During scans, three of the rats did exit the tube once and were replaced in the tube immediately, but since their head motion was being tracked this had no effect on the final reconstruction, except for a short period were no PET data were acquired, which is automatically corrected for during reconstruction as explained in section 3.2.3.

On the first day of the acclimatisation (3 days before the scan) the rats were anaesthetised with isoflurane for approximately 15 minutes to have the fur on their forehead removed for better marker attachment. The marker was attached to the rat's forehead using "superglue", which bonds and dries rapidly, but does not irritate the skin of the rat, thereby minimising discomfort, and which comes off by itself after several days. The marker and tube can be seen in Fig. 3.1(c). Whenever used, isoflurane was administered with a concentration of 2.5% in 2 L/min O_2.

A schematic of the experimental protocol is shown in Fig. 3.2; a pre-determined protocol was used for the rats, but there were some deviations (as can be seen in Fig. 3.2) due to unforeseen circumstances beyond our control, but nonetheless these did not invalidate any of the data sets.

It is known that there are many factors which can affect FDG uptake (Fueger et al. 2006; Wong et al. 2011; Schiffer et al. 2007) such as the blood glucose level, muscle usage, tracer administration route, body temperature, stress, etc., and so where possible these were minimised or kept consistent across the rats. Preceding the scans the rats were fasted overnight for 12 - 15 hours, with free

[1]One rat (not counted in the eight data sets) was excluded from the study after it was established (post-mortem) that the inserted catheter had come out of the vein.

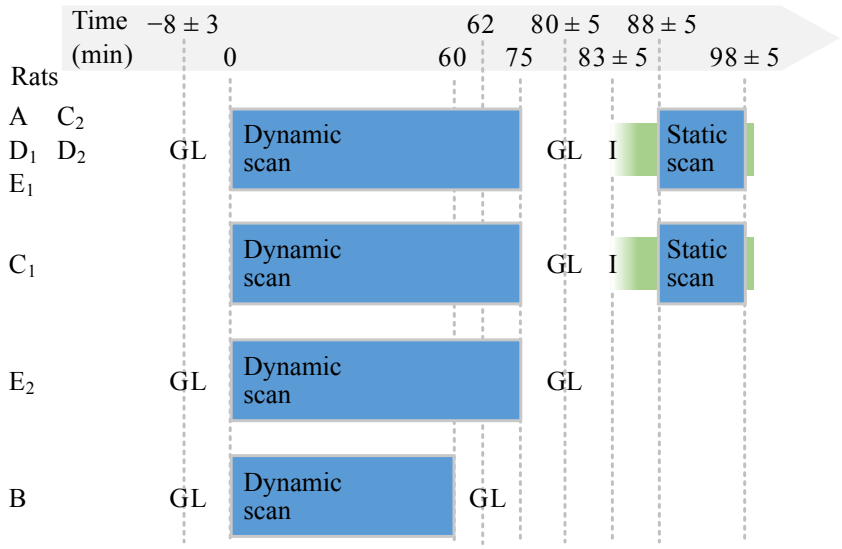

(a) Conscious studies

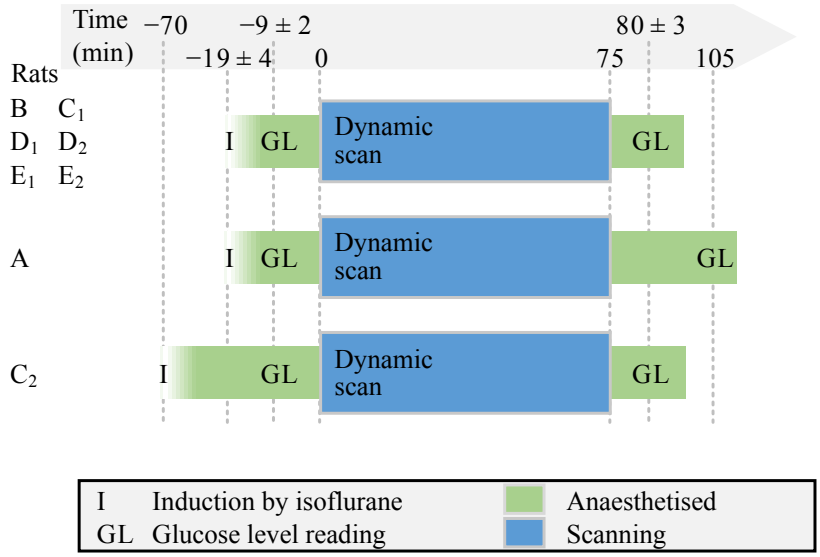

(b) Unconscious studies

Figure 3.2: The timeline of the experimental protocol for the (a) conscious and (b) unconscious studies, for each rat. Time 0 is when the tracer was infused and the scan was started. For the time points with some spread the mean ± standard deviation is quoted. Most rats followed the ideal protocol (first line), but there were some deviations for rats A, C_1, C_2, E_2, and B, as can be seen.

access to water (Deleye et al. 2014). The rats were scanned while conscious for 60 - 75 minutes, starting from the tracer infusion. The tracer was infused via the intra-femoral vein catheter with 20 - 30 MBq of ^{18}F-FDG in a total injected volume of 0.8 mL (including saline for flushing) using an infusion pump over 25 seconds. Immediately following this scan the rats were anaesthetised with isoflurane and scanned for an additional 10 minutes while unconscious, to provide a validation of the MC reconstruction of the last frame of the conscious scan since the activity distribution in these reconstructions should be very similar. Two to three days after the conscious scan the rats were again fasted and scanned with the same procedure, but while anaesthetised with isoflurane, which was administered before the tracer infusion and constantly throughout the scan. During all unconscious scans the rats were placed on a heated mat to maintain body temperature. As suggested in (Deleye et al. 2014) the blood glucose level of each rat was measured before and after each scan in duplicate using a drop of venal blood from a tail prick, with the GlucoCard Memory 2 meter (A. Menarini Diagnostics S.r.l., Florence, Italy), with exceptions being rat C_1 where no reading was taken before the conscious scan, and rats C_2, D_1, and E_1 where the readings were not taken in duplicate for the conscious scans.

While rat stress is a difficult factor to quantify, a similar set up was used by Fulton et al. (2009) where body temperature was measured as a stress indicator using peritoneally implanted temperature sensors; Fulton *et al.* found that the body temperature did not elevate to levels indicative of stress while the rats were in the tube for up to 60 minutes. In our experiments the rats exhibited no observable behavioural signs of stress: they engaged in grooming, resting, and exploring their (limited) surroundings.

3.2.3 Reconstruction

After correcting each of the list-mode events' endpoints according to the recorded motion, the reconstructions were performed using list-mode ordered subsets expectation-maximisation (OSEM) (Shepp et al. 1982; Hudson et al. 1994; Parra et al. 1998; Reader et al. 1998), using 10 iterations and 10 subsets, and a pixel size of [0.475, 0.475, 0.798] mm. The resolution was modelled using an image-based convolution (Reader et al. 2003) with a Gaussian kernel with a FWHM of 1.3 mm (Tai et al. 2005). An attenuation map was constructed by extracting the body contour of the rat from a preliminary reconstruction (without attenuation correction) and filling it with the attenuation coefficient of soft tissue, ignoring the skull since it is very thin (Angelis et al. 2013). As suggested by Rahmim et al. (2004b), the data were pre-corrected for attenuation, and the sensitivity image was calculated as a weighted average of all poses. By analysing reconstructions of an unconscious rat scan using the commercial software with and without scatter and randoms correction, it was established that the effect of scatter on the brain was less than 2.5%, and of randoms was

around 1%, on a pixel-by-pixel basis, which was sufficiently small to ignore in the reconstructions.

If the rat temporarily moved out of the scanner field-of-view (such as in the few occurrences where the rat exited the tube), and whenever motion data was not available because, for example, the rat moved its head to an orientation where the marker could not be seen by the tracker, then the time-averaged sensitivity image would automatically have a zero contribution from those time points, and thus would automatically scale the reconstruction to correct for these periods. In the latter case any PET data acquired during these periods were ignored.

The rats were observed to touch the marker intermittently 1 - 4 times during the scans, and four rats managed to move the marker and cause some relative motion between the marker and the brain, which resulted in inter- and intra-frame motion in the reconstructions. Inter-frame motion was corrected for by frame-by-frame registration (after selecting a reference frame and ignoring early frames with low uptake). While this was necessary in only four of the studies (in the worst case resulting in a shift of about 3 mm within the brain over two frames), it was performed by default. Intra-frame motion of the marker relative to the brain would result in residual motion blur in the reconstructed image.

The unconscious and conscious scan reconstructions were aligned by an affine registration to the Johnson rat brain atlas (Johnson et al. 2012), which was used to delineate regions-of-interest (ROIs). Since no arterial blood sampling could be performed on the conscious rats, and FDG has no reference tissue model in the rat brain, no input function could be derived and therefore the tracer kinetics could not be modelled.

3.2.4 Data Analysis

After correcting for deadtime and decay, the standard uptake values (SUVs) were calculated for each reconstruction using,

$$\mathrm{SUV}_j = \Lambda_j \frac{w}{d}, \tag{3.1}$$

where Λ_j is the reconstructed activity concentration in pixel j, w is the rat's body weight, and d is the injected dose.

Due to the variability in the glucose levels (as discussed in 3.3.1), the data analysis was performed by calculating the ratio of various ROIs to the whole brain average. Such ratios are thus not affected by the scaling by the glucose level and yield information regarding how the regional distribution of the tracer was affected by the isoflurane. The ratios were calculated using,

$$R_{rik} = \frac{\bar{\Lambda}_{rik}}{\bar{\Lambda}_{0ik}}, \tag{3.2}$$

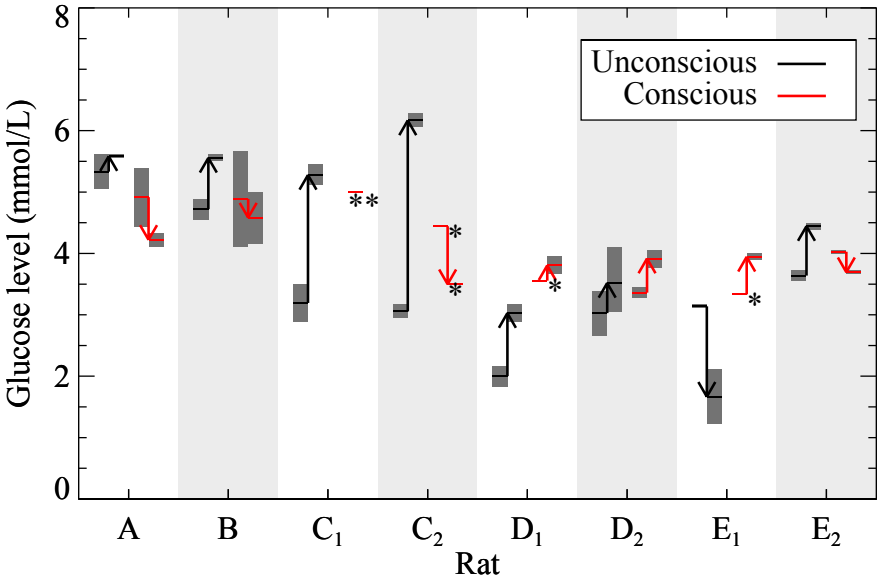

Figure 3.3: Blood glucose level measurements for each rat at the time of the unconscious (black) and conscious (red) scans. For each rat, the arrows start at the measurements taken before the scan and end at those taken after the scan. Most measurements were taken in duplicate, the extent of which are indicated by the dark grey bars. *Only a single measurement was taken. **No measurement was taken before the scan.

where r, i, and k are the ROI, frame, and rat indices, respectively, $\bar{\Lambda}_{rik}$ is the mean value of the pixels inside the ROI r, and where $r = 0$ indicates the whole brain ROI. The ROIs considered were the cortex, cerebellum, diencephalon, striata, vestibular nuclei, and inferior colliculi[2], shown in Fig. 3.7(a) and (b). The mean ratios across the rats are then denoted by $\bar{R}_{ri}$.

Since each rat was scanned with and without the anaesthetic they can be considered to be their own controls. A paired t-test between the unconscious and conscious scans was conducted on the ratios of six ROIs under consideration (using a Bonferroni correction factor of 6), at equilibrium, i.e. the sum of the last five frames spanning from 38 minutes to 75 minutes post-injection.

3.3 Results & Analysis

3.3.1 Blood glucose level

The blood glucose measurements taken before and after each of the scans have been summarised in Fig. 3.3. For the conscious scans the glucose level was relatively constant from before to after the scan across the rats, falling within a range of $[3.3, 5.0]$ mmol/L. During the unconscious scans, on the other hand, the glucose levels were often very different from before to after the scan, and exhibited a greater range across the rats, falling within $[1.7, 6.2]$ mmol/L. For all unconscious scans, except E_1, the glucose level rose, some substantially, from before to after the scan, while for E_1 it dropped. This indicates an effect of the anaesthetic on the glucose level. Significant responses of the glucose level to isoflurane have been reported by other groups; an increase in the blood glucose level in the brain was observed for adult rats in (Kofke et al. 1987) and (Zapp et al. 1992) after 60 to 75 minutes of isoflurane, while in neonatal mice a decrease in the glucose level was observed in (Loepke et al. 2006). An increase in glucose level was also observed in humans administered with isoflurane, and it is thought that this may be due to a decreased insulin response (Diltoer et al. 1988). These effects all suggest that glucose regulation is affected by isoflurane, which is a further confounding factor in studies involving isoflurane.

Due to this variation of the glucose level it was not evident which measurement (before, after, or the mean) should be used to normalise the reconstructions, as suggested in (Deleye et al. 2014). Therefore it was decided to analyse relative changes in the uptake of FDG in the rat brain, which are independent of the glucose level, for the various ROIs, as shown in equation (3.2). In addition, however, a comparison of the whole brain average in the conscious and unconscious scans was also conducted.

3.3.2 Reconstructions

The measured motion of a conscious rat during a 10 minute scan is shown in Fig. 3.4(a) and (b), with the MC reconstruction in 3.5(a) along with the subsequent unconscious scan reconstruction. Much of the resolution lost due to the motion has been recovered, and the activity distribution is very similar between the conscious and unconscious scan reconstructions. Since the rat moved significantly during the scan the activity concentration is much lower in the non-MC reconstruction, however the total activity is approximately equal to the MC reconstruction, as expected.

[2] These ROIs were chosen because they are either common regions to consider (cortex, cerebellum, and striata) or they exhibited noticeable differences between the conscious and unconscious scans (vestibular nuclei, diencephalon and inferior colliculi) which were of interest to investigate further.

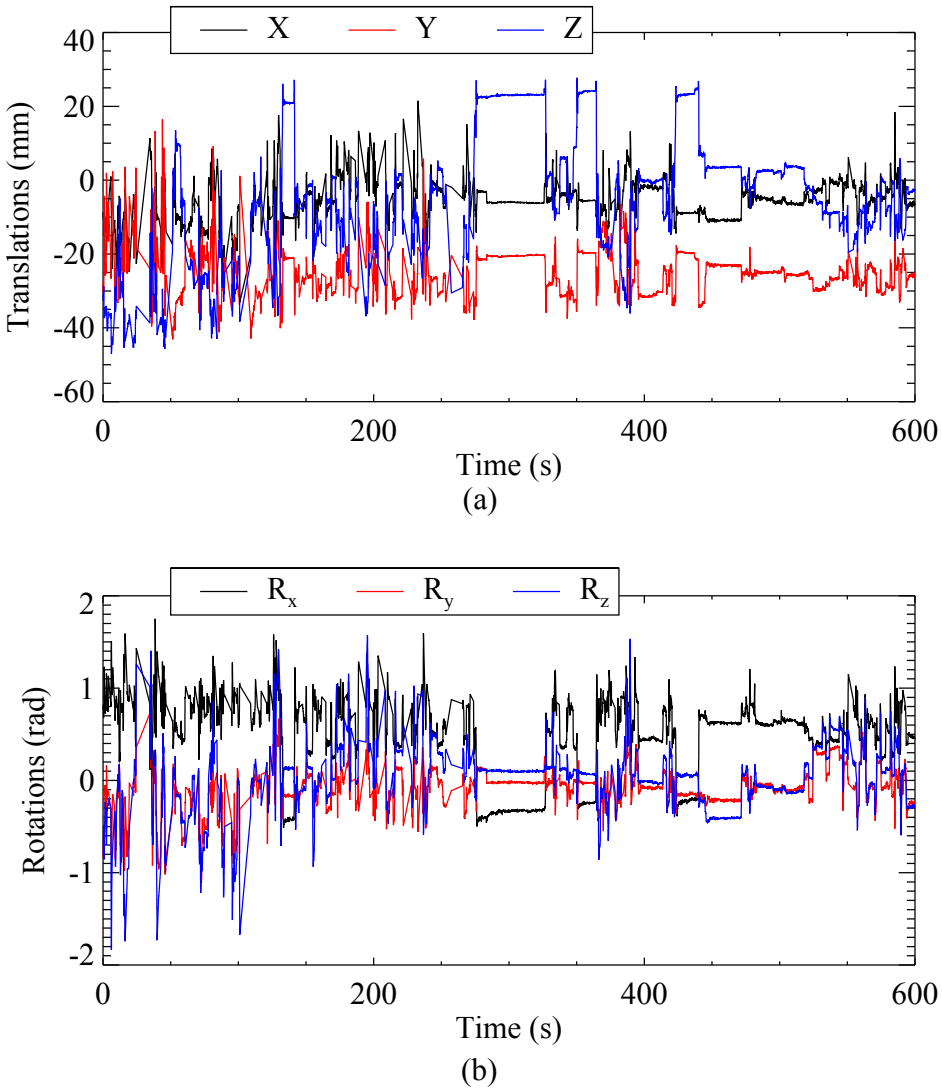

Figure 3.4: The translations (a) and rotations (b) of a rat's head during a 10 minute conscious scan.

A selection of the dynamic frames for the average of the eight data sets is shown in Fig. 3.5(b) for the conscious and unconscious scans. In Fig. 3.6 the time activity curves (TACs) for the whole brain region for all eight data sets is shown. The unconscious, static scans taken after the conscious scans are in good agreement with the last frames of the conscious scans, possibly showing some degree of washout (Casteels et al. 2013), a trend which is observable in the last few frames of the dynamic scan.

To investigate whether there was a correlation between the SUVs and glucose levels, a Pearson product-moment correlation analysis was conducted on the SUVs at equilibrium (i.e. the sum of the last five frames) versus both the pre-

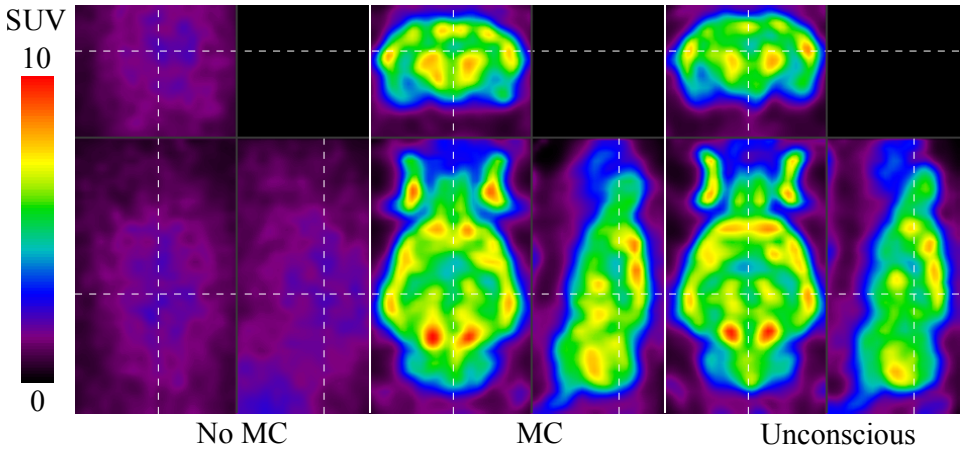

(a)

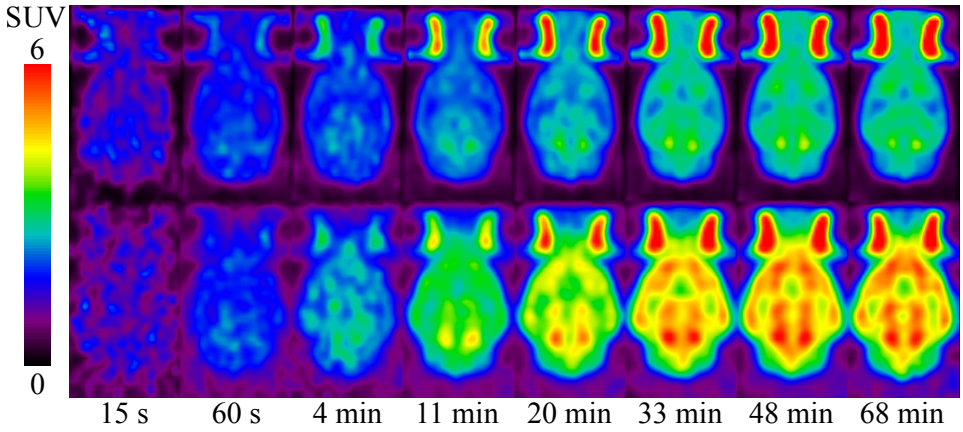

(b)

Figure 3.5: (a) Non-MC (left) and MC (middle) reconstructions of the conscious scan, which started 60 minutes after tracer injection, along with a reconstruction (right) of an unconscious scan of 10 minutes taken of the same rat, 91 minutes after tracer injection. The dashed lines indicate where the image slices are located. (b) A selection of dynamic frames from the unconscious (top) and conscious (bottom) scan reconstructions, averaged over all eight data sets. The times below the frames indicate the frame start time since the tracer injection.

and post-scan glucose levels. In the conscious case the correlation coefficients were -0.19 and -0.28 for the pre- and post-scan glucose level, respectively, (indicating no correlation) and in the unconscious case they were 0.62 and 0.53 for the pre- and post-scan glucose level, respectively. However, the p-values for

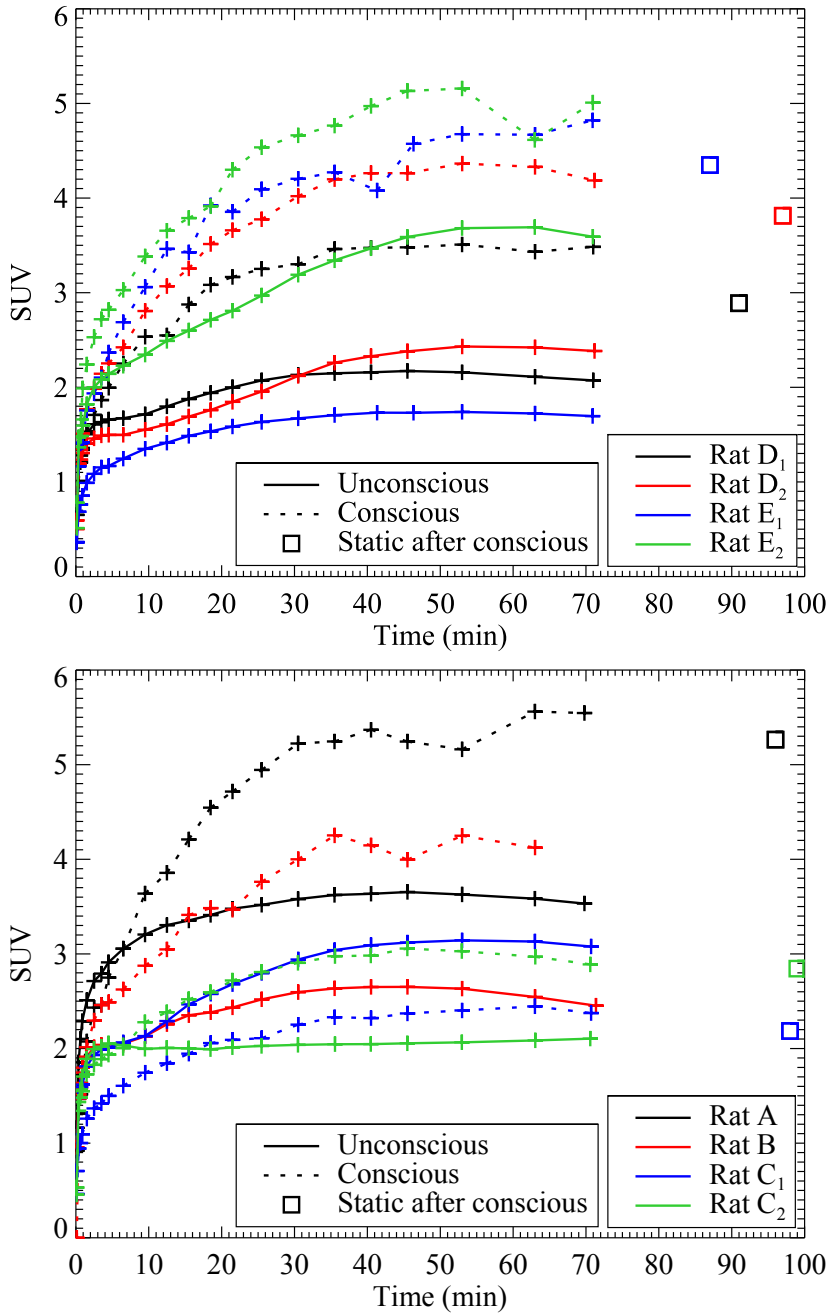

Figure 3.6: TACs for all eight data sets for the whole brain ROI, for the conscious (dotted lines) and unconscious (solid lines) scans, as well as the static scan with anaesthesia following the conscious scan (square points). The data sets are divided over two plots for clarity. For rats B and D_2 the static scan data was not available. No error bars are plotted since the ROI is non-uniform.

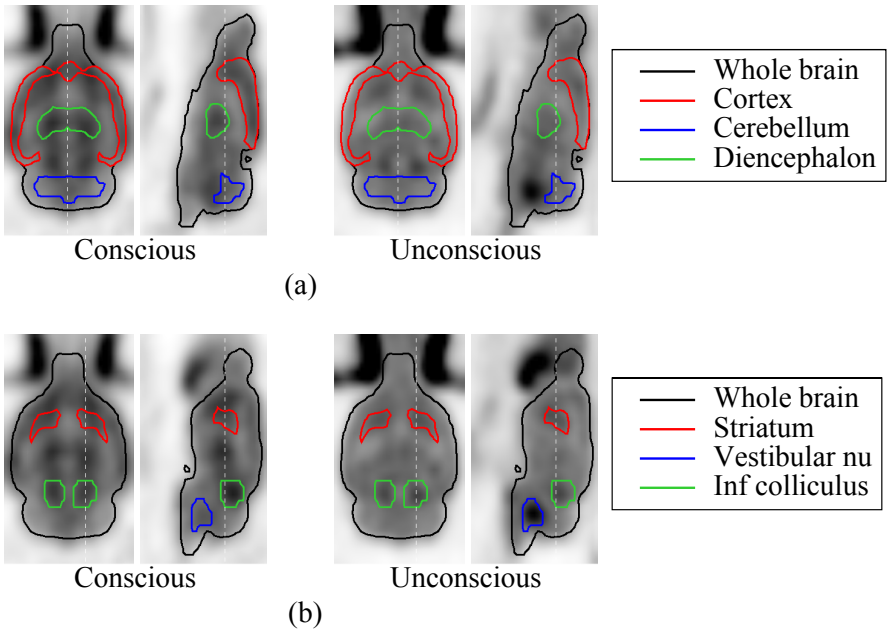

Figure 3.7: The ROIs under consideration are indicated on the last frame from the average of the eight reconstructions.

Table 3.1: Average ratio between ROIs and whole brain at equilibrium

	Uncon.	Con.	Change ± SD (%)	p	Sig.
Cortex	0.90	1.06	18.2 ± 7.1	7.4×10^{-5}	Yes
Vestibular Nu.	1.57	1.10	-29.5 ± 6.2	2.7×10^{-5}	Yes
Diencephalon	1.10	1.22	10.3 ± 4.7	0.0004	Yes
Inf. Colliculi	1.20	1.26	5.3 ± 3.4	0.0030	Yes
Cerebellum	1.05	1.00	-3.7 ± 8.9	0.2322	No
Striata	1.12	1.15	3.7 ± 8.0	0.2920	No

these fits were higher than 0.05 and therefore there is insufficient evidence to conclude that a correlation exists between the SUVs and the glucose levels.

A paired t-test was performed on the SUVs at equilibrium for the whole brain region to determine whether the uptake in that ROI was significantly different between the conscious and unconscious scans. The change from unconscious to the conscious scan had a mean of $59 \pm 52\%$, and the p-value of the test was 0.007, which is significant at the $p < 0.05$ level.

The TACs for the six ROIs for the average of the eight data sets are shown in Fig. 3.8(a) and (b). Plots of the ratios between each of the ROIs and the whole brain average are shown in Fig. 3.9(a) and (b). Again, the unconscious, static scans show good agreement with the last frames of the

conscious scan. The results of the paired t-test analysis on the ROI ratios at equilibrium are summarised in Table 3.1. For the conscious scans, the relative changes in the cortex ($18.2 \pm 7.1\%$), vestibular nuclei ($-29.5 \pm 6.2\%$), diencephalon ($10.3 \pm 4.7\%$), and inferior colliculi ($5.3 \pm 3.4\%$) compared to the unconscious scan were significant with $p < 0.05$ (i.e. $p < 0.008$ after the Bonferroni correction). No significant changes (at the same p-level) were observed in the cerebellum and striata.

3.4 Discussion

In this study we have demonstrated the efficacy of using a motion compensation technique to study fully conscious and unrestrained rats in a dynamic study. We investigated the effect of the anaesthetic isoflurane on the uptake of FDG in the rat brain, and a clear and significant impact of the isoflurane on the regional distribution of FDG uptake in the rat brain was observed.

From the blood glucose level measurements before and after the scans, we observed a large variability in the glucose levels of the unconscious rats, and a substantial change in the glucose level from before to after the scan, which is in agreement with other reported studies (Kofke et al. 1987; Zapp et al. 1992). In one test-retest (for rat E) the behaviour of the glucose level was not consistent. No statistical correlation was found between the SUVs at equilibrium and the glucose levels. Therefore, if a glucose correction is to be performed on the SUVs when using isoflurane then this variability must be taken into consideration. On the other hand, the glucose levels of the conscious rats were much more constant from before to after the scan, and between different rats.

Even though the conscious rats exhibited a large range of motion during the scan, the data were successfully compensated for motion and much of the resolution lost was regained. All of the rats tolerated the acclimatisation and scanning very well, with only three actually exiting the tube during a scan (before being placed back in the tube) which did not adversely affect the reconstructions. On occasion some rats did try to remove the marker during the scan, thus possibly inducing relative motion between the marker and the brain. This resulted in some inter- and intra-frame motion, the former of which was corrected for by frame-by-frame registration, and the latter possibly causing some residual motion blur in the reconstructions. The motion compensation was verified by comparing the last frame of the conscious scan to the subsequent, static, unconscious scan.

Since no blood input function could be measured for the conscious rats, and FDG has no reference tissue model in rats, a full kinetic analysis could not be performed. Nonetheless, from the results of the dynamic scans presented in Fig. 3.6, 3.8, and 3.9 it is clear that the isoflurane has a substantial impact on the tracer uptake. A paired t-test confirmed that there was a significant

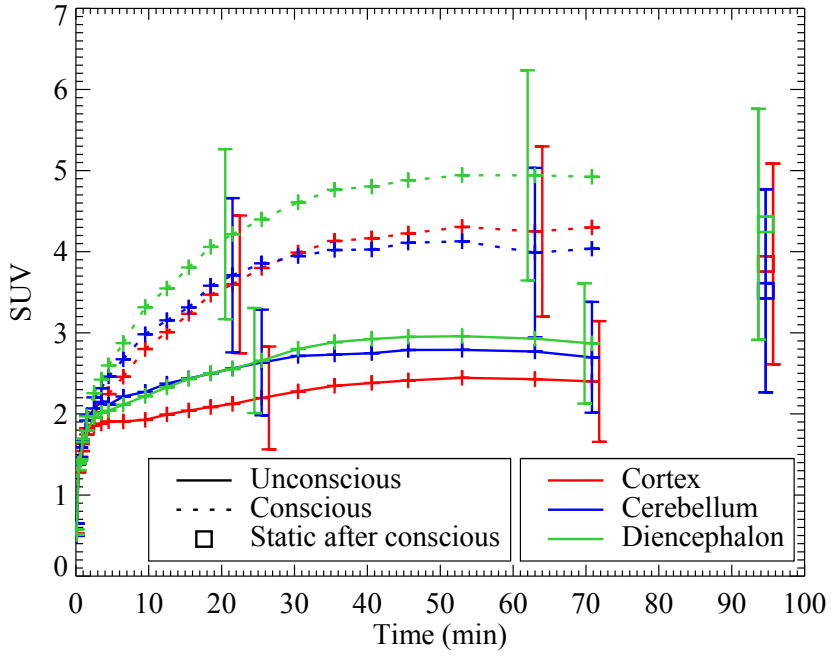

(a)

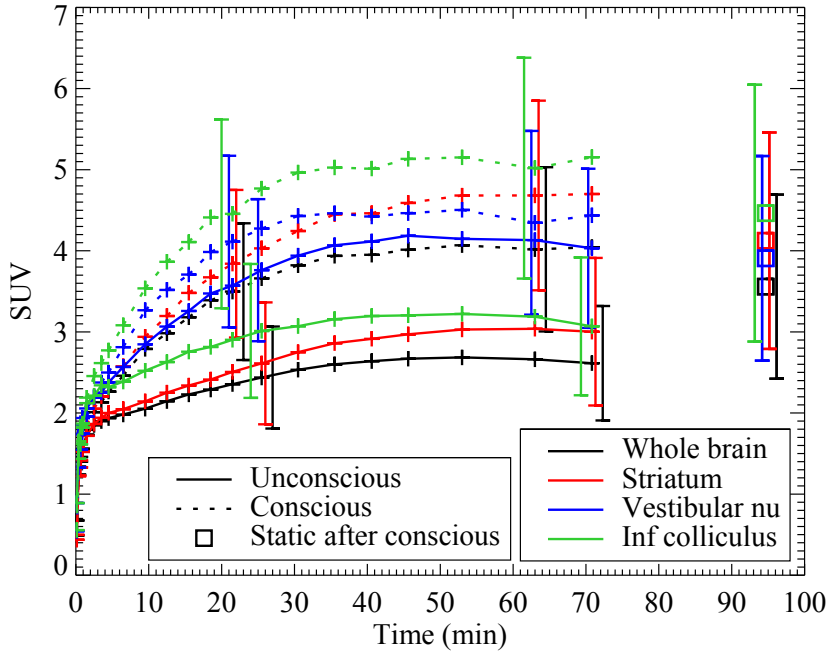

(b)

Figure 3.8: TACs for various ROIs for the average of the eight data sets, for the conscious (dotted lines) and unconscious (solid lines) scans, as well as the static scan with anaesthesia following the conscious scan (square points). The overlapping error bars are staggered for clarity.

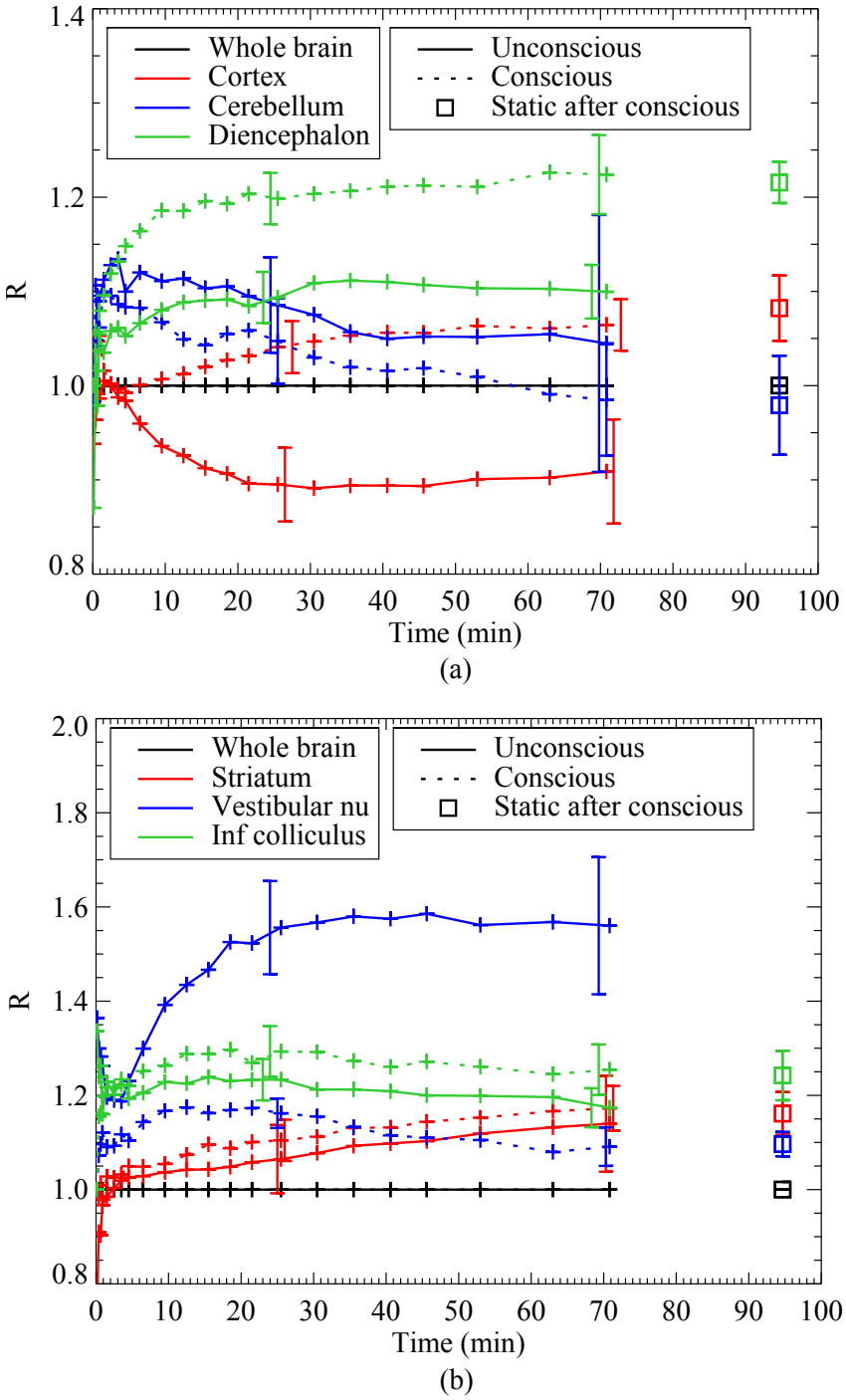

Figure 3.9: The ratio of various ROIs to the whole brain average, averaged over the eight data sets. In all plots the error bars are the standard deviations across the data sets and are only shown in two representative locations for clarity.

difference between the whole brain SUVs at equilibrium in the conscious and unconscious scans ($p < 0.05$). Furthermore, an analysis of the regional distributions within the brain showed a significant difference in the cortex, diencephalon, vestibular nuclei, and inferior colliculi between the conscious and unconscious scans ($p < 0.05$). Previously, Matsumura et al. (2003) conducted a study into the effect of various anaesthetics (including isoflurane) on FDG uptake in rats. They acquired static images of anaesthetised rats after allowing for a conscious uptake period and found similar regional differences to those found in this study: a decrease in the frontal cortex (although with a smaller magnitude increase in the posterior cerebral cortex), a decrease in the thalamus (a substructure of the diencephalon), and no change in the cerebellar cortex (a substructure of the cerebellum) and the striata. Their approach, unlike that presented in this work, cannot be used to investigate the effect of anaesthesia on tracer kinetics, which requires dynamic scanning from the time of injection.

In the unconscious scans there was a strong contrast between the vestibular nuclei and the whole brain, while this contrast was not observed in the conscious scans. Gupta et al. (2016) investigated the effect of isoflurane on the vomiting reflex. They used musk shrews instead of rats since the latter do not exhibit a vomiting reflex (however the rat brain may nonetheless respond similarly to isoflurane). They found that isoflurane induced a high c-Fos cell count (a protein related to neuronal activity) in the vestibular nuclei, where vestibular inputs are integrated with inputs from other sensory systems and the cerebellum for the perception of balance. High neuronal activity in the vestibular nuclei would likely be accompanied by an increased glucose uptake, explaining the high FDG uptake in the vestibular nuclei in the unconscious scans compared to the whole brain average.

3.5 Conclusion

The effect of isoflurane on the uptake of FDG in the rat brain has been investigated using a motion compensation technique to scan fully conscious and unrestrained rats dynamically from the time of tracer infusion. Although relatively few animals were studied, since each animal could be considered to be its own control, our results show a clear and significant impact of the isoflurane on the regional distribution of FDG in the rat brain. A significant difference was observed in the cortex, diencephalon, vestibular nuclei, and inferior colliculi, while no significant effect was observed in the cerebellum and striata. A strong variability was observed in the blood glucose levels of the anaesthetised rats between scans, and from before to after the scan, which suggests that this could be a further confounding factor of isoflurane on FDG studies. This work demonstrates that if isoflurane is to be used in FDG studies, these confounding factors should be recognised and taken into account.

In the future we will perform similar studies on other common PET tracers, especially those with a reference tissue model where kinetic modelling can be performed, such as raclopride or fallypride. For many such tracers the influence of anaesthesia is not completely understood.

Competing interests

The authors declare that they have no competing interests.

Funding

This work has been funded by the IMIR project of KU Leuven and the MIRIAD SBO project of the IWT.

Author's contributions

MSB conducted the experiments, performed the analysis, and wrote the text for this article. BdL assisted in the experiments and, together with GB, in the data analysis. RF was involved in the implementation of the motion compensation technique. JN was the supervisor of MSB and assisted in all aspects of the work. All authors contributed actively to the editing of the article, and read and approved the final version.

Acknowledgements

The authors would like to acknowledge the help of Julie Cornelis and Tao Sun during the rat training and scans, and Willy Gsell, Michel Koole and Patrick Dupont for the many helpful discussions.

Chapter 4

Rigid Motion Correction for Clinical PET scanners

Segments of this chapter have been published in:

M. G. Bickell, T. Koesters, F. Boada, and J. Nuyts (2014). "PET motion correction using MR-derived motion parameters". In: *EJNMMI Physics* 1.Suppl 1, A53

M. G. Bickell, J.-H. Kim, A. Rezaei, J. Nuyts, and R. Fulton (2015a). "Rigid motion correction of PET and CT for PET/CT brain imaging". In: *IEEE Nuclear Science Symposium and Medical Imaging Conference*, M5DP–124

Abstract

A rigid motion correction technique has been applied to four clinical PET scanners. Motion tracking was performed using two different marker-based motion trackers, or derived from simultaneously acquired MR data. In the case of the PET/CT scanner, the motion during both the CT and the PET, as well as between them, was corrected. Results are shown for a moving Hoffman brain phantom as well as for patients, which indicate the strengths and weaknesses of current motion correction techniques.

4.1 Introduction

Motion during a PET or CT scan can corrupt the data and significantly reduce the diagnostic value of the subsequent reconstructions. Even small motion during a PET scan can result in a significant loss of spatial resolution in the final reconstruction. For brain imaging, techniques such as head restraints can reduce motion, but with the high resolution of modern scanners these techniques are often inadequate. Paediatric, psychiatric, and elderly patients are especially likely to move during a scan, and in such cases sedation or

general anaesthesia can be used, but these approaches carry significant risks of hypoxaemia, respiratory depression, and oxygen desaturation (Malviya et al. 2000).

Motion constitutes one of the major sources of artefacts in CT (Yazdi et al. 2007; Popilock et al. 2008). When used for attenuation correction, a motion corrupted CT image can induce artefacts in a PET reconstruction. Such data sets often result in an additional CT scan being performed, thereby increasing the patient dose and scan time per patient. Motion during a scan is especially likely for paediatric patients, who are more vulnerable to the long-term effects of a high radiation dose (Brenner et al. 2001).

In the case of brain imaging where motion can be treated as rigid, the motion of the head can be corrected for before, during, or after the reconstruction. Such techniques have primarily been developed for PET imaging where the longer scan duration increases the risk of significant motion. The multiple acquisition frame (MAF) technique (Picard et al. 1997; Fulton et al. 2002) reconstructs short frames, aligns these to a reference frame, and sums them. This technique can not correct for intraframe motion. The so-called line-of-response (LOR) rebinning approach (Daube-Witherspoon et al. 1990; Menke et al. 1996; Bloomfield et al. 2003) allows for event-by-event motion correction by reorientating each detected LOR according to the recorded motion and binning them to a sinogram. If a motion corrected LOR falls outside of the sinogram, then either the sinogram must be extended or the event discarded. The event-based approach was further developed to be implemented in a list-mode reconstruction (Carson et al. 2003; Rahmim et al. 2004b). All of these approaches rely on externally tracked motion data, usually using video cameras placed behind the scanner gantry, which provide the 6 degrees-of-freedom necessary to describe the position of the head at a sufficiently high frequency. In a PET/MR scanner the motion can be derived directly from the simultaneously acquired MR data by reconstructing and aligning short MR frames (for example, Bickell et al. (2014)), or using MR navigators (fast, one dimensional acquisitions). More recently, our colleagues have demonstrated motion correction in CT (Nuyts et al. 2011; Kim et al. 2015) using an external motion tracking device. Each measured projection is reorientated according to the measured motion, thus producing a motion free reconstruction.

In this report we present results from implementing motion correction techniques for two PET/CT scanners and two PET/MR scanners. Applying motion correction techniques to CT data is also discussed, although this was not the focus of this research. The motion was tracked using one of three techniques: two different marker-based motion trackers, and high frequency MR data simultaneously acquired with the PET.

Table 4.1: Specifications of clinical scanners used during this research

	mCT	Hirez	mMR	Signa
Vendor	Siemens	Siemens	Siemens	GE
Ring diameter (mm)	842	830	656	620
Axial length (mm)	218	162	258	250
Crystal	LSO	LSO	LSO	LYSO
Scintillation converter	PMT	PMT	PMT	SiPM
TOF resolution (ps)	527.5	n/a	n/a	< 400
Detector size (mm)	4.0×4.0	4.0×4.0	4.0×4.0	4.0×5.3
Detector depth (mm)	20	20	20	25
No. rings	52	39	64	45
No. detectors per ring	624	624	448	448
Transaxial resolution (mm) *	4.4	4.61	4.3	4.4
Axial resolution (mm) *	4.4	5.1	4.3	5.3

* At a radial distance of 1 cm from the FOV centre.

4.2 Method & Materials

4.2.1 Scanners

Four clinical systems were used for these studies, all of which were multi-modal systems, namely the Siemens mCT PET/CT (Jakoby et al. 2011) (Siemens Medical Solutions Inc., Knoxville, TN, USA), the Siemens Hirez PET/CT (Brambilla et al. 2005), the Siemens mMR PET/MR (Delso et al. 2011), and the GE Signa PET/MR (Grant et al. 2016) (GE Healthcare, Chicago, IL, USA). A summary of the specifications of these systems is given in table 4.1.

4.2.2 Motion Trackers

OptiTrack

For the mCT and the Hirez PET/CT scanners the OptiTrack Flex-13 system (NaturalPoint Inc. Corvallis, OR, USA) was used to track the motion. This system is comprised of several free-standing cameras which emit infrared light and record the reflections from spherical markers attached to the object being tracked; see figure 4.1. Three or six cameras were used. The cameras were operated at 30 Hz, although frequencies of up to 120 Hz are possible. The cameras can be placed arbitrarily, and thus a calibration of the cameras is performed each time they are set up by moving a pre-defined marker set throughout the field-of-view (FOV) of the cameras. The system software then calculates a suitable calibration. This procedure usually takes approximately 5

Figure 4.1: Shown on the left is one of the OptiTrack Flex-13 cameras, in the middle are three of the cameras arranged for motion tracking, and on the right is an example of the tracking markers attached to a cap worn by a volunteer, lying on the patient bed of the scanner.

minutes. Markers are attached to the object to be scanned in any arrangement, taking care to maximise the visibility of the markers by the cameras. The marker set on the object to be tracked and any additional marker sets such as reference markers, etc., are then registered in the tracking software interface, and tracking can begin.

Spatial Calibration It is necessary to determine a 4×4 transformation matrix, referred to as the calibration matrix T_c, which converts from the OptiTrack coordinate system to the PET or CT coordinate system. We used the image-based registration method described previously by Kim et al. (2013). A phantom with some detail along each of the three axes is imaged at between six and ten stationary and distinct positions within the scanner. A pair-wise transformation between each of the positions can be obtained from both the OptiTrack data, as well as the PET or CT reconstructions (by registering the images to each other). These transformations can then be compared to fit a single calibration matrix which converts from the OptiTrack coordinate space to the scanner coordinate space. The more basic alternative to this method is to compare absolute coordinates in each space, but, as discussed in section 1.2.2, the image-based registration method has the advantage that it requires no careful measurement of the origin of the object in PET or tracker space, and the PET transformation matrices are determined to a high precision since they are derived from the registration of entire images.

A permanent reference marker set is attached to the scanner gantry which enables the reuse a single calibration matrix regardless of the camera arrange-

ment.

Temporal Synchronisation For PET data, to determine which measured poses need to be applied to which recorded PET events, it is necessary to synchronise the two data streams. This is performed by starting the motion tracking after the PET has started, and having the OptiTrack system insert a gate tag into the list-mode stream via the gate input port every time a pose is recorded. The gate tags and pose time stamps can then be aligned to each other to achieve synchronisation.

For CT data the synchronisation can be achieved by tracking the motion of the bed. Since the start and end of the bed motion is reported in the CT data, this can be used to synchronise the time-stamps between the two systems.

HobbitView

For the Signa PET/MR scanner an optical system developed by HobbitView Inc. (Palo Alto, CA, USA) was used to track motion. The system tracks a single large marker attached to the patient's forehead using a small MR-compatible camera mounted on the head coil. All experimental data using the HobbitView system were acquired at Stanford University (Stanford, CA, USA) or at General Electric Global Research (Niskayuna, NY, USA) and (GE Healthcare, Waukesha, WI, USA).

Spatial Calibration A calibration transformation was determined between the HobbitView and MR systems by measuring an object in the MR which was also being tracked by the HobbitView system. The locations of the object in each space could then be compared to determine the necessary transformation between the coordinate systems. The relationship between the MR and PET coordinate systems has been accurately measured by the manufacturer, allowing for the transformation from the HobbitView to the PET system to be determined.

Temporal Synchronisation A tag was inserted into the PET list-mode data stream each time the HobbitView system acquired a measurement, thereby enabling the temporal synchronisation between the two data streams.

MR sequences

Since a PET/MR scanner acquires the PET and MR data simultaneously it is possible to use the MR to perform short, quick acquisitions from which the motion of the object within the scanner can be determined. This motion can then be used to correct the PET data. Our colleagues at the New York University utilised the Golden Angle Radial Sparse Parallel (GRASP) sequence

(Feng et al. 2013) to perform such motion tracking in the mMR PET/MR scanner. This sequence acquires data in radial spokes in k-space, with each spoke separated from the last by the golden angle (137.5°) to optimise the sampling. After the acquisition the radial samples can be combined chronologically into any subsets to create framed data. Each frame can then be reconstructed and the resultant images used to determine the motion parameters. To ensure a reasonable MR reconstruction of each frame, a frame rate of 1 Hz was used. While this motion sampling is much coarser than that used for other trackers, using the MR in this way has two main advantages:

- no external motion tracking devices are necessary,
- the acquired motion data are in the PET coordinate system (except, possibly, for a small but known offset between the MR and the PET).

However, this technique has the disadvantage that the MR needs to acquire a sequence which can be used for motion tracking. While the GRASP sequence is suitable and the acquired data can be used for clinical investigations, many other common clinical sequences would not be able to be used for motion tracking, thereby limiting the usefulness of the MR. In addition, the coarse sampling rate means that only slow motion will be captured reliably.

To solve these issues some groups are investigating using so called "MR navigators" to track the motion (for example, Catana et al. (2011) and Van Der Kouwe et al. (2006)). Navigators are very fast (on the order of milliseconds) one dimensional acquisitions which can be acquired along a particular line (two and three dimensional navigators are possible but take longer to acquire). Navigators can be inserted into many standard clinical sequences and have minimal affect on the acquisition. By acquiring navigators many times per second, along different (possibly orthogonal) lines, the motion of the object can be estimated. While additional studies are still needed to investigate the feasibility of this approach, navigators may offer a suitable motion tracking technique for use in PET/MR systems.

Spatial Calibration The PET and MR are designed to image the same FOV, and therefore are in the same coordinate system. Usually there is some small offset between the two scanners, but this is measured once by the manufacturer and does not change.

Temporal Synchronisation Since the PET and MR are connected to each other their time stamps should be synchronised. Alternatively it is possible to insert a tag into the PET list-mode stream whenever an MR sequence is performed, which would allow for synchronisation.

4.2.3 Reconstruction

In-house software was used to perform the motion correction and reconstruction of the PET (and CT) data. The acquired motion data were usually smoothed and interpolated, as described in appendix B. The PET data were reconstructed using a list-mode based ordered-subsets expectation-maximisation (OSEM) algorithm (Shepp et al. 1982; Hudson et al. 1994; Parra et al. 1998; Reader et al. 1998), and when modelling the resolution the image based convolution technique using a stationary Gaussian kernel was used (Reader et al. 2003). The time-averaged sensitivity image was calculated as proposed by Rahmim et al. (2004b). Note that non motion corrected reconstructions were usually performed without attenuation correction since it is non-trivial to construct an attenuation map for a moving object.

The CT reconstructions were performed using the maximum-likelihood for transmission tomography (MLTR) algorithm (Nuyts et al. 1998), incorporating the motion correction into the projections during the reconstruction (Nuyts et al. 2011; Kim et al. 2015).

4.3 Experiments

mCT PET/CT

A Hoffman brain phantom was filled with ^{18}F-FDG with an activity of 186 MBq and scanned in the mCT PET/CT scanner based at the Westmead Hospital, Sydney, Australia, in collaboration with Prof. Roger Fulton and Dr. Jung-Ha Kim of the University of Sydney, Sydney, Australia. The OptiTrack system was used to track 4 spherical markers attached to the phantom. The phantom was scanned in the CT scanner using a pitch of 0.8 and a scan time of 10.5 s, with a collimation of 64×0.6 mm. During the CT scan the phantom was made to roll on the bed. The phantom was then scanned by the PET scanner for 10 minutes, during which time it was manually moved throughout the scan. The data were acquired in 64-bit list-mode format. A stationary CT and PET scan were also acquired for reference. The PET and CT data sets were reconstructed to the same reference pose (after accounting for the offset between the scanners) which allowed the motion corrected CT to be used for attenuation correction in the PET reconstruction.

Hirez PET/CT

The motion correction technique was used during a study into tracers which target tau in the brain, the accumulation of which is believed to be an indicator of dementia. Two tracers were being investigated, namely ^{18}F-THK5351 (Harada et al. 2015) and ^{18}F-AV1451 (Chien et al. 2013). Healthy control volunteers

were scanned for 90 or 100 minutes from the time of injection, and patient volunteers were scanned for 30 minutes starting 50 minutes post-injection. A total of 11 volunteers were scanned with the AV tracer, and 6 with the THK tracer. The Hirez PET/CT scanner used was based at the Universitair Ziekenhuis Leuven, Leuven, Belgium. The study was led by Prof. Koen Van Laere and Prof. Karolien Goffin of the Department of Nuclear Medicine, UZ Leuven, and Prof. Rik Vandenberghe and Prof. Patrick Dupont of the Department of Neurology, UZ Leuven, and was conducted with the PhD candidates Jolien Schaeverbeke and Charlotte Evenepoel of KU Leuven, Leuven, Belgium. The ethical approval for these studies can be seen in appendix E.

A tight-fitting cap was placed on the volunteer's head, and five spherical markers were attached by velcro to the cap. These markers were then tracked by the OptiTrack system at 30 Hz. The volunteer lay on the scanner bed with their head in a head restraint since we wanted to make no changes to the standard protocol. The head restraint consisted of a pillow which was inflated with air such that it became rigid about the head. The volunteer was then scanned in the CT and then the PET after being injected with 180 ± 5 MBq of the THK or AV tracer.

Signa PET/MR

A volunteer was injected with FDG and scanned for 10 minutes in the Signa PET/MR scanner based at the University of Stanford, Stanford, CA, USA, in collaboration with Dr. Floris Jansen, Dr. Michel Tohme, and Dr. Mehdi Khalighi of General Electric Healthcare, Chicago, IL, USA, and Dr. Roland Bammer of HobbitView Inc., Palo Alto, CA, USA. The volunteer was asked to move their head during the scan, while being tracked by the HobbitView system at a frequency of 50 Hz. An attenuation map was constructed from a thresholded water-MR image acquired simultaneously with the PET scan.

mMR PET/MR

A patient was injected with FDG with an activity of 374 MBq and scanned in the mMR PET/MR scanner based at the New York University, New York, NY, USA, in collaboration with Prof. Fernando Boada and Dr. Thomas Kösters. An MR scan was acquired using the GRASP sequence, simultaneously with a 5 minute PET scan (started 80 minutes post-injection), while the patient was asked to move their head repetitively from side to side for proof-of-principle purposes. A 60 minute static scan was also acquired prior to the motion scan and immediately after injection, and used as a control. The MR data were divided into a series of 268 images with a frequency of approximately 1 Hz and used to derive the motion parameters by registering each MR image

to a reference image. An MR-based attenuation map was used during the reconstruction.

4.4 Results

mCT PET/CT

The CT reconstructions are shown in figure 4.2 and the PET reconstructions in figure 4.3. The motion corrected CT reconstruction suffered from a uniform 4% scaling in comparison to the reference reconstruction. This has not been observed in previous CT motion correction studies we have performed and requires further investigation. The PET reconstructions were performed using either the attenuation map derived from the reference CT scan or the motion corrected CT scan. The profiles through these two reconstructions are shown in figure 4.4. The effect of the aforementioned scaling in the CT attenuation maps can be seen in these profiles since the two PET reconstructions match closely except for a slight scaling between them.

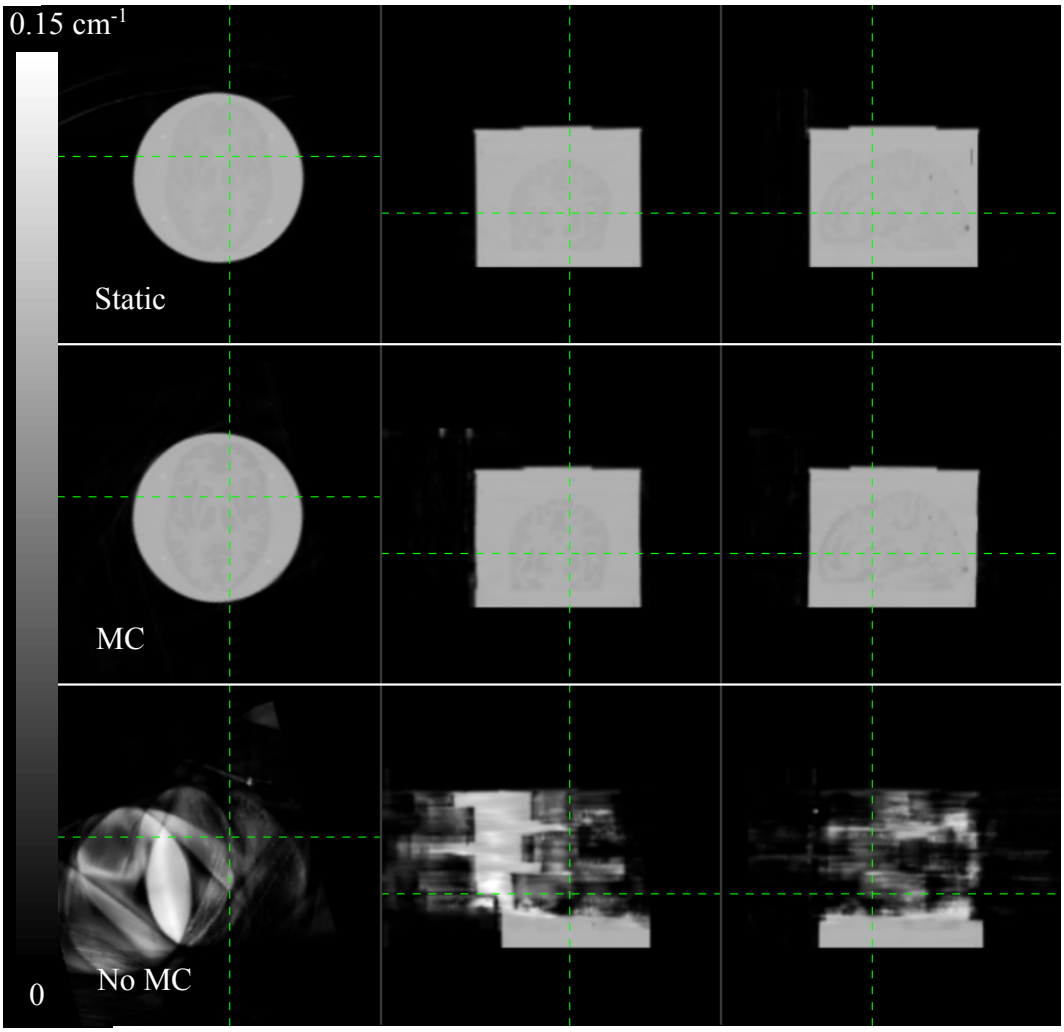

Figure 4.2: The reconstruction of the CT acquisition of the stationary phantom is shown in the top row, with the motion corrected reconstruction of the moving phantom in the middle row, and without motion correction in the bottom row. Residual motion artefacts can be seen in the motion corrected reconstruction, but much of the motion has been corrected for. Note that the phantom was filled with liquid and therefore there is not much contrast between the "brain" region and the surrounding cylinder.

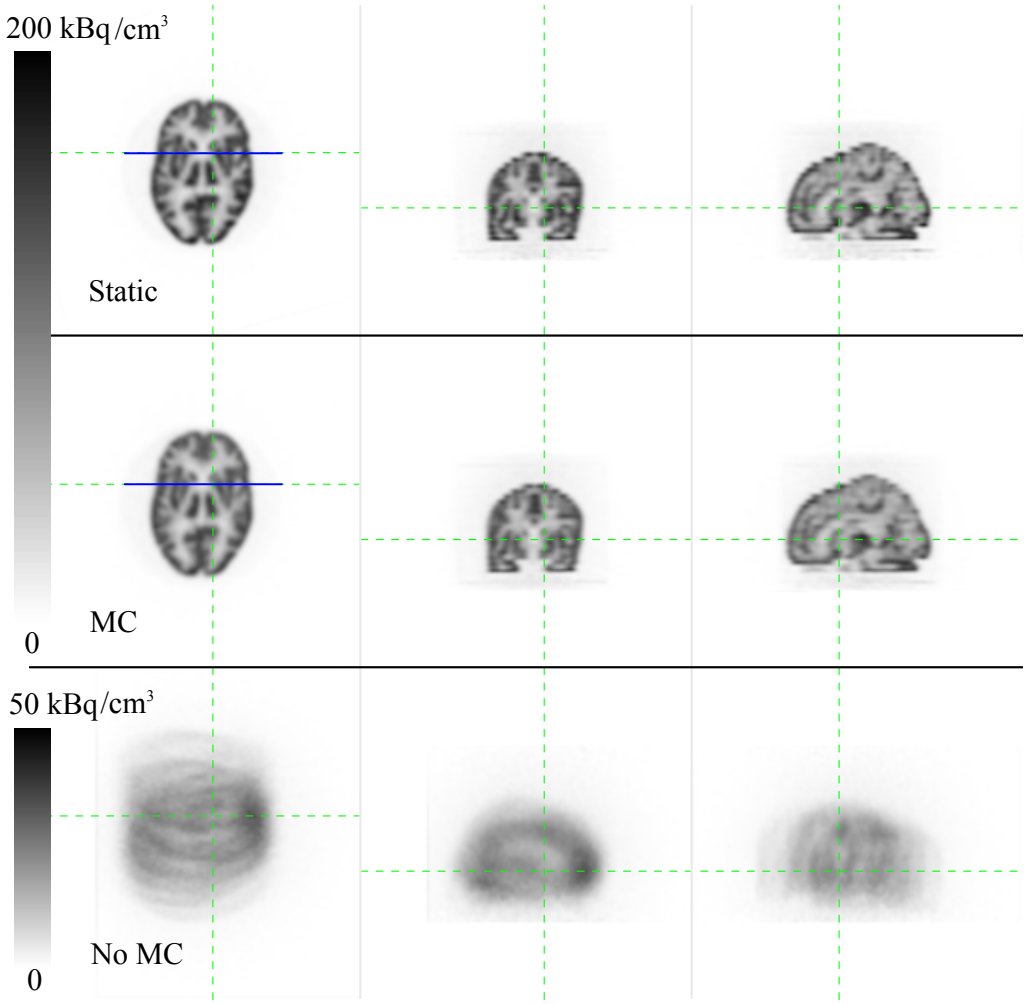

Figure 4.3: The reconstruction of the stationary phantom is shown in the top row, with the motion corrected reconstruction of the moving phantom in the middle row, and without motion correction in the bottom row. The blue lines indicate where the profiles shown in figure 4.4 are located.

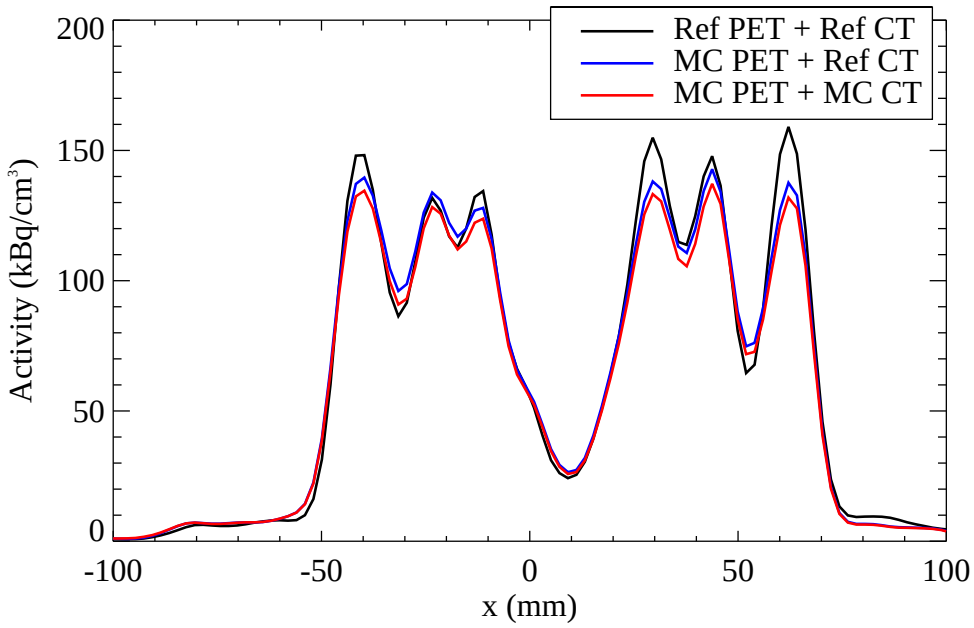

Figure 4.4: Profiles through the PET reconstructions (as indicated in figure 4.3) of data without motion using the reference CT for attenuation correction (AC) (black curve), and PET reconstructions with motion correction using the reference CT for AC (blue curve), the motion corrected CT for AC (red curve). Some resolution loss can be observed between the motion corrected and reference PET reconstructions. The motion corrected PET reconstructions using the reference and motion corrected CT for AC match closely.

Hirez PET/CT

Since a head restraint was always used the motion of the subjects was very limited, if present at all. In fact, in half of the scans no significant motion was detected by the OptiTrack (significant being motion around 2 mm or more) and no motion blur was observable in the non-MC reconstructions for those scans. In a further 5 studies some motion was observed and could be seen in the non-MC reconstructions, and was then corrected for. The remaining 4 studies exhibited some motion which was then not accurately corrected for by the MC procedure. This failure of the MC is most likely due to the fact that the cap worn by the subjects to which the markers were attached was in physical contact with the head restraint, and when a subject moved their head the motion of the cap may have been restricted by the head restraint and hence not have moved rigidly with the head. This is a significant limitation of this setup, and will be discussed further in the discussion in section 4.5.

An example reconstruction of data from a 30 minute patient volunteer scan with the THK tracer is shown in figure 4.5, with and without motion correction. Since the volunteer was in a head restraint the degree of motion was very small. This volunteer moved by about 2 mm during the scan, which was a normal magnitude amongst those volunteers who did exhibit motion. A slight improvement in the motion corrected reconstruction can be seen in the profile plots through the reconstructions.

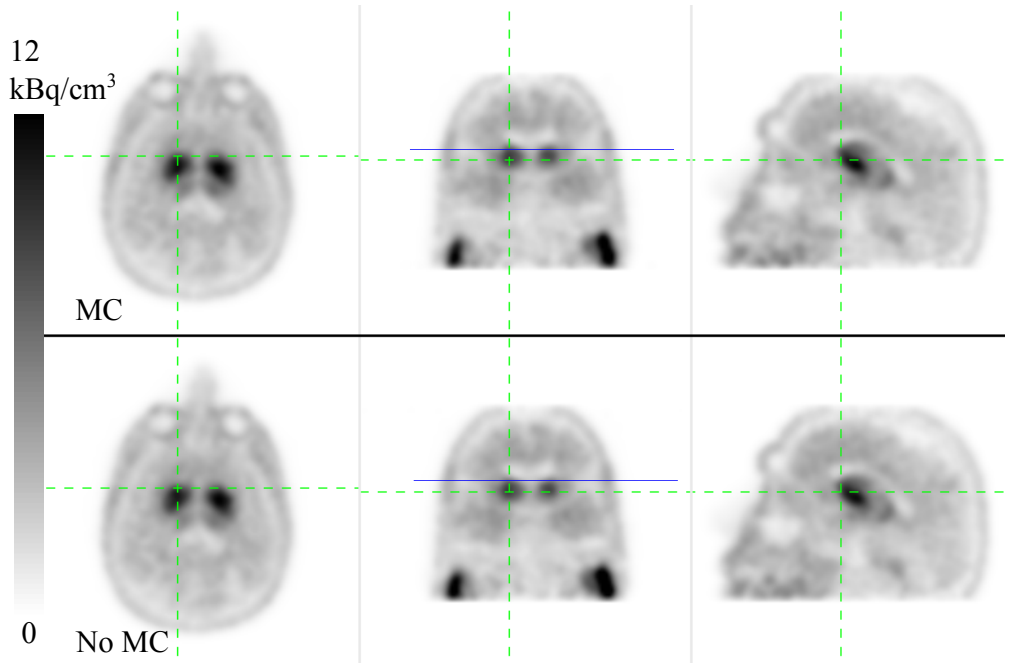

(a)

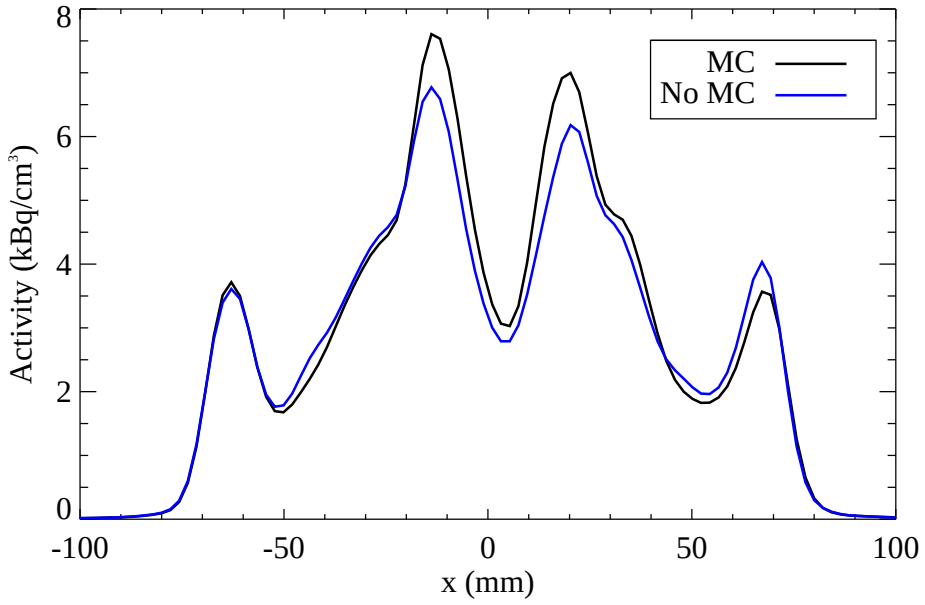

(b)

Figure 4.5: (a) Reconstructions of the PET data with (top) and without (bottom) motion correction of a patient volunteer. The green lines indicate where the slices are located, and the blue lines indicate where the profiles in (b) are located. Since the volunteer's motion was only slight, the attenuation map was used during the non motion corrected reconstruction as well.

Signa PET/MR

The reconstructions of the 10 minute brain scan with motion are shown in figure 4.6(a), with and without motion correction, and the profiles through the reconstructions are shown in figure 4.6(b). An improvement in the resolution of the motion corrected reconstruction can be seen.

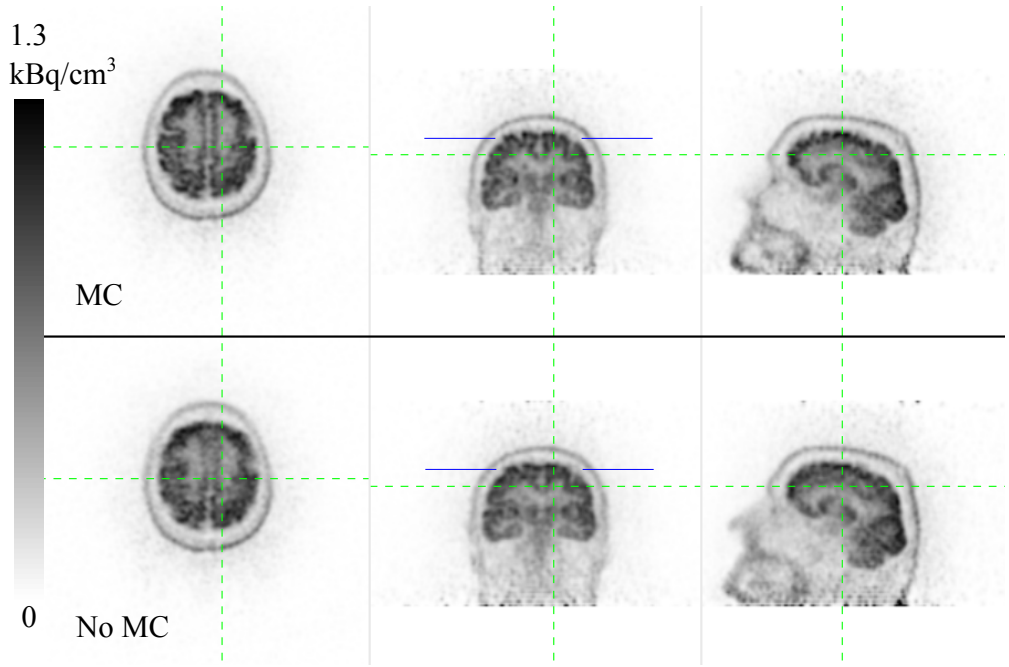

(a)

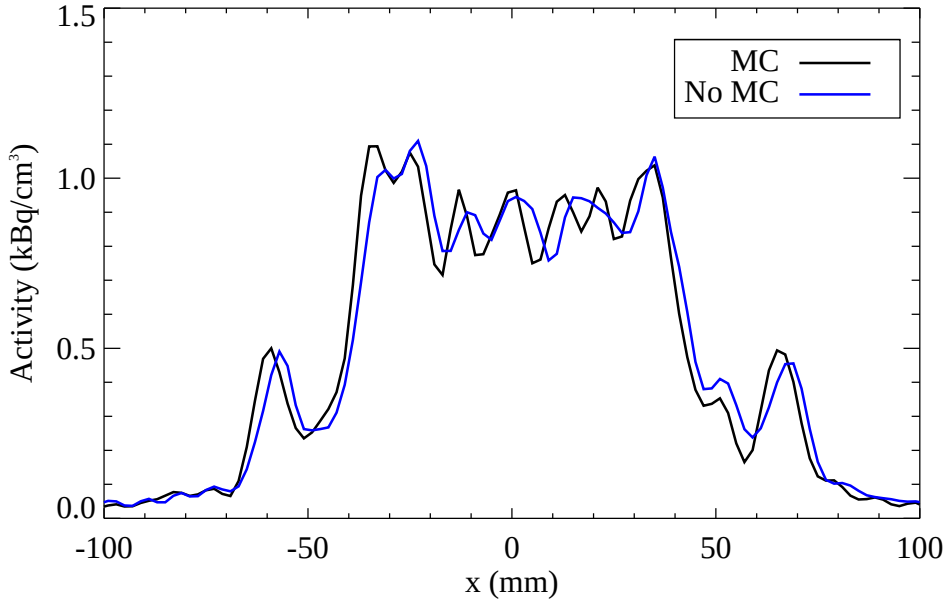

(b)

Figure 4.6: (a) Reconstructions of the motion data with (top) and without (bottom) motion correction. The green lines indicate where the slices are located, and the blue lines indicate where the profiles in (b) are located. Since the volunteer's motion was only slight, the attenuation map was used during the non motion corrected reconstruction as well.

mMR PET/MR

The reconstructions of the 60 minute static and 5 minute motion acquisitions are shown in figure 4.7. The profiles through the reconstructions are shown in figure 4.8, although they are not completely comparable since the tracer uptake period was very different in the two cases. Much of the motion has been corrected for.

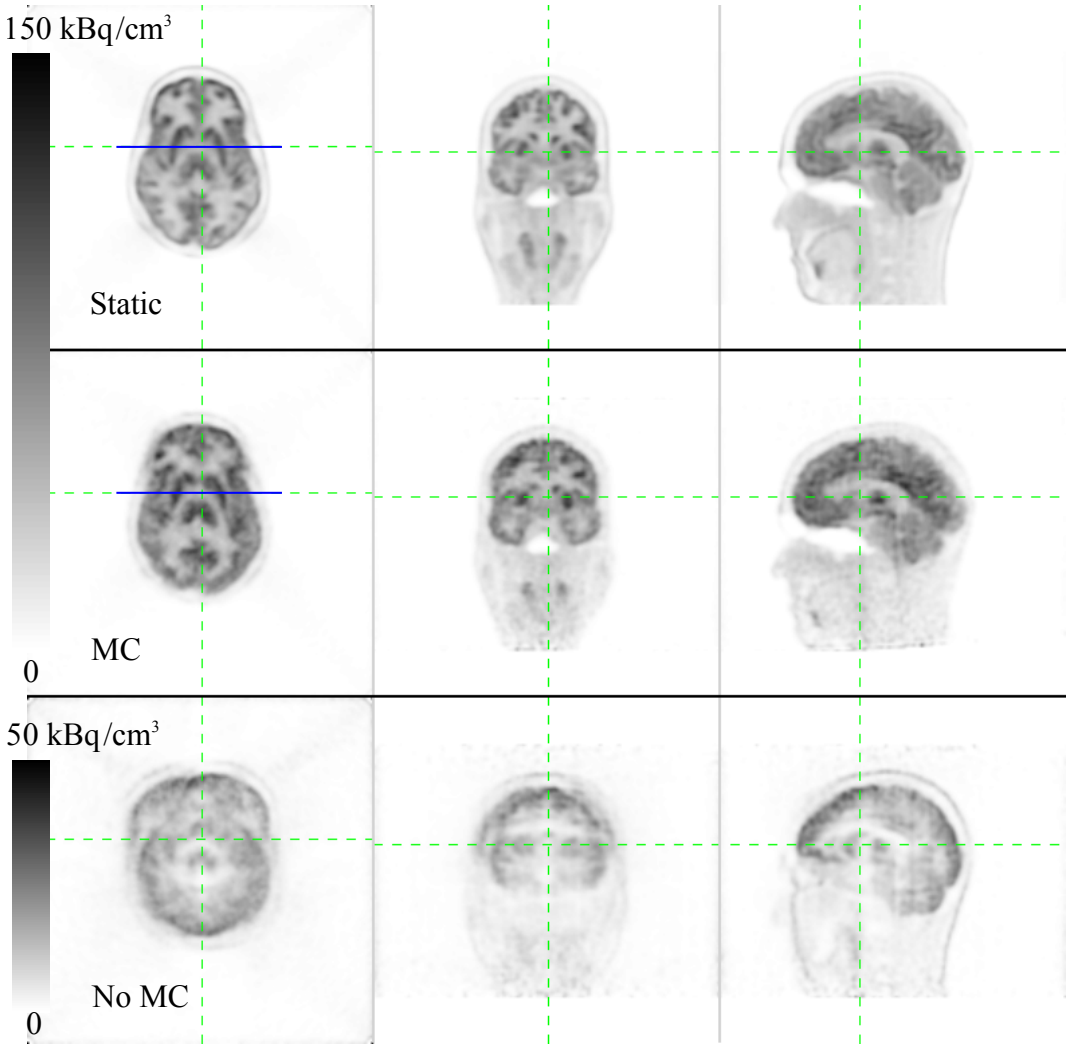

Figure 4.7: Reconstructions of the static and motion acquisitions, with and without motion correction. The green lines indicate where the slices are located, and the blue lines indicate where the profiles in figure 4.8 are located.

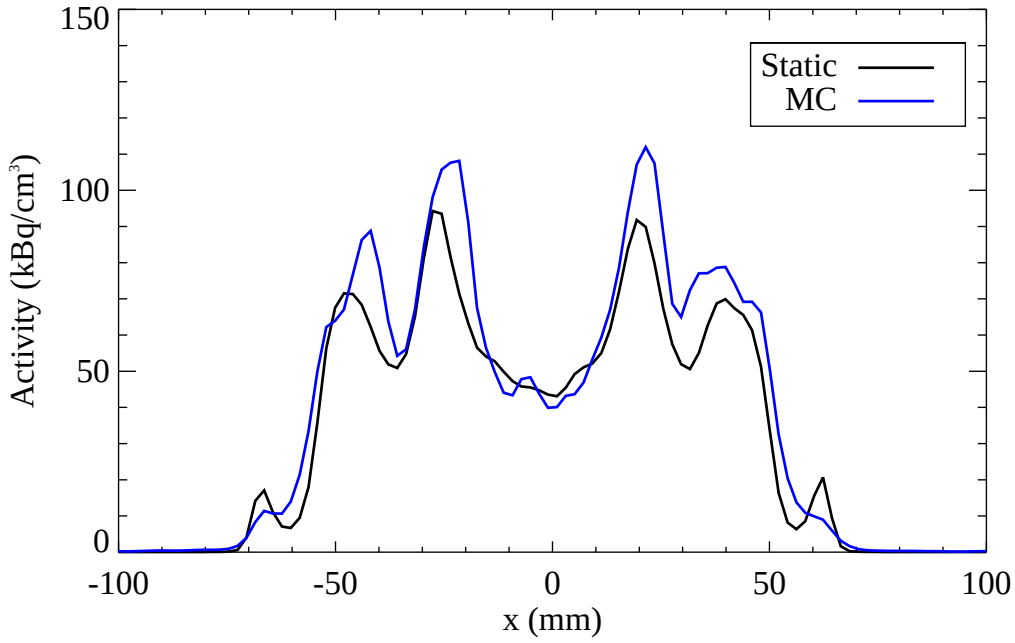

Figure 4.8: Profiles through the reconstructions shown in figure 4.7. Note that the static data were acquired over 60 minutes from the time of injection, while the motion data was acquired over 5 minutes starting 60 minutes after the tracer injection, and thus the tracer uptake is not expected to be the same.

4.5 Discussion

A number of motion tracking techniques have been explored and motion correction has been applied to various clinical scanners. Regardless of the source of the motion data, the implementation of the motion correction scheme was almost identical across all scanners. The trackers used offered various advantages and disadvantages:

OptiTrack The OptiTrack system provides accurate motion tracking, and is well suited to being used inside a clinical setting.

- ⊕ It can be quickly assembled and disassembled, in about 20 minutes. The system can also be left in place to avoid this assembly, assuming it does not interfere with the rest of the clinical routine.
- ⊕ It has little impact on the patient and the scan protocol, requiring only that a cap with the markers be placed on the patient's head, and the data be acquired in list-mode format.
- ⊕ The markers can be placed arbitrarily on the patient.

- ⊕ There is a user-friendly interface for defining and tracking the rigid bodies.
- ⊖ When used with a head restraint, the current setup using the cap sometimes fails to accurately capture the head motion since the contact between the head restraint and the cap may cause it to not move rigidly with the head. This results in imperfect motion correction in the reconstruction.
- ⊖ Even though the impact on the standard routine of this system is small, it is still significant. This is mostly due to the markers which must be attached to the patient's head.
- ⊖ The system is not MR compatible.

The problem of the head restraint interfering with the motion of the markers may be solved by simply removing the head restraint and providing rather a small head support. Motion would then most likely be observed in all studies (since there would be no restraint), and every scan would therefore require motion correction. Alternatively, using a tracking system which did not use markers would also solve this problem, and would simultaneously greatly reduce the impact on the standard clinical routine.

HobbitView During this research we did not have access to this system directly. Data was acquired by our collaborators and provided to us. As a result a thorough description of its advantages and disadvantages cannot be made. However, the following is noted:

- ⊕ It is MR compatible.
- ⊕ It can track motion at a very short distance, enabling it to be placed on the head coil in an MR scanner.
- ⊖ The marker is attached to the forehead, which can move relative to the brain with a change of facial expression. Of course this problem is common to all head motion tracking techniques.

MR sequence Such an approach can only be used in PET/MR scanners, which have only become available in the past few years.

- ⊕ No external tracker is needed.
- ⊕ No additional spatial calibration is required, and temporal synchronisation can easily be achieved.
- ⊖ The implementation we used limits the possible clinical MR sequences to those that can be used to track motion.

⊖ The frequency of the tracking was low since a reasonable MR reconstruction is required at each time point.

If an implementation of MR navigators can be used, then other clinical MR sequences can be employed. The tracking frequency can also be much higher since navigators are quick to acquire. However, incorporating navigators into a clinical sequence requires expertise in sequence programming which is not available at all sites, and may be difficult for the manufacturers to generalise for all sequences. Nonetheless, this technique can benefit from further investigation.

The adoption of motion correction techniques in the clinical setting is being hindered by two main obstacles: the markers used to track motion, and the fact that a list-mode based implementation of the reconstruction algorithm is not common in most clinical scanners.

Several groups have presented work on markerless tracking techniques (Olesen et al. 2013; Noonan et al. 2015), and these are very promising. These techniques either track a structured light pattern projected onto the patient's face (Olesen et al. 2013), or identify and track the features of the face directly (Noonan et al. 2015). The latter technique is currently being explored at our institution.

The number of crystals in modern scanners is increasing, and with TOF information the size of the sinograms required to hold data from a scan is becoming very large to the point where they are comparable to the size of the raw list-mode data. This means that there is not much of a computational advantage to be had by reconstructing the sinograms instead of the list-mode data directly. If the scanner manufacturers start implementing a list-mode reconstruction then it will become much simpler for them to incorporate a motion correction scheme into the reconstruction.

4.6 Conclusion

We have demonstrated that a motion correction technique can be implemented on four different PET scanners using three different sources of motion data. The implementation of the motion correction schemes could bring a significant improvement to the clinical setting. Patients who before would not have been scanned because motion was expected, or for whom a scan is often spoiled due to motion, would benefit greatly from motion correction. The clinical protocol could be simplified by removing the need for a head restraint, thereby also improving the comfort of the patient. The issue of motion between the CT and PET scan causing a misalignment of the emission image and the attenuation map could simultaneously be solved. And now, with the advent of markerless motion tracking, incorporating motion correction into the clinical routine has

become much more likely since a markerless system will have almost no impact on the standard clinical routine.

Chapter 5

Spatially Variant Resolution Modelling for Iterative List-Mode PET Reconstruction

Published as:

M. G. Bickell, L. Zhou, and J. Nuyts (2016). "Spatially variant resolution modelling for iterative list-mode PET reconstruction". In: *IEEE Transactions on Medical Imaging* 35.7, pp. 1707 –1718

Abstract

A spatially variant resolution modelling technique is presented which estimates the system matrix on-the-fly during iterative list-mode reconstruction. This is achieved by redistributing the endpoints of each list-mode event according to derived probability density functions describing the detector response function and photon acollinearity, at each iteration during the reconstruction. Positron range is modelled using an image-based convolution. When applying this technique it is shown that the maximum-likelihood expectation maximisation (MLEM) algorithm is not compatible with an obvious acceleration strategy. The image space reconstruction algorithm (ISRA), however, after being adapted to a list-mode based implementation, is well-suited to the implementation of the model. A comparison of ISRA and MLEM is made to confirm that ISRA is a suitable alternative to MLEM. We demonstrate that this model agrees with measured point spread functions and we present results showing an improvement in resolution recovery, particularly for off-centre objects, as compared to commercially available software, as well as the standard technique of using a stationary Gaussian convolution to model the resolution, for equal iterations and only slightly higher computation time.

5.1 Introduction

In positron emission tomography (PET) imaging accurately modelling the physical measurement process to account for the point spread function (PSF) can improve the subsequent resolution of the reconstruction (Derenzo 1986). In statistical reconstruction methods, such a model can be incorporated into the system matrix, which is a mapping between the detector elements and the voxels in the image space, and is referred to as resolution, or PSF, modelling. The state of the art in resolution modelling techniques has been summarised in (Rahmim et al. 2013).

In iterative reconstruction resolution modelling can be performed in the image domain or the projection domain. In the image domain a blurring kernel can be used to model the resolution. Reader et al. (2003) use a spatially invariant Gaussian kernel, which is simple to implement and produces images of high quality in terms of resolution recovery and noise reduction. Bowen et al. (2013) extend this technique by using a combination of a stationary Gaussian kernel and a radially varying kernel to model the spatially variant nature of the resolution. A set of measured point sources is used to determine the necessary kernel parameters. Similar techniques using different parameterisations of the PSF are presented in (Rahmim et al. 2004a; Rapisarda et al. 2010; Cloquet et al. 2010). Projection domain techniques incorporate the system model directly into the system matrix. The system matrix can be measured (e.g. (Panin et al. 2006)), determined analytically (e.g. (Lecomte et al. 1984; Huesman et al. 2000)), or determined by Monte Carlo techniques (e.g. (Mumcuoglu et al. 1996; Qi et al. 1998; Yao et al. 2012)). The propagation of errors in the system matrix through to the reconstructed image was studied by Qi et al. (2005).

In this paper, a spatially variant resolution modelling technique, which we reported on initially in (Bickell et al. 2013) and refer to as the "Redistribution technique", is presented. In this model the dominant factors affecting the PSF, namely the detector response function, the acollinearity of the photon pair, and the positron range, are modelled for the Siemens microPET Focus220 small animal scanner (Preclinical Solutions, Siemens Healthcare Molecular Imaging, Knoxville, TN, USA). The model as derived in this paper can be applied to any ring scanner where the axial length is much less than the diameter; it can, however, be extended to other geometries. Probability density functions (PDFs) are derived which represent the statistical distribution of where the photons were absorbed in the detecting crystals. These PDFs are randomly sampled to redistribute the endpoints of each list-mode event, thereby distributing the events over the scanner field-of-view (FOV) in a way which is statistically more representative of the true photon flight paths, and hence modelling the system response. It is the intention to use this technique for list-mode based, event-by-event rigid motion correction. Sinogram-based motion correction approaches do exist, but these usually entail a significant loss in measured

events (Bloomfield et al. 2003), while a list-mode based approach is able to use all measured events which have corresponding motion information (Kyme et al. 2008). Therefore it was necessary to develop a list-mode technique which models the resolution in the projection domain, and does so for each individual event before it is motion corrected. For this application, it is computationally impractical to use a pre-calculated system matrix. Likewise, motion correction built into the reconstruction procedure is not generally amenable to spatially variant resolution modelling techniques operating in image space.

Similar techniques have been employed before in various ways to model the system matrix (Huesman et al. 2000; Moehrs et al. 2008; Chen et al. 2007; Bickell et al. 2011; Gonzalez et al. 2011; Jin et al. 2013; Gillam et al. 2013; Autret et al. 2013). Moehrs et al. (2008) used multiple integrations of lines of response associated with each detecting pair to determine the entire system matrix and use it within a sinogram-based MLEM reconstruction; Chen et al. (2007) used a multi-ray approach based on Monte Carlo techniques to construct a sensitivity image, and used this sensitivity image during simulated data reconstructions; Gillam et al. (2013) use a multi-ray technique to model the system matrix during MLEM reconstruction for an axial PET system, however they report that, to observe an improvement in resolution recovery, the method can be computationally expensive.

The approach which is presented in the current work models the system matrix on-the-fly without the need to perform a lengthy pre-calculation or storage of the system matrix, it uses very few and very simple point source measurements to fit one parameter, a multi-ray approach is approximated while only using each list-mode event once per iteration, and it produces a significantly enhanced resolution recovery for off-centre phantoms, with very similar noise levels to standard resolution modelling techniques. It is shown that, for our implementation, the MLEM algorithm may produce artefacts due to mathematical inconsistencies introduced when using an accelerated form of the list-mode based implementation. Therefore the use of the image space reconstruction algorithm (ISRA) (Daube-Witherspoon et al. 1986) is recommended and demonstrated to avoid these mathematical inconsistencies.

5.2 Theory

The physical processes which contribute to a degradation of image resolution are: positron range, photon acollinearity, and the detector response function which incorporates the finite crystal stopping power, inter-crystal scattering of the photon, and imperfect scintillation light propagation through the light-guide to the photomultiplier tube (PMT) (i.e. the block effect). By analytically modelling these physical factors, suitable PDFs can be derived to describe the effect of each factor on the photon detection.

Each list mode event identifies a pair of photons detected by a particular detector pair (DP). The line which connects a predefined point on one detector to a similar point on the other at a predefined depth of interaction (DOI) along the centreline through the detectors is referred to as the line of response (LOR). This LOR is typically used in reconstructions without resolution modelling. The endpoints of the LOR can be redistributed according to the derived PDFs describing the physical factors affecting the resolution, thus creating one of infinitely many possible redistributed LORs (rLORs) associated with that DP. By repeating this redistribution many times for a single event, thus creating many rLORs, the true system matrix row for that DP can be sufficiently sampled. These redistributions can be performed during the reconstruction, thereby avoiding the need to precalculate and store the system matrix.

Since the scanner under consideration is the microPET Focus220 where the axial extent is much less than the scanner diameter, in the following sections the axial and transaxial components of the distributions are assumed to be separable. This is approximately true for all DPs except those which are very oblique, but these appear in the list-mode stream only rarely.

5.2.1 Photon acollinearity

If the annihilation location of the electron-positron pair were known exactly then either endpoint of the measured LOR could be shifted such that the resulting rLOR passes through the annihilation location. Since the annihilation location is not known, but rather the distribution of photon acollinearity angles, we can redistribute each endpoint of an LOR individually (while keeping the other fixed) many times according to this distribution to statistically represent the possible annihilation locations.

The distribution of the angular deviation of the photon pair acollinearity was measured by Colombino et al. (1965) and Trumpy (1960), and described analytically as a sum of two Gaussians by Shibuya et al. (2007). In (Colombino et al. 1965) and (Trumpy 1960) the line integral over the axial component of the acollinearity angle was measured, i.e.

$$Q(\phi_t) = C \int_{-\infty}^{\infty} \left(\frac{A_1}{\sqrt{2\pi}\sigma_1} e^{-\frac{\phi(\phi_t,\phi_z)^2}{2\sigma_1^2}} + \frac{1-A_1}{\sqrt{2\pi}\sigma_2} e^{-\frac{\phi(\phi_t,\phi_z)^2}{2\sigma_2^2}} \right) d\phi_z, \tag{5.1}$$

where the fit parameters are $A_1 = 0.791$, $\sigma_1 = 0.242°$, $\sigma_2 = 0.0695°$, C is a normalisation constant, and ϕ_t and ϕ_z are the transaxial and axial components of ϕ, respectively. Since ϕ is a small angle, it can be approximated by $\phi^2 = \phi_t^2 + \phi_z^2$. In our work we require the distribution at each angle of ϕ,

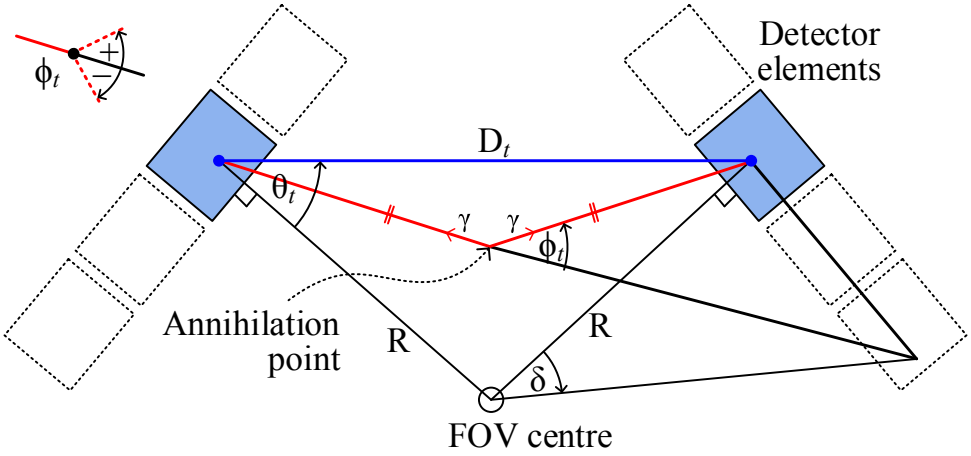

(a) The transaxial angle ϕ_t yields an angular shift δ.

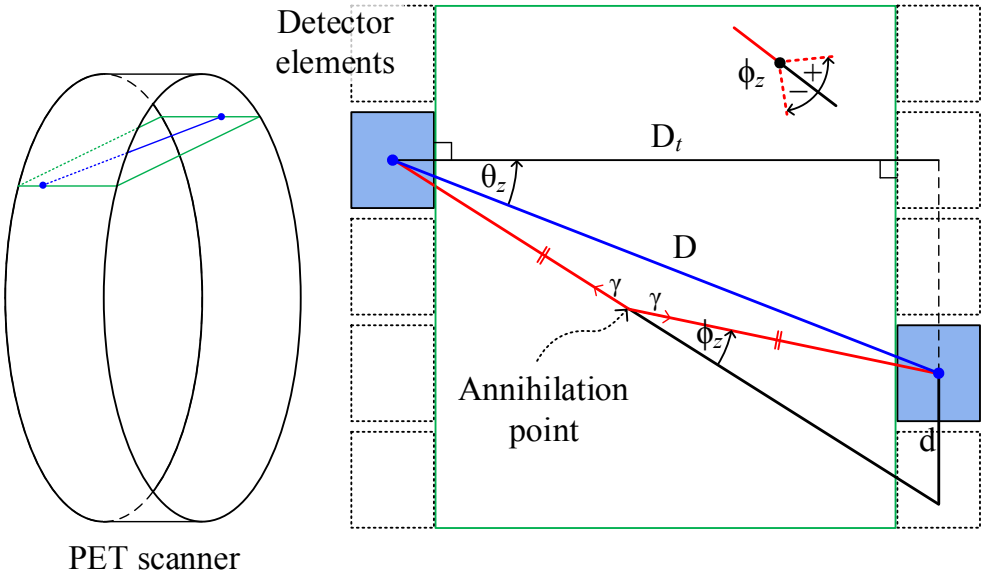

(b) The axial angle ϕ_z yields an spatial shift d.

Figure 5.1: A diagram showing how an angle of acollinearity translates to a shift of one of the LOR endpoints. The flight path of the two photons is shown in red while the measured LOR is shown in blue. Only the photon acollinearity is being considered here, therefore the photon flight paths are assumed to terminate at the LOR endpoints. The detector response function is handled independently. The diagram is not to scale.

i.e. only the integrand in (5.1), hence this integrand was used to model the acollinearity distribution.

An LOR which makes an angle of (θ_t, θ_z) with the normal to the detector surface in the transaxial and axial directions, respectively, can be redistributed by choosing a ϕ_t and ϕ_z according to the distribution given by the integrand of

(5.1), as shown in figure 5.1. As a simplification we assume that the annihilation occurred midway between the detector surfaces. In the transaxial case, as shown in figure 5.1a, by shifting one endpoint of the LOR by a small angle δ it can be suitably redistributed. This shift is given by

$$\delta = \arctan\left(\frac{D_t \sin\frac{\phi_t}{2}}{R\cos\left(\theta_t + \frac{\phi_t}{2}\right)}\right), \tag{5.2}$$

where R is the effective scanner radius taking the DOI into account, and D_t is transaxial distance between the LOR endpoints. By using a small angle approximation for ϕ_t we arrive at

$$\delta \simeq \arctan\phi_t \simeq \phi_t. \tag{5.3}$$

Similarly, in the axial direction, the spatial shift d along the detecting surface of an LOR endpoint (see figure 5.1b) is given by

$$d = \frac{D\sin\frac{\phi_z}{2}}{\cos\left(\theta_z + \frac{\phi_z}{2}\right)}, \tag{5.4}$$

where θ_z is the angle between the LOR and the normal to the detecting surface within the plane parallel to the axial direction, and D is the distance between the LOR endpoints. Again making a small angle approximation, equation (5.4) simplifies to

$$d \simeq \frac{D^2\phi_z}{2D_t}. \tag{5.5}$$

The rLOR is formed by redistributing one endpoint of the LOR, and selecting which endpoint at random. By repeating this procedure many times with different values of (ϕ_t, ϕ_z) for the same LOR, and backprojecting, the distribution of possible annihilation locations which could have resulted in that list-mode event being measured is approximated.

Note that we are ignoring all other effects here, and we are therefore assuming that the point of scintillation is known exactly, there is no positron range, and no block effect. These other effects are handled separately. Therefore, as shown in figure 5.1, the photon flight paths are assumed to terminate at the LOR endpoints.

The above approach can be validated by comparing it to a theoretical distribution of the annihilation locations. Such a theoretical distribution can be determined for a given DP by calculating the probability that an annihilation in a particular voxel could have caused this DP to measure an event, resulting in an image-based PDF for the probability of a detection for each annihilation location. The comparison between the backprojection of the rLORs and the

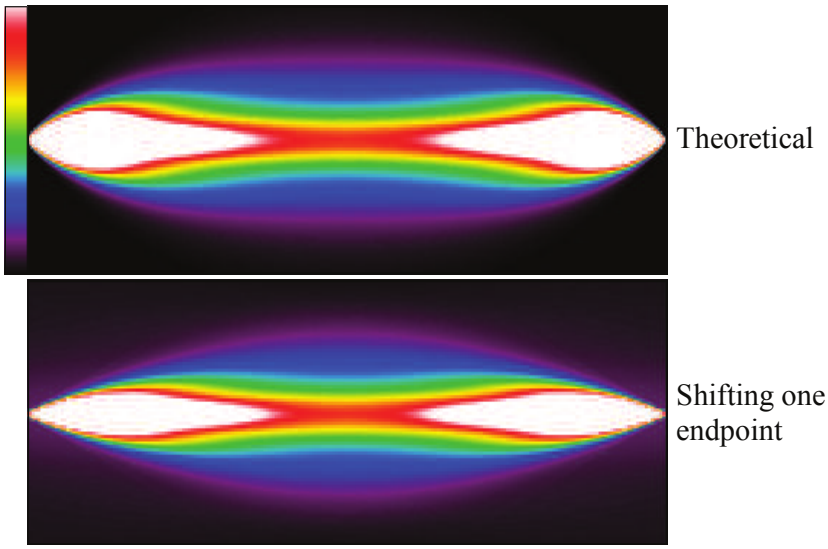

Figure 5.2: Shown in the top frame is a 2D cross-section of the theoretical distribution of the possible annihilation location for a given LOR as a result of photon acollinearity. The resultant distribution using the proposed procedure, i.e. shifting each LOR endpoint individually many times, is shown in the lower frame. The profiles of the two distributions at the point midway between the DP match. The vertical axis has been greatly exaggerated: actual spatial extents are 272 mm × 1.5 mm. Note that the values become very large at locations close to the LOR endpoints, therefore the colour table has been thresholded to 5% of the values near to the LOR endpoints in the theoretical distribution.

theoretical distributions is shown in figure 5.2. The central profile (midway between the DP) of the distribution from the rLORs matches that of the theoretical distribution. In the regions close to the endpoints the distribution is narrower than the theoretical prediction, which is due to the approximation that the annihilation event occurred on the line midway between the two detector surfaces. However, the distribution provides a reasonable approximation to the theoretical prediction.

5.2.2 Detector response function

The probability distribution of a photon being absorbed by one element of a DP when its trajectory is at a perpendicular distance, s, within the tube connecting the DP (see figure 5.3), can be approximated by

$$P_{\theta_t,\theta_z}(s) = \left(1 - e^{-\mu_c y(s)}\right) e^{-\mu_c h(s) - \mu_g g(s)}, \tag{5.6}$$

where $h(s)$ is the distance traversed in the neighbouring crystals, $y(s)$ is the total potential distance traversed in the crystal under consideration, $g(s)$ is

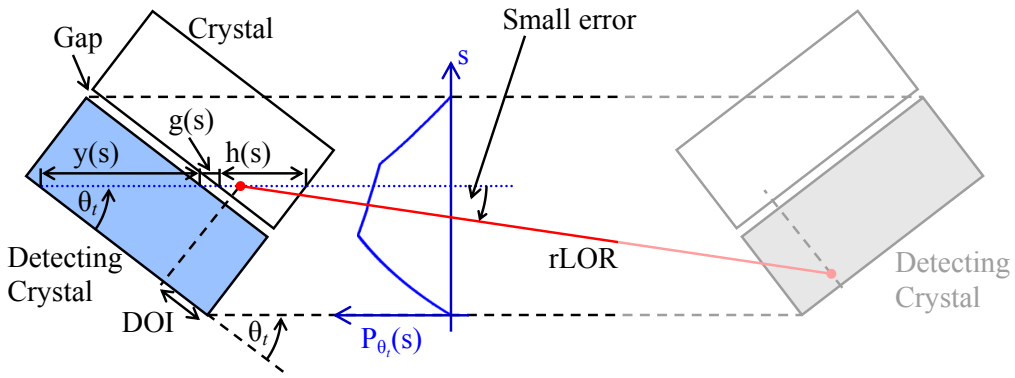

Figure 5.3: The detector response function, $P_{\theta_t}(s)$, gives the probability that a photon with incident angle θ_t on the crystal surface will be detected at a distance s along the line perpendicular to the LOR. Each LOR endpoint is handled independently. This diagram is for the transaxial case; the axial case is the same except that the crystal surfaces are parallel.

the distance traversed through the gaps between the crystals, and μ_c and μ_g are the attenuation coefficients of the crystals and the material filling the gaps between the crystals, respectively, (Lecomte et al. 1984; Liang 1994; Strul et al. 2003). Equation (5.6) holds in both the transaxial and axial directions, and these two cases are assumed to be separable. The flight path of the photon is assumed to be parallel to the LOR. While this greatly simplifies the calculation of $y(s)$, $h(s)$ and $g(s)$, a small error is introduced since the resultant rLOR need not be parallel to the LOR (as shown in figure 5.3), but this error is negligible since the width of $P_{\theta_t}(s)$ is very small in comparison to the distance between the two detecting crystals.

In the transaxial direction, once a shift, s_t, has been randomly selected from the distribution in (5.6), the angular shift, δ', to be applied to the LOR endpoint under consideration (similar to δ in figure 5.1a) is given by

$$\delta' = \arctan \frac{s_t}{R \cos \theta_t}, \tag{5.7}$$

where, as before, R is the effective scanner radius taking the DOI into account. In the axial direction the spatial shift, d', along the detecting surface for a given shift, s_z, is given by

$$d' = \frac{s_z}{\cos \theta_z}. \tag{5.8}$$

5.2.3 The block effect

For the scanner under consideration in this work, namely the Siemens microPET Focus220, the detecting elements are arranged in blocks of 12 crystals in a 42-

sided polygon. This arrangement of the blocks is accounted for in the detector response function. Each detector block is attached to 4 photomultiplier tubes (PMTs). The so-called "block effect" contributes to resolution loss due to imperfect scintillation light propagation through the light-guide to the PMTs (Moses et al. 1993; Tomic et al. 2005). This effect was modelled as suggested by (Brzeziński et al. 2014) by allowing an LOR endpoint to be assigned to a neighbouring detecting element within the same block with a certain probability. This probability was determined empirically and is discussed in section 5.6.1.

5.2.4 Positron Range

The 2D projection of the positron range distribution can be modelled by

$$V(\rho) = Ae^{-\rho/B} + (1 - A)e^{-\rho/C}, \tag{5.9}$$

where ρ is the projected radial distance from the emission point and, for ^{18}F in water, $A = 0.851$, $B = 0.054$ mm and $C = 0.254$ mm, which were determined experimentally (Derenzo 1979; Derenzo 1986). For all of our studies, this isotope was used. A sinogram was constructed where each 2D projection was identical and given by equation (5.9) (since the positron range is isotropic). This sinogram was then reconstructed using a filtered backprojection to determine the 3D positron range distribution. The resulting 3D profile was sampled with a pixel size of 20 μm. A single hot pixel of the reconstruction pixel size was placed in a cold background and supersampled to match the pixel size of the positron range profile, by which it was then convolved. The resulting image was rebinned to the reconstruction pixel size to produce the final blurring kernel. This approach assumes that the radioactivity is uniformly distributed inside each pixel. The positron range was then incorporated into the resolution modelling by convolving the image by this blurring kernel before each projection and after each backprojection which used Redistribution.

5.3 Implementation

The endpoints of each recorded LOR are independently redistributed firstly according to the block effect, then the detector response function, and finally the acollinearity distribution, in both the transaxial and axial directions. The new rLOR endpoints after handling each effect are used for the subsequent effect, thereby producing a superposition of the various factors. These rLORs are then used in the reconstruction. During the reconstruction an image-space convolution is applied to model the positron range.

The system matrix can be denoted by a_{ij}, where i is the LOR index and j is the image voxel index. Let Ψ^i denote the infinite set of all possible rLORs

associated with LOR i, and let $\psi \in \Psi^i$ be a random sample from the set of Ψ^i. Then the system matrix elements can be written as

$$s_i a_{ij} = s_i \lim_{R\to\infty} \frac{1}{R} \sum_{r}^{R} g^i_{\psi_r j} \simeq \frac{s_i}{R} \sum_{r}^{R} g^i_{\psi_r j}, \tag{5.10}$$

where $g^i_{\psi_r j}$ is the contribution of the rLOR ψ_r to the voxel j, and s_i is the combined normalisation coefficient (as determined during the system calibration) and the attenuation coefficient for LOR i. The infinite summation can be truncated to R terms to be computationally feasible. Each system matrix element, $g^i_{\psi_r j}$, is calculated using a ray-tracing algorithm.

The next two sections discuss how this system matrix was incorporated into two reconstruction algorithms. In the derivations and all experiments the additive contribution due to randoms and scatter was ignored.

5.3.1 List-mode MLEM with the Redistribution technique

The standard MLEM formulation, when applied to list-mode data (Parra et al. 1998; Reader et al. 1998), is

$$\lambda_j^{n+1} = \frac{\lambda_j^n}{\sum_i^I s_i a_{ij}} \sum_m^M a_{i_m j} \frac{1}{\sum_k^J a_{i_m k} \lambda_k^n} \tag{5.11}$$

$$= \frac{\lambda_j^n}{\sum_i^I s_i a_{ij}} \sum_i^I \sum_\ell^{y_i} a_{ij} \frac{1}{\sum_k^J a_{ik} \lambda_k^n}, \tag{5.12}$$

where λ_j^n is the value of voxel j of the current reconstruction at iteration n, J is the number of voxels in the image, M is the number of measured events, the index i_m is the LOR associated with event m, I is the total number of possible LORs, and y_i is the number of times that LOR i appears in the list-mode data. Such a list-mode formulation allows for event-by-event motion correction (Rahmim et al. 2004b). Subsets can be utilised when implementing this algorithm, in which case it is referred to as the ordered-subsets expectation-maximisation (OSEM) algorithm (Hudson et al. 1994). When we incorporate the redistribution model, (5.10), into (5.12), we arrive at

$$\lambda_j^{n+1} = \frac{\lambda_j^n}{\frac{1}{R}\sum_i^I s_i \sum_r^R g^i_{\psi_r j}} \left(\sum_i^I \sum_\ell^{y_i} \sum_r^R g^i_{\psi'_r j} \frac{1}{\sum_k^J \sum_{r'}^R g^i_{\psi''_{r'} k} \lambda_k^n} \right), \tag{5.13}$$

where ψ'_r and ψ''_r are different for every ℓ to ensure that the modelling in the forward and backprojections are independent of each other. Since each LOR usually appears many times within the list-mode stream, i.e. $y_i > 1$, it is tempting to set $R = 1$ in the factor between the brackets and rely on the repetitions of each LOR to sample the system matrix sufficiently,

$$\lambda_j^{n+1} = \frac{\lambda_j^n}{\frac{1}{R}\sum_i^I s_i \sum_r^R g^i_{\psi_r j}} \left(\sum_i^I \sum_\ell^{y_i} g^i_{\psi'_\ell j} \frac{1}{\sum_k^J g^i_{\psi''_\ell k} \lambda_k^n} \right). \tag{5.14}$$

This ensures that the implementation is computationally feasible since each list-mode event is only redistributed twice per iteration (once for the forward and once for the backprojection). At each iteration a new redistribution of the LORs is used, thereby further increasing the number of redistributed samples per LOR. However, it is immediately obvious that, with the summation over multiple instances of $g^i_{\psi''_\ell k}$ now occurring in the numerator, the system matrix element a_{ik} in the denominator is no longer approximated as defined by (5.10). By absorbing the summation over R into the summation over ℓ, we have essentially replaced a ratio of sums (sums over r and r' in (5.13)) with a sum of ratios (sum over ℓ in (5.14)). This is a very poor approximation which induces artefacts in the reconstruction. Reconstructions of simulated and real data when using the Redistribution technique with a large R and $R = 1$ are shown in figure 5.4. An artefact can be seen around the edge of the phantom which is due to the inaccurate approximation of a_{ik} as discussed above. Such artefacts tend to appear at the junction of high and low activity regions, specifically when rLORs which have very low projection values appear near to rLORs with much higher projection values. This artefact does not appear when R is large.

5.3.2 List-mode ISRA with the Redistribution technique

The structure of the image space reconstruction algorithm (ISRA) (Daube-Witherspoon et al. 1986) is well suited to be used with this Redistribution technique since the forward and backprojection of the LORs both occur in the denominator. ISRA has the following sinogram-based formulation:

$$\lambda_j^{n+1} = \lambda_j^n \frac{\sum_i^I s_i a'_{ij} y_i}{\sum_i^I s_i^2 a'_{ij} \sum_k^J a_{ik} \lambda_k^n}, \tag{5.15}$$

where y is the measured sinogram. If the system matrix used for the backprojection is the same as that used for the forward projection, i.e. $a'_{ij} = a_{ij}$, then the

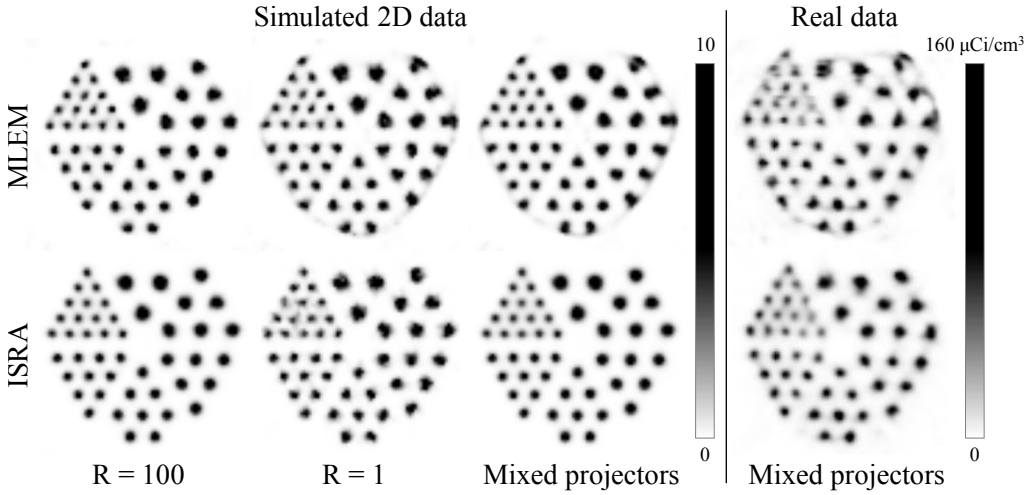

Figure 5.4: Reconstructions of simulated 2D data with noise using 200 iterations and no subsets, and real data using 30 iterations and 9 subsets, for MLEM and ISRA. These data sets were obtained as described in sections 5.5.2 and 5.5.3, respectively. To approximate the effect of scatter and randoms, a constant projection value for all possible LORs was added to the simulated data with total projection counts at 10% of those of the phantom; these were not corrected for in the reconstruction. In the third and fourth column the mixed projectors were used with $R = 1$. In the MLEM reconstructions with $R = 1$ (which includes the "Mixed projectors") artefacts can be observed along the edge of the phantom, while the corresponding ISRA reconstructions are artefact free.

algorithm is a non-negative unweighted least squares algorithm (Titterington 1987). In (Reader et al. 2011) Reader *et al* discuss a generalised weighted least squares version of ISRA.

The formulation in (5.15) was adapted to be list-mode based. This was achieved by forward and backprojecting along all possible LORs in the denominator, which is equivalent to the sinogram-based approach except that no LORs were combined through mashing and spanning. The list-mode formulation can be written as

$$\lambda_j^{n+1} = \lambda_j^n \frac{\sum_m^M s_{i_m} a_{i_m j}}{\sum_i^I s_i^2 a_{ij} \sum_k^J a_{ik} \lambda_k^n}, \tag{5.16}$$

using the same definitions as in (5.11). Incorporating the redistribution model,

(5.10), into (5.16) we obtain

$$\lambda_j^{n+1} = \lambda_j^n \frac{\sum_m^M s_{i_m} \sum_r^R g_{\psi_r j}^{i_m}}{\frac{1}{R}\sum_i^I s_i^2 \sum_r^R g_{\psi'_r j}^i \sum_k^J \sum_{r'}^R g_{\psi''_{r'} k}^i \lambda_k^n}. \tag{5.17}$$

To reduce the computational burden we can again set $R = 1$. In doing so we note that we now avoid the problem of approximating a ratio of sums with a sum of ratios, as was the case for MLEM. This is due to the fact that both the forward and backprojection of the current activity image estimate occur in the denominator. As can be seen in figure 5.4, ISRA does not produce any reconstruction artefacts when $R = 1$. As before, at each iteration a new redistribution is performed, thereby increasing the number of samples of the distributions.

5.3.3 Noise reduction using mixed projectors

To ensure that the implementation of the technique is computationally feasible, it is preferable to use $R = 1$. Therefore it is necessary to use ISRA instead of MLEM. However, as can be seen in figure 5.4, a significant amount of noise is introduced into the reconstructions when $R = 1$ due to the random nature of the Redistribution technique. In the standard image-based resolution modelling technique (Reader et al. 2003), a smoothing operator is applied to the image before forward projection and after backprojection. We explored replacing the redistribution in the backprojection by a similar smoothing operator which matched the PSF in the FOV centre. By performing this smoothing operation the noise introduced by the Redistribution technique is suppressed while still maintaining the accurate model for the resolution during the forward projection.

Other authors have successfully applied unmatched projectors, for example (Zeng et al. 2000). We have found empirically that the proposed algorithm converges, but have not yet been able to definitively prove it.

Using these projectors, the MLEM algorithm can then be formulated as

$$\lambda_j^{n+1} = \frac{\lambda_j^n}{\sum_\xi^\Xi G_{j\xi} \sum_i^I s_i g_{0\xi}^i} \left(\sum_\xi^\Xi G_{j\xi} \sum_i^I \sum_\ell^{y_i} g_{0\xi}^i \times \frac{1}{\frac{1}{R}\sum_k^J \sum_r^R g_{\psi''_r k}^i \lambda_k^n} \right), \tag{5.18}$$

where $g_{0\xi}^i$ is the unredistributed LOR i and G is a Gaussian convolution kernel containing Ξ elements per voxel. For the microPET Focus220 the FWHM of

Table 5.1: Noise levels used for the 2D simulations.

Noise level	High	Medium	Low
Total counts ($\times 10^6$)	1.12	3.36	6.73
Mean of non-zero counts	84.0	263.4	523.5

this Gaussian kernel is 1.3 mm in all 3 directions (Tai et al. 2005). For ISRA we obtain the following implementation

$$\lambda_j^{n+1} = \lambda_j^n \frac{\sum_{\xi}^{\Xi} G_{j\xi} \sum_{m}^{M} s_{i_m} g_{0\xi}^{i_m}}{\frac{1}{R} \sum_{\xi}^{\Xi} G_{j\xi} \sum_{i}^{I} s_i^2 g_{0\xi}^{i} \sum_{k}^{J} \sum_{r}^{R} g_{\psi_r k}^{i} \lambda_k^n} \,. \tag{5.19}$$

The results of this implementation with $R = 1$ are shown in figure 5.4, labelled as "Mixed projectors". For both MLEM and ISRA the noise is greatly reduced, however, for MLEM, the artefact is still present. Hence, in this work we made use of ISRA with $R = 1$ and the mixed projectors.

5.4 Comparing MLEM and ISRA

To further justify the use of ISRA instead of MLEM, a short comparison of the two algorithms was performed. In MLEM the noise is modelled as a Poisson distribution, which is not true for ISRA, and constitutes a significant advantage of MLEM over ISRA. Reader *et al* compared the performance of MLEM and ISRA in (Reader et al. 2011) for a sinogram-based implementation. We conduct a similar investigation here and also include a list-mode implementation, which is of interest in the current context. Two dimensional simulations were conducted for 100 noise realisations at three noise levels, and the bias and standard deviation of OSEM and ordered subsets (OS) ISRA reconstructions were compared. Since it is not computationally feasible to use the Redistribution technique with a large R for MLEM, and to avoid confounding factors by using the Redistribution technique, for both algorithms the resolution was modelled using the standard Gaussian convolution in image space. The properties of the three noise levels are summarised in table 5.1.

The absolute difference bias and standard deviation were calculated as

follows:

$$b^k = \frac{1}{P}\sum_j^P \left|\bar{\lambda}_j^k - t_j\right|, \tag{5.20}$$

$$\sigma^k = \sqrt{\frac{1}{NP-1}\sum_j^P\sum_n^N \left(\lambda_{jn}^k - \bar{\lambda}_j^k\right)^2}, \tag{5.21}$$

where $\bar{\lambda}_j^k$ is the j^{th} pixel of the average reconstruction over all noise realisations at iteration k, P is the number of pixels in the region-of-interest (ROI), t_j is the ground truth image, and λ_{jn}^k is the reconstruction of the noisy data at iteration k for noise realisation n, of which there are N. MLEM will rapidly reconstruct the support of the phantom in a cold background, while ISRA, being an unweighted least squares optimiser, will do so much more slowly. As a result, the bias of MLEM was observed to be significantly lower than that of ISRA at the boundary of the reconstructed object. Assuming that for most applications the exact reconstruction of the boundary is not as important as the intensities inside the support of the object, we chose to analyse the bias and standard deviation in a ROI which was obtained by eroding the object support by 2 pixels. Bias and standard deviation images were calculated using

$$B_j^k = \bar{\lambda}_j^k - t_j, \tag{5.22}$$

$$S_j^k = \sqrt{\frac{1}{N-1}\sum_n^N \left(\lambda_{jn}^k - \bar{\lambda}_j^k\right)^2}. \tag{5.23}$$

5.4.1 Sinogram implementation with subsets

As can be seen in figure 5.5, the standard deviation and bias of the sinogram-based OSEM and OS-ISRA are similar for all iterations. See also the bias and standard deviation images in figure 5.6 where the efficacy of OSEM at reconstructing the object support can be seen in comparison to OS-ISRA, and an example reconstruction in figure 5.8.

5.4.2 List-mode implementation with subsets

In the list-mode case, if subsets are to be used to accelerate the reconstructions, certain approximations need to be made for both OSEM and OS-ISRA. In OSEM the backprojection of the sensitivity sinogram is over all possible LORs. In a sinogram-based implementation the backprojection can be computed independently for each subset to match the projections of the measured data (Hudson et al. 1994), but in a list-mode implementation this is not easy since the events in the list-mode stream are in no particular order. In OS-ISRA

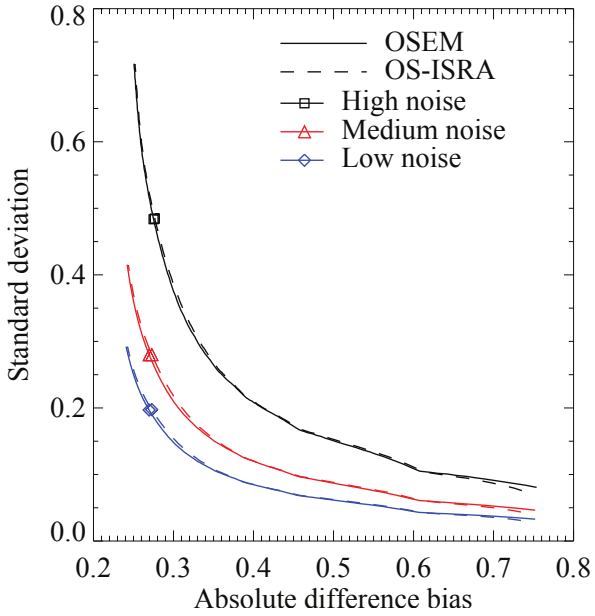

Figure 5.5: A bias versus standard deviation plot for a sinogram implementation of OSEM and OS-ISRA for 3 noise levels and 100 noise. Reconstructions were performed using 25 iterations and 21 subsets. In these plots the iterations are increasing with increasing standard deviation. The small symbols indicate where the end of iteration 12 lies.

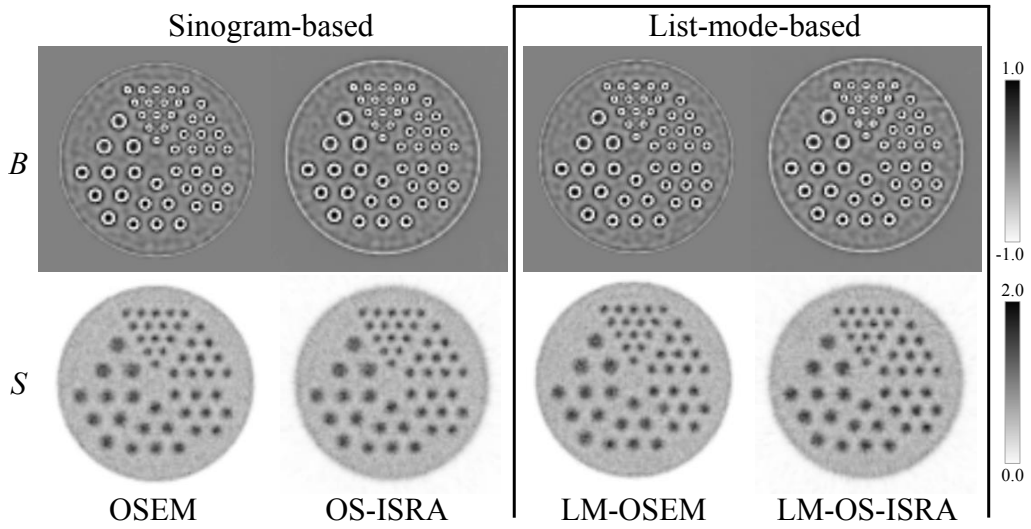

Figure 5.6: The bias and standard deviation images at the last iteration for the high noise case.

(Kontaxakis et al. 1998), a similar argument applies: the measured data, which are backprojected in the numerator of (5.16), can not easily be divided into subsets to match the projections in the denominator. For this reason, in OSEM the backprojection of the entire sensitivity sinogram is simply scaled by the number of subsets, as is the backprojection of all the measured data in OS-ISRA. It is then assumed that each subset of the events used in the projections will be sufficiently statistically representative of the entire set to match the scaled backprojections. After each iteration the events are randomly shuffled to ensure that the subsets are never identical from one iteration to the next.

Figure 5.7 shows the standard deviation versus bias results for the list-mode reconstructions, with the corresponding images in figure 5.6 and an example reconstruction in figure 5.8. While OS-ISRA exhibits a higher standard deviation than OSEM in earlier iterations, it converges to a result similar to that of OSEM. For matched biases though OS-ISRA does have a higher standard deviation.

5.4.3 Discussion

In (Reader et al. 2011) Reader *et al* found that sinogram-based ISRA and MLEM converge to similar quantitative values, as we conclude here. Their results on the mean absolute error, which is similar to our definition of the absolute bias (5.20), demonstrate that, while ISRA converges more slowly, it reaches quantitative values similar to that of MLEM within the support of the object.

In the sinogram case OSEM and OS-ISRA produce similar bias-standard deviation curves. This was also verified in the list-mode case when no subsets are used (results not presented here). However, when subsets are introduced the standard deviation of list-mode OS-ISRA increases. In the denominator of the list-mode ISRA equation (5.16), each LOR which passes through the reconstruction image space is used once per iteration. In list-mode MLEM (5.11), however, all the measured events are used in each iteration. In the 2D case considered here, for the microPET Focus220, there are several million measured list-mode events while only 20000 LORs passing through the image space. Therefore OS-ISRA uses far fewer projections per subset than OSEM, leading to a significantly reduced computation time (by a factor of 50 in the high noise case, and more in the others). However, each subset in OS-ISRA may introduce significantly more noise than those in OSEM, leading to an increased standard deviation in the reconstructions, as can be seen in figure 5.7. In the real 3D case the OS-ISRA computation time and noise propagation will be more similar to those of OSEM since the number of possible LORs is then on the same order of magnitude as the number of measured list-mode events; this was not fully investigated though.

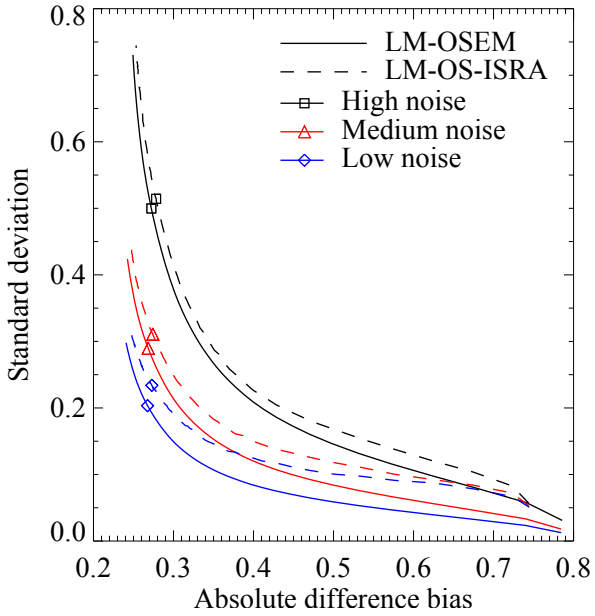

Figure 5.7: A bias versus standard deviation plot for a list-mode implementation of OSEM and OS-ISRA for 3 noise levels and 100 noise realisations. Only the points at the end of each iteration are plotted. Reconstructions were performed using 105 iterations and 5 subsets. The iteration number is increasing with increasing standard deviation, and the small symbols indicate where the end of iteration 52 lies.

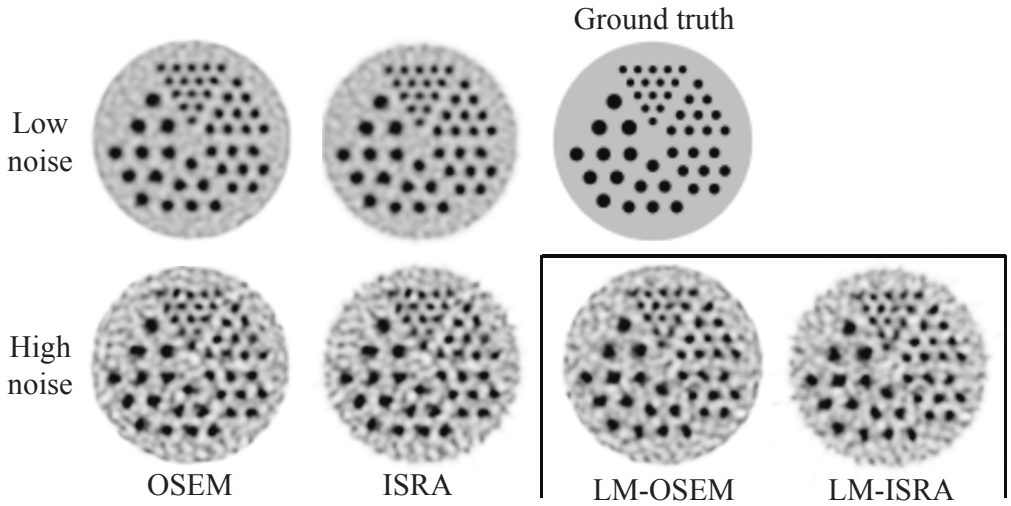

Figure 5.8: On the left are the sinogram-based reconstructions using 21 subsets of the high and low noise data after 12 complete iterations of a single noise realisation. On the lower right are the list-mode reconstruction using 5 subsets after 52 complete iterations of the high noise case. The ground truth is also shown for reference. All images are shown to the same scale.

Nonetheless, we assert that the potential gain in using ISRA with the Redistribution technique to achieve spatially variant resolution modelling (as demonstrated below) may outweigh the noise-performance differences observed between the two algorithms.

5.5 Experiments

For all experiments and simulations the Siemens microPET Focus220 small animal scanner was used and modelled. This scanner has an internal diameter of 258 mm, and a spatial resolution of 1.3 mm at the centre of the FOV. At a radial distance of 60 mm the spatial resolution degrades to $[1.9, 2.1, 3.2]$ mm in the tangential, axial, and radial components respectively (Tai et al. 2005).

5.5.1 Spatially variant resolution response verification

To investigate the spatially variant nature of the Redistribution technique, a point source was measured within the microPET scanner. The point source was a porous microsieve with a diameter of 2.1 mm and was placed inside putty to provide a uniform surrounding material. For each measurement the centre-of-mass position of the point source was determined from a reconstruction of the data, and a point source of the same size was then simulated in that position. The point source was convolved with the positron range kernel described in section 5.2.4. Two forward projection models were used to create simulated sinograms:

A The resolution was modelled by convolving the image with a spatially invariant Gaussian kernel with FWHM = 1.3 mm. The resulting image was then forward projected to sinogram space.

B The resolution was modelled with the proposed technique: a forward projection was performed using the system matrix elements given in equation (5.10) with $R = 500$, and the projection values were binned into a sinogram.

The resulting sinograms were compared to the measured sinogram to determine the accuracy of each model in estimating the PSF.

5.5.2 Simulations

Two 2D phantoms were simulated: a hot-rod phantom of diameter 40 mm and with rods of diameter $1.5 - 3.0$ mm, similar to the one used in our experiments, and a Shepp-Logan phantom. The total activity in the Shepp-Logan phantom was 6 times that in the hot-rod phantom. These were placed 54 mm off-centre of

the scanner FOV and used to simulate list-mode data. A comparison was made of ISRA reconstructions using no resolution modelling, the standard Gaussian convolution model with FWHM = 1.3 mm, and the Redistribution technique. One hundred iterations with no subsets, using a pixel size of 0.4745 mm in both directions, were used for the reconstructions.

For these simulations the so-called "inverse crime" was committed: to model the physics during the generation of the list-mode data the Redistribution technique was used during the forward projection of the ground truth, with $R = 500$ (however, a different seed was used to generate the random numbers used during the reconstruction). A Poisson realisation of the projection values was made to yield the expected count rates; these could then be used to create the list-mode data. The data was randomised and time stamps were assigned to each list-mode event.

5.5.3 Real data

A hot-rod phantom of diameter 40 mm and with rods of diameter $1.5 - 3.0$ mm was scanned in the microPET scanner. The phantom was filled with between $1.0 - 1.5$ mCi of FDG and scanned for 2 minutes in the centre of the scanner, 5 minutes at a radial distance of 35 mm horizontally to the right of the FOV centre, and again for 5 minutes at a radial distance of 54 mm. The data were reconstructed with OS-ISRA using the Redistribution technique, and compared to reconstructions with OSEM using the standard Gaussian convolution technique, as well as a commercial maximum a-posteriori (MAP) OSEM reconstruction algorithm by Siemens. The OS-ISRA and OSEM reconstructions were performed using 20 iterations and 9 subsets, and the MAP-OSEM reconstruction used 2 OSEM iterations and 9 subsets followed by 18 MAP iterations, with a target resolution of 0.5 mm and enforcing uniform resolution. The MAP-OSEM algorithm models the resolution using PSF tables based on point source measurements for this particular scanner. The pixel size of all reconstructions was $[0.4745, 0.4745, 0.796]$ mm.

5.6 Results

5.6.1 Spatially variant resolution response verification

By minimising the difference between the profiles of the measured and simulated sinograms for various point source locations and block effect parameters, the probability parameter for the modelling of the block effect was empirically set. It was determined that an LOR endpoint should be redistributed to a neighbouring detector crystal with a probability of $\frac{N}{64}$, where N is the number of neighbours: 8 for endpoints within the block, 5 for those at the edge of the

block, and 3 for those at a corner. Tomic et al. (2005) found a similarly small probability for a block detector of a different scanner.

Figure 5.9 shows a comparison of the FWHM of each projection index of the simulated sinograms with those of the measured data. To reduce the effect of noise in all sinograms, in the transaxial case the three planes immediately about the maximal plane were summed before calculating the FWHM for each projection. Similarly, in the axial case the three projection values immediately about the maximal value were summed.

For a point source located near the centre of the FOV the FWHMs of the projections are quite constant, as expected. However, for transaxially off-centre point sources the FWHMs of the measured data vary with the projection angle, and this behaviour is accurately modelled by the Redistribution technique. Since the Gaussian convolution is spatially invariant, the FWHMs are not affected by the point source position and it thus underestimates the FWHM of the PSF for angles where the projection of the point source is off-centre.

5.6.2 Simulations

The results from the simulations are shown in figure 5.10. In the case of the hot-rod phantom, since the phantom is off-centre, the Gaussian convolution technique has underestimated the width of the PSF and distorted the rods away from the centre. On the other hand, the Redistribution technique has preserved the circular shape of the rods. A similar effect can be seen at the edge of the Shepp-Logan phantom.

Even though the inverse crime is committed here, these results demonstrate that the method works well under ideal conditions, and also demonstrates the effect of using the stationary Gaussian convolution model on data with a spatially variant PSF.

5.6.3 Real data

The reconstructions of the centred phantom are shown in figure 5.11 with two profiles through the reconstructions shown in figure 5.12. The ground truth image was created and scaled to have the same total activity as the Siemens reconstruction, and the total activities in all reconstructions are equal to within 4%. All three algorithms have produced very similar reconstructions with regards to resolution recovery, as expected for a phantom near the FOV centre.

Figure 5.13 shows the reconstruction of the off-centre phantom at 35 mm from the centre. The total activity of the reconstructions agree to within 3%. The resolution recovery of the Redistribution and Gaussian techniques is superior to the MAP-OSEM reconstruction, as can be seen by comparing the smallest rods. However the Redistribution technique and MAP-OSEM algorithm have produced less rod distortion than the Gaussian technique. From

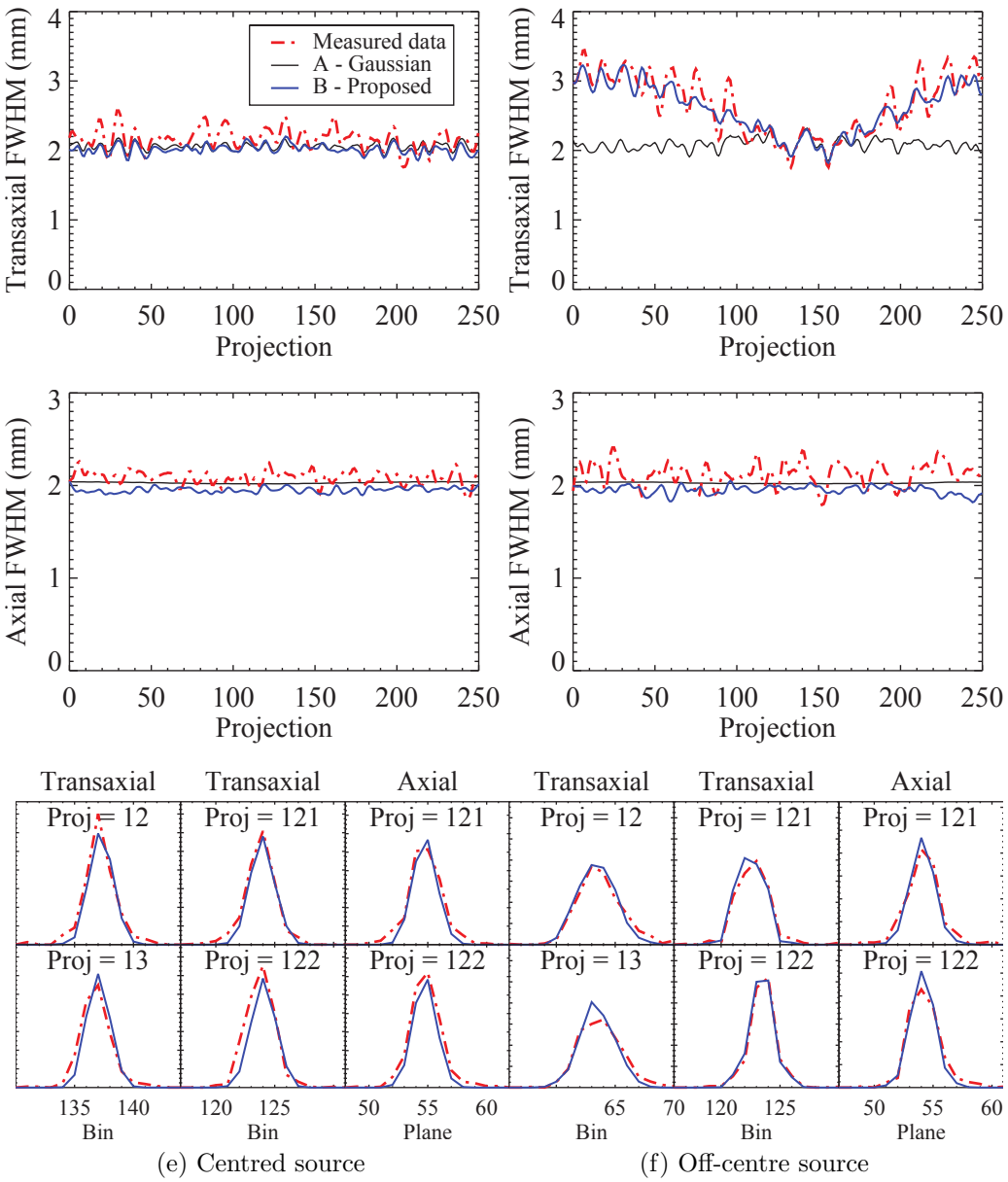

(e) Centred source (f) Off-centre source

Figure 5.9: The FWHMs in the transaxial and axial directions as a function of projection index in the measured sinogram and the sinogram produced when using the models described in section 5.5.1. In the left column the point source was located 16.9 mm transaxially from the centre of the FOV, and in the right column the point source was at a transaxial distance of 65.1 mm; both sources were at an axial distance of 6.0 mm from the FOV centre. The FWHM plots have been smoothed, and the sinograms were not deconvolved by the size of the point source before calculating these FWHMs. The profiles through the measured and the proposed model sinograms are also shown below.

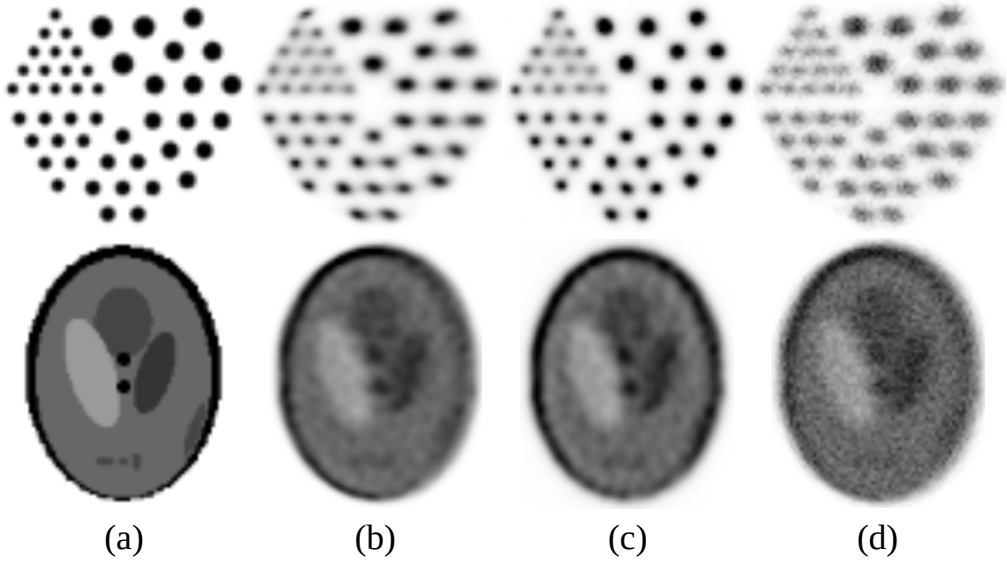

Figure 5.10: Results from 2D simulations using different resolution modelling techniques for two phantoms: (a) the ground truth; (b) using the standard Gaussian convolution model; (c) using the Redistribution technique; (d) no resolution modelling. The phantoms were placed to the right of the centre of the scanner FOV. For each phantom, all images are shown to the same scale.

figure 5.14 it can be seen that, of the three reconstructions, the Redistribution technique has produced the best resolution recovery.

The reconstructions of the second off-centre phantom at 54 mm from the centre are shown in figures 5.15 and two profiles in figures 5.16. Due to limitations in the commercial software, it was not possible to reconstruct this data using the Siemens MAP-OSEM algorithm since the phantom was outside the reconstructable volume. For comparison's sake, the data was reconstructed using OSEM without any resolution modelling. The total activity of the reconstructions are equal to within 1.5%, and the OS-ISRA reconstruction was used to scale the ground truth image. The Redistribution technique has produced a reconstruction with a superior resolution recovery to the Gaussian convolution model, as can be seen in figure 5.16. It has also preserved the circular shape of the rods while the Gaussian model has distorted them away from the FOV centre (i.e. to the right). Both models have produced better resolution recovery than the reconstruction without any resolution modelling, as expected.

5.7 Discussion

The accuracy of the spatially variant nature of the resolution model using the

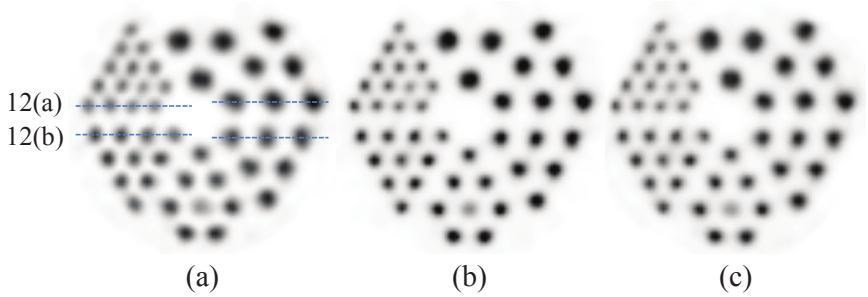

Figure 5.11: Reconstructions of the centred phantom: (a) reconstruction using the standard Siemens software (a MAP-OSEM algorithm); (b) using OS-ISRA and the Redistribution technique; (c) using OSEM and the standard Gaussian convolution model. All images are shown to the same scale. Note that the smallest rod closest to the centre had an air pocket and did not contain any activity during the scan. The ground truth of this phantom is shown in figure 5.10(a).

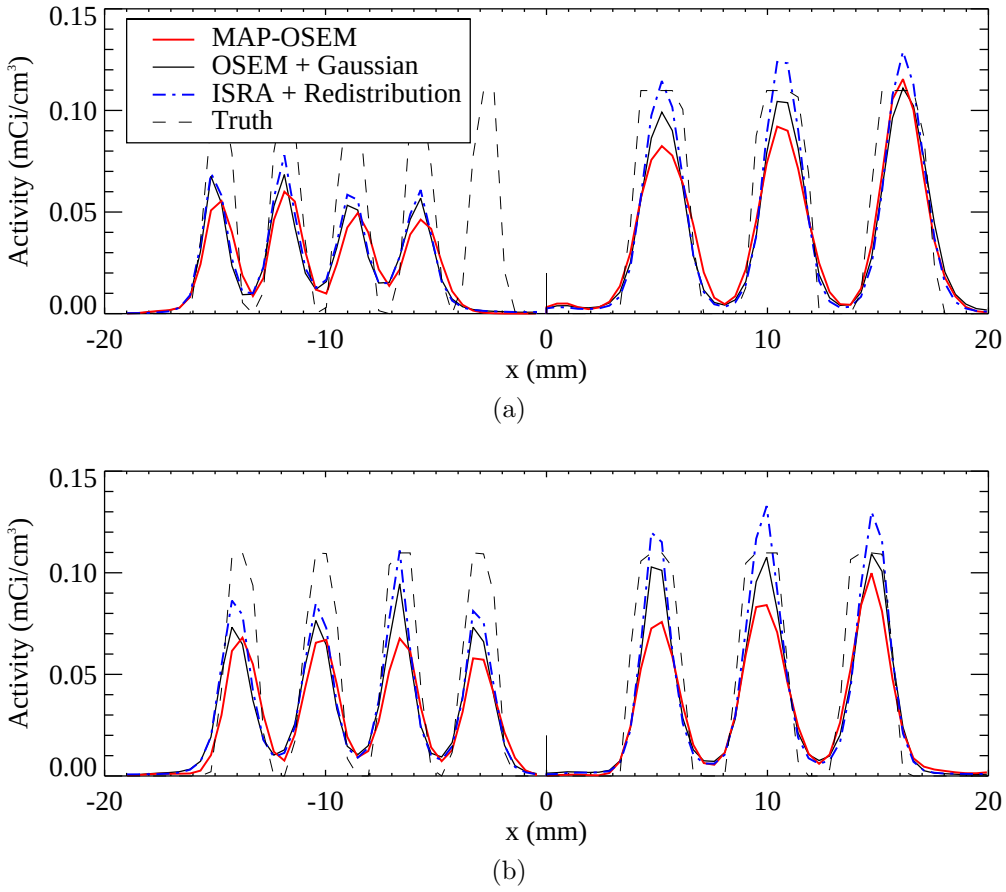

Figure 5.12: Profiles through the reconstructions shown in figure 5.11, as indicated in figure 5.11(a).

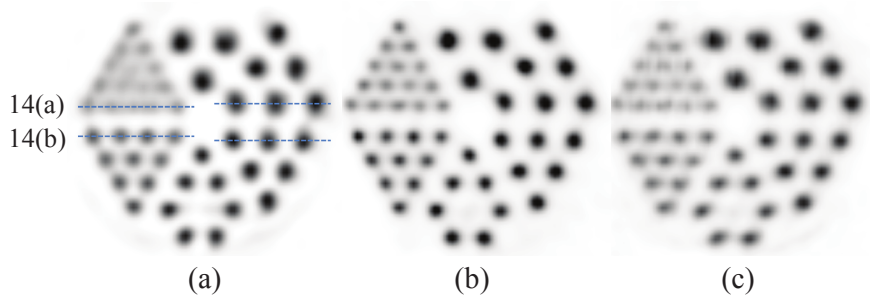

Figure 5.13: Reconstructions of the off-centre phantom (positioned 35 mm to the right of the FOV centre): (a) reconstruction using the standard Siemens software (a MAP-OSEM algorithm); (b) using OS-ISRA and the Redistribution technique; (c) using OSEM and the standard Gaussian convolution model. All images are shown to the same scale. By comparing the smallest rods, one can see that the resolution recovery of (b) and (c) is superior to that of (a).

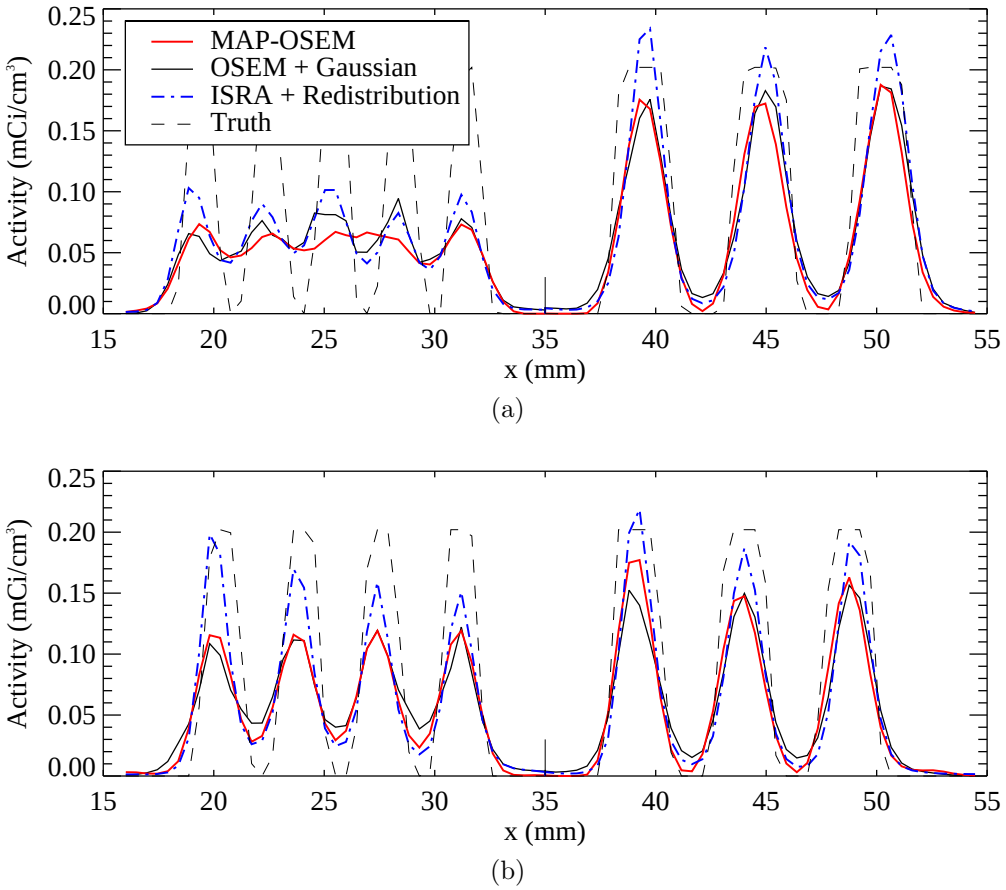

Figure 5.14: Profiles through the reconstructions shown in figure 5.13, as indicated in figure 5.13(a).

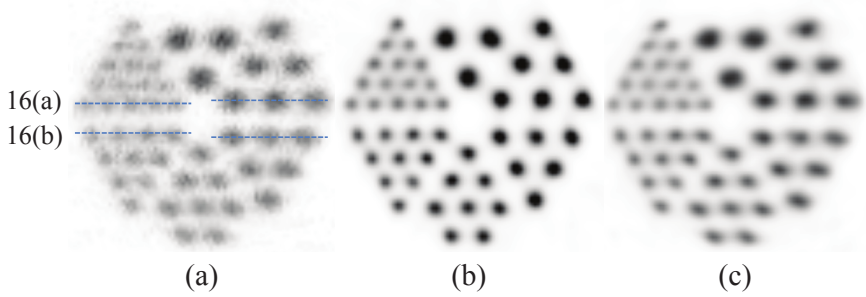

Figure 5.15: Reconstructions of the off-centre phantom (positioned 54 mm to the right of the FOV centre): (a) reconstruction using OSEM without any resolution modelling; (b) using OS-ISRA and the Redistribution technique; (c) using OSEM and the standard Gaussian convolution model. All images are shown to the same scale. Note that the circular shape of the rods has been preserved in (b) but have been distorted away from the FOV centre (i.e. to the right) in (c).

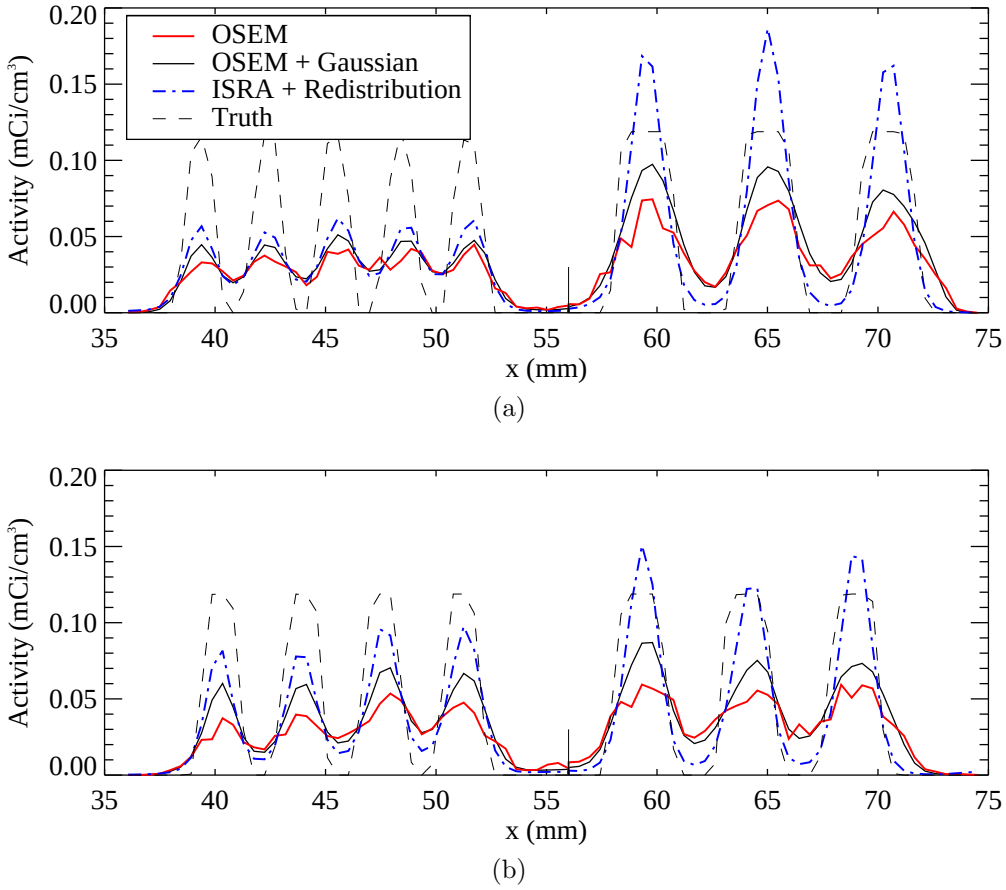

Figure 5.16: Profiles through the reconstructions shown in figure 5.15, as indicated in figure 5.15(a).

Redistribution technique was verified by using it as a forward projection model and comparing it to measured data. The FWHMs of the resultant projections in the sinograms matched those of the measured data, for centred and off-centre locations in the FOV.

Using this result, the Redistribution technique was used as a forward projection model in 2D phantom simulations, and the results demonstrated that, for off-centre phantoms, the Redistribution technique produces reconstructions which preserve the true shape of the phantom, while the spatially invariant Gaussian convolution technique distorts the activity away from the centre.

Reconstructions of real data demonstrated that OS-ISRA with the Redistribution technique, OSEM with the Gaussian convolution technique, and the Siemens MAP-OSEM algorithm all produce very similar results for centred phantoms, which is expected since all algorithms provide a good approximation to the resolution of the system near the centre of the FOV. For off-centre phantoms, however, the Redistribution technique produces superior resolution recovery which matches the ground truth quite well and preserves the shape of the phantom, while the Gaussian convolution technique distorts the phantom away from the FOV centre. This effect becomes more pronounced with increasing radial distance.

The Redistribution technique has caused overshoot to occur on some of the rods, as can be seen in figure 5.16. This is due to the Gibbs effect, which can produce pronounced results in small structures (Nuyts 2014).

The projectors used for the in-house reconstructions were ray-tracing projectors and since the pixel size was usually smaller than the detector cell size, the known artefacts associated with these projectors were observed (De Man et al. 2004), as can be seen in figure 5.15(a). The distance-driven projector is known to solve this issue, however it is not easy to implement for list-mode data. It is interesting to note that both the Gaussian convolution and the Redistribution techniques have removed these artefacts.

Since a list-mode implementation of OSEM and OS-ISRA has been used, a direct comparison of the number of computations per iteration is not straightforward. For OSEM, the number of forward and backprojections in one iteration is exactly the number of measured list-mode events. Whereas in OS-ISRA, the measured data are backprojected once before the reconstruction begins, and then a list of all possible LORs which pass through the reconstruction image space is generated and these LORs are forward and backprojected in each iteration. Therefore, for OSEM, the number of computations per iterations is proportional to the number of measured events, while for OS-ISRA this number depends on the size and location of the image space. As an indication though, for a centred phantom filled with approximately 1 mCi of FDG and scanned for 2 minutes in the microPET Focus220 scanner, approximately 55 million events were recorded, which is approximately the same number of possible LORs which pass through a centred image space of size $[61.0, 61.0, 76.0]$ mm (the

image space used for the reconstructions in figure 5.11). The reconstruction of this data in this image space takes about 35% more time for an OS-ISRA reconstruction with Redistribution than for an OSEM reconstruction with the Gaussian convolution.

For a small animal scanner such as the microPET Focus220, the effect of photon acollinearity on the spatial resolution is very small. Also, for ^{18}F, the effect of the positron range is very small. Nonetheless both these effects were modelled in the presented work for the sake of generality, and to allow for an easy conversion to clinical scanners, and other isotopes, where these effects are more pronounced. The positron range was modelled in a spatially invariant manner; we will adapt this in the future to be more physically realistic.

Since the Redistribution technique models the resolution during the projections, and not in image-space, it is well-suited to be used in conjunction with event-by-event list-mode rigid motion correction. The LORs can be redistributed before being motion corrected, and then used in the reconstruction, thus accurately modelling the spatial variance of the system response. This approach is beyond the scope this report and will be implemented in future work.

5.8 Conclusion

The Redistribution technique, a resolution modelling technique which models the system response on-the-fly during iterative reconstruction, has been presented. The system response is described analytically using PDFs which are sampled to redistribute the endpoints of the LORs used during the reconstruction. By adjusting the endpoints of the LORs in this way, a system matrix is estimated which varies radially, axially and transaxially. We found that the proposed geometric model accurately captures the spatial variance of the system resolution of the microPET Focus220. The only parameter that was tuned based on measurements is the one modelling the "block effect", i.e. the cross-talk between crystals. Once this parameter was determined, the model was found to agree very well with all projections of point sources placed at different positions in the scanner.

It was demonstrated that the formulation of the MLEM algorithm is not well-suited to use the Redistribution technique in a computationally feasible implementation, and so the ISRA algorithm was used as an alternative.

A comparison of phantom reconstructions using standard Siemens software (a MAP-OSEM algorithm), the OSEM algorithm with and without resolution modelling using a stationary Gaussian convolution, and the OS-ISRA algorithm with the Redistribution technique demonstrated that all the algorithms produce very similar reconstructions for phantoms near the centre of the scanner FOV, as expected, while the presented technique produces reconstructions with superior

resolution recovery for off-centre phantoms. The Redistribution technique accurately preserves the shape of the imaged object and does not distort the reconstructions away from the centre, as a spatially invariant technique does.

Chapter 6

Joint Activity and Attenuation Reconstruction of List-mode TOF-PET data

Published as:

A. Rezaei, M. G. Bickell, R. Fulton, and J. Nuyts (2015). "Joint Activity and Attenuation Reconstruction of Listmode TOF-PET data". In: *IEEE Nuclear Science Symposium and Medical Imaging Conference* 1.2, pp. 2–3

Abstract

Different methods have been proposed for simultaneous reconstruction of activity and attenuation from TOF-PET sinogram data. In this work we present the list-mode maximum likelihood activity and attenuation reconstruction (MLAA) and the list-mode maximum likelihood attenuation correction factors (MLACF) algorithms building on their established sinogram implementation. Our list-mode MLAA differs from a recently proposed list-mode algorithm by incorporating the maximum likelihood transmission reconstruction (MLTR) algorithm in MLAA. The list-mode MLTR algorithm has some similarity to the list-mode image based reconstruction algorithm (ISRA), since it reconstructs the image from the backprojection of the acquired data. We investigate the reconstruction results on a scan of the NEMA IEC body phantom.

6.1 Introduction

It has been shown that the information in time-of-flight (TOF) positron emission tomography (PET) emission data is rich enough to solve the long-standing problem of activity and attenuation cross-talk (Defrise et al. 2012; Rezaei et al. 2012). The majority of algorithms that have been developed for joint

reconstruction of activity and attenuation require an initial histogramming of the list-mode data into a sinogram. In an attempt to directly use the list-mode data in the joint reconstruction framework, Mollet et al. (Mollet et al. 2014) proposed a method that combines the list-mode TOF-MLEM reconstruction of the activity image (Parra et al. 1998; Rahmim et al. 2004b) with an MLTR-like algorithm for the reconstruction of the attenuation image.

In the same spirit, we extend the previously developed sinogram implementation of the MLAA algorithm to handle list-mode data. In reconstruction from transmission data which are subject to Poisson noise, the backprojection of the data is a sufficient statistic. Because of this, MLTR reconstructs the image from the backprojection of the transmission data. This makes it similar to ISRA (Daube-Witherspoon et al. 1986), which was developed for emission data and for which a list-mode implementation has been proposed (Bickell et al. 2016). Furthermore, we extend the maximum likelihood attenuation correction factors (MLACF) algorithm to handle list-mode data. We find that although the attenuation correction factors (ACFs) are not computed explicitly, they are corrected for during reconstructions. The results of the list-mode transmission reconstruction algorithm are shown for the NEMA IEC body phantom and then the list-mode joint reconstructions are compared to the sinogram reconstructions of the TOF-PET emission data.

6.2 Methods

The list-mode-MLAA algorithm uses an interleaved updating of the activity/attenuation reconstruction while keeping the attenuation/activity reconstruction fixed. The algorithm can be written as follows:

$$\forall i : a_i^{(n)} = e^{-\sum_j l_{ij}\mu_j^{(n)}} \tag{6.1}$$

$$\forall j : \lambda_j^{(n+1)} = \frac{\lambda_j^{(n)}}{\sum_i c_{ij} a_i^{(n)}} \sum_m c_{i_m j t_m} \frac{1}{\sum_\xi c_{i_m \xi t_m} \lambda_\xi^{(n)}} \tag{6.2}$$

$$\forall i : \bar{y}_i^{(n+1)} = a_i^{(n)} \sum_j c_{ij} \lambda_j^{(n+1)} \tag{6.3}$$

$$\forall j : \mu_j^{(n+1)} = \mu_j^{(n)} - \frac{\sum_m l_{i_m j} - \sum_i l_{ij} \bar{y}_i^{(n+1)}}{\sum_i l_{ij} \bar{y}_i^{(n+1)} \sum_\xi l_{i\xi}} \tag{6.4}$$

where μ and λ are the attenuation and activity reconstructions, the superscript denotes the iteration number, l_{ij} is the intersection length of LOR i and voxel j and a_i is the attenuation correction factor along LOR i. c_{ij} (c_{ijt}) is the sensitivity of voxel j to LOR i (and TOF-bin t), i_m and t_m are the LOR and TOF-bin corresponding to event m, and $\bar{y}_i$ is the expected non-TOF counts

along LOR i. Note that the range of the sums over index i are over all possible LORs whereas the sums over i_m are over all the list mode events.

The algorithm was accelerated using ordered subsets as well as applying multiple attenuation updates for each update of activity. For summations involving the measurements, the events in a subset were chosen by taking every kth event, where k is the number of subsets. For the summation over all possible LORs, a set of r LORs were sub-sampled from the list of all possible LORs, where r is the number of list-mode events in the emission subset. Furthermore, similar to ISRA we took advantage of backprojecting the measured counts once and re-using this backprojection in (6.4) during the iterations.

In contrast to MLAA, the MLACF algorithm uses an interleaved updating of the attenuation correction factors (ACFs) together with the activity reconstruction. When the additive contributions of randoms and/or scatter are ignored, MLACF gives an immediate update of the ACFs (Defrise et al. 2014). The list-mode extension of this algorithm can be written as follows:

$$\forall i_m : p_{i_m}^{(n)} = \sum_{\xi} c_{i_m \xi} \lambda_{\xi}^{(n)} \tag{6.5}$$

$$\forall j : \lambda_j^{(n+1)} = \frac{\lambda_j^{(n)}}{\sum_m c_{i_m j} \frac{1}{p_{i_m}^{(n)}}} \sum_m c_{i_m j t_m} \frac{1}{p_{i_m t_m}^{(n)}} \tag{6.6}$$

where $p_{i_m}^{(n)}$ is the non-TOF projection of the activity reconstruction (and similarly $p_{i_m t_m}$ is the TOF projection at list-mode event (i_m, t_m)). Note that the list-mode MLACF algorithm does not explicitly estimate the ACF values along all measured LORs; however, the effects of the ACFs are corrected for during reconstructions through the estimation of their backprojection commonly referred to as the sensitivity image. Furthermore, the list-mode MLACF reconstruction benefits from using two matched backprojections compared to the list-mode MLEM and MLTR algorithms where the reconstructions involve backprojections of the measured events as well as the backprojections of all possible LORs.

6.3 Experiment Design

The NEMA IEC body phantom was filled with 200 MBq of ^{18}F-FDG, and scanned with the Siemens Biograph mCT for 1 hour. The emission data were acquired 3 hours post-injection. Only a subset of the TOF-PET emission data corresponding to the first 10 minutes were used in the reconstruction. An initial MLEM activity reconstruction with CT-based attenuation correction was obtained and used to produce a blank scan to test the list-mode transmission reconstruction algorithm. Since we wanted to compare the results with the

sinogram reconstructions, the 64-bit list-mode events were mashed with the typical sinogram mashing to give 32-bit list-mode event data. Activity and attenuation reconstructions were then obtained from the 32-bit list-mode data using the list-mode implementations of MLAA and MLACF. The list-mode data were subsequently histogrammed to create the TOF-PET emission sinogram and the list-mode reconstructions were compared to the reconstructions of the sinogram implementation of MLAA and MLACF. The TOF-PET emission sinogram consisted of 400 detectors, 168 angles, a total of 621 planes and 13 TOF-bins of 312 ps resolution. The effective TOF resolution of the system was 580 ps. In both implementations, the additive scatter/randoms contribution was ignored.

6.4 Results

Figure 6.2 shows the list-mode MLTR attenuation reconstructions of the data, when the TOF-MLEM activity reconstruction (shown in figure 6.1) was used as the known activity. The MLTR$^+$ attenuation reconstruction of figure 6.2 was regularized by the relative difference prior (Nuyts et al. 2002) during reconstruction. In our experience, little effort was needed to limit the attenuation build-up in the background region of the image (region with no activity present).

Figures 6.3 and 6.4 show the list-mode and sinogram reconstructions of MLAA and MLACF for the NEMA IEC body phantom, respectively. The total MLEM counts were used to scale the joint activity reconstructions, and as in the case of MLTR, for MLAA no extra measures were taken to limit the attenuation build-up in the background region. Although the activity and attenuation images look cross-talk free, some differences are still observed especially close to edge of the phantom (the region with limited TOF sampling along some LORs). In both (list-mode and sinogram) attenuation reconstructions, some excess attenuation was put outside the support of the activity which is most likely because the scatter/randoms were not corrected for. A visual comparison of reconstructions of 64-bit list-mode data (the results not shown here) revealed a slight improvement in the reconstructions mostly visible at high gradients of the activity reconstruction. A more comprehensive comparison between the reconstructions is underway.

Although the attenuation correction factors cannot be explicitly computed with list-mode data, the activity reconstructions of the list-mode and sinogram MLACF reconstructions (figures 6.3 and 6.4, respectively) are visually similar. Furthermore, in the case of reconstructions of motion-corrected list-mode events, the computation of a time-averaged sensitivity image can become challenging and computationally demanding. Since a backprojection of all possible LORs does not appear in the list-mode MLACF update (equation (6.6)) as opposed to

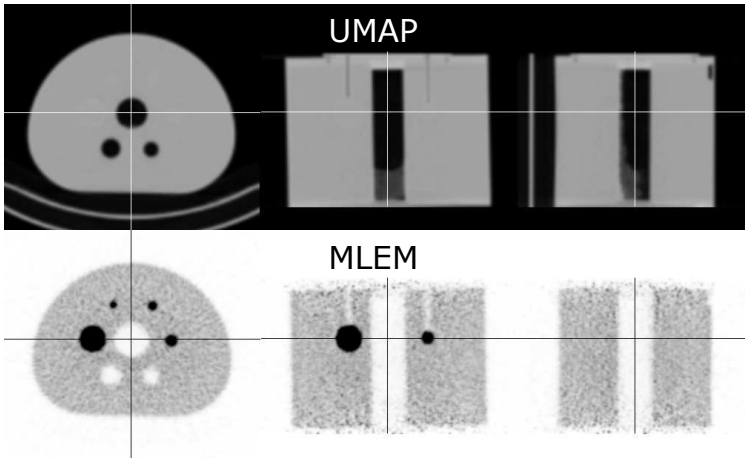

Figure 6.1: CT-based attenuation image of the NEMA IEC phantom (top) and the TOF-MLEM activity reconstruction (bottom) used as a blank scan which is required for the MLTR algorithm. The activity reconstruction is post-smoothed with a Gaussian of 3 mm FWHM.

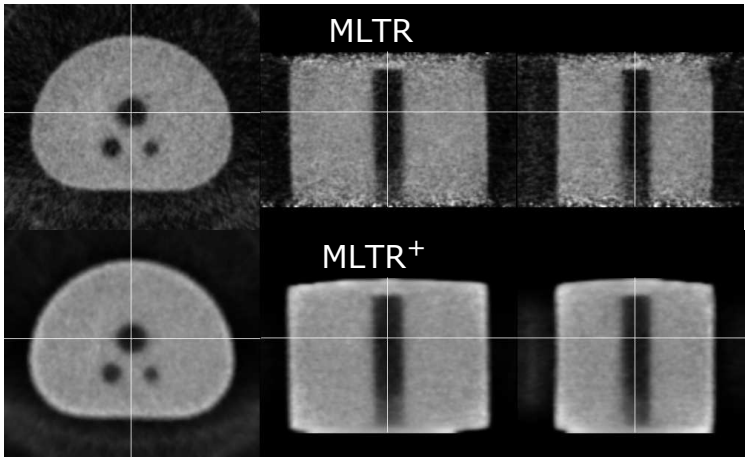

Figure 6.2: list-mode MLTR attenuation reconstructions using the TOF-MLEM reconstruction (Fig. 6.1 - bottom) as a blank scan. The reconstructions are obtained without a smoothing prior (top) and with the relative difference prior (bottom) to suppress the background attenuation during iterations. The attenuation reconstructions are post-smoothed with a Gaussian of 3 mm FWHM.

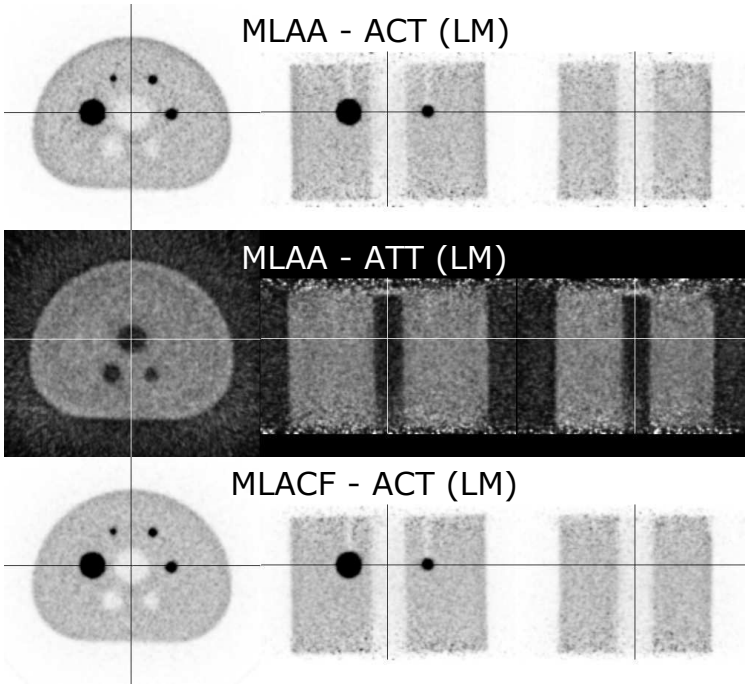

Figure 6.3: List-mode activity and attenuation reconstructions of MLAA (top and center) and the MLACF activity reconstruction (bottom).

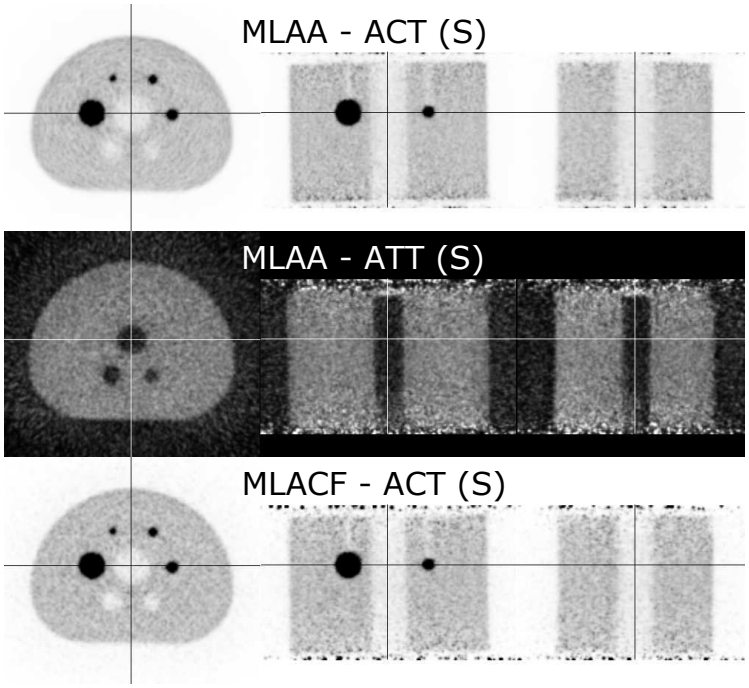

Figure 6.4: Sinogram activity and attenuation reconstructions of MLAA (top and center) and the MLACF activity reconstruction (bottom).

the update of MLEM (equation (6.2)), the algorithm benefits by automatically incorporating the time-averaged sensitivity image during reconstruction. We intend to investigate this property in more detail in the future.

6.5 Conclusion

The MLAA and MLACF reconstruction algorithms were originally developed for reconstructions of activity and attenuation images using the TOF-PET sinogram of the emission data. In this study, we present the list-mode version of these algorithms for the case of no randoms and/or scatter contribution. The list-mode and sinogram reconstructions of a 10 minute NEMA scan seem visually comparable, however further investigation is required to explain some of the differences observed especially at the edge of the phantom. Our results currently suggest that the typical mashing of the list-mode data required to obtain the emission sinogram does not greatly influence the activity and attenuation reconstructions.

6.6 Acknowledgements

The authors would like to thank Jung-Ha Kim for data collection as well as Georgios Angelis, John Gillam and Will Ryder for the very insightful discussions.

Chapter 7

Conclusion

Patient motion during a PET scan has always been a problem for those who struggle to remain motionless throughout the duration of the scan, such as paediatric, psychiatric, and elderly patients. This problem has been exacerbated over the past few decades with the continuous improvement in the spatial resolution of PET scanners, which has caused the effect of even slight motion of the subject during the scan to become a significant factor of image degradation. Efforts to minimise head motion by using head restraints often prove to be insufficient. Therefore the use of motion correction techniques has attracted much attention in recent years.

The use of anaesthesia in preclinical studies introduces a confounding factor in those studies. While this fact is well-known, the anaesthesia is seen as unavoidable. The advent of motion correction techniques now provides an avenue to conduct studies without anaesthesia, as well as the possibility of directly investigating how anaesthesia affects the tracer uptake.

The aims of my research have been to implement a motion correction technique at our research institute, to improve and optimise the experimental procedure, the data processing, and the reconstruction algorithm, and to use the developed motion correction techniques in preclinical and clinical studies.

7.1 Discussion

7.1.1 Motion Correction: Preclinical Studies

The MicronTracker (MT) was implemented in the preclinical setting for use in rat brain studies. This system was found to have sufficiently high accuracy (< 0.25 mm) and to be able to track markers small enough to attach to a rat's head. The MT has a fixed focal length, and thus a study was conducted to determine the optimal distance which balances the out-of-focus blurring with the magnification of the marker when the MT is brought closer. This distance

was found to be around 300 mm.

Initially the MT was made to send a strobe signal to the microPET gate input to insert a tag into the list-mode stream whenever a pose was recorded. However, it was found that at times a pose was not recorded, or a gate tag was not inserted. This meant that the tags and poses could not always be reliably aligned to each other. To improve the temporal synchronisation a novel method was developed whereby a block wave generator was used which would, at random, intermittently increase the period of a pulse. The pulses from this generator would trigger the MT to record a pose, and the microPET to insert a gate tag. The unique pattern introduced by the increased periods of the pulses would thus be present in the time stamps of the poses and gates, and therefore enable robust and reliable synchronisation of the two streams. Any gaps in the poses or gates could easily be identified and handled, and the alignment of the two data streams preserved.

A systematic delay between the MT and the microPET gate tags was identified and quantified. While we were not able to determine a predictive model for this delay, the necessary values at the most common frequencies were found empirically. Further improvements in motion correction during reconstruction were investigated, such as pose smoothing and interpolation, with the former having a more significant effect on the spatial resolution of the final reconstruction.

The protocol for training the rats was developed in order for the rats to become reliably acclimatised to the scanning scenario with three days of training. The tube and support used to hold the rats within the scanner were designed to be adjustable so that they could be used for a variety of rat sizes. The surgically implanted femoral vein catheter was found to be an important development in the experimental protocol improving on the earlier method of inserting a catheter into the tail vein. The rats had almost no response to the tracer infusion through the femoral vein catheter, while they responded negatively to the insertion of the tail vein catheter and could then sense the tracer infusion. While there were occasionally difficult rats, 8 out of the 9 rats studied while using the latest protocol responded well to the training and could be scanned successfully for between 60 and 90 minutes. This was a large improvement in the success rate of earlier variations of the experimental protocol.

The developed MC techniques were then implemented during a study on the effect of the anaesthetic isoflurane on the uptake of FDG in the rat brain. While the effect of isoflurane on FDG uptake had been studied by other groups using various strategies, this study was the first time that the effect was investigated in fully conscious rats from the time of injection, i.e. in a dynamic study. The results of the study showed that isoflurane reduces the overall uptake of FDG in the brain, and causes significant changes in the regional distribution of the tracer. While a full kinetic modelling analysis was not possible since no arterial

blood input function could be measured for the conscious rats and since FDG has no reference tissue model in the rat brain, the ability to dynamically scan conscious rats over an extended period of time was demonstrated and can be conducted with other tracers or anaesthetics.

7.1.2 Motion Correction: Clinical Studies

For clinical studies the OptiTrack (OT) system was primarily used to perform motion tracking. This system is designed to operate at a further distance from the subject being tracked than the MicronTracker, making it more conducive to the clinical setting where the tracker must not interfere with the standard clinical protocol. The markers that the OT system tracks can be conveniently arranged on a cap on a patient's head, and easily registered with the operating software. During a clinical study on the Siemens Hirez PET/CT scanner of healthy and dementia patient volunteers, a head restraint was used (in the form of a pillow which became rigid when inflated) to minimise head motion even though motion tracking was being performed. This head restraint was found to interfere with the cap on the subject's head due to the physical contact between the cap and the pillow, which at times prevented the cap from moving rigidly with the head. This resulted in imperfect motion correction. This problem would be alleviated if a head support could be devised which did not have contact with the cap. A better solution, however, may be to use a markerless tracking technique where features on the subject's face are tracked. This will be discussed further in the section on future work (7.2).

The utility of motion correction in the clinical setting was demonstrated for four PET scanners, namely:

- the Siemens mCT PET/CT, based at the University of Sydney, Australia, in collaboration with Prof. Roger Fulton and Dr. Jung-Ha Kim, performing the motion tracking using the OptiTrack system;
- the Siemens Hirez PET/CT, based at Universitair Ziekenhuis Leuven, Belgium, including a study (as dicussed above) in collaboration with Prof. Patrick Dupont and the PhD candidates Jolien Schaeverbeke and Charlotte Evenepoel, also using the OptiTrack system;
- the GE Signa PET/MR, based at the University of Stanford, U.S.A, and General Electric Global Research, New York, U.S.A, in collaboration with Dr. Floris Jansen and Dr. Michel Tohme, amongst others, using the HobbitView tracking system;
- the Siemens mMR PET/MR, based at the New York University, U.S.A., in collaboration with Prof. Fernando Boada and Dr. Thomas Kösters, using a continuous MR-sequence acquired simultaneously with the PET for motion tracking.

While the source of the motion data varied for these systems, the implementation of the motion corrected reconstruction was almost identical.

For the PET/CT systems, the motion was tracked during both the PET and CT scan. While motion during the CT scan is rare, it does nonetheless occur from time to time. Motion correction for CT has been demonstrated by members of my group and my collaborators (Kim et al. 2016), using the same motion tracking hardware, namely the OptiTrack system. Tracking the motion during the entire PET/CT scan also enables the correction of any motion between the CT and PET scan which would cause a misalignment of the emission data and the attenuation map.

7.1.3 Motion Correction Reconstruction

For accurate motion correction, an event-based list-mode reconstruction algorithm should be used. The most common such algorithm is the maximum-likelihood expectation-maximisation (MLEM) algorithm. The ideal implementation of the algorithm requires a very computationally expensive calculation of the sensitivity image, incorporating attenuation correction. Rahmim et al. (2004b) proposed an acceleration of this calculation by performing an averaging of the sensitivity image in the image domain, rather than the LOR domain. This approach, however, requires that the measured PET data be pre-corrected for attenuation. Alternatively, Carson et al. (2003) proposed reducing the computational load of the sensitivity image calculation by only using a randomised subset of the possible LORs. However, care must be taken though in how this random subset is generated. The former approach, proposed by Rahmim et al. (2004b), was primarily used during this research.

7.1.4 Spatially Variant Resolution Modelling

A resolution modelling technique was developed which accurately accounts for the spatially variant point spread function of the PET system, even in combination with motion correction. This was achieved by modelling the resolution in the projection domain of the list-mode events, rather than in image or sinogram space. The model could thus be applied before performing motion correction. To enable the technique to be computationally feasible it was necessary to employ an alternative reconstruction algorithm, namely the image space reconstruction algorithm (ISRA). A list-mode implementation of this algorithm was developed. While this algorithm does not model the noise properties of the data as accurately as MLEM, its use was justified by the computational acceleration it enabled. However, combining ISRA with motion correction can be much more computationally expensive that MLEM. Methods to accelerate the ISRA reconstruction were explored, including pose grouping and subsampling (as discussed in appendix A), although with limited success.

7.1.5 List-mode MLAA and MLACF

As a result of our work on list-mode ISRA, we implemented a list-mode version of two algorithms which utilise the TOF information available from modern PET scanners to simultaneously estimate both the activity image and the attenuation correction factors, from only the list-mode emission data. The first algorithm, list-mode MLAA, iteratively and alternately updates the activity and attenuation images using MLEM and an algorithm similar to ISRA, respectively. The second, list-mode MLACF, updates the activity and a backprojection of the product of the sensitivity and estimated attenuation correction factors. Both algorithms make use of the list-mode data directly. For MLAA it is possible to extend the algorithm to use motion corrected list-mode data, but this is complicated and requires further investigation (for precisely the same reason that combining ISRA and motion correction is complicated). For MLACF, on the other hand, it is trivial to incorporate motion corrected list-mode data. Since the algorithm actually estimates the product of the attenuation and sensitivity factors, there is no longer the need to perform the lengthy calculation of the time-averaged sensitivity image for motion corrected data. Additionally, the attenuation correction is performed during the reconstruction rather than as a pre-correction to the data, thus solving two significant problems in motion correction studies at once. It should be noted though that both MLAA and MLACF introduce a new problem: they can only estimate the attenuation up to a constant scale. This scale needs to be fixed, usually using some prior knowledge of the data.

7.2 Future Work

7.2.1 Motion Tracking and Correction

Motion correction for brain studies promises to significantly improve the clinical routine. It will greatly simplify the scan procedure for paediatric or elderly patients and those with psychological pathologies by removing the need for sedation or anaesthesia. It will also benefit all other patients where head motion is possible. Indeed, it will not be necessary to use head restraints at all, and patients could even intentionally move during the scan to keep comfortable.

Perhaps the most significant hindrance to motion correction being incorporated into standard clinical routine is that it slightly increases the complexity of that routine. For a new technique to be effective and widely applied in the clinic it should be simple, robust, and have minimal effect on the standard routine. Currently, markers need to be attached to the patient's head and, as the technique is implemented now, there are a few extra tasks which need to be performed to set up the cameras, calibrate them, and register the tracking markers (it should be noted that these latter three points could potentially be

automated or rendered unnecessary with some further development). Thus, an obvious and necessary improvement in motion correction is to move to a markerless approach, where the facial features are tracked directly. A markerless approach could be set up to have zero impact on the standard clinical procedure, and the motion corrected reconstructions could be automatically generated along side the standard reconstructions in the case of patient motion. Such an approach is being explored at our institution.

A markerless approach would also benefit preclinical studies where a marker adds an additional complication to the protocol since it needs to be attached to the animal's head, and is susceptible to being moved relative to the brain by the animal.

All the rats used for the pre-clinical studies performed during this research were healthy. Rats with some pathology or those under the influence of some narcotic, for example, might not respond as well to the training and scanning protocol. The protocol could perhaps be adapted to handle some special cases, but it might simply not work in others. Our collaborators at the University of Sydney have been working on a possible solution to this problem by placing the awake rats inside a spacious enclosure (rather than a tube) and tracking its head wherever it is in the enclosure (sometimes using a second tracking camera behind the scanner) (Kyme et al. 2012; Angelis et al. 2014). While this approach is promising it is nonetheless technically challenging. For now there are many studies which can be performed in healthy rats using a tube-bound protocol, and further work is needed to allow for more challenging cases.

Most current PET scanners perform reconstructions on sinogram data, instead of directly from the list-mode data. The reason for this is that, with almost all earlier scanners, sinograms presented an effective means of compressing the data since the number of detected events in a scan would usually be more than the number of sinogram bins. However, for modern scanners with higher numbers of detecting crystals, and with TOF data, the size of the sinograms is becoming comparable to that of the list-mode data for a typical scan. For motion correction studies, the reconstruction is ideally performed on the list-mode data. Therefore, as the scanner manufacturers turn towards incorporating list-mode reconstructions into their standard software, the possibility of them also implementing motion correction opens up.

7.2.2 Effect of Anaesthesia Studies

A summary of what is currently known about the effect of various anaesthetics on various PET tracers is presented in (Alstrup et al. 2013). In this article the authors state that "[i]deally, confirmatory PET studies could be carried out in unanaesthetized, freely-moving animals, but that goal is currently out of reach in most cases". With the motion correction technique presented in this thesis, this is now possible. Therefore, many studies can now be conducted

to investigate the effect of various anaesthetics on various tracers, and our proof-of-concept study with ^{18}F-FDG has shown that the approach is feasible and effective.

For many central nervous system tracers a reference tissue is available, enabling an image-based input function to be estimated and a full, quantitative kinetic investigation of the effect of anaesthesia on the kinetics of these tracers to be performed. A second study investigating the effect of isoflurane on a different tracer, namely 2-[18F]fluoroethyl 8-[(2E)-3-iodoprop-2-en-1-yl]-3-(4-methylphenyl)-8-azabicyclo[3.2.1]octane-2-carboxylate (^{18}FE-PE2i), which targets the dopamine transporters, has been commenced and is on-going at the time of publication of this thesis. The kinetics of this tracer can be modelled using the cerebellum as a reference tissue. The effect of isoflurane on the kinetics of this tracer has not been reported in the literature, and would greatly aid in the translation of any preclinical findings to the clinical setting.

7.2.3 Resolution Modelling

When developing the spatially variant resolution modelling technique, namely the redistribution technique, it was found that to correctly apply the technique with MLEM it was necessary to use many (i.e. more than 10) instances of each measured LOR during the reconstruction, leading to an equal increase in the number of computations for a reconstruction. In researching a method to avoid this, it was found that the ISRA algorithm was structured such that only one instance of each LOR was necessary for the correct implementation of the redistribution technique, therefore offering a significant advantage over MLEM.

We then explored incorporating motion correction into ISRA. This is discussed in appendix A and turns out to be a very computationally expensive task. Further methods to accelerate the reconstruction can be explored. However, since the reason for using ISRA was that MLEM with the redistribution technique was too computationally expensive, it is very possible that after incorporating motion correction both ISRA and MLEM will become similarly expensive. Therefore a reasonable avenue would be to work on accelerating MLEM with the redistribution technique by using, for example, a parallelised implementation.

7.2.4 List-mode MLACF

The proposed MLACF algorithm, which jointly estimates the activity image and the product of the sensitivity and attenuation correction factors from only the list-mode TOF-PET data, offers a promising solution to two of the primary problems in motion correction reconstructions: the lengthy calculation of the time-averaged sensitivity image, and the pre-correction of the emission data for attenuation. However, a solution to the scaling problem inherent in MLACF

needs to be found. Prior information, such as the expected total activity, could be used. A similar scaling problem appears in other joint-estimation algorithms, which a number of researchers are currently trying to solve, and which may perhaps lead to findings that could be of use in studying the similar scaling problem in MLACF.

Appendix A

Simulator

For the purposes of testing various aspects of the motion correction reconstruction, of the spatially variant resolution modelling technique, and of the ISRA reconstruction algorithm, a simulator was developed. This appendix will give a brief description of the simulator and how it was used.

The simulator can be broken into three main sections: data generation, pre-analysis of data (e.g. perform motion correction), and reconstruction.

A.1 Data Generation

The simulator generates data primarily by performing a forward projection through a digital phantom which is created with a higher pixel resolution than which will be used for the reconstruction. The values in the phantom's pixels represent activity. The phantom and data can be generated to be two or three dimensional. If motion is desired the phantom is transformed discreetly according to a set of poses (either explicitly specified or taken from measured data), and a projection is performed for each transformed image. The resulting data from these projections can then be concatenated. A simple forward projection can be applied which will ignore any resolution effects of the scanner, in the form of a ray-tracing projection through the phantom. Alternatively the resolution of the scanner can be simulated in one of two ways: either the digital phantom can be convolved with a smoothing kernel (usually a Gaussian) before the forward projection is performed, or for each LOR considered the endpoints of that LOR can be randomly moved in such a way as to model the effects of the resolution (exactly as is done in the redistribution technique presented in chapter 5). The latter technique requires that the redistribution of the endpoints is performed many times to statistically represent the system resolution.

However the projection is performed the result is a long list of non-integer projection values for each possible LOR, which are of course free of noise at this

point. These projection values are, in essence, sinogram data since a sinogram is simply an arrangement of projection values for each LOR. The projection can be thought of as being performed in one unit of time, and therefore the projection values are in units of counts. The projection values can be scaled to change the duration of the simulated scan. A non-uniform system sensitivity can be simulated by multiplying the projection values by suitable sensitivity factors. Poisson noise can be added to each LOR projection value by treating each value as a Poisson mean, and computing a Poisson realisation based on that mean. This results in integer counts. A projection value with a count of N can then be split up into a list of N repeated single events for that LOR, thus generating list-mode data. The list-mode data is randomised to make it realistic. It is clear that list-mode data is necessarily noisy since it is created after computing a Poisson realisation of the simulated data.

Therefore two forms of data can be generated: a list of noiseless projection values, one for each possible LOR, or a list of single events with possibly repeated LORs (effectively with projection values of 1).

A.2 Data Pre-analysis

Once the data has been generated it can be prepared for reconstruction. If motion correction is to be applied it is performed now by moving the endpoints of the generated data according to the poses. These applied poses need not be exactly the same as those used when transforming the phantom, for example the poses can have noise added to them before being applied to the generated data to simulate the real-world scenario.

If the MLEM algorithm is to be used for the reconstruction, then the sensitivity image must be calculated, and if motion correction is applied then the time-averaged sensitivity image should also be calculated. Even if a uniform sensitivity is used during the data generation, the sensitivity image will still incorporate the geometric sensitivity factors and thus must be calculated.

A.3 Reconstruction

The reconstruction can then be performed on the data, using either MLEM or ISRA. When using subsets these algorithms are formulated slightly differently and are referred to as ordered-subsets expectation-maximisation (OSEM) and ordered-subsets ISRA (OS-ISRA), respectively. Both reconstructions can be performed on the sinogram or list-mode data.

When performing motion correction with MLEM, the motion correction is performed before the reconstruction starts, and a standard list-mode reconstruction is performed on this data. For ISRA, the motion corrected data

are backprojected once, and the resulting image is iteratively compared to a forward and backprojection of the reconstruction. These latter projections are performed along all possible LORs in the scanner, and to incorporate the motion correction these LORs need to be transformed according to each recorded pose. Thus ISRA with motion correction can be a very computationally expensive task.

Either reconstruction can be performed using a resolution model, which can be the Gaussian convolution or the redistribution technique.

A.4 Investigations

The simulator was used in a number of investigations:

- It was used to develop the implementation of the redistribution technique, which involved developing effective methods for handling the positron range, the photon acollinearity, the detector response function, and the block effect.
- It was used to conduct an investigation into how MLEM and ISRA compare to each other, in a sinogram and list-mode based implementation, with and without subsets, and with the two resolution modelling techniques.
- It was used to develop a technique for implementing motion correction with ISRA, since this had not been reported on in the literature.
- It was used to test how particular parameters affect the motion correction reconstructions, such as the frequency of the motion tracker, the effect of noise in the motion data, and the effect of stationary objects in the FOV when the object of interest is moving (such as the body of a rat while the head is being tracked). This investigation was performed by a masters student, Abdo Redha Sultan, for whom I was the daily supervisor. The result of this investigation was his thesis entitled "Evaluation of microPET Simulator with Motion Correction", which he successfully defended in 2015.
- It was used to conduct a comparative investigation into motion correction in MLEM and ISRA, and how motion correction with ISRA can be accelerated. This investigation was performed by another masters student, Frederik Moyaert, for whom I was also the daily supervisor. The title of his thesis was "Comparing motion correction with two PET reconstruction algorithms: MLEM and ISRA", which he successfully defended in 2015.

Appendix B

Motion Correction Work-Flow

B.1 Motion Data

Two motion trackers were used during the course of this research, the MicronTracker Sx60 (ClaroNav Inc., Toronto, Canada) for preclinical studies and the OptiTrack (NaturalPoint Inc. Corvallis, OR, USA) for clinical studies, the details of which are discussed in chapter 1. Both trackers have different data output formats, but both involve reporting the six degrees-of-freedom (DOF) in an ASCII text file.

B.1.1 MicronTracker

After a measurement has been acquired with the MicronTracker (MT) the data can be exported to ASCII. Only selected parameters need to be exported: "Time stamp", "Marker origin position", "Marker Angular position", "Marker 3D rotation matrix", and "Hazards". Code to read the raw data which were developed by colleagues at the University of Sydney were adapted to our purposes. The program "readmt_mod.pro" will read the MT data file and return a structure containing the relevant data.

B.1.2 OptiTrack

In the OptiTrack (OT) software, when exporting the recorded data to a text file, one can choose the units (imperial or metric) and the format of the rotations (quaternion or Euclidean). The format of the resultant data file is "comma separated values" (CSV). The code I developed to read this data file, namely "readot.pro" assumes that the units are metric and metres, and that the rotations are Euclidean and in the order "XYZ". The output from the "readot.pro" function is a structure with the same format as for the MT file reader.

B.2 Motion Correction

One primary program, namely "mc_interface.pro", was written to execute the full motion correction procedure. After a script is created which describes a particular experiment, this program is called. The workflow of this program is as follows:

- The motion data is read in, as well as the gate times in the list-mode data. The motion data time stamps are synchronised with the gate tag time stamps and any gaps in the poses or gate tags are filled such that the synchronisation is maintained throughout the duration of the data. For the MT and microPET this synchronisation is performed by aligning the unique pattern present in both the pose time stamps and the gate tag time stamps. For the OT and Hirez or mCT scanners this is performed by simply assigning the first pose to the first gate tag, the second pose to the second gate tag, etc.

- The motion data, with their synchronised time stamps, are written to a file referred to as the "posefile" so that future analyses of the data do not need to reperform the synchronisation.

- The calibration matrices are read in and applied to the motion data to transform them from the tracker coordinate system to that of the PET, using,

$$T'_c = T_c T_R (T'_R)^{-1}, \tag{B.1}$$

$$X_t^{\mathrm{PET}} = T'_c X_0^{\mathrm{T}} \left(T'_c X_t^{\mathrm{T}}\right)^{-1}, \tag{B.2}$$

  where X_t^{T} is the transformation matrix for the pose measured at time t in tracker coordinates, and when $t = 0$ the pose in a reference position is used (usually the pose at the start of the scan, but it could be any other pose), T_R is the pose matrix of the reference marker during the calibration, while T'_R is the pose matrix of the reference marker on the day of the experiment, T_c is the calibration matrix determined on the day of the calibration to convert from tracker to PET coordinates, and X_t^{PET} is the corrective matrix to be applied to the endpoints of the list-mode events at time t.

- If necessary, the poses (X_t^{PET}) are smoothed according to the travelling cosine average method suggested by Stavdahl et al. (2005).

- If necessary, the poses (X_t^{PET}) are interpolated using cubic splines to the specified frequency of interpolated points (usually 1000 Hz).

- The sensitivity image is created by backprojecting the inverse of the normalisation sinogram. The image is saved to file so that it can be read in directly in future executions.
- The average sensitivity image is calculated by transforming the sensitivity image according to each pose and averaging these weighted by the duration of each corresponding pose. To decrease the computation time, a subset of the poses can be used by stepping over a specified number of poses after each transformation.
- The scatter and randoms sinograms are read in.
- The list-mode data is read in, and are motion corrected according to the poses using the matrices X_t^{PET} from (B.2).
- The attenuation correction factors are calculated by forward projecting the motion corrected list-mode events through the attenuation map. This map should be in the same pose as the reference pose ($T_c' X_0^{\mathrm{T}}$) to which all the events were corrected. The list-mode data are then pre-corrected by these attenuation correction factors.
- The reconstruction parameters are initialised, and the list-mode reconstruction is performed.
- The reconstruction, λ_j, is quantified using,

$$\lambda_j' = \lambda_j \frac{DF}{T_e}, \tag{B.3}$$

  where j is the pixel index, D is the decay correction factor using the actual scan duration, F is the deadtime correction factor, and T_e is the effective duration of the scan after removing the times when no poses were recorded and thus the corresponding list-mode events ignored.

Inter-frame Registration

During the conscious rat studies the rats were observed to touch the marker on their head intermittently 1 - 4 times during the scans which could lead to relative motion between the marker and the brain and thus result in inter- and intra-frame motion in the reconstruction. Intra-frame motion would lead to residual motion blurring in the final reconstruction and there is not much that can be done to rectify it. Inter-frame motion could be corrected for by frame-by-frame registration. This was implemented by visually inspecting the frames and selecting one which seemed to exhibit the least motion blur; this frame was then used as a reference frame. All other frames (excluding the first few where the activity was very low and the brain was not discernible) were then registered

rigidly (using six degrees-of-freedom) to this reference frame. The registration was performed using a simple multi-resolution optimisation algorithm with the cost function being the pixelwise normalised cross correlation. Even though this was only found to be necessary in a few studies, it was applied by default to all rat studies.

Appendix C

Experiment Hardware

A number of hardware components were used during this research. This appendix discusses how these components were designed and developed.

C.1 Robotic Arm

To test the motion correction techniques that were being developed during this research, a robotic arm was acquired to be able to move a phantom in the scanner. Prior to acquiring the robotic arm such experiments were performed manually, which obviously involves increasing the radiation exposure of the researcher, and means that motion cannot be reproduced.

The "AX-12A Smart Robotic Arm" kit was purchased from CrustCrawler Inc. (Gilbert, AZ, USA). This kit consists of seven AX-12A servo "dynamixel" motors, which are produced by Robotis Ltd. (Seoul, South Korea), and metallic struts for support. The arm was constructed to allow for 5 degree-of-freedom movement at the end of the arm: three rotations and two translations. The arm is controlled via the USB2Dynamixel controller which allows for communication between the motors and a computer via a USB port. Robotis supplies a software development kit (SDK) with which to program the robotic arm in the C programming language. The arm was assembled and programmed by me during this research.

The servo motors in the arm are each controlled directly by specifying the angle to which they should rotate, and the speed with which they should do so. A packaged command is assembled and then communicated to the servos via the USB2Dynamixel controller so that the servos will all execute the given command at the same time. A stream of such packaged commands thus constitutes a motion.

For a particular position of the arm it is theoretically possible to estimate the resultant position of the endpoint of the arm by multiplying the transformations matrices which define the state of each servo as well as the offset between the

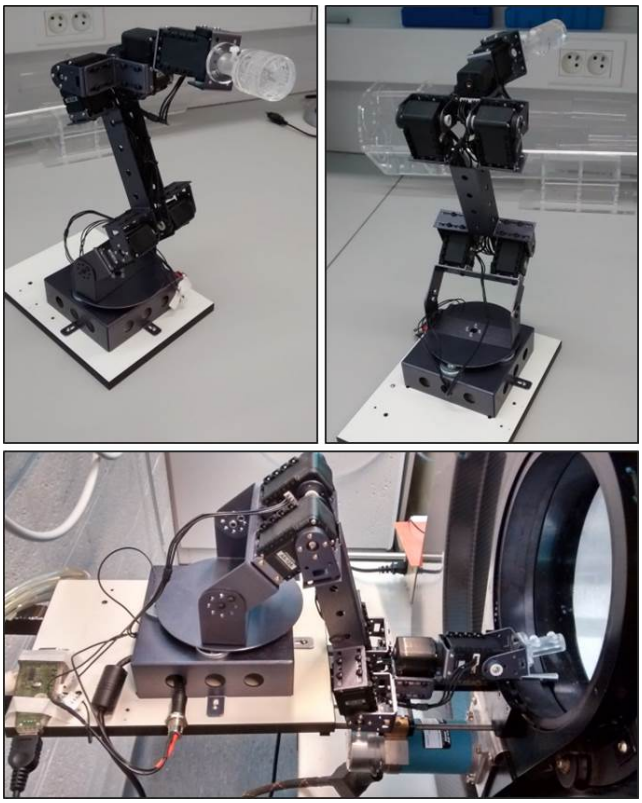

Figure C.1: At the top is the robotic arm constructed to aid in experiments, holding a small Derenzo phantom. At the bottom the arm can be seen attached to its support behind the microPET.

servos due to the supporting struts. This requires a careful calibration of these transformation matrices and was not deemed necessary for our studies.

The robotic arm was programmed to be used in one of three ways:

Continuous motion A string of positions is sent to the arm for it to move between, and then repeat. A number of such motions were defined, and the speed with which the robot performs a specific motion could be provided before compilation.

Teach mode To learn a new motion the arm can be put into "teach mode" and moved to each desired position. At each position a log of the position is created which allows for the easy creation of a motion between these positions.

Static mode For some studies it was necessary to scan the stationary phantom at various positions in the scanner. In this mode the arm can be moved to a position and the servos locked so that it remains there, and the servos can then be released to move the arm to a new position.

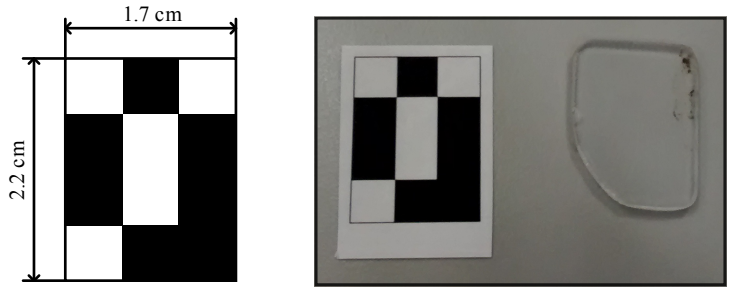

Figure C.2: The marker used for most rat studies. On the right the marker can be seen next to a perspex platform with one corner removed.

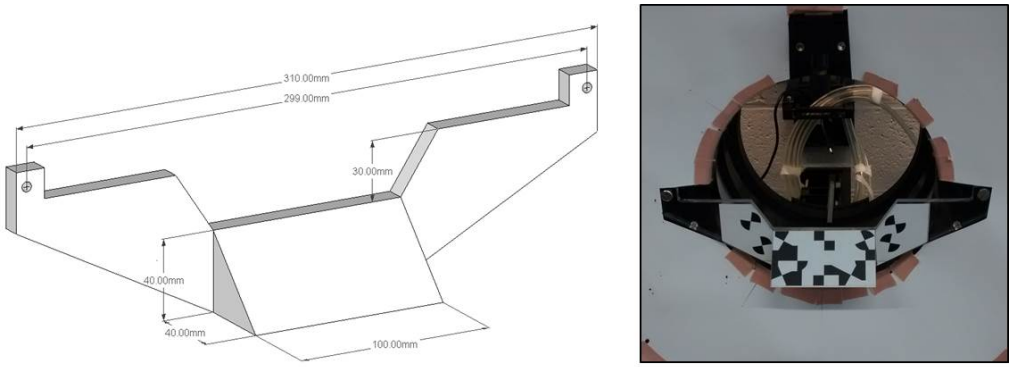

Figure C.3: The reference marker designed to be placed in front of the scanner such that the MicronTracker could be moved as close as possible to the scanner. The reference marker is attached to the scanner via two screws at either side of the bore, as can be seen on the right.

C.2 Markers

The marker used for the motion tracking was designed in MicroSoft Visio 2013 which allows for accurate drawing and alignment of various shapes. When printing Visio respects the scale of the image, and thus accurate prints can be produced. A high quality printer is necessary to achieve a good resolution and contrast between black and white regions. The markers were printed on labelling paper which is adhesive on one side, allowing for easy transfer onto the marker platform. The marker was stuck to a small perspex platform 2 mm thick. The marker used for most studies had a size of 1.7×2.2 cm and can be seen in figure C.2. One corner of the marker was removed, this corner was placed between the ears of the rat so that it did not touch the rat's neck if the rat were to raise its head.

A reference marker was designed to be attached to the front of the microPET scanner. This marker was measured while performing a calibration between the

MicronTracker and the microPET and since it was in the same position during every experiment it enabled a conversion of the calibration transformation matrix from the day of the calibration to the day of an experiment. Initially this marker was stuck onto the front face of the gantry. After conducting the study into optimising the distance between the MicronTracker and the microPET (reported in chapter 2), the reference marker was redesigned to cross in front of the scanner bore and thus allow the MicronTracker to be positioned as close as possible to the scanner while still being able to see the reference marker. The (redesigned) reference marker is shown in figure C.3. The marker was attached to the microPET by two screws on the front of the gantry such that it was removable but could be reliably placed in the same position during all experiments.

C.3 Tube & Support

Initially the tubes used to hold the rats inside the scanner were cylindrical tubes made of perspex. However, once the surgically implanted catheter started to be used the access port between the scapulae would not fit comfortably within the tube. Therefore a rectangular tube was designed, as shown in figure C.4. This tube was made of two telescopic components which allowed the length of the tube to be easily adjusted. The tube was supported from above by an arm, as can be seen in figure C.5. The part of the support within the FOV was made of perspex, and the rest was made of compacted wood.

C.4 Block Wave Generator

A block wave generator was used for all studies using the MicronTracker and the microPET. The generator would produce a square waveform pulse, and could operate at a number of frequencies in the range $[22, 42]$ Hz. These pulses would be sent to the MicronTracker and would trigger a pose to be recorded. The MicronTracker would then send a strobe signal to the gate input of the microPET and a gate would be inserted into the list-mode data. It was found that the MicronTracker would occasionally not record a pose and a gate would occasionally be missing from the PET list-mode stream. Thus, to aid in synchronising the motion and PET data streams the generator was equipped with a random number generator which would cause a randomly selected pulse to have its period increased by a pre-determined factor (20%, or 6.6 ms for a frequency of 30 Hz). This factor provided a sufficient contrast to be able to reliably identify these pulses from regular ones above the noise on the period (which was on the order of 1 ms). The probability for a pulse length to be increased was set at $\frac{1}{32}$. This probability ($\frac{1}{32}$) and factor (20%) were chosen

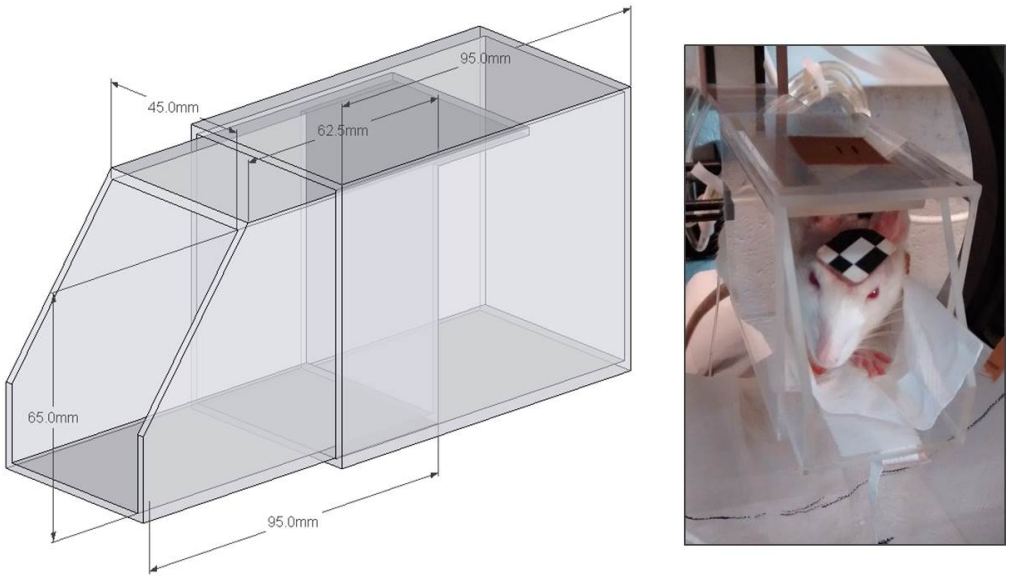

Figure C.4: The tube used to hold the rat within the scanner FOV. The tube consists of two telescopic components which allows the length of the tube to be increased or decreased. On the right the rat can be seen inside the tube, in the scanner.

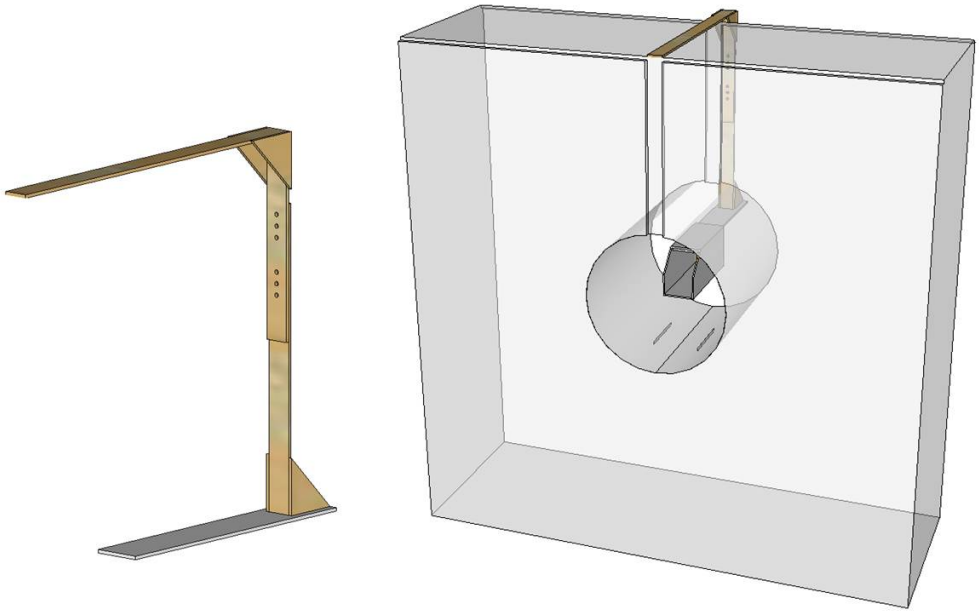

Figure C.5: The supporting arm used to hold the tube in the scanner. On the right the arrangement of the tube and support can be seen with the microPET scanner. A weight was usually placed on the arm on the top of the scanner to secure it.

to provide an optimal balance between the robustness of the synchronisation and the effective decrease in the frequency due to the lengthened pulses. The random number generator generated a 16-bit number and therefore had a repetition period of $2^{16} - 1$ pulses, or 36.4 minutes at a frequency of 30 Hz. The randomly lengthened pulses would produce a unique pattern in both the pose and gate time stamps, and would thus facilitate a robust synchronisation between the two data streams.

C.5 Strobe Modifier

The OptiTrack system was found to be very reliable in recording every pose, and the Hirez and mCT PET/CT scanners were found to be very reliable in inserting a gate tag. Therefore the block wave generator described above was not necessary for studies involving these systems. The OptiTrack had its own hardware for synchronising the individual cameras and which could output a strobe signal to the gate input of the scanner. The strobe signal sent by the OptiTrack system had a duration of the shutter time used for the cameras, i.e. on the order of 0.5 ms. However, it was found that the Hirez scanner expected the incoming strobe signal to have a minimum length, which was empirically determined to be around 1 ms, in order to insert a gate tag. Therefore a strobe modifier was constructed which would increase the length of an incoming strobe to 8 ms and output it again. This modifier was installed between the OptiTrack hardware and the Hirez scanner gate input. The increased duration of 8 ms was chosen such that a motion tracking frequency of 100 Hz (which the OptiTrack system is capable of) would still be possible without subsequent strobes overlapping.

Appendix D

Experimental Protocol for Rat Studies

All animal experiments were approved by the ethical committee of KU Leuven and performed in accordance with the European Communities Council Directive (86/609/EEC). The ethical clearance form is provided in appendix E.

For all experiments female Wistar rats were used. The rats varied between 6 - 10 weeks old, and were 200 - 300 g in weight. All rats were housed in pairs or in threes, except for those rats which had had a catheter implanted which were housed individually. The rats had free access to food pellets, except when they were fasted before a scan, and water.

The experimental protocol was adapted and improved over the course of this PhD. In this appendix I will give details of some earlier methods as well as the most recent ones in order to describe both the methods which worked and those which did not.

D.1 Marker

A number of marker designs and sizes were investigated during this research. The markers were placed on a piece of perspex 2 mm thick. It was found that the simple design shown in figure D.1 had a good balance of detectability and tolerability by the rats. Slightly different sizes of this marker were created so that an appropriate marker could be used depending on the size of the rat's head. However, since we used rats of similar age and weight, their sizes did not vary very much, and so a single size (figure D.1) was used almost exclusively in later studies. A corner of the marker was removed and this part of the marker was usually placed between the rat's ears to avoid contact between the marker and the neck if the rat were to raise its head.

To ensure adequate marker attachment the rat's forehead is shaved, and a chemical depilatory (e.g. "Veet") is applied, while it is anaesthetised either

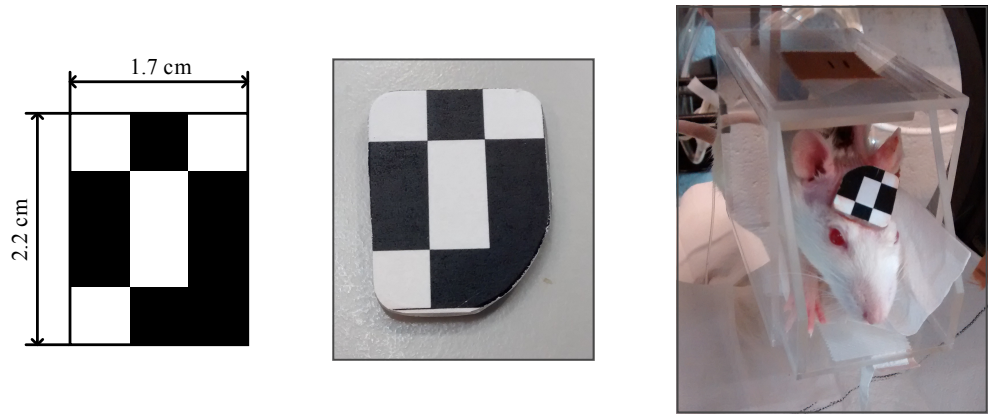

Figure D.1: On the left is the standard marker used during most rat studies. The marker has a size of 2.2×1.69 cm, with vectors of length 5.5 mm and 11.0 mm. In the middle the marker can be seen on its perspex platform; the corner of the marker has been removed. On the right the rat can be seen in the tube in the scanner, with the marker attached to its forehead.

before the training begins, or on the first day of the training. This ensures that the forehead is free of fur for around 4 or 5 days, after which some regrowth is visible. The marker is attached to the rat's forehead using an adhesive. It was found that "superglue" (cyanoacrylate) is very effective since it dries rapidly, bonds very well, and after 2 - 3 days the marker falls off due to skin regeneration, or the appearance of fur.

D.2 Acclimatisation

During a scan the rat is placed inside a tube in the PET scanner. The tube can be seen in figure D.1 and is described in appendix C. Each rat undergoes training for at least three days prior to the scan to acclimatise it to being inside the tube and also having the marker attached to its forehead. As already mentioned, either before the training begins, or on the first day of the training, the fur on the rat's forehead must be removed. Following this, the training procedure is as follows:

Day 1 The marker is attached to the rat's head; this usually requires two people. The marker is covered in a thin layer of adhesive, one person firmly restrains the rat while the second presses the marker onto the forehead, ensuring that the rounded corner is between the ears. It usually helps if the person with the marker places a finger on the bridge of the rat's nose. The glue takes a few seconds to dry, and any pressure applied during this time aids in the adhesion. The rat should then be watched

and stopped from trying to remove the marker for 1 - 2 minutes. The rat is then placed in the tube and held above its cage at a height of at most 50 cm. Usually the rat will try to exit the tube (usually at the back), and it is allowed to fall into its cage. The rat is then immediately replaced in the tube and the process is repeated. Most rats would stop trying to exit the tube after one or two attempts. The rat then remains in the tube for approximately 10 minutes, while supported from above by the support arm.

Day 2 Sometimes the rat manages to remove the marker by itself since the previous day. The marker is then replaced following the same procedure as on day 1. The rat is placed into the tube and held above the tube for a few minutes. Usually the rat would not try exit the tube. The rat and the tube are then placed into the scanner, using the support arm to hold the tube from above. An iron weight is usually placed on the upper arm of the support, on the scanner gantry, to counter-balance the rat. All additional hardware which the rat would see during the actual scan is setup, i.e. the MicronTracker on the bed mount, the reference marker on the front of the scanner gantry, and the lamps (switched on) in front of the scanner. On this first day inside the scanner the rat will usually try to exit the front of the tube at some point, this is discouraged by distracting the rat with some object (e.g. a pen, or pincers). If the rat does exit the tube it is replaced immediately. Sometimes it helped to keep the rat slightly further back in the scanner so that it could not reach the reference marker. The rat is kept in the scanner for 15 - 20 minutes.

Day 3 If the marker has been removed, it is not replaced since a new marker must be attached on the scan day. The same procedure as day 2 is repeated, but now an attempt is made to replicate the scanning procedure by keeping the rat's head approximately in the centre of the scanner FOV, by moving the tube back or forth, or shortening it, as necessary. The rat is kept in the scanner for 20 - 30 minutes.

A note on the marker: The marker is expected to remain attached for 2 - 3 days. Therefore, the marker attached on day 1 is a surrogate marker (one that was used previously, for example) since it may become spoiled during the training. The marker does sometimes get removed by the rat between day 1 and day 2, and it is then replaced on day 2. If it is removed on day 3 it is not replaced since it may not come off by the scan day (i.e. usually day 4). A new marker is then attached on the scan day. Only once did it occur that the training marker was still attached on the scan day, and in this case a new marker was simply attached on top of the training marker using the same adhesive.

D.3 Tracer Infusion

Initially, prior to October 2014, only static scans were conducted with the rats, spanning at most 20 minutes. For these scans the tracer was infused by inserting a catheter into the tail vein of the rat, while the rat was inside a restraining tube. It was evident that this was a stressful occurrence for the rat by vocalisations and the rat's movement inside the restraining tube. Dynamic studies began around October 2014 and initially the same tail catheterisation was used, but the catheter was left in the tail so that the infusion could be performed while the rat was in the scanner. However, the rats were agitated after the catheter insertion, and it appeared that they could sense the infusion of the tracer into their tail. These factors led to many scans being unsuccessful. Therefore we began using a jugular vein catheterisation which was surgically implanted the week before the training and scan. An access port was placed dorsally between the scapulae. Due to difficulties in the surgical procedure we soon changed to performing a femoral vein catheterisation, with the same access port between the scapulae. Attaching a tube to the access port was trivial and did not appear to cause any stress in the rat, making it much easier to use than the tail vein catheter. Additionally, the rats showed no signs of being able to sense when a tracer was infused into this catheter. This adaption greatly improved the success rate of our experiments: when using the tail vein catheterisation at least 50% of the scans would fail or have significant complications, the reasons for which were mostly linked to the catheterisation; while after switching to the femoral vein catheterisation 8 out of the 9 rats scans were successful, with any complications begin due to the rat manually moving the marker or exiting the tube.

The tracer infusion setup used is shown in figure D.2. This setup allowed the rat to be positioned inside the scanner with only the saline line attached, and when the rat seemed settled the tracer line could be attached and shortly thereafter the infusion started. An infusion pump was used, usually infusing a volume of 0.8 mL at a rate of 2 mL/min.

D.4 Experiment Setup

The full experimental setup can be seen in figure D.3. The rat is placed in the tube, in the scanner, held by the support arm. The MicronTracker is placed in front of the scanner, on the bed mount. The horizontal bed position is set to 230 mm, and the vertical position to 60 mm, in the microPET manager software. The positioning laser is unfastened and held out of the line of view of the MicronTracker using tape. The reference marker is attached to the front of the scanner gantry. The block wave generator is connected to a relay point which sends the block wave on to the MicronTracker, then receives the

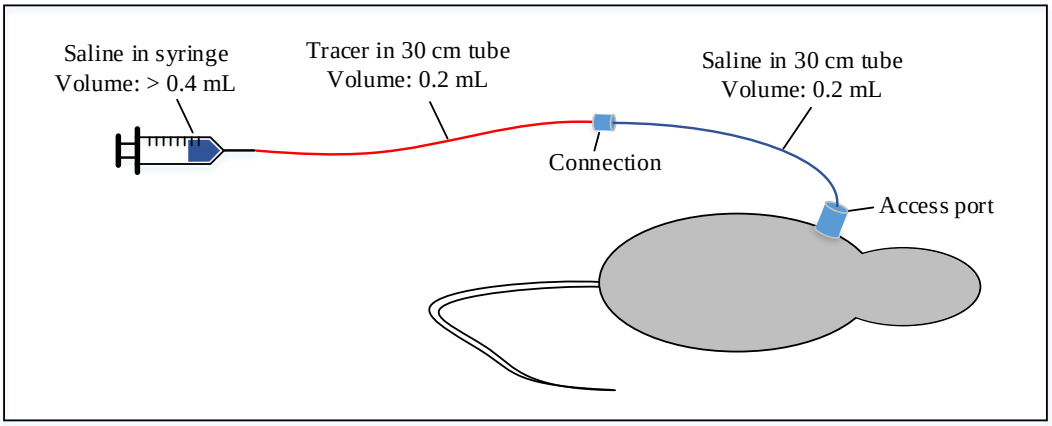

Figure D.2: The setup used to infuse the tracer. A tube filled with saline (blue) was attached to the access port on the rat. A tube filled with the tracer (red) could then be prepared and connected to the blue tube just before infusion. The red tube was connected to a syringe filled with saline for flushing, which was placed in an infusion pump. At an appropriate time the infusion pump could be started, after which the red tube could be removed to measure the remaining dose. The dose in the blue tube could only be measured after the scan.

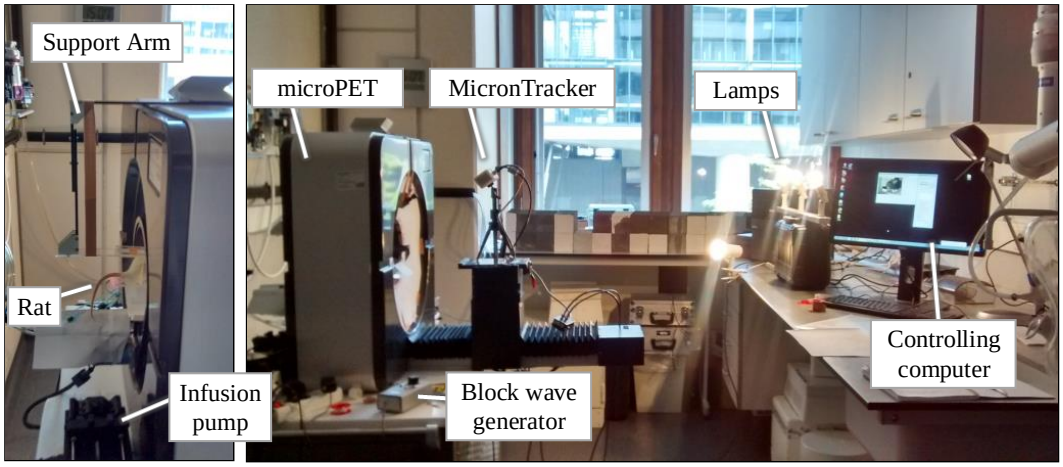

Figure D.3: The setup of a rat experiment.

strobe signal from the MicronTracker and sends it on to the gate input of the microPET. The MicronTracker is connected to a controlling computer. Five lamps are used to provide lighting, and the overhead, fluorescent lamps are switched off (to avoid aliasing effects due to their flickering).

Appendix E

Ethical Clearance Forms

On the following pages are the letters granting ethical clearance for the study on rats presented in chapter 3 and the clinical study conducted on the Hirez PET/CT scanner presented in chapter 4 section 4.3 using the THK5351 and AV1451 tracers.

P143/2014

De ondertekende aanvraagformulieren sturen naar: Erna Dewil, Proefdierencentrum, Herestraat 49 bus 501, 3000 Leuven. ecd@pfd.kuleuven.be
Document geldig van/valid from: 15/03/2014

KATHOLIEKE UNIVERSITEIT LEUVEN

FORMULIER ETHISCHE COMMISSIE
Form Ethical Committee

Gebruiker (*User*): Labo voor Radiofarmacie
Erkenningsnummer Gebruiker (*license number*): LA1210261.

Projectverantwoordelijke of proefleider (ZAP) (*PI*):

Naam/*Name*	**Voornaam**/*first name*	**Diploma** /*degree*	**Certificaat proefdierkunde**/*certificate lab animal science*
Celen	Sofie	PhD	☒

Uitvoerende onderzoeker(s) (AAP/BAP) (*researchers and technicians*):

Naam/*Name*	**Voornaam**/*First name*	**Diploma**/*degree*	**Certificaat proefdierkunde**/*certificate lab animal science*
Ooms	Maarten	Apr	☒
Cornelis	Julie	Laborant	☒
.....	.....	.....	☐

Proefdierantenne (*animal antenna*):

Naam/*Name*	**Voornaam**/*first name*	**Diploma** /*degree*	**Certificaat proefdierkunde**/*certificate lab animal science*
Cornelis	Julie	Laborant	☒

☒ **Nieuw project** (*new project*) ☐ **Verbonden aan een project (Nr. .....)**/*linked to project P...*

Titel van het onderzoeksproject (*title of the research project*):

Invloed van anesthesie op microPET visualisatie.

Duur van het project (maximum 5 jaar) (*duration of the project, max 5 years*)
Begindatum (*start date*): 01-07-2014 Einddatum (*end date*): 01-07-2019

Handtekening van deprojectverantwoordelijke/*signature PI* Datum/*date*

27/6/2014

Advies (voorbehouden aan de Ethische Commissie) (*for the Ethical Committee*):
☒ gunstig/*favorable* ☐ gunstig mits aanpassingen/*provided favorable adjustment* ☐ ongunstig/*rejected* 30 VI 2014

Inschatting van pijn, lijden of letsel door de Ethische Commissie/*estimate bij the Ethical Comittee*
☐ geen/*none* ☒ gering/*minor* ☐ matig/*moderate* ☐ ernstig/*severe* ☐ terminaal/*terminal* Datum/*date:*

Commentaar en opmerkingen/*comments and remarks*

De Voorzitter/ *the Chairman*

De Leden/ *the members*

LEUVEN

Leuven, 14 september 2015

Commissie Medische Ethiek
UZ KU Leuven / Onderzoek
U.Z. Gasthuisberg
Herestraat 49
B 3000 Leuven (Belgium)

prof. dr. Rik Vandenberghe
NEUROLOGIE

Ons kenmerk:	EudraCT-nr:	Belg. Regnr:
S57168(ML11174)	2014-004053-14	

Molecular imaging in cognitively intact older adults to study amyloid- and tau-based mechanisms of Alzheimer's disease.

AMENDEMENT/BIJKOMENDE STUDIEDOCUMENTEN
DEFINITIEF GUNSTIG ADVIES AMEND-Id: 0002

Geachte Collega,

De Commissie Medische Ethiek van UZ KU Leuven / Onderzoek heeft vermeld protocol initieel goedgekeurd op 17 december 2014.

Met betrekking tot vermeld protocol werden bijkomende documenten ingediend bij de Commissie Medische Ethiek van UZ KU Leuven / Onderzoek.

Bij het beoordelen van dit amendement werd rekening gehouden met alle aan dit amendement gerelateerde documenten die ingediend werden op 18 augustus 2015.

Het amendement werd goedgekeurd op 4 september 2015.

Dit gunstig advies betreft:

Protocol
Protocol v8 dated 10-08-2015
Informatie en toestemmingsformulier
IC T807 S57168 patiënt v4 dated 18-08-2015
IC T807 S57168 vrijwilliger v3 dated 18-08-2015

Volgende documenten werden ter notificatie ingediend :

Tel +32 16 34 86 00
Fax +32 16 34 86 01

website: www.uzleuven.be/ec/
e-mail : ec@uzleuven.be

Niet van toepassing

De Commissie bevestigt dat ze werkt in overeenstemming met de ICH-GCP principes (International Conference on Harmonization Guidelines on Good Clinical Practice), met de meest recente versie van de Verklaring van Helsinki en met de van toepassing zijnde wetten en regelgeving.

De Commissie bevestigt dat in geval van belangenconflict, de betrokken leden niet deelnemen aan de besluitvorming omtrent het amendement.

Een ledenlijst wordt bijgevoegd.

Aandachtspunten: (indien van toepassing)

De opdrachtgever is verantwoordelijk voor de conformiteit van de anderstalige documenten met de Nederlandstalige documenten.

*Indien het **Clinical Trial Agreement** aangepast moet worden naar aanleiding van dit amendement kan de studie in ons centrum pas aangevat worden wanneer dit Clinical Trial Agreement goedgekeurd en ondertekend is door de gedelegeerde bestuurder van UZ Leuven (en/of desgevallend door bevoegde vertegenwoordiger(s) van KU Leuven R&D).*

Studies met geneesmiddelen en sommige studies met "medische hulpmiddelen" dienen door de opdrachtgever aangemeld te worden bij het FAGG.
Studies met geneesmiddelen mogen slechts aanvangen op voorwaarde dat de minister (FAGG) geen bezwaren heeft kenbaar gemaakt binnen de wettelijke termijnen zoals beschreven in art.13 van de Belgische wet van 7/5/2004 inzake experimenten op de menselijke persoon.
Voor bepaalde studies met medische hulpmiddelen gelden eveneens wettelijke termijnen (zie KB van 17/3/2009). Voor meer informatie hieromtrent verwijzen we naar de website van het FAGG www.fagg-afmps.be.

Onderzoek op embryo's in vitro valt onder de wet van 11 mei 2003. Voor dergelijk onderzoek is er naast een positief advies van het Ethisch Comité ook een goedkeuring van de Federale Commissie voor medisch en wetenschappelijk onderzoek op embryo's in vitro noodzakelijk vooraleer dit onderzoeksproject kan doorgaan.

Gelieve ook rekening te houden met de regelgeving van het ziekenhuis betreffende weefselbeheer en met de beschikkingen van de wet van 19 december 2008.

Dit gunstig advies van de Commissie houdt niet in dat zij de verantwoordelijkheid voor de geplande studie op zich neemt. U blijft hiervoor dus zelf verantwoordelijk. Bovendien dient U erover te waken dat uw mening als betrokken onderzoeker wordt weergegeven in publicaties, rapporten voor de overheid enz., die het resultaat zijn van dit onderzoek.
U wordt eraan herinnerd dat bij klinische studies iedere door U waargenomen ernstige verwikkeling onmiddellijk zowel aan de opdrachtgever (desgevallend de producent) als aan de commissie medische ethiek moet worden gemeld, ook al is het oorzakelijke verband met de studie onduidelijk.

Tel +32 16 34 86 00
Fax +32 16 34 86 01
website: www.uzleuven.be/ec/
e-mail : ec@uzleuven.be

Gelieve ons mee te delen indien een studie niet wordt aangevat of wanneer ze wordt afgesloten of vroegtijdig onderbroken (met opgave van reden).

*Indien de studie niet binnen het jaar beëindigd is, vereist de ICH-GCP dat een **jaarlijks vorderingsrapport** aan de commissie wordt bezorgd.*

*Gelieve tenslotte het (vroegtijdige of geplande) stopzetten van een studie binnen de door de wet vastgestelde termijnen mee te delen en een **Clinical Study Report** aan de Commissie te bezorgen.*

Met de meeste hoogachting,

PROF DR G. VERHOEVEN

Prof. Dr. W. Van den Bogaert
Voorzitter
Commissie Medische Ethiek UZ KU Leuven / Onderzoek

UZ LEUVEN
COMMISSIE VOOR MEDISCHE ETHIEK
KLINISCH ONDERZOEK

Cc:
FAGG (Federaal Agentschap voor Geneesmiddelen en Gezondheidsproducten)

CTC (Clinical Trial Center UZ Leuven)

Deelnemende centra

Lokale Commissie *Onderzoeker*

Tel +32 16 34 86 00
Fax +32 16 34 86 01

website: www.uzleuven.be/ec/
e-mail : ec@uzleuven.be

Ledenlijst/Samenstelling van de Commissie op 4 september 2015:

prof. dr. em. Walter Van den Bogaert	Radiotherapy-Oncology
prof. dr. em. Guido Verhoeven	Experimental Medicine
dr. Sabine Graux	Physician
dr. Sonja Haesendonck	Physician
De heer Karel Op de Beeck	Head Nurse
Mevr. Christine Mathieu	Medical Legislation
dr. José Thomas	Medical Oncology
dr. Lut De Groote	General Practitioner
prof. Ben Van Calster	Statistics
prof. J.R. Thomas	Clinical Pharmacology
prof. dr. Dominique Bullens	Paediatrics
prof. dr. Jan Van Hemelrijck	Anesthesiology
prof. dr. Jan de Hoon	Clinical Pharmacology
prof. dr. Xavier Bossuyt	Immunology
prof. dr. em. Ivo De Wever	Surgical Oncology
prof. dr. em. Raymond Verhaeghe	Cardiology
prof. dr. em. Willem Daenen	Cardiac Surgery

Tel +32 16 34 86 00
Fax +32 16 34 86 01

website: www.uzleuven.be/ec/
e-mail : ec@uzleuven.be

FANC

federal agency for nuclear control

Brussels, 08 JAN. 2015

Prof. R. Vandenberghe
Neurology Dept.
UZ Leuven
Herestraat 49

3000 LEUVEN

Health and Environment
Health Protection

Your correspondence:	Your references:	Our references:	Enclosure(s):
November 12th, 2015		PK-0012941	

Subject: Clinical trial EudraCT 2014-0002976-10

Cc: Dienst R&D – Fagg

Dear Professor,

We carefully reviewed your application for a clinical trial involving the products [^{18}F]-THK5351 and [^{11}C]-PIB.

The conclusions of the review are the following:

A. The application file is complete.

B. The required authorizations are in place:

Licensed Facility:

1) UZ Leuven – Site Gasthuisberg (BH-0010499 and BA-0009417)

Quality Control Pharmacists:

1) K. Serdons (FANC/36368/PH/F/1), B. Vanbilloen (MIN 02/07/1983), G. Bormans (MIN 1983)

Physician authorized to use radioactive sources for medical purposes:

1) Dr. K. Van Laere (ENM-0005603)

Health Physics Services and Recognized Control Bodies:

1) AIB-Vinçotte Controlatom and N. Bergans (FANC 11354/EBP-5353-B)
2) BelV

Occupational Physician qualified for Medical Surveillance of Occupationally Exposed Workers:

1) Dr. C. Verbeek (E75-0011088)

Qualified Medical Radiation Physicist:

1) K. Baete (FANC/40029/RP/P/1)

Correspondence: Rue Ravenstein 36, BE-1000 Brussels
Tel.: +32 (0)2 289 21 11
Fax: +32 (0)2 289 21 12

For further information regarding this subject, please contact:
Sylviane Carbonnelle – sylviane.carbonnelle@fanc.fgov.be
Tel.: +32 (0)2 289 21 75

C. The study is justified, the expected benefits outweighing the risks associated with the dose charge to the patient;

D. The radiation risks are mentioned on the Patient Informed Consent version 1 d.d. 26-06-2014;

E. An authorization set forth in article 45 is not required for this clinical trial.

The FANC issues a positive advice for this clinical trial under the above-mentioned conditions.

Yours Sincerely,

Dr Sylviane Carbonnelle
Medical Expert

Dr Patrick van der Donckt
Director Health & Environment

Correspondence: rue Ravenstein 36, BE-1000 Brussels
Tel.: +32 (0)2 289 21 11
Fax: +32 (0)2 289 21 12

For further information regarding this subject, please contact:
Sylviane Carbonnelle – sylviane.carbonnelle@fanc.fgov.be
Tel.: +32 (0)2 289 21 75

CURRICULUM VITAE

MATTHEW GILBERT SPANGLER-BICKELL

CONTACT DETAILS

Postal Address: Dekenstraat 86A - 002, Leuven, 3000, Belgium
Email Address: matthew.bickell@gmail.com; matthew.bickell@uzleuven.be
Contact Number: +32 (0)476 65 41 94
Date of Birth: 1 September 1987
Nationality: South African

EDUCATION

2012 (Sept) – 2017 (Jan) Katholieke Universiteit Leuven, Belgium

PhD in Biomedical Sciences

Title: Rigid Motion Correction Techniques for Positron Emission Tomography Brain Imaging

2010 (July) – 2012 (June) University of Cape Town, South Africa

Masters of Science in Physics

Thesis title: "Investigations into a Positron Emission Imaging Algorithm"

Degree was awarded with Academic Distinction (no other grade is given)

2010 (Sept) Attended the NRF South African Students Summer School in Russia for 3 weeks where I studied parallel processor coding using Message Passing Interface (MPI).

2009 – 2009 University of Cape Town, South Africa

Bachelors of Science (Honours) in Mathematical and Theoretical Physics

Degree was awarded with Academic Distinction, finishing top of the class.

Thesis: "A Positron Emission Particle Tracking technique for tracking multiple particles"

Courses: Non-linear Optimisation; Computational Physics; Finite Element Modelling; Various theoretical physics courses

2006 – 2008 University of Cape Town, South Africa

Bachelors of Science in Physics and Applied Mathematics

Degree was awarded with Academic Distinction.

Languages: English (native), Dutch & Afrikaans (conversational), Italian & French (basics).

PUBLICATIONS

2016 M. G. Spangler-Bickell, B. de Laat, R. Fulton, G. Bormans, J. Nuyts, "The Effect of Isoflurane on 18F-FDG Uptake in the Rat Brain: A Fully Conscious Dynamic PET Study using Motion Compensation". *EJNMMI Res.* (2016), 6, pp. 86.

M. G. Spangler-Bickell, L. Zhou, A. Z. Kyme, B. de Laat, R. R. Fulton, J. Nuyts, "Optimising rigid motion compensation for small animal brain PET imaging," *Phys. Med. Biol.*, (2016), 61.19, pp. 7074–7091.

M. G. Bickell, L. Zhou, J. Nuyts, "Spatially Variant Resolution Modelling for Iterative List-Mode PET Reconstruction," *IEEE Trans. Med. Imaging* (2016), 35:7, pp. 1707-1718.

2015 M. G. Bickell, B. De Laat, R. Fulton, G. Bormans, J. Nuyts, "The Effect of Anaesthesia on ^{18}F-FDG Uptake in the Rat Brain: A Fully Conscious Dynamic Study using Motion Correction," *IEEE Nucl. Sci. Symp. Conf. Rec.*, (2015).

M. G. Bickell, J.-H. Kim, A. Rezaei, J. Nuyts, R. Fulton, "Rigid motion correction of PET and CT for PET/CT brain imaging," *IEEE Nucl. Sci. Symp. Conf. Rec.*, (2015).

2014 M. G. Bickell, T. Koesters, F. Boada, J. Nuyts, "PET motion correction using MR-derived motion parameters," *EJNMMI Physics* (2014), vol. 1:Suppl 1, pg. A53.

2013 M. G. Bickell, L. Zhou, J. Nuyts, "Spatially Variant Resolution Modelling for Iterative List-Mode PET Reconstruction, " *IEEE Nucl. Sci. Symp. Conf. Rec.*, (2013).

2012 M. G. Bickell, A. Buffler, I. Govender, D. J. Parker, "A new line density tracking algorithm for PEPT and its application to multiple tracers," *Nucl. Instr. Meth. Phys. Res. A* (2012), pp. 36-41

ACADEMIC ACHIEVEMENTS AND AWARDS

2010 – 2012	National Research Foundation (NRF) Scarce Skills Scholarship
2009 – 2012	UCT Merit Scholarship
2007	Dick & Dorothy Borcherds Prize (for Astrophysics)
2006 – 2008	Science Faculty Scholarship
2006 – 2008	Richard Solomon Scholarship (for Applied Mathematics)
2006 – 2009	Listed in the Science Faculty Dean's Merit List.
2006 – 2009	Class Medal as top student for the BSc (Honours) degree, 1st and 2nd year Applied Mathematics, and 2nd year Astrophysics.
2006 – 2009	A first class pass (the highest achievable grade) was achieved in all courses.

WORK EXPERIENCE

2009 – 2011	UCT Physics Department	Tutor
2009 – 2011	UCT Mathematics Department	Tutor
2006 – 2008	Private	High school and GCE A-level tutor
2005	Accurate Automation CC	Engineer's assistant

COMMUNITY INVOLVEMENT

2011 Chairperson of UCT Students for Life

2011 A founding member of Pamoja Mentorship Programme for pregnant and parenting students

OTHER INTERESTS

My greatest extracurricular passions are rock climbing and mountaineering, which I pursue actively throughout the year. During 2011 I was an active member of the Mountain Club of South Africa Search and Rescue team. My other interests include astronomy, archaeology and travelling.

DEVELOPED SKILLS

My studies and research have helped me develop strong problem solving skills, and my work experience has made me able to clearly explain and clarify complex ideas to others. The leadership and teamwork skills which I have acquired during my tenure as chairperson of the UCT Students for Life society has prepared me to work in groups effectively. My research during my Masters and PhD degrees have given me extensive experience with various PET scanners: the Siemens ECAT EXACT3D, microPET Focus220, Hirez PET/CT, mCT PET/CT, mMR PET/MR scanners, and the GE Signa PET/MR scanners, in the areas of PET instrumentation, data handling, image reconstruction and motion correction. During my research and studies I have coded extensively in IDL, MATLAB and C, and I am also familiar with Python, Java and parallel processor coding using the Message Passing Interface (MPI).

REFEREES

Prof. Johan Nuyts
PhD promoter
Dept. of Nuclear Medicine
KU Leuven
Leuven, Belgium
Email: johan.nuyts@uzleuven.be
Tel: +32 (0)163 34 90 18

Prof. Andy Buffler
MSc thesis supervisor
Dept. of Physics
University of Cape Town
Cape Town, South Africa
Email: andy.buffler@uct.ac.za
Tel: +27 (0)21 650 3339

Fr. Graham Pugin
(character referee)
Catholic Chaplain
University of Cape Town
Kolbe House
Cape Town, South Africa
Email: grahampugin@sj.org.za
Tel: +27 (0)83 587 7322

List of Publications

International Journal Articles

Bickell, M. G., L. Zhou, and J. Nuyts (2016). "Spatially variant resolution modelling for iterative list-mode PET reconstruction". In: *IEEE Transactions on Medical Imaging* 35.7, pp. 1707 –1718.

Spangler-Bickell, M. G., L. Zhou, A. Z. Kyme, B. de Laat, R. R. Fulton, and J. Nuyts (2016a). "Optimising rigid motion compensation for small animal brain PET imaging". In: *Physics in Medicine and Biology* 61.19, pp. 7074–7091.

Spangler-Bickell, M. G., B. de Laat, R. Fulton, G. Bormans, and J. Nuyts (2016b). "The effect of isoflurane on 18F-FDG uptake in the rat brain: a fully conscious dynamic PET study using motion compensation". In: *EJNMMI Research* 6, p. 86.

Conference Proceedings

Angelis, G., **Bickell, M. G.**, A. Kyme, W. Ryder, L. Zhou, J. Nuyts, and S. Meikle (2013). "Calculated attenuation correction for awake small animal brain PET studies". In: *IEEE Nuclear Science Symposium and Medical Imaging Conference*.

Rezaei, A., **Bickell, M. G.**, R. Fulton, and J. Nuyts (2015). "Joint Activity and Attenuation Reconstruction of Listmode TOF-PET data". In: *IEEE Nuclear Science Symposium and Medical Imaging Conference* 1.2, pp. 2–3.

Bickell, M. G., L. Zhou, and J. Nuyts (2013). "Spatially Variant Resolution Modelling for Iterative List-Mode PET Reconstruction". In: *IEEE Nuclear Science Symposium and Medical Imaging Conference*.

Bickell, M. G., T. Koesters, F. Boada, and J. Nuyts (2014a). "PET motion correction using MR-derived motion parameters". In: *EJNMMI Physics* 1.Suppl 1, A53.

Bickell, M. G., J. Gillam, R. Fulton, and J. Nuyts (2014b). "Spatially Variant Resolution Modelling Using Redistributed Lines-of-Response and the Image Space Reconstruction Algorithm". In: *IEEE Nuclear Science Symposium and Medical Imaging Conference*, pp. 1–5.

Bickell, M. G., J.-H. Kim, A. Rezaei, J. Nuyts, and R. Fulton (2015a). "Rigid motion correction of PET and CT for PET/CT brain imaging". In: *IEEE Nuclear Science Symposium and Medical Imaging Conference*, M5DP–124.

Bickell, M. G., B. de Laat, R. Fulton, G. Bormans, and J. Nuyts (2015b). "The Effect of Anaesthesia on 18F-FDG Uptake in the Rat Brain: A Fully Conscious Dynamic Study using Motion Correction". In: *IEEE Nuclear Science Symposium and Medical Imaging Conference*.

Zhou, L., **Bickell, M. G.**, A. Kyme, R. Fulton, and J. Nuyts (2013). "Improvement in motion correction technique for microPET brain imaging". In: *IEEE Nuclear Science Symposium and Medical Imaging Conference*, pp. 1–4.

Bibliography

Alessio, A. M. and A. Rahmim (2013). "Resolution modeling enhances PET imaging". In: *Medical Physics* 40.12, pp. 1–4.

Alstrup, A. K. O., M. Simonsen, and A. M. Landau (2011). "Type of anesthesia influences positron emission tomography measurements of dopamine D2/3 receptor binding in the rat brain". In: *Scandinavian Journal of Laboratory Animal Science* 38.3, pp. 195–200.

Alstrup, A. K. O. and D. F. Smith (2013). "Anaesthesia for positron emission tomography scanning of animal brains." In: *Laboratory Animals* 47.1, pp. 12–18.

Angelis, G. I., a. Z. Kyme, W. J. Ryder, R. R. Fulton, and S. R. Meikle (2014). "Attenuation correction for freely moving small animal brain PET studies based on a virtual scanner geometry." In: *Physics in Medicine and Biology* 59.19, pp. 5651–66.

Angelis, G., M. G. Bickell, A. Kyme, W. Ryder, L. Zhou, J. Nuyts, and S. Meikle (2013). "Calculated attenuation correction for awake small animal brain PET studies". In: *IEEE Nuclear Science Symposium and Medical Imaging Conference*.

Angelis, G. I., J. E. Gillam, W. J. Ryder, A. Z. Kyme, R. R. Fulton, and S. R. Meikle (2015). "Direct Estimation of Neurotransmitter Response in Awake and Freely Moving Animals". In: *IEEE Nuclear Science Symposium and Medical Imaging Conference*.

Autret, A., J. Bert, O. Strauss, and D. Visvikis (2013). "Fully 3D PET List-Mode reconstruction including an accurate detector modeling on GPU architecture". In: *FULLY 3D 2013: International meeting on fully three dimensional image reconstruction in radiology and nuclear medecine*, pp. 229–232.

Balcerzyk, M., G. Kontaxakis, M. Delgado, L. Garcia-Garcia, C. Correcher, A. J. Gonzalez, A. Gonzalez, J. L. Rubio, J. M. Benlloch, and M. a. Pozo (2009). "Initial performance evaluation of a high resolution Albira small animal positron emission tomography scanner with monolithic crystals and depth-of-interaction encoding from a user's perspective". In: *Measurement Science and Technology* 20.10, p. 104011.

Bickell, M. G., J.-H. Kim, A. Rezaei, J. Nuyts, and R. Fulton (2015a). "Rigid motion correction of PET and CT for PET/CT brain imaging". In: *IEEE Nuclear Science Symposium and Medical Imaging Conference*, M5DP–124.

Bickell, M. G., B. de Laat, R. Fulton, G. Bormans, and J. Nuyts (2015b). "The Effect of Anaesthesia on 18F-FDG Uptake in the Rat Brain: A Fully Conscious Dynamic Study using Motion Correction". In: *IEEE Nuclear Science Symposium and Medical Imaging Conference*.

Bickell, M. G., A. Buffler, and I. Govender (2011). "A fully 4D mesh parameterisation PET image reconstruction algorithm for list-mode data". In: *IEEE Nuclear Science Symposium and Medical Imaging Conference*, pp. 2620–2624.

Bickell, M. G., L. Zhou, and J. Nuyts (2013). "Spatially Variant Resolution Modelling for Iterative List-Mode PET Reconstruction". In: *IEEE Nuclear Science Symposium and Medical Imaging Conference*.

Bickell, M. G., T. Koesters, F. Boada, and J. Nuyts (2014). "PET motion correction using MR-derived motion parameters". In: *EJNMMI Physics* 1.Suppl 1, A53.

Bickell, M. G., L. Zhou, and J. Nuyts (2016). "Spatially variant resolution modelling for iterative list-mode PET reconstruction". In: *IEEE Transactions on Medical Imaging* 35.7, pp. 1707 –1718.

Bloomfield, P. M., T. J. Spinks, J. Reed, L. Schnorr, A. M. Westrip, L. Livieratos, R. Fulton, and T. Jones (2003). "The design and implementation of a motion correction scheme for neurological PET." In: *Physics in Medicine and Biology* 48.8, pp. 959–978.

Bowen, S. L., L. G. Byars, C. J. Michel, D. B. Chonde, and C. Catana (2013). "Influence of the partial volume correction method on (18)F-fluorodeoxyglucose brain kinetic modelling from dynamic PET images reconstructed with resolution model based OSEM." In: *Physics in Medicine and Biology* 58.20, pp. 7081–106.

Brambilla, M., C. Secco, M. Dominietto, R. Matheoud, G. Sacchetti, and E. Inglese (2005). "Performance Characteristics Obtained for a New 3-Dimensional Lutetium Oxyorthosilicate-Based Whole-Body PET/CT Scanner with the National Electrical Manufacturers Association NU 2-2001 Standard". In: *Journal of Nuclear Medicine* 46.12, pp. 2083–2091.

Brenner, D. J., C. D. Elliston, E. J. Hall, and W. E. Berdon (2001). "Estimated Risks of Radiation- Induced Fatal Cancer from Pediatric CT". In: *American Journal of Roentgenology* 176.2, pp. 289–296.

Brzeziński, K, J. F. Oliver, J Gillam, and M Rafecas (2014). "Study of a high-resolution PET system using a Silicon detector probe". In: *Physics in Medicine and Biology* 59.20, pp. 6117–6140.

Bühler, P., U. Just, E. Will, J. Kotzerke, and J. Van Den Hoff (2004). "An Accurate Method for Correction of Head Movement in PET". In: *IEEE Transactions on Medical Imaging* 23.9, pp. 1176–1185.

Carson, R., W. Barker, J.-S. Liow, and C. A. Johnson (2003). "Design of a motion-compensation OSEM list-mode algorithm for resolution-recovery reconstruction for the HRRT". In: *IEEE Nuclear Science Symposium and Medical Imaging Conference* 20892, pp. 3281–3285.

Casey, M. E. and R. Nutt (1986). "A Multicrystal Two Dimensional BGO Detector System for Positron Emission Tomography". In: *IEEE Transactions on Nuclear Science* 33.1, pp. 460–463.

Casteels, C., K. Vunckx, S.-A. Aelvoet, V. Baekelandt, G. Bormans, K. Van Laere, and M. Koole (2013). "Construction and evaluation of quantitative small-animal PET probabilistic atlases for [18F]FDG and [18F]FECT functional mapping of the mouse brain." In: *PloS one* 8.6, e65286.

Catana, C., T. Benner, A. van der Kouwe, L. Byars, M. Hamm, D. B. Chonde, C. J. Michel, G. El Fakhri, M. Schmand, and A. G. Sorensen (2011). "MRI-Assisted PET Motion Correction for Neurologic Studies in an Integrated MR-PET Scanner". In: *Journal of Nuclear Medicine* 52.1, pp. 154–161.

Chen, Y. and S. J. Glick (2007). "Determination of the System Matrix Used in List-Mode EM Reconstruction of PET". In: *IEEE Nuclear Science Symposium and Medical Imaging Conference*, pp. 3855–3858.

Chien, D. T., S. Bahri, A. K. Szardenings, J. C. Walsh, F. Mu, M. Y. Su, W. R. Shankle, A. Elizarov, and H. C. Kolb (2013). "Early Clinical PET Imaging Results with the Novel PHF-Tau Radioligand [F-18]-T807". In: *Journal of Alzheimer's Disease* 34.2, pp. 457–468.

Cloquet, C, F. C. Sureau, M Defrise, G Van Simaeys, N Trotta, and S Goldman (2010). "Non-Gaussian space-variant resolution modelling for list-mode reconstruction." In: *Physics in Medicine and Biology* 55.17, pp. 5045–5066.

Colombino, P, B Fiscella, and L Trossi (1965). "Study of positronium in water and ice from 22 to-144 C by annihilation quanta measurements". In: *Il Nuovo Cimento Series 10* 38.2.

Daube-Witherspoon, M. and G. Muehllehner (1986). "An iterative image space reconstruction algorithm suitable for volume ECT". In: *IEEE Transactions on Medical Imaging* MI-5.2, pp. 61–66.

Daube-Witherspoon, M., Y. Yan, M. Green, R. Carson, K. Kempner, and P Herscovitch (1990). "Correction for motion distortion in PET by dynamic monitoring of patient position". In: *Journal of Nuclear Medicine* 31.5, p. 816.

De Man, B. and S. Basu (2004). "Distance-driven projection and backprojection in three dimensions". In: *Physics in Medicine and Biology* 49.11, pp. 2463–2475.

Defrise, M., A. Rezaei, and J. Nuyts (2012). "Time-of-flight PET data determine the attenuation sinogram up to a constant." In: *Physics in Medicine and Biology* 57.4, pp. 885–899.

Defrise, M., A. Rezaei, and J. Nuyts (2014). "Transmission-less attenuation correction in time-of-flight PET: analysis of a discrete iterative algorithm." In: *Physics in Medicine and Biology* 59.4, pp. 1073–1095.

Deleye, S., J. Verhaeghe, L. Wyffels, S. Dedeurwaerdere, S. Stroobants, and S. Staelens (2014). "Towards a reproducible protocol for repetitive and semi-quantitative rat brain imaging with 18 F-FDG: Exemplified in a memantine pharmacological challenge". In: *NeuroImage* 96, pp. 276–287.

Delso, G., S. Fürst, B. Jakoby, R. Ladebeck, C. Ganter, S. G. Nekolla, M. Schwaiger, and S. I. Ziegler (2011). "Performance Measurements of the Siemens mMR Integrated Whole-Body PET/MR Scanner". In: *Journal of Nuclear Medicine* 52.12, pp. 1914–1922.

Derenzo, S. E. (1979). "Precision measurement of annihilation point spread distributions for medically important positron emitters". In: *5th International Conference on Positron Annihilation*.

Derenzo, S. E. (1986). "Mathematical Removal of Positron Range Blurring in High Resolution Tomography". In: *IEEE Transactions on Nuclear Science* 33.1, pp. 565–569.

Diltoer, M. and F. Camu (1988). "Glucose homeostasis and insulin secretion during isoflurane anesthesia in humans." In: *Anesthesiology* 68.6, pp. 880–886.

Dinelle, K., S. Blinder, J.-C. Cheng, S. Lidstone, K. Buckley, T. Ruth, and V. Sossi (2006). "Investigation of Subject Motion Encountered During a Typical Positron Emission Tomography Scan." In: *IEEE Nuclear Science Symposium and Medical Imaging Conference*, pp. 1–5.

Feng, L., R. Grimm, K. Tobias Block, H. Chandarana, S. Kim, J. Xu, L. Axel, D. K. Sodickson, and R. Otazo (2013). "Golden-angle radial sparse parallel MRI: Combination of compressed sensing, parallel imaging, and golden-angle radial sampling for fast and flexible dynamic volumetric MRI". In: *Magnetic Resonance in Medicine* 00.

Fueger, B. J., J. Czernin, I. Hildebrandt, C. Tran, B. S. Halpern, D. Stout, M. E. Phelps, and W. A. Weber (2006). "Impact of animal handling on the results of 18F-FDG PET studies in mice." In: *Journal of Nuclear Medicine* 47.6, pp. 999–1006.

Fulton, R. R., B. F. Hutton, M Braun, B Ardekani, and R Larkin (1994). "Use of 3D reconstruction to correct for patient motion in SPECT". In: *Physics in Medicine and Biology* 39.3, p. 563.

Fulton, R. R., S. Member, S Eberl, B. F. Hutton, S. Member, and M Braun (1999). "A Practical 3D Tomographic Method for Correcting Patient Head Motion in Clinical SPECT". In: *IEEE Transactions on Nuclear Science* 46.3, pp. 667–672.

Fulton, R., I. Nickel, L. Tellmann, S. Meikle, U. Pietrzyk, and H. Herzog (2003). "Event-by-Event Motion Compensation in 3D PET". In: *IEEE Nuclear Science Symposium and Medical Imaging Conference* 5, pp. 3286–3289.

Fulton, R., S. Meikle, A. Z. Kyme, V. Zhou, K. Popovic, M. Kassiou, and M. Akhtar (2009). "Motion-Corrected MicroPET Brain Imaging of Conscious Rats". In: *World Molecular Imaging Conference, Montreal* 12, s304–s305.

Fulton, R., S. Meikle, and S. Eberl (2002). "Correction for head movements in positron emission tomography using an optical motion-tracking system". In: *IEEE Transactions on Nuclear Science* 49.1, pp. 116–123.

Gillam, J. E., P Solevi, J. F. Oliver, and M Rafecas (2013). "Simulated one-pass list-mode: an approach to on-the-fly system matrix calculation". In: *Physics in Medicine and Biology* 58.7, pp. 2377–94.

Goldstein, S. R., M. E. Daube-Witherspoon, M. V. Green, and A Eidsath (1997). "A head motion measurement system suitable for emission computed tomography." In: *IEEE Transactions on Medical Imaging* 16.1, pp. 17–27.

Gonzalez, E., J.-y. Cui, and G. Pratx (2011). "Point spread function for PET detectors based on the probability density function of the line segment". In: *IEEE Nuclear Science Symposium and Medical Imaging Conference*, pp. 4386–4389.

Grant, A. M., T. W. Deller, M. M. Khalighi, S. H. Maramraju, G. Delso, and C. S. Levin (2016). "NEMA NU 2-2012 performance studies for the SiPM-based ToF-PET component of the GE SIGNA PET/MR system". In: *Medical Physics* 43, pp. 2334–2343.

Green, M. V., J Seidel, S. D. Stein, T. E. Tedder, K. M. Kempner, C Kertzman, and T. a. Zeffiro (1994). "Head movement in normal subjects during simulated PET brain imaging with and without head restraint." In: *Journal of Nuclear Medicine* 35.9, pp. 1538–1546.

Gupta, R. G., C. Schafer, Y. Ramaroson, M. G. Sciullo, and C. C. Horn (2016). "Role of the abdominal vagus and hindbrain in inhalational anesthesia-induced vomiting". In: *Autonomic Neuroscience*.

Harada, R., N. Okamura, S. Furumoto, K. Furukawa, A. Ishiki, N. Tomita, T. Tago, K. Hiraoka, S. Watanuki, M. Shidahara, M. Miyake, Y. Ishikawa, R. Matsuda, A. Inami, T. Yoshikawa, Y. Funaki, R. Iwata, M. Tashiro, K. Yanai, H. Arai, and Y. Kudo (2015). "18F-THK5351: A Novel PET Radiotracer for Imaging Neurofibrillary Pathology in Alzheimer's Disease." In: *Journal of Nuclear Medicine* 57.2, pp. 1–43.

Hildebrandt, I. J., H. Su, and W. A. Weber (2008). "Anesthesia and other considerations for in vivo imaging of small animals." In: *ILAR journal / National Research Council, Institute of Laboratory Animal Resources* 49.1, pp. 17–26.

Hoffman, E. J., S. C. Huang, M. E. Phelps, and D. E. Kuhl (1981). *Quantitation in positron emission computed tomography: 4. Effect of accidental coincidences.*

Horn, B. K. P. (1987). "Closed-Form Solution of Absolute Orientation Using Orthonormal Matrices". In: *Journal of the Optical Society of America A* 4, p. 629.

Hosoi, R., A. Matsumura, S. Mizokawa, M. Tanaka, F. Nakamura, K. Kobayashi, Y. Watanabe, and O. Inoue (2005). "MicroPET detection of enhanced 18F-

FDG utilization by PKA inhibitor in awake rat brain." In: *Brain Research* 1039.1-2, pp. 199–202.

Hudson, H. M. and R. S. Larkin (1994). "Accelerated image reconstruction using ordered subsets of projection data". In: *IEEE Transactions on Medical Imaging* 13.4, pp. 601–609.

Huesman, R. H., G. J. Klein, W. W. Moses, J Qi, B. W. Reutter, and P. R. Virador (2000). "List-mode maximum-likelihood reconstruction applied to positron emission mammography (PEM) with irregular sampling." In: *IEEE Transactions on Medical Imaging* 19.5, pp. 532–7.

Hutton, B. F., A. Z. Kyme, Y. H. Lau, D. W. Skerrett, and R. R. Fulton (2002). "A Hybrid 3-D Reconstruction / Registration Algorithm for Correction of Head Motion in Emission Tomography". In: *IEEE Transactions on Nuclear Science* 49.1, pp. 188–194.

Jakoby, B. W., Y Bercier, M Conti, M. E. Casey, B Bendriem, and D. W. Townsend (2011). "Physical and clinical performance of the mCT time-of-flight PET/CT scanner." In: *Physics in Medicine and Biology* 56.8, pp. 2375–2389.

Jin, X., C. Chan, T. Mulnix, V. Panin, M. E. Casey, C. Liu, and R. E. Carson (2013). "List-mode reconstruction for the Biograph mCT with physics modeling and event-by-event motion correction". In: *Physics in Medicine and Biology* 58.16, pp. 5567–5591.

Johnson, G. A., E. Calabrese, A. Badea, G. Paxinos, and C. Watson (2012). "A multidimensional magnetic resonance histology atlas of the Wistar rat brain". In: *NeuroImage* 62.3, pp. 1848–1856.

Jong, H. W. de, F. H. van Velden, R. W. Kloet, F. L. Buijs, R Boellaard, and A. A. Lammertsma (2007). "Performance evaluation of the ECAT HRRT: an LSO-LYSO double layer high resolution, high sensitivity scanner". In: *Physics in Medicine and Biology* 52.5, pp. 1505–1526.

Kim, J.-H., J Nuyts, A Kyme, Z Kuncic, and R Fulton (2015). "A rigid motion correction method for helical computed tomography (CT)". In: *Physics in Medicine and Biology* 60, pp. 2047–2073.

Kim, J.-H., T Sun, a. R. Alcheikh, Z Kuncic, J Nuyts, and R Fulton (2016). "Correction for human head motion in helical x-ray CT". In: *Physics in Medicine and Biology* 61.4, pp. 1416–1438.

Kim, J.-H., J. Nuyts, Z. Kuncic, and R. Fulton (2013). "The feasibility of head motion tracking in helical CT: a step toward motion correction." In: *Medical Physics* 40.4, p. 041903.

Kofke, W. A., R. A. Hawkins, D. W. Davis, J. F. Biebuyck, and R. D. Miller (1987). "Comparison of the Effects of Volatile Anesthetics on Brain Glucose Metabolism in Rats". In: *Anesthesiology* 66(6), pp. 810–813.

Kontaxakis, G, L. Strauss, and G. van Kaick (1998). "Optimized image reconstruction for emission tomography using ordered subsets, median root

prior and a web-based interface". In: *IEEE Nuclear Science Symposium and Medical Imaging Conference* 1, pp. 1347–1352.

Kyme, A, J Eisenhuth, V Zhou, W Ryder, G Angelis, K Popovic, R Bashir, R Fulton, and S Meikle (2012). "Developing a system for the molecular imaging of freely moving rats". In: *World Molecular Imaging Congress 2012, Dublin, Ireland*.

Kyme, A., J. Maclaren, S. Meikle, C. Baldock, and R. Fulton (2011a). "The effect of time domain pose filtering on accuracy of small marker based motion correction in awake animal PET". In: *IEEE Nuclear Science Symposium and Medical Imaging Conference* 3, pp. 2290–2294.

Kyme, A., S. Se, S. Meikle, G. Angelis, W. Ryder, K. Popovic, D. Yatigammana, and R. Fulton (2014). "Markerless motion tracking of awake animals in positron emission tomography". In: *IEEE Transactions on Medical Imaging* 33.11, pp. 2180–2190.

Kyme, A. Z., B. F. Hutton, R. L. Hatton, D. W. Skerrett, and L. R. Barnden (2003). "Practical aspects of a data-driven motion correction approach for brain SPECT." In: *IEEE Transactions on Medical Imaging* 22.6, pp. 722–9.

Kyme, A. Z., V. W. Zhou, S. R. Meikle, and R. R. Fulton (2008). "Real-time 3D motion tracking for small animal brain PET". In: *Physics in Medicine and Biology* 53.10, pp. 2651–2666.

Kyme, A. Z., V. W. Zhou, S. R. Meikle, C. Baldock, and R. R. Fulton (2011b). "Optimised motion tracking for positron emission tomography studies of brain function in awake rats". In: *PloS one* 6.7, e21727.

Langner, J. (2009). "Event-Driven Motion Compensation in Positron Emission Tomography: Development of a Clinically Applicable Method". PhD thesis, p. 153.

Lecomte, R., D. Schmitt, and G. Lamoureux (1984). "Geometry Study of a High Resolution PET Detection System Using Small Detectors". In: *IEEE Transactions on Nuclear Science* NS-31.1, pp. 556–561.

Levin, C. S. and E. J. Hoffman (1999). "Calculation of positron range and its effect on the fundamental limit of positron emission tomography system spatial resolution". In: *Physics in Medicine and Biology* 44.3, pp. 781–99.

Liang, Z (1994). "Detector response restoration in image reconstruction of high resolution positron emission tomography". In: *IEEE Transactions on Medical Imaging* 13.2, pp. 314–21.

Loepke, A. W., J. C. McCann, C. D. Kurth, and J. J. McAuliffe (2006). "The physiologic effects of isoflurane anesthesia in neonatal mice". In: *Anesthesia and Analgesia* 102.1, pp. 75–80.

Lopresti, B., A. Russo, W. Jones, T. Fisher, D. Crouch, D. Altenburger, and D. Townsend (1999). "Implementation and performance of an optical motion tracking system for high resolution brain PET imaging". In: *IEEE Transactions on Nuclear Science* 46.6, pp. 2059–2067.

Malviya, S, T Voepel-Lewis, O. P. Eldevik, D. T. Rockwell, J. H. Wong, and a. R. Tait (2000). "Sedation and general anaesthesia in children undergoing MRI and CT: adverse events and outcomes." In: *British Journal of Anaesthesia* 84.6, pp. 743–748.

Matsumura, A, S Mizokawa, M Tanaka, Y Wada, S Nozaki, F Nakamura, S Shiomi, H Ochi, and Y. Watanabe (2003). "Assessment of microPET performance in analyzing the rat brain under different types of anesthesia: comparison between quantitative data obtained with microPET and ex vivo autoradiography". In: *NeuroImage* 20.4, pp. 2040–2050.

McLaughlin, K. J., J. L. Gomez, S. E. Baran, and C. D. Conrad (2007). "The effects of chronic stress on hippocampal morphology and function: An evaluation of chronic restraint paradigms". In: *Brain Research* 1161.1, pp. 56–64.

Menke, M., M. Atkins, and K. Buckley (1996). "Compensation methods for head motion detected during PET imaging". In: *IEEE Transactions on Nuclear Science* 43.1, pp. 310–317.

Miranda, A, S Staelens, S Stroobants, and J Verhaeghe (2015). "Fast motion tracking of radioactive markers for motion correction of awake and unrestrained rat brain". In: *IEEE Nuclear Science Symposium and Medical Imaging Conference*, pp. 6–9.

Moehrs, S., M. Defrise, N. Belcari, A. D. Guerra, A. Bartoli, S. Fabbri, and G. Zanetti (2008). "Multi-ray-based system matrix generation for 3D PET reconstruction". In: *Physics in Medicine and Biology* 53.23, pp. 6925–45.

Mollet, P. and S. Vandenberghe (2014). "Comparison of transmission- and emission-based attenuation correction for TOF-PET / MRI". In: *IEEE Nuclear Science Symposium and Medical Imaging Conference*, pp. 1–5.

Moses, W. W. and S. E. Derenzo (1993). "Empirical observation for spatial resolution degradation in positron emission tomographs utilizing block detectors". In: *Journal of Nuclear Medicine* 34.5, p. 101.

Moses, W. W. (2011). "Nuclear Instruments and Methods in Physics Research A Fundamental limits of spatial resolution in PET". In: *Nuclear Instruments and Methods in Physics Research, A* 648, S236–S240.

Mumcuoglu, E. and R. Leahy (1996). "Accurate geometric and physical response modelling for statistical image reconstruction in high resolution PET". In: *IEEE Nuclear Science Symposium and Medical Imaging Conference*, pp. 1569–1573.

Noonan, P. J., J Howard, W. a. Hallett, and R. N. Gunn (2015). "Repurposing the Microsoft Kinect for Windows v2 for external head motion tracking for brain PET". In: *Physics in Medicine and Biology* 60.22, pp. 8753–8766.

Noonan, P. and J Howard (2012). "Realtime markerless rigid body head motion tracking using the Microsoft Kinect". In: *IEEE Nuclear Science Symposium and Medical Imaging Conference*, pp. 2241–2246.

Nuyts, J. (2014). "Unconstrained image reconstruction with resolution modelling does not have a unique solution". In: *EJNMMI Physics* 1.98, pp. 1–7.

Nuyts, J., D Beque, P. Dupont, and L. Mortelmans (2002). "A concave prior penalizing relative differences for maximum-a-posteriori reconstruction in emission tomography". In: *IEEE Transactions on Nuclear Science* 49.1, pp. 56–60.

Nuyts, J., J.-h. Kim, and R. Fulton (2011). "Iterative CT reconstruction with correction for known rigid motion". In: *11th International Meeting on Fully 3D Reconstruction in Radiology and Nuclear Medicine*, pp. 132–135.

Nuyts, J., B. D. Man, P. Dupont, and M. Defrise (1998). "Iterative reconstruction for helical CT : a simulation study". In: *Physics in Medicine and Biology* 43, pp. 729–737.

Olesen, O. V., J. M. Sullivan, T. Mulnix, R. R. Paulsen, L. Højgaard, B. Roed, R. E. Carson, E. D. Morris, and R. Larsen (2013). "List-mode PET motion correction using markerless head tracking: proof-of-concept with scans of human subject." In: *IEEE Transactions on Medical Imaging* 32.2, pp. 200–9.

Panin, V. Y., F. Kehren, C. Michel, and M. Casey (2006). "Fully 3-D PET reconstruction with system matrix derived from point source measurements". In: *IEEE Transactions on Medical Imaging* 25.7, pp. 907–21.

Parra, L and H. H. Barrett (1998). "List-mode likelihood: EM algorithm and image quality estimation demonstrated on 2-D PET". In: *IEEE Transactions on Medical Imaging* 17.2, pp. 228–235.

Patel, V. D., D. E. Lee, D. L. Alexoff, S. L. Dewey, and W. K. Schiffer (2008). "Imaging dopamine release with Positron Emission Tomography (PET) and 11C-raclopride in freely moving animals". In: *NeuroImage* 41.3, pp. 1051–1066.

Picard, Y. and C. J. Thompson (1997). "Motion correction of PET images using multiple acquisition frames." In: *IEEE Transactions on Medical Imaging* 16.2, pp. 137–144.

Popilock, R., K. Sandrasagaren, L. Harris, and K. a. Kaser (2008). "CT artifact recognition for the nuclear technologist." In: *Journal of Nuclear Medicine Technology* 36.2, pp. 79–81.

Qi, J, R. M. Leahy, S. R. Cherry, A Chatziioannou, and T. H. Farquhar (1998). "High-resolution 3D Bayesian image reconstruction using the microPET small-animal scanner". In: *Physics in Medicine and Biology* 43.4, pp. 1001–13.

Qi, J. and R. H. Huesman (2005). "Effect of errors in the system matrix on maximum a posteriori image reconstruction." In: *Physics in Medicine and Biology* 50.14, pp. 3297–3312.

Rahmim, A., M. Lenox, C. Michel, A. Reader, and V. Sossi (2004a). "Space-variant and anisotropic resolution modeling in list-mode EM reconstruction".

In: *IEEE Nuclear Science Symposium and Medical Imaging Conference* 1, pp. 3074–3077.

Rahmim, A., P. Bloomfield, S. Houle, M. Lenox, C. Michel, K. R. Buckley, T. J. Ruth, and V. Sossi (2004b). "Motion Compensation in Histogram-Mode and List-Mode EM Reconstructions: Beyond the Event-Driven Approach". In: *IEEE Transactions on Nuclear Science* 51.5, pp. 2588–2596.

Rahmim, A., J. Qi, and V. Sossi (2013). "Resolution modeling in PET imaging: theory, practice, benefits, and pitfalls." In: *Medical Physics* 40.6, p. 064301.

Rapisarda, E, V Bettinardi, K Thielemans, and M. Gilardi (2010). "Image-based point spread function implementation in a fully 3D OSEM reconstruction algorithm for PET". In: *Physics in Medicine and Biology* 55.14, pp. 4131–4151.

Reader, A., P. Julyan, H. Williams, D. Hastings, and J. Zweit (2003). "EM Algorithm System Modeling by Image-Space Techniques for PET Reconstruction". In: *IEEE Transactions on Nuclear Science* 50.5, pp. 1392–1397.

Reader, A., E. Letourneau, and J. Verhaeghe (2011). "Generalization of the image space reconstruction algorithm". In: *IEEE Nuclear Science Symposium and Medical Imaging Conference* 6, pp. 4233–4238.

Reader, A. J., K. Erlandsson, M. A. Flower, and R. J. Ott (1998). "Fast accurate iterative reconstruction for low-statistics positron volume imaging". In: *Physics in Medicine and Biology* 43.4, pp. 835–46.

Rezaei, A., M. Defrise, G. Bal, C. Michel, M. Conti, C. Watson, and J. Nuyts (2012). "Simultaneous reconstruction of activity and attenuation in time-of-flight PET." In: *IEEE Transactions on Medical Imaging* 31.12, pp. 2224–2233.

Rezaei, A., M. G. Bickell, R. Fulton, and J. Nuyts (2015). "Joint Activity and Attenuation Reconstruction of Listmode TOF-PET data". In: *IEEE Nuclear Science Symposium and Medical Imaging Conference* 1.2, pp. 2–3.

Schiffer, W. K., M. M. Mirrione, and S. L. Dewey (2007). "Optimizing experimental protocols for quantitative behavioral imaging with 18F-FDG in rodents." In: *Journal of Nuclear Medicine* 48.2, pp. 277–87.

Schulz, D., S. Southekal, S. S. Junnarkar, J.-F. Pratte, M. L. Purschke, S. P. Stoll, B. Ravindranath, S. H. Maramraju, S. Krishnamoorthy, F. A. Henn, P. O'Connor, C. L. Woody, D. J. Schlyer, and P. Vaska (2011). "Simultaneous assessment of rodent behavior and neurochemistry using a miniature positron emission tomograph". In: *Nature Methods* 8.4, pp. 347–352.

Shepp, L. A. and Y. Vardi (1982). "Maximum Likelihood Reconstruction for Emission Tomography". In: *IEEE Transactions on Medical Imaging* 1.2, pp. 113–122.

Shibuya, K., E. Yoshida, F. Nishikido, T. Suzuki, T. Tsuda, N. Inadama, T. Yamaya, and H. Murayama (2007). "Annihilation photon acollinearity in

PET: volunteer and phantom FDG studies". In: *Physics in Medicine and Biology* 52.17, pp. 5249–61.

Spangler-Bickell, M. G., L. Zhou, A. Z. Kyme, B. de Laat, R. R. Fulton, and J. Nuyts (2016a). "Optimising rigid motion compensation for small animal brain PET imaging". In: *Physics in Medicine and Biology* 61.19, pp. 7074–7091.

Spangler-Bickell, M. G., B. de Laat, R. Fulton, G. Bormans, and J. Nuyts (2016b). "The effect of isoflurane on 18F-FDG uptake in the rat brain: a fully conscious dynamic PET study using motion compensation". In: *EJNMMI Research* 6, p. 86.

Stavdahl, O., A. K. Bondhus, K. Y. Pettersen, and K. E. Malvig (2005). "Optimal statistical operators for 3-dimensional rotational data: geometric interpretations and application to prosthesis kinematics". In: *Robotica* 23.3, pp. 283–292.

Strul, D, R. B. Slates, M Dahlbom, S. R. Cherry, and P. K. Marsden (2003). "An improved analytical detector response function model for multilayer small-diameter PET scanners". In: *Physics in Medicine and Biology* 48.8, pp. 979–94.

Sun, T., J. Nuyts, J.-h. Kim, and R. Fulton (2016). "An iterative projection-based motion estimation and compensation scheme for head X-ray CT". In: *Medical Physics*, pp. 1–22.

Tai, Y.-C., A. Ruangma, D. Rowland, S. Siegel, D. F. Newport, P. L. Chow, and R. Laforest (2005). "Performance evaluation of the microPET Focus: a third-generation microPET scanner dedicated to animal imaging". In: *Journal of Nuclear Medicine* 46.3, pp. 455–63.

Thielemans, K., P. Schleyer, J. Dunn, P. K. Marsden, and R. M. Manjeshwar (2013). "Using PCA to detect head motion from PET list mode data". In: *IEEE Nuclear Science Symposium and Medical Imaging Conference*, pp. 1–5.

Titterington, D. M. (1987). "On the Iterative Image Space Reconstruction Algorthm for ECT." In: *IEEE Transactions on Medical Imaging* MI-6.1, pp. 52–6.

Tomic, N., C. J. Thompson, and M. E. Casey (2005). "Investigation of the "block effect" on spatial resolution in PET detectors". In: *IEEE Transactions on Nuclear Science* 52.3 I, pp. 599–605.

Toyama, H., M. Ichise, J.-S. Liow, D. C. Vines, N. M. Seneca, K. J. Modell, J. Seidel, M. V. Green, and R. B. Innis (2004). "Evaluation of anesthesia effects on [18F]FDG uptake in mouse brain and heart using small animal PET." In: *Nuclear Medicine and Biology* 31.2, pp. 251–256.

Trumpy, G (1960). "Positron annihilation in aqueous solutions". In: *Physical Review* 118.3, pp. 668–674.

Van Der Kouwe, A. J. W., T. Benner, and A. M. Dale (2006). "Real-time rigid body motion correction and shimming using cloverleaf navigators". In: *Magnetic Resonance in Medicine* 56.5, pp. 1019–1032.

Vaska, P., C. L. Woody, D. J. Schlyer, S. Shokouhi, S. P. Stoll, J. F. Pratte, P. O'Connor, S. S. Junnarkar, S. Rescia, B. Yu, M. Porschke, A. Kandasamy, A. Villanueva, A. Kriplani, V. Radeka, N. Volkow, R. Lecomte, and R. Fontaine (2004). "RatCAP: Miniaturized head-mounted PET for conscious rodent brain imaging". In: *IEEE Transactions on Nuclear Science* 51.5 II, pp. 2718–2722.

Watson, C. C., D. Newport, and M. E. Casey (1996). "A single scatter simulation technique for scatter correction in 3D PET". In: *Three-Dimensional Image Reconstruction in Radiology and Nuclear Medicine*. Ed. by P. G. Amans and J .-L. Vol. 4. Kluwer, Dordrect, The Netherlands, pp. 255–268.

Weisenberger, A. G., S. S. Gleason, J. Goddard, B. Kross, S. Majewski, S. R. Meikle, M. J. Paulus, M. Pomper, V. Popov, M. F. Smith, B. L. Welch, and R. Wojcik (2005). "A restraint-free small animal SPECT imaging system with motion tracking". In: *IEEE Transactions on Nuclear Science* 52.3 I, pp. 638–644.

Wong, K.-P., W. Sha, X. Zhang, and S.-C. Huang (2011). "Effects of Administration Route, Dietary Condition, and Blood Glucose Level on Kinetics and Uptake of 18F-FDG in Mice". In: *Journal of Nuclear Medicine* 52.5, pp. 800–807.

Yao, R., R. M. Ramachandra, N. Mahajan, V. Rathod, N. Gunasekar, A. Panse, T. Ma, Y. Jian, J. Yan, and R. E. Carson (2012). "Assessment of a three-dimensional line-of-response probability density function system matrix for PET." In: *Physics in Medicine and Biology* 57.21, pp. 6827–48.

Yazdi, M. and L. Beaulieu (2007). "Artifacts in Spiral X-ray CT Scanners : Problems and Solutions". In: *World Academy of Science, Engineering and Technology* 11.11, pp. 96–100.

Zapp, M, W. Kofke, and D. Davis (1992). "Comparison of the effects of volatile anesthetics in varying concentrations on brain energy metabolism with brain ischemia in rats." In: *Neurochemical Research* 14.4, pp. 301–305.

Zeng, G. L. and G. T. Gullberg (2000). "Unmatched projector/backprojector pairs in an iterative reconstruction algorithm". In: *IEEE Transactions on Medical Imaging* 19.5, pp. 548–555.